Dissertation
submitted to the
Combined Faculty of Natural Sciences and Mathematics
of Heidelberg University, Germany
for the degree of
Doctor of Natural Sciences

Put forward by
Sabrina Gronow
born in: Kiel, Germany
Oral examination: 15.06.2021

Contribution of Type Ia supernovae to the chemical enrichment of the Milky Way: explosions of sub-M_{Ch} white dwarfs

Referees: Prof. Dr. Friedrich K. Röpke
apl. Prof. Dr. Stefan Jordan

Zusammenfassung

Type Ia supernovae (SNe Ia) sind wichtig für die chemische Entwicklung von Galaxien, da schwere Elemente in den Explosionen produziert werden. Sub-Chandrasekhar Massen Kohlenstoff-Sauerstoff Weiße Zwerge mit Heliumschalen stellen favorisierte Vorgänger für SNe Ia dar. Diese Arbeit untersucht Doppeldetonations-Explosionsscenarios. Ein Fokus liegt auf einer genauen Berechnung der Heliumdetonationspropagation in der Schale des Weißen Zwerges und der Berücksichtigung von Mischen zwischen Kern und Schale. Parameterstudien wurden durchgeführt, um zu analysieren, ob Variationen in beobachteten SNe Ia reproduziert werden, und, um (metallizitätsabhängige) Isotopenhäufigkeiten für anschließende Strahlungstransportrechnungen und galaktisch-chemische Evolutionsmodelle zur Verfügung zu stellen. Dreidimensionale Simulationen wurden mit dem Arepo Code durchgeführt. Ein zuvor vernachlässigter Zündungsmechanismus der Kohlenstoffdetonation wurde gefunden, welcher zeigt, dass die Konvergenze der Heliumdetonationswelle ausreicht, um eine Kohlenstoffdetonation in einer Übergangsregion zwischen Kern und Schale auszulösen. Die Modelle reproduzieren außerdem eine Reihe von Helligkeiten, welche mit SNe Ia assoziiert werden. Metallizitätsabhängige Isotopenhäufigkeiten zeigen, dass eine hohe Metallizität des Sterns die Produktion stabiler Isotope unterstützt, während die Manganproduktion deutlich verstärkt wird. Ein Model zur galaktisch-chemischen Entwicklung legt nahe, dass es mit Hilfe dieser Explosionsart möglich ist, 80% der solaren Manganproduktion wieder zugeben. Eine Berücksichtigung der metallizitätsabhängigen Isotopenhäufigkeiten unterstützt die Korrelation von [Mn/Fe] mit Metallizität in der Umgebung der Sonne.

Abstract

Type Ia supernovae (SNe Ia) are important for galactic chemical evolution (GCE) because they produce heavy elements. Sub-Chandrasekhar mass carbon-oxygen white dwarfs with helium shells are favored progenitors for SNe Ia. This thesis investigates the double detonation explosion scenario. A focus lies on an accurate calculation of the detonation propagation in the white dwarf shell and the assumption of core-shell mixing. Parameter studies were conducted to analyse whether variations found in observables of SNe Ia can be reproduced and to provide (metallicity-dependent) nucleosynthetic yields for subsequent radiative transfer calculations and GCE models. Three-dimensional simulations were carried out using the Arepo code. A previously neglected carbon detonation ignition mechanism was found showing that the helium detonation wave convergence is sufficient to ignite carbon in a core-shell transition region. The study shows that various luminosities coinciding with SNe Ia can be reproduced. Metallicity-dependent yields illustrate that a high stellar metallicity shifts the production to stable isotopes while supporting the manganese production. GCE models suggest that the inclusion of this explosion type allows to account for about 80% of the solar manganese abundance. The correlation of [Mn/Fe] with metallicity in the solar neighborhood is supported by the inclusion of metallicity-dependent SNe Ia yields.

Contents

List of Figures

List of Tables

List of Abbreviations

SN	supernova
SN Ia	Type Ia supernova
CC	core-collapse
WD	white dwarf
M_{Ch}	Chandrasekhar mass
sub-M_{Ch}	sub-Chandrasekhar mass
H-R diagram	Hertzsprung-Russel diagram
ZAMS	zero-age main sequence
RGB	red giant branch
AGB	asymptotic giant branch
p	proton
n	neutron
H	hydrogen
He	helium
C	carbon
N	nitrogen
O	oxygen
Ne	neon
Mg	magnesium
Si	silicon
Ti	titanium
V	vanadium
Cr	chrome
Mn	manganese
Fe	iron
Co	cobalt
Ni	nickel
Cu	copper
Zn	zinc
IME	intermediate mass element
IGE	iron group element
LIMS	low and intermediate-mass stars
GCE	galactic chemical evolution
DTD	delay time distribution
1D, 2D, 3D	one-, two-, three-dimensional

List of Physical Constants

$M_\odot$	$1.989 \times 10^{33}\,\mathrm{g}$
$R_\odot$	$6.955 \times 10^{10}\,\mathrm{cm}$
$Z_\odot$	0.013
$L_\odot$	$3.839 \times 10^{33}\,\frac{\mathrm{erg}}{\mathrm{s}}$
N_A	$6.02214076 \times 10^{23}\,\frac{1}{\mathrm{mol}}$
G	$6.673 \times 10^{-8}\,\mathrm{dyn\,cm^2\,g^{-2}}$
c	$299.792.458\,\mathrm{m\,s^{-1}}$

Chapter I

Context and theoretical background

I.1 Supernovae

Supernovae (SNe) are stellar explosions and occur upon the death of a star. A first observation of a SN dates back to 185 while multiple observations of one SN are only made since 1006 (see Green and Stephenson 2003 for a description of the history of SNe). That year astronomers in China and Japan found a new 'star' in the sky which was visible for several years. It is among the brightest transient events recorded in history. Figure I.1.1 shows an image of a SN, SN 1994D (lower left), which has a brightness similar to the center of the galaxy it belongs to. Other observations include a new transient emerging in 1572 with a brightness similar to Venus. Its description in 'De Nova Stella' by Brahe (1573) coined the name of these transients. A more detailed classification of the transient events was introduced as many more observations were made in successive centuries. W. Baade and F. Zwickey first used the term 'supernova' in the 1930s (e.g. Baade and Zwicky 1934). Following the large amount of SN observations, differences were found in the spectra leading to a subdivision of the luminous transients into several groups.

Figure I.1.1: Image of SN 1994D (lower left) in galaxy NGC 4526 taken by the Hubble Space Telescope; Credit: NASA/ESA, The Hubble Key Project Team and The High-Z Supernova Search Team.

I.1.1 Supernova classification

SNe are classified based on their observables. The classification by absorption lines in the spectrum was first introduced by Minkowski (1941) who separated observed SNe into two groups: those showing hydrogen (H) absorption lines and those who do not. These groups are called Type II SNe and Type I SNe, respectively. Li et al. (2011b) find that 57% of all SNe are of Type II. SNe with neither H nor strong helium (He) lines, but a prominent silicon (Si) line at a wavelength of about 6100 Å are classified as SNe Ia and make up about 24% of all SNe (Li et al. 2011b). If Si and H are absent, but He is found in the spectrum, the SN is of Type Ib. None of the three elements are observed in SNe Ic. In sum, about 19% of all SNe are of Type Ib or Ic (Li et al. 2011b). A simplified classification scheme is illustrated in Figure I.1.2 listing the four main classes of SNe. Several more subclasses, such as SNe Iax (Li et al. 2003, Foley et al. 2013) and SNe IIn (Schlegel 1990, Wegner and Swanson 1996), have been identified until today (see also Branch and Wheeler 2017).

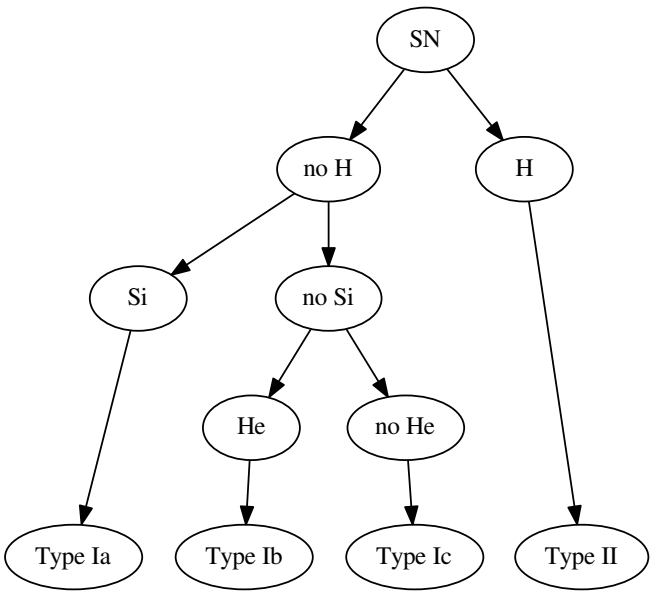

Figure I.1.2: Simplified SN classification scheme.

The classification scheme does not capture the explosion mechanism of the different SN types. While SNe Ia are the result of a thermonuclear explosion, other SNe pass through a core-collapse.

A thermonuclear explosion following a runaway can take place in degenerate matter. It can best be explained by a comparison of degenerate matter to an ideal gas. In an ideal gas, nuclear reactions cause an increase in temperature. This temperature rise can support further nuclear reactions, but also increases the pressure. A pressure increase then leads to a volume increase and decrease in density. As a consequence the temperature as well as the nuclear energy generation rate decrease again (see left sketch in Figure I.1.3).

This behavior is different in degenerate matter which is comprised of fermions. An increase in temperature due to nuclear reactions takes place independent of pressure and density. A temperature increase therefore does not cause a rise in pressure. A subsequent expansion of the

matter does not take place and the temperature is not decreased (see right sketch in Figure I.1.3). The positive feedback loop between nuclear reactions and temperature leads to a runaway. This develops in a hotspot in the SN Ia progenitor and a flame gets ignited. Stellar material is burnt and the star gets disrupted (Hoyle and Fowler 1960).

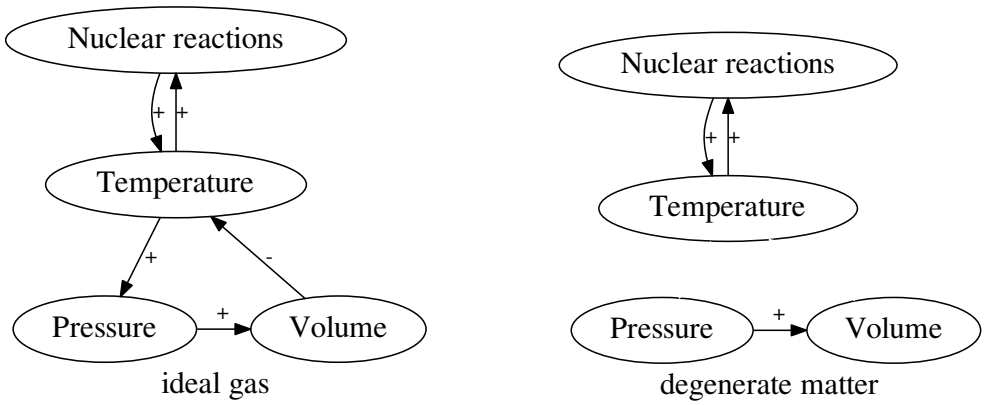

Figure I.1.3: Dependencies of pressure, volume, temperature, and nuclear reactions on each other for an ideal gas (*left*) and degenerate matter (*right*).

I.1.2 Type Ia supernovae

Normal SNe Ia form a homogeneous class of luminous transients. Studies have found that about one takes place per century in the Milky Way (MW, see e.g. Li et al. 2011a who find a value of 0.54 ± 0.12 per century for the MW), but they can be detected regularly in all types of galaxies (Tammann et al. 1994, Li et al. 2011a). In some cases they can be observed with the naked eye, like SN 1604 (Kepler's Supernova) which had a maximum apparent magnitude of -2.25 to -2.5 mag (Baade 1943) which corresponds to a maximum brightness of $M_{V,\,\mathrm{max}} = -19.3 \pm 0.7$ mag in the V-band (van den Bergh and Kamper 1977). The peak luminosity of a SN Ia can be about $10^{10}\,L_\odot$ (Contardo et al. 2000), indicating that they can be as bright as a galaxy (see Figure I.1.1). SNe Ia can often be observed for several hundred days while the explosion itself only takes about 2 s. Moore et al. (2015) show that the gravitational wave signal of SNe Ia lies between 10^{-1} and 10 Hz, while the characteristic strain is expected to be below 10^{-21}. Despite these low values, detections might be possible with future gravitational wave detectors BBO, DECIGO, and ALIA (Moore et al. 2015).

SNe Ia play an important role in galactic chemical evolution (GCE). They induce turbulence to their host galaxy and can cause a compression of interstellar material which supports the formation of new stars in these places. Furthermore, nucleosynthesis is taking place during the explosion of the star producing elements heavier than oxygen (O), especially iron (Fe), indicating that SNe Ia are an important Fe source (see Section I.2.7). They lead to an enrichment of the interstellar material with these heavy elements, including manganese (Mn) and Fe.

The progenitor of a SN Ia and details of the explosion mechanism are not known to date. Thermonuclear explosions of white dwarfs (WDs) with carbon-oxygen (CO) cores are well discussed in the literature (e.g. Whelan and Iben 1973, Nomoto 1982a, Webbink 1984, Livne 1990,

Livne and Glasner 1990, 1991, Shigeyama et al. 1992, Livne and Arnett 1995, Nugent et al. 1997, Hoeflich et al. 1998, García-Senz et al. 1999, Fink et al. 2007, 2010, Sim et al. 2010, Guillochon et al. 2010, Pakmor et al. 2010, 2011, Sim et al. 2012, Pakmor et al. 2013, Sim et al. 2013a, Moll and Woosley 2013, Shen and Bildsten 2014, Kashyap et al. 2015, Blondin et al. 2017a, Tanikawa et al. 2018, Shen et al. 2018a, Liu et al. 2018, Rebassa-Mansergas et al. 2019, Polin et al. 2019, Leung and Nomoto 2020, Gronow et al. 2020). WDs are generally split into two groups: those of Chandrasekhar mass (M_{Ch}) and those with a lower total mass, sub-M_{Ch} WDs (see Section I.2.2 for a description of the M_{Ch}). This thesis investigates sub-M_{Ch} WDs as progenitors of SNe Ia, their explosions as thermonuclear SNe and their contribution to the chemical enrichment of the MW. Different progenitor systems are presented in Section I.2 including a description of a possible detonation mechanism for a SN Ia in Section I.2.6. The theoretical and computational basis for simulations of such thermonuclear explosions are described in Section I.3. Chapters II, III, and IV summarize the results of different studies carried out in the framework of this thesis. They involve explosion simulations of sub-M_{Ch} WDs and investigate the impact of core-shell mixing on the detonation ignition mechanism (Chapter II), different mass configurations of the WD (Chapter III), and assume a varying metallicity of the WD (Chapter IV). A conclusion including a discussion on future SNe Ia modeling is presented in Chapter V.

I.1.2.1 Observables of Type Ia supernovae

As described in Section I.1.1 the SN classification is based on spectral features. The spectrum of a SN Ia does, however, change over time (see Figure I.1.4). The classification is made using the most prominent spectral features around peak luminosity in the B-band light curve, with a light curve showing the development of the luminosity as a function of time. At maximum light the spectrum is dominated by intermediate mass elements (IMEs) which are present in the outer layers of the ejecta (Filippenko 1997). At later times, features of iron group elements (IGEs) become distinctive. These originate from the inner ejecta where central core material was burnt. Typical ejecta velocities are of the order of 10.000 km/s, with outer ejecta having higher velocities than inner ejecta (Hillebrandt and Niemeyer 2000). The change in the spectrum is illustrated in Figure I.1.4 for SN 1998aq whose maximum light was on April 27, 1998 (Branch et al. 2003, compare black and red colored spectrum in Figure I.1.4). The most prominent absorption lines are highlighted. A comparison of the spectra of various normal SNe Ia, like SN 1998aq, illustrates a homogeneity indicating that they have the same progenitor.

However, some variations are visible in the light curve shapes of SNe Ia (see top panel in Figure I.1.5). These are attributed to different masses of the exploding star (Fink et al. 2010 and see Section I.2.5 for details). The maximum luminosity of the explosion is about -19.5 mag which is reached within 20 days of explosion. In the first few weeks since peak brightness the luminosity decreases by three orders of magnitude followed by a linear decrease in magnitudes. The light curve is powered by the radioactive decay of ^{56}Ni to ^{56}Co in the first few days and from ^{56}Co to stable ^{56}Fe in the subsequent $\sim$ 100 days (Bodansky et al. 1968, Colgate and McKee 1969) due to the different half lives of the isotopes. Phillips (1993) and Phillips et al. (1999) found a relation between the peak brightness of a SN Ia and the decline rate over 15 days after maximum B-band luminosity, Δm_{15}: Brighter light curves have a broader shape. This is the so-called width-luminosity relation or Phillips relation. A value of $\Delta m_{15} = 0.5$ indicates a broad light curve compared to a light curve with $\Delta m_{15} = 1.5$.

Several SN searches have been carried out. Among those are the Nearby Supernova Factory (Pereira et al. 2013), the Supernova Cosmology Project (e.g. Perlmutter et al. 1999), and the High-z Supernova Search (Schmidt et al. 1998). Many observed objects can be attributed to SNe Ia. Among those are, for example, SN 2011fe (Nugent et al. 2011), SN 2012cg (Graur et al.

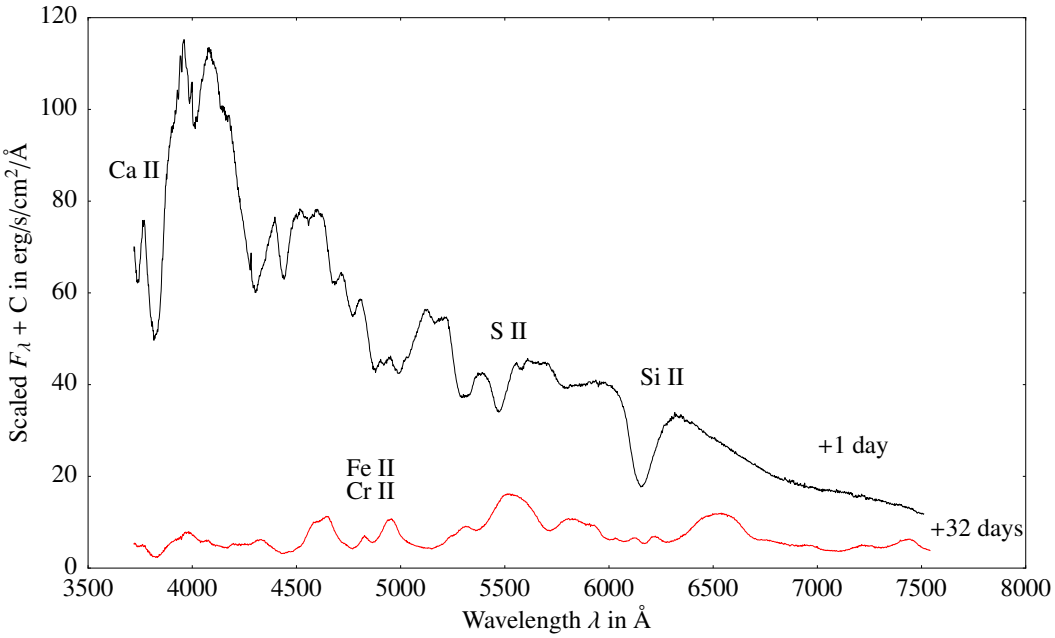

Figure I.1.4: Spectra of SN1998aq around (black) and 32 days after (red) maximum light in the B-band, based on Matheson et al. (2008) using data of the CfA Supernova Archive, which is funded in part by the National Science Foundation through grant AST 0907903; plotted is the scaled flux F_λ (plus offset) over wavelength λ.

2016), SN 2014J (Graur and Woods 2019), SN 2016jhr (Jiang et al. 2017), and SN 2018byg (De et al. 2019) which are used as objects of comparison in this thesis.

I.1.2.2 Type Ia supernovae in cosmology

SNe Ia are so-called standard candles (Branch and Tammann 1992), or more accurately standardisable, due to the self-similar light curve shape (see Figure I.1.5). Standard candles have a known luminosity. If such an object is observed, it can be used as distance measure to determine previously unknown or not well known parameters. The luminosity distance d_L (in parsec) to the object is given by

$$m - M = 5 \log d_L - 5. \tag{I.1.1}$$

with the absolute and apparent magnitudes M and m, respectively. Due to their spread in peak luminosity, SNe Ia are presumed to be standardisable. In order to use these observations as distance measures, the width-luminosity relation needs to be considered as it connects the luminosity to the decline rate. This is illustrated in the bottom panel of Figure I.1.5. The SNe Ia are scaled to match the brightness of SN 1991T. Furthermore, a stretch factor of 1.16 is applied (Takanashi et al. 2008, but also see Goldhaber et al. 2001) to account for the width-luminosity relation. However, this value only represents an average found by Takanashi et al. (2008). Therefore, the scaled light curves in the bottom panel of Figure I.1.5 are only approximations. For a more accurate treatement further corrections involving the redshift of the SNe Ia need to be applied. Riess et al. (1998) and Perlmutter et al. (1999) make use of these methods and derive an accelerated expansion of the universe using a set of SNe Ia at high redshifts. Figure I.1.6

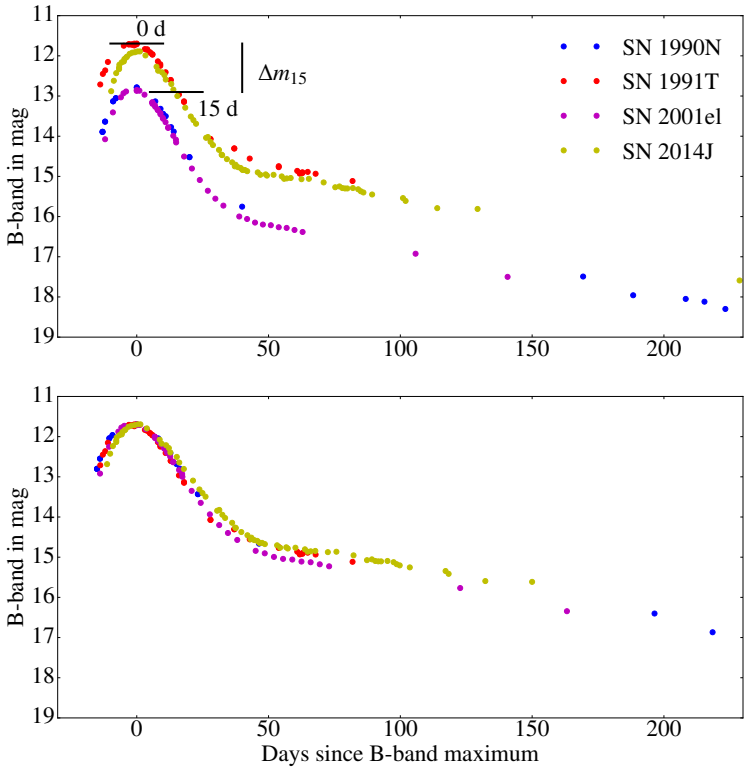

Figure I.1.5: Light curves of SN 1990N, SN 1991T (Lira et al. 1998), SN 2001el (Krisciunas et al. 2003), and SN 2014J (Li et al. 2019b) as measured in apparent magnitudes (*top*) and scaled to match SN 1991T in peak brightness employing a stretch factor for the light curve width (*bottom*).

illustrates the distribution of the SNe Ia in the brightness-redshift plane (see also Perlmutter et al. 1999). Via the relations

$$d_L = \frac{c}{H_0}\left(z + z^2\frac{1-q_0}{2} + \mathcal{O}(z^3)\right) \text{ and} \tag{I.1.2}$$

$$q_0 = \frac{1}{2}\sum_i \Omega_i(1+3w_i) = \frac{\Omega_M(a)}{2} - \Omega_\lambda(a) \tag{I.1.3}$$

(see Perlmutter and Schmidt 2003 for a derivation) cosmological parameters, such as the Hubble constant H_0, mass density Ω_M, and vacuum energy density Ω_λ can be inferred. The variables in Equations (I.1.2) and (I.1.3) are the speed of light c, redshift z, acceleration/deceleration parameter q_0 and equation of state parameter $w_i = \frac{p_i}{\rho_i c^2}$. In a universe that only consists of normal matter and the cosmological constant the right term in Equation (I.1.3) is derived, given $w_M = 0$ and $w_\lambda = -1$.

The two teams of Riess et al. (1998) and Perlmutter et al. (1999) deduce an age of the universe equal to 14.2 ± 1.7 Gyr and 14.5 ± 1.0 Gyr, respectively. A detailed description of the analysis is not given here, because the impact of SNe Ia to cosmology is not the aim of this thesis. The reader is referred to the work of S. Perlmutter, B. P. Schmidt, and A. G. Riess (Riess et al. 1998, Perlmutter et al. 1999) instead who received the Nobel Prize in Physics for their research in 2011.

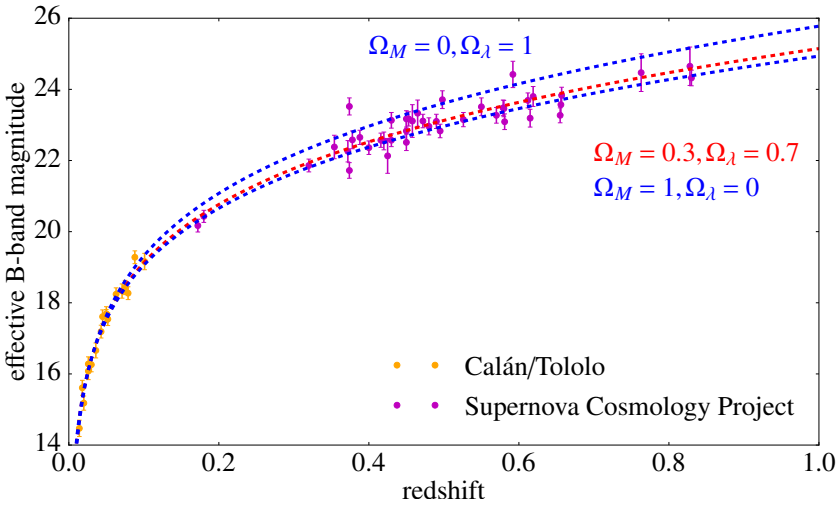

Figure I.1.6: Effective B-band magnitude over redshift for observed SNe Ia (data from Perlmutter et al. 1999). Cosmological predictions are shown as dashed lines for different vacuum energy and mass densities assuming a flat universe ($\sum_i \Omega_i = 1$). The best fit is plotted in red with mass density $\Omega_M = 0.3$ and vacuum energy density $\Omega_\lambda = 0.7$.

I.1.2.3 Type Ia supernovae and galactic chemical evolution

Only H and He were produced in the Big Bang. Heavier elements are synthesized in astrophysical processes, such as SN explosions or neutron star mergers, or in stellar interiors. Observations of objects of different ages confirm this, as older stars are deficient in heavy elements which are present in younger stars. Generally, the abundance of heavy elements increases over time starting with zero at the Big Bang until it reaches today's values.

As stated above, IGEs are produced in SNe Ia. These elements are ejected into the interstellar medium with the explosion causing an enrichment of the matter with such elements. Among those elements that are largely produced in SNe Ia is Fe. Fe is used as a measure of time for chemical enrichment in the form of [Fe/H] (McWilliam 1997). It is defined as

$$[\mathrm{Fe/H}] = \log\left(\frac{X(\mathrm{Fe})}{X(\mathrm{H})}\right) - \log\left(\frac{X_\odot(\mathrm{Fe})}{X_\odot(\mathrm{H})}\right) \tag{I.1.4}$$

with the mass fractions of Fe, $X(\mathrm{Fe})$, and H, $X(\mathrm{H})$, of the star. The subscript $_\odot$ denotes the respective solar values (Asplund et al. 2009). The ratio can be used as time measure since the Fe abundance in old stellar population is low and increases toward young population I stars.

SNe Ia occur following a delay time distribution (DTD) in the Universe (see Section I.2.6.1). This delay originates in the expected long evolution of the progenitor star before a SN Ia is ignited. The observed knee in the ratio of α-elements to Fe (see Figure I.1.7) is attributed to the onset of SN Ia explosions because of the large Fe production compared to the one of IMEs. It is, however, necessary to carry out simulations of these SN Ia explosions along with nucleosynthesis and GCE calculations in order to get detailed estimates in which way SNe Ia contribute to the enrichment (Greggio and Renzini 1983, Matteucci and Greggio 1986, Lach et al. 2020). Seitenzahl et al. (2013a), for example, show that SNe Ia provide a significant amount of Mn to the galactic abundance (see also Cescutti and Kobayashi 2017, Kobayashi et al. 2020, Eitner et al. 2020). Hendricks et al. (2014) find a knee in the distribution of the α-elements at [Fe/H] ≈ -1.9 for the Fornax dwarf spheroidal galaxy which corresponds to values found for other dwarf

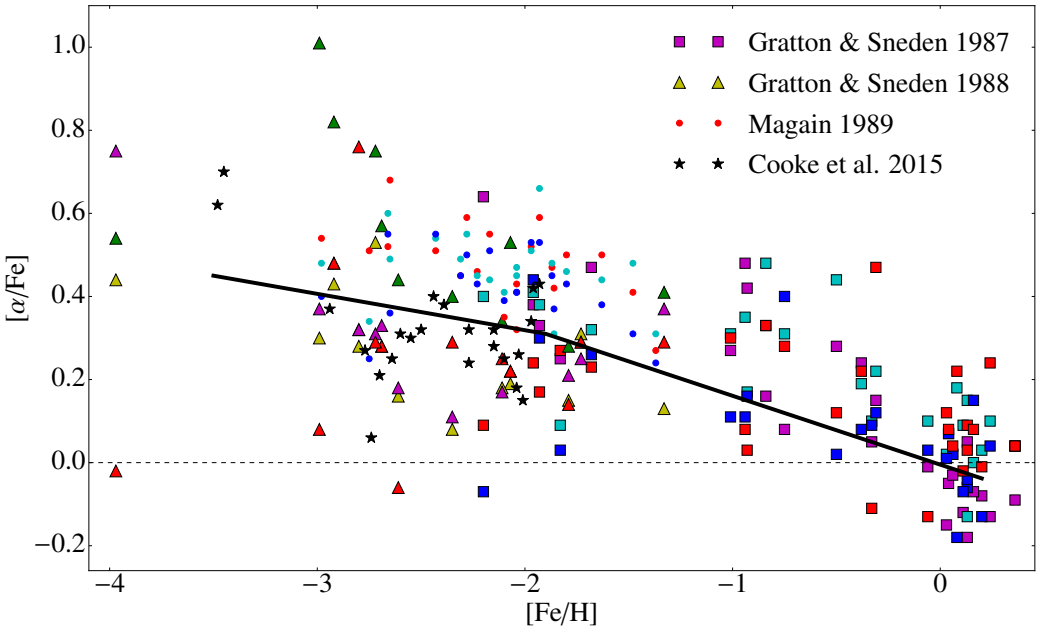

Figure I.1.7: α-elements (magnesium, calcium, silicon, titanium) over [Fe/H] based on data from Gratton and Sneden (1987, 1988), Magain (1989), and Cooke et al. (2015) similar to Wheeler et al. (1989) and Matteucci (1992); the black line illustrates an average evolution with a knee at [Fe/H] $= -1.9$.

spheroidal galaxies. A sketch of an average evolution of the α-elements over time with a knee at [Fe/H] $= -1.9$ is shown by the black line in Figure I.1.7. Different to this, the location is at [Fe/H] $= -1.04 \pm 0.02$ for the MW halo field stars (de Boer et al. 2014). Variations in the location of the knee are associated with the different total stellar mass of the galaxies as low mass dwarfs are less chemically enriched.

I.2 Progenitors of Type Ia supernovae: White dwarfs

To date no progenitor of a SN Ia has been observed. Therefore, details of a progenitor are not well known. A detection of a progenitor is challenging given the assumption that it is a faint and compact star as described below (see also Hillebrandt and Niemeyer 2000). Only McCully et al. (2014) claim to have found a progenitor of a SN Iax, a sub-luminous subclass of SNe Ia: A WD accreting matter from a He star.

Some constrains on the progenitor exist based on observations. As such, Bloom et al. (2012) state that the radius of the progenitor star must be smaller or equal to $0.02\,R_\odot$. This is based on a non-detection of a progenitor 4 h prior to the explosion of SN 2011fe. Further observations limit the density of the progenitor to be at least $10^4\,\mathrm{g\,cm^{-3}}$. In addition, the observed velocities of the SN ejecta are found to be of the order of 10.000 km/s (Hillebrandt and Niemeyer 2000). The associated kinetic energy (about 10^{51} erg, Thielemann et al. 2004) can only be reached by fusion of $1\,M_\odot$ of C and O to heavier elements (IMEs or IGEs, Contardo et al. 2000, Hillebrandt and Niemeyer 2000). All these findings imply that a compact object like a WD or neutron star is the progenitor.

The homogeneity of the light curves and spectra indicate that the progenitor is always the same. However, some variations of the progenitor star must be allowed in order to account for the small differences found in the observables of individual SNe Ia (Hillebrandt and Niemeyer 2000, Section I.1.2.1). An explosion of the progenitor star must further produce the observed amounts of ^{56}Ni as well as IMEs. The absence of H in the spectra also indicates that the initial H mass in the progenitor must be below $0.1\,M_\odot$. Taking these constrains into account and the fact that neutron stars are the product of another type of SN, WDs are found to be promising progenitors of SNe Ia (Hoyle and Fowler 1960), which is widely discussed in literature (see e.g. Maoz et al. 2014, Livio and Mazzali 2018 for reviews of possible progenitors).

I.2.1 WD formation

In this section the creation of a WD following stellar evolution is discussed. A description of different possible progenitor systems is given in the next section. Details on the numerical implementation of a WD and its detonation are explained in Section I.3.

Many stars become WDs at the end of their evolution. In fact, Napiwotzki (2009) state that a large fraction of the stars in our galaxy are WDs corresponding to about 10% of the mass in the MW.

The evolution of a star over time can be visualized in a Hertzsprung-Russel diagram (H-R diagram, see Figure I.2.1). An H-R diagram illustrates the stellar population in the luminosity and temperature regime. Further, changes in luminosity and temperature of a star during its lifetime can be displayed visualizing alterations in the stellar structure. The details of such a

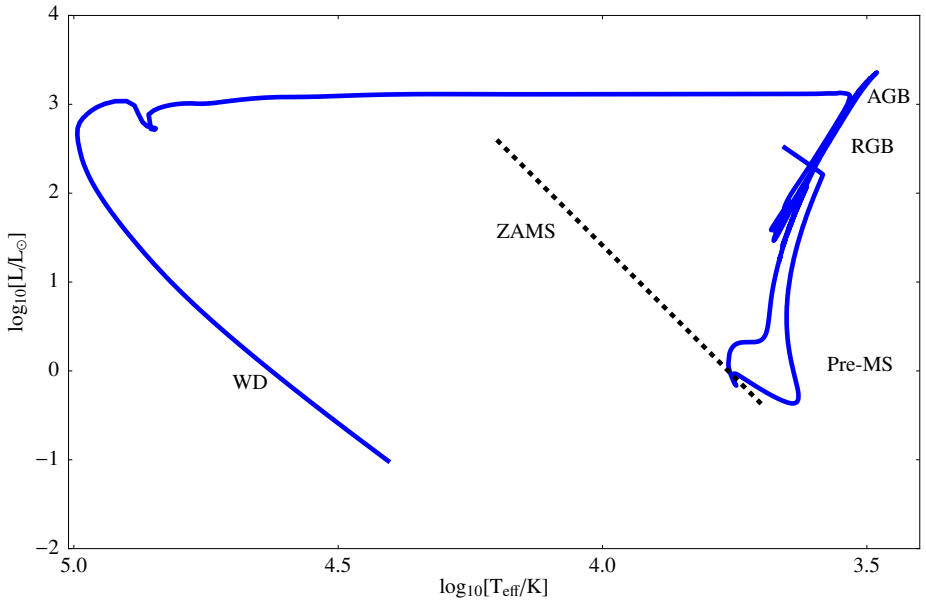

Figure I.2.1: Stellar evolution track of a $1\,M_\odot$ star with metallicity $Z = 0.02$ in a Hertzsprung-Russel diagram following Koester and Chanmugam (1990) and Farag et al. (2020) using the Modules for Experiments in Stellar Astrophysics code (MESA, Paxton et al. 2011, 2013, 2015, 2018, 2019) in revision 10108.

track depend on the mass of the star. Figure I.2.1 shows the evolutionary track for a $1\,M_\odot$ star.

In its pre-main sequence evolution gravitational pressure causes a contraction of the stellar core which results in a temperature increase as the H matter is non-degenerate (Koester and Chanmugam 1990). This rise in temperature allows the formation of heavier elements. A star primarily consists of H when it enters the main sequence (ZAMS in the figure) in the H-R diagram which is later burnt to He once high enough temperatures are reached for the ignition of H burning. Burning halts only when H is exhausted in the core leaving behind a star with a He core and a H envelope. At this point the star has left the main sequence and its luminosity has increased due to an increase in the mean molecular weight μ ($L \propto \mu^4$). Depending on the mass of the star further burning phases set in (see Hayashi and Cameron 1962, Iben 1967 for a description). Here, the discussion is limited to lower mass stars (total masses of $8\,M_\odot$ at most), focusing on a $1\,M_\odot$ star, as these are expected to form CO WDs (Koester and Chanmugam 1990, and see Iben 1967 for a description of the evolution of a $5\,M_\odot$ star). Degeneracy is an important parameter in these low mass stars. At high densities, ions and electrons contribute to the total pressure in the center of such stars as ideal gas and degenerate electron gas, respectively.

After H exhaustion in the core, H burning starts in a shell producing more He and causing the core to grow in mass. The growth leads to a contraction of the core. In order to counter balance this, the shell expands and the luminosity increases: The star becomes a giant star (Koester and Chanmugam 1990). The density of the core matter becomes higher as the core contracts while the star moves along the red giant branch (RGB). The core becomes degenerate. Due to this, the contraction does not cause a temperature increase (see Figure I.1.3), which is different to the pre-MS phase. He burning starts once high enough temperatures (of about 10^8 K) are reached in core material. The start of He fusion leads to a thermal runaway. The process results in an extreme surplus of nuclear energy in a short time period which gives this evolutionary stage its name, He flash (Gautschy 2012). Depending on the mass, a star can experience several He

flashes. The energy released in these flashes is absorbed by the outer non-degenerate matter of the star and does not reach its surface. The degeneracy of the core is lifted as the temperature rises at constant core density. At the high temperatures the pressure contribution of the ideal gas is larger than the one of the degenerate matter. The matter behaves like an ideal gas and the core expands due to the high pressure. The energy generation rate decreases until the core is in thermal equilibrium again and the luminosity of the star drops. The core mass stays almost constant during this phase.

He burning becomes stable in the core and is surrounded by a H burning shell. When He is exhausted in the core, He shell burning sets in. During the He burning phase the luminosity increases again with rising core mass moving along the asymptotic giant branch (AGB, Koester and Chanmugam 1990). This is the case because a core contraction is mirrored by an expansion of the shell. The matter becomes degenerate again until the increasing gravity force is balanced by the Fermi pressure force in the degenerate state. At this point the star consists of a CO core. In stars with masses of at least $4\,M_\odot$ H shell burning is extinguished in the early AGB phase (Pols et al. 2001). It is re-ignited as the convective envelope reaches up to the H layer (see Kippenhahn et al. 2012) and thermal pulses occur. They can result in the admixture of core material to the outer layers in so-called dredge-ups.

It is assumed that the H-rich envelope is lost either by stellar winds or interactions with other stars (see e.g. Iben and Renzini 1983, Blöcker 1995) once the star reaches the end of the AGB phase. When only small amounts of H remain (of the order of $10^{-4}\,M_\odot$, Koester and Chanmugam 1990), the star moves to the left of the H-R diagram. In the following, the luminosity of the star decreases as the star cools. The star becomes a WD. Over the next billion years the WD becomes a black dwarf as the temperature decreases.

The stellar evolution track shown in Figure I.2.1 differs for stars of other masses. However, the outcome is qualitatively the same for stars with masses below about $8\,\mathrm{M}_\odot$. Higher mass stars, with masses between $8\,\mathrm{M}_\odot$ and $10\,\mathrm{M}_\odot$, are expected to form oxygen-neon(-magnesium, ONe-Mg) cores. The location of the zero-age main sequence (ZAMS) is sketched in Figure I.2.1 based on Farag et al. (2020). The overlap of the dashed line with the blue line approximately indicates the current position of the Sun in the H-R diagram. A detailed description of the stellar evolution of a star can be found in Kippenhahn et al. (2012).

I.2.2 Characteristics of WDs

Koester and Chanmugam (1990) state that a first distinction of WDs from 'normal' stars goes back to the 1910's. Now, several hundred thousand WD candidates have already been identified by the space satellite Gaia of the European Space Agency (Data Release R2, see Gaia Collaboration et al. 2016, 2018) as stated in Jiménez-Esteban et al. (2018), and other observational surveys. The WD closest to Earth is Sirius B located at a distance of 8.6 Lyr (Bond et al. 2017). Jiménez-Esteban et al. (2018) find a peak in the WD mass distribution around $0.8\,M_\odot$ while Kleinman et al. (2013) estimate an average mass of 0.6 to $0.7\,M_\odot$ using data of the Sloan Digital Sky Survey (SDSS-DR7). Based on these observations WDs have radii of about 9.000 km (Shipman 1972). Taking this and their masses into account, average densities are about $2.16 \times 10^6 \frac{M}{M_\odot}\,\mathrm{g\,cm^{-3}}$, with mass M of the WD (e.g. Chandrasekhar 1994). The central density, however, is about six times higher (Chandrasekhar 1994).

The maximum mass is found to be $1.46\,M_\odot$ for a non-rotating, non-magnetic WD (Chandrasekhar 1931). The derivation is given in Chandrasekhar (1931) under the assumptions of a uniform density distribution and using the relativistic form of the Fermi-Dirac statistics for degenerate matter. This so-called $\mathrm{M_{Ch}}$ describes the maximum mass until which gravity is balanced

by the electron degeneracy pressure. If the WD exceeds this mass, it collapses and becomes a different stellar remnant, like for example a neutron star. For details the reader is referred to Chandrasekhar (1931). Das and Mukhopadhyay (2013) and others find that the upper limit for the WD mass is increased by the presence of magnetic fields. Further work by, for example, Anand (1965) adds that rotation raises the mass limit as well. Althaus et al. (2021) illustrate in their Figure 2 what kind of WD forms given varying initial parameters. Depending on the initial mass of the progenitor star and its rotation a CO or ONe WD is created. They show that rotation supports the formation of ultra-massive CO WDs rather than ONe WDs.

With central temperatures of some 10^7 K (Marshak 1940) and central densities of about $10^7\,\mathrm{g\,cm^{-3}}$ WDs are degenerate. The (self-)gravity is balanced by the pressure gradient in this case, meaning that the WD is in hydrostatic equilibrium. As such an isolated WD is stable. It needs to interact with a companion in order to be disrupted in a thermonuclear explosion.

I.2.3 Single- and double-degenerate systems

As stated at the beginning of this section, WDs fulfill the requirements for SN Ia progenitors. However, they have to be in binary systems in order for a thermonuclear explosion to be ignited. Further, it has to be noted that WDs can have He, CO or ONe(Mg) cores. The formation depends on several parameters such as mass of the progenitor star, mass loss rate during the evolution and rotation (see above Sections I.2.1 and I.2.2). The discussion in this work is limited to CO WDs which are widely examined as SN Ia progenitors (e.g. Whelan and Iben 1973, Nomoto 1982a,b, Webbink 1984, Livne 1990, Livne and Glasner 1990, 1991, Shigeyama et al. 1992, Fink et al. 2007, 2010, Sim et al. 2010, Shen and Bildsten 2014, Blondin et al. 2017a, Tanikawa et al. 2018, Shen et al. 2018a, Polin et al. 2019, Leung and Nomoto 2020, Gronow et al. 2020). While He WDs can be excluded as progenitor for SNe Ia due to the absence of strong He lines in SNe Ia spectra, a study on ONeMg WDs as progenitors can be found in Marquardt et al. (2015). Possible explosion mechanisms for a CO WD as SN Ia progenitor are presented in Sections I.2.4 to I.2.6.

In a close binary system a WD can interact with its companion via accretion. In addition to the ignition of an explosion, an accretion process allows the WD to gain mass. As the average mass of a WD is about $0.7\,M_\odot$, the total mass needs to increase so that a high enough ^{56}Ni production is reached in the explosion to match observations. A binary system can consist of a CO WD and another WD, such as a He WD. The system is called double-degenerate (e.g. Whelan and Iben 1973, Webbink 1984, Tutukov and Yungelson 1996, Kashyap et al. 2015, Tanikawa et al. 2018, Rebassa-Mansergas et al. 2019). If the companion star is, for example, a red giant the system is single-degenerate instead (e.g. Whelan and Iben 1973, Iben et al. 1987, Dave et al. 2017). There is no uniform conclusion on which system is favored. Fisher and Jumper (2015) state that explosions of M_{Ch} WDs in the single-degenerate channel lead to over-luminous SNe Ia (so-called SN 1991T-like). Based on their three-dimensional (3D) models this channel only contributes 1% to 30% of the total SNe Ia rate. However, Hillebrandt and Niemeyer (2000) favor the single-degenerate channel as hardly any observations of double-degenerate systems were made so far involving M_{Ch} WDs that would merge within the Hubble time. The contribution of the double-degenerate channel to SNe Ia is estimated to about 64% by Liu et al. (2018) derived from their model sample. Belczynski et al. (2005), Ruiter et al. (2009), and Toonen et al. (2012) agree on a rather large contribution via the double-degenerate channel based on population synthesis calculations. In addition, Li et al. (2019a) point out that there has been no clear observation of a surviving non-degenerate companion in a SN remnant. In contrast to that, three hypervelocity white dwarfs have been found in Gaia data supporting the argumentation for double-degenerate systems (Shen et al. 2018a).

Figure 1 of Yungelson (2005) illustrates possible formation channels for a close binary system. In order for the separation of the two stars to be so low, at least one common envelope phase is needed. However, some uncertainties remain in the evolutionary scenarios as indicated by Yungelson (2005).

I.2.4 Chandrasekhar mass WDs

As stated before, two groups of WDs are regarded as possible progenitors for a SN Ia. M_{Ch} WDs are discussed in this section. In Section I.2.5 progenitor systems of sub-M_{Ch} WDs are explained. A discussion of super-M_{Ch} WDs as progenitors can be found in Howell et al. (2006). However, these are unlikely candidates for normal SNe Ia as their luminosities are too bright. They can, nevertheless, account for a subclass of SNe Ia (Taubenberger 2017).

The high homogeneity of SNe Ia observations indicates that the progenitor star is always the same (see Section I.1.2.1). M_{Ch} WDs fit this criterion as the WD would explode at a fixed mass (e.g. Hoyle and Fowler 1960). Riess et al. (1999) state that the standard candle SNe Ia arise from explosions of such WDs. Further studies are carried out by Arnett (1969), Thielemann et al. (1986), Iwamoto et al. (1999), Reinecke et al. (2002), García-Senz and Bravo (2005), Bravo et al. (2019), and Seitenzahl et al. (2013b).

In order for a M_{Ch} WD to explode, the WD first needs to reach this mass limit. This occurs through accretion of matter from a companion, such as a red giant or main sequence star. Nomoto (1982b) and Sim et al. (2010) assume that the accreted material consists of H or He which stably burns on the surface of the WD core until it is converted to CO and contributes to an increase of the core mass. The central density of the WD increases during the accretion until a thermonuclear runaway sets in which can develop due to the degenerate state of the matter (Section I.1.1).

However, it was found that explosions of M_{Ch} WDs do not result in synthetic observables representing the majority of SNe Ia (Arnett et al. 1971). Instead, they are proposed to be the progenitors of a subclass of SNe Ia (e.g. Foley et al. 2013, Galbany et al. 2019). Sim et al. (2013b) show the width-luminosity relation for their M_{Ch} models in their Figure 5. In a comparison to observations it becomes obvious that the extreme homogeneity of this progenitor channel is problematic. While observations show an increase in Δm_{15} with decreasing maximum B-band magnitude, the models have rather uniform values of Δm_{15} between 1.1 mag and 1.4 mag (see Figure 5 of Sim et al. 2013b). Further, Arnett et al. (1971) points out that these explosions can produce too much IGEs and too little IMEs compared to observations as all material is burnt to heavy elements.

I.2.4.1 Explosion mechanisms

M_{Ch} WDs can explode in different ways. A burning front either propagates super- or subsonically. Depending on this, it is a detonation or deflagration, respectively. Both are allowed by the Rankine-Hugoniot jump conditions (see Röpke 2006, references therein, and Section I.3.1.3).

In a **deflagration** the ashes expand directly behind the burning front. They have lower densities than the unburnt material. In this case the matter is heated by heat transport between the fuel and ash. Pure deflagrations of M_{Ch} WDs are for example discussed by Thielemann et al. (1986), Livne (1993), Niemeyer and Hillebrandt (1995), Iwamoto et al. (1999), Reinecke et al. (2002), Gamezo et al. (2003), García-Senz and Bravo (2005), Röpke et al. (2007a), Long et al. (2014), and Fink et al. (2014). A much discussed model is the W7 model of Nomoto et al. (1984) and Thielemann et al. (1986) which is widely used in further studies though its one-dimensional

(1D) nature. Deflagrations can leave behind a bound remnant as they are not strong enough to unbind the whole star (Jordan et al. 2012, Kromer et al. 2013). This depends on the ignition conditions as found by Fink et al. (2014).

In an explosion, the deflagration flame burns until it is quenched by the expansion or until it turns into a detonation. These **delayed detonations** are investigated by Blinnikov and Khokhlov (1986), Khokhlov (1991), Gamezo et al. (2005), Röpke and Niemeyer (2007), Röpke (2007), Seitenzahl et al. (2013b), Bravo et al. (2019), and Bravo (2019), among others. In a detonation the shock wave heats the matter by compression. The speed of the burnt matter is further equal to the sound speed in it. The freed energy from burning in the shock leads to a pressure increase behind it and with that supports the shock propagation. The concept of a delayed detonation is suggested based on combustion experiments showing such a spontaneous transition according to Hillebrandt and Niemeyer (2000). Höflich and Khokhlov (1996) and Iwamoto et al. (1999) show that a transition to a detonation occurs at densities of about $10^7\,\mathrm{g\,cm^{-3}}$. Their models are able to match observational features of SNe Ia and their expected elemental abundances.

It is to be noted that an initial deflagration phase is needed in order to expand the material. During the expansion the density decreases which allows the production of elements other than IGEs. Without such a deflagration phase almost only IGEs, like ^{56}Ni, would be produced in the explosion of a M_{Ch} WD as pure detonation (Nomoto et al. 1976, 1984, Woosley et al. 1986). This would be too bright for a normal SN Ia and the resulting abundances of IMEs would not match those found in observations (Arnett et al. 1971).

A **pulsational delayed detonation** as possible explosion mechanism is not explained here. However, details can be found in Hillebrandt and Niemeyer (2000). The reader is referred to the above referenced works for details on the different explosion mechanisms.

I.2.5 Sub-Chandrasekhar mass WDs

Contrary to M_{Ch} WDs, the total mass of sub-M_{Ch} WDs is not fixed. Changes in the total mass allow a potential match to variations found in observations. Generally, sub-M_{Ch} WDs are assumed to have total masses between 0.8 and $1.2\,M_\odot$ which enables a reproduction of luminosities found for normal SNe Ia. Due to their lower mass, sub-M_{Ch} WDs are assumed to have a higher occurrence rate than M_{Ch} WDs. This is in part because less matter needs to be accreted. In addition, the companion might not provide enough mass to reach the M_{Ch} limit (Kenyon et al. 1993). Work on sub-M_{Ch} WD progenitor stars is carried out by, for example, Nomoto (1982b), Shigeyama et al. (1992), Woosley and Weaver (1994b), Livne and Arnett (1995), Nugent et al. (1997), Hoeflich et al. (1998), García-Senz et al. (1999), Bildsten et al. (2007), Fink et al. (2007, 2010), Kromer et al. (2010), Sim et al. (2010), Ruiter et al. (2011), Moll and Woosley (2013), Sim et al. (2013a), Blondin et al. (2017a), Wilk et al. (2018), Liu et al. (2018), Shen et al. (2018a), Tanikawa et al. (2018), Polin et al. (2019), Leung and Nomoto (2020), and Gronow et al. (2020, 2021a).

Sim et al. (2010) find that explosions of sub-M_{Ch} WDs match the width-luminosity relation relatively well (also see Kasen et al. 2009, Blondin et al. 2017b, Shen et al. 2018b). They compare 1D pure detonations of sub-M_{Ch} WDs to data in their Figure 4. Details of the abundances and the synthetic observables of sub-M_{Ch} WD explosion are influenced by the total mass (Fink et al. 2010), the C mass fraction (Ohlmann et al. 2014) and other parameters.

A sub-M_{Ch} WD can interact with its companion in different ways that result in thermonuclear explosions. In a close binary with another sub-M_{Ch} CO WD a merger of the two stars is possible. If the sub-M_{Ch}, however, is in a binary with a He star or He WD, accretion of He onto the surface

of the sub-M_{Ch} CO WD takes place. In the case of a sub-M_{Ch} WD a C detonation is not ignited by the accretion process directly as in the M_{Ch} case. A He detonation is ignited at the base of the shell due to thermal instabilities instead.

I.2.5.1 Explosion mechanisms

Three different explosion mechanisms are mainly discussed in literature: violent mergers (Guillochon et al. 2010, Pakmor et al. 2010, 2011, 2013), pure detonations (Blondin et al. 2017a,b), and double detonations (e.g. Woosley and Weaver 1994b, Fink et al. 2007, 2010, Moll and Woosley 2013, Shen et al. 2018a, Townsley et al. 2019, Leung and Nomoto 2020, Gronow et al. 2020). Liu et al. (2018) estimate that **violent mergers** make up 16% of all SNe Ia. In this scenario two WDs of $0.9\,M_{\odot}$ each merge after a common envelope phase (Pakmor et al. 2010) and a detonation is ignited dynamically (also see Iben and Tutukov 1984). The mass ratio can slightly deviate from one. However, the masses need to be between $0.83\,M_{\odot}$ and $0.9\,M_{\odot}$ according to Pakmor et al. (2011). This mass limit is lifted by Pakmor et al. (2013) who analyse mergers of WDs with thin He shells. These mergers of CO WDs produce sub-luminous 1991bg-like SNe, a subclass of SNe Ia (Pakmor et al. 2010). A more violent explosion mechanism is the collision model (see Piro et al. 2014, Wygoda et al. 2019 for details).

Double detonations can occur when a sub-M_{Ch} CO WD accretes He from a companion so that it becomes a WD with CO core and He shell. The work in this thesis focuses on this explosion mechanism. Its details are described in Section I.2.6.

In **pure detonations** of sub-M_{Ch} WDs the WD is assumed not to have a He shell. It is used as toy model in Sim et al. (2010). Blondin et al. (2017a,b) compare their pure detonation model to a delayed detonation of a M_{Ch} WD. However, spectral comparisons to observations show discrepancies as the ^{56}Ni production is high.

I.2.6 Double detonations of sub-M_{Ch} WDs

Details of the double detonation scenario are presented in the following. It was first proposed in the 1980's by Nomoto (1982a,b). Jiang et al. (2017) and De et al. (2019) propose that SNe 2016jhr and 2018byg originate from double detonations, respectively.

I.2.6.1 Basics

In the double detonation scenario it is assumed that a CO WD accretes He from its companion forming a He shell around the CO core. If the accreted layer is massive enough, critical conditions for a He detonation ignition are reached at the base of the shell. Glasner et al. (2018) argue that the minimum accreted mass depends on the accretion rate. A higher accretion rate (e.g. $2.00 \times 10^{-8}\,M_{\odot}\mathrm{yr}^{-1}$ compared to $0.86 \times 10^{-8}\,M_{\odot}\mathrm{yr}^{-1}$) allows a more efficient compression of the matter and heating proceeds faster. Glasner et al. (2018) are able to confirm a successful He detonation ignition based on two-dimensional (2D) models using two different numerical codes. A He shell of $0.05\,M_{\odot}$ is high enough to trigger a He detonation ignition when considering the higher accretion rate given above (Glasner et al. 2018). Neunteufel et al. (2016) carry out simulations on the accretion process onto the WD. In their models the accreted mass depends on various parameters, among those is the accretion rate.Further, Shen et al. (2010) and Glasner et al. (2018) describe a mechanism that triggers a He detonation in more detail: The accretion of matter from a companion heats up the shell material by compression and convection starts to set in. The

convective burning in the shell introduces temperature fluctuations. Along with He burning the temperature increases further leading to an increase in the burning rates. This allows hotspots to develop with burning time scales smaller than the dynamical time scale and convective turnover time which leads to a detonation ignition. Different hotspot sizes are investigated by Shen and Moore (2014), assuming a C enrichment of the shell as well. In the case of the double detonation scenario, the ignition occurs due to thermal instabilities and not dynamically like in the violent merger scenario.

The He detonation in the shell triggers a second, C detonation which disrupts the whole star. Woosley and Weaver (1994b) investigate different accretion rates from the companion onto the WD. They find that a rate of $10^{-8}\,M_\odot\,\mathrm{yr}^{-1}$ is sufficient to ignite a He detonation in a shell of $0.2\,M_\odot$ followed by a successful core ignition. Fink et al. (2010) argue that a core detonation can always be triggered if a He detonation ignition was successful based on their study of minimum He shell masses.

A C detonation can be ignited in different ways as part of a double detonation. The He detonation can directly trigger a C detonation close to the core-shell interface which is named edge-lit mechanism (e.g., Livne and Glasner 1990, Sim et al. 2012). García-Senz et al. (1999) point out that the He detonation should be ignited at some distance from the base of the shell. This allows a pressure-spike to develop which is strong enough to ignite C (Benz 1997).

In case a direct ignition is unsuccessful, a C detonation can be ignited as part of the converging shock mechanism. In this scenario the He detonation propagates through the shell and sends a shock wave into the CO core. The shock wave has a lower velocity than the detonation wave in the shell due to the higher densities in the core. Once the He detonation propagated around the whole core, it moves into the core as shock wave. The shock waves converge off-center in the core at densities of about $2.0 \times 10^7\,\mathrm{g\,cm^{-3}}$ and cause a compression and heating of the material. A C detonation is triggered (e.g., Livne 1990, Livne and Glasner 1991, Woosley and Weaver 1994b, Livne and Arnett 1995, Fink et al. 2007, 2010, Woosley et al. 2011, Moll and Woosley 2013, Shen and Bildsten 2014, Blondin et al. 2017a, Shen et al. 2018a, Townsley et al. 2019, Leung and Nomoto 2020, Gronow et al. 2021a).

It is also possible that the convergence of the He detonation wave at the antipode of the He detonation ignition spot is strong enough to ignite a C detonation in a C enriched shell which is described as the 'scissors mechanism'. This mechanisms is neglected in literature so far, first fully presented in Gronow et al. (2020) and in Chapter II (however, see also Livne and Arnett 1995, García-Senz et al. 1999, Forcada 2007). If no second detonation is ignited, the ejecta are similar to those of a SN .Ia (see Bildsten et al. 2007, Waldman et al. 2011, Sim et al. 2012). The edge-lit, converging shock, and scissors mechanism form a set of three different C detonation ignition mechanisms.

In order for a C detonation ignition to be successful critical values for the density and temperature have to be reached. Röpke et al. (2007b) and Seitenzahl et al. (2009) investigate these values as well as critical masses for a so-called spontaneous C detonation ignition in the CO core which is caused by a hotspot in the fuel with a sufficiently steep temperature gradient. According to Röpke et al. (2007b) temperatures of $2.3 \times 10^9\,\mathrm{K}$ and densities of $1.41 \times 10^6\,\mathrm{g\,cm^{-3}}$ are sufficient. Seitenzahl et al. (2009) derive densities of at least $5.0 \times 10^6\,\mathrm{g\,cm^{-3}}$ and temperatures of $2.0 \times 10^9\,\mathrm{K}$. These values are used throughout this thesis to investigate whether a C detonation ignition is plausible and physical.

Ruiter et al. (2011) list rates for explosions of sub-$\mathrm{M_{Ch}}$ WDs in the double detonation scenario. The rates are given as a function of time following a star formation burst, which corresponds to a DTD. This is a more accurate description for the time dependent rate than an averaged rate employed at all times.

I.2.6.2 Open questions

Explosions of sub-M_{Ch} WDs are found to cover a range of different brightnesses (Sim et al. 2010, Polin et al. 2019) as well as rise and decline rates (Sim et al. 2010, Blondin et al. 2017b). However, despite past studies on double detonations (e.g. Fink et al. 2007, 2010, Moll and Woosley 2013, Shen et al. 2018a, Leung and Nomoto 2020) some question are not completely answered so far. As such, the exact mechanism of the He detonation ignition is unknown. Glasner et al. (2018) approach this by investigating whether a He detonation can be ignited successfully in an accreted He layer (see also Woosley and Kasen 2011, Holcomb et al. 2013, Shen and Moore 2014).

The details of the He detonation are undetermined as well. Höflich and Khokhlov (1996) and Nugent et al. (1997) find that synthetic observables of double detonations show nickel (Ni) at high velocities which originates from the He detonation, but this is not found in observations. Ruiter et al. (2011), however, argue that detonations of thinner He shells produce less ^{56}Ni and, therefore, weaken the deviation. This is confirmed by simulations of Bildsten et al. (2007), Shen and Bildsten (2009), and Townsley et al. (2012, 2019). Kromer et al. (2010) further state that titanium (Ti) and chrome (Cr) as products of the shell detonation are too prominent in synthetic spectra compared to observations. The spectral color is too red according to Kromer et al. (2010), Boyle et al. (2017), and Botyánszki et al. (2018) as well. An admixture of C into the shell can decrease the amount of IGEs produced in the shell detonation as suggested by Yoon et al. (2004), Fink et al. (2010), Kromer et al. (2010), and Fink et al. (2013). This effect is investigated in this work (see Chapter II and Gronow et al. 2020). The propagation of the He detonation is further analysed in more detail in this work as the resolution in the shell is increased compared to previous studies (e.g. Fink et al. 2007, Moll and Woosley 2013).

Further, unknown parameters are details of the C detonation ignition. Critical values for a successful C detonation ignition are found by Röpke et al. (2007b) and Seitenzahl et al. (2009). However, only few full 3D simulations have been carried out so far which leaves some uncertainties.

I.2.6.3 Simulations of double detonations

Simulations of double detonations of sub-M_{Ch} WDs were carried out in this work. However, the accretion process onto the WD was omitted. In the beginning, the simulations rather presume that a WD with CO core and He shell is in hydrostatic equilibrium. The hydrodynamic explosion simulations were followed by a postprocessing step to get detailed nucleosynthetic yields (see Section I.3.3) and radiative transfer calculations to obtain synthetic observables (Section I.3.4). Details of the numerical implementation and the employed codes are given in Section I.3.

I.2.7 Nucleosynthesis in sub-M_{Ch} WD explosions

The nucleosynthesis in double detonations of sub-M_{Ch} WDs can be described by explosive He and Si burning. Explosive He burning takes place in the He shell, while explosive Si burning occurs in the core with C and O serving as fuel. A detailed description of the different forms of explosive burning can be found in Lach et al. (2020) (see also Arnett 1996).

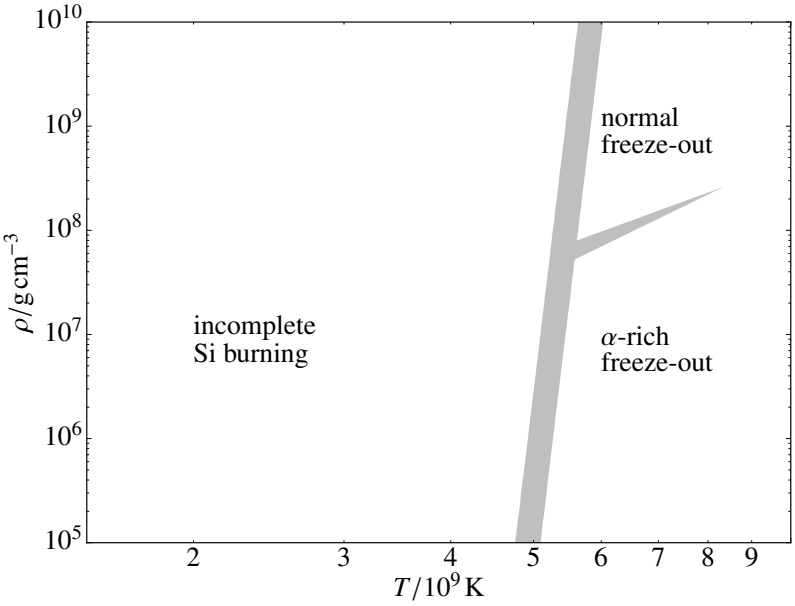

Figure I.2.2: Illustration of the different burning regimes of explosive Si burning in the $T_{\mathrm{peak}} - \rho_{\mathrm{peak}}$–plane following Woosley et al. (1973). Gray areas cover varying χ values in the range from 1 to 10 (similar to Figure 1 of Lach et al. 2020).

I.2.7.1 Explosive Si burning

Woosley et al. (1973) describe explosive Si burning by identifying three different burning regimes, namely normal freeze-out from nuclear statistical equilibrium (NSE), α-rich freeze-out, and incomplete Si burning. They are split by gray areas in Figure I.2.2. The separation of the burning regimes depends on the cooling time scale after the burning front was crossed. The effect can be described by the variable χ which influences the hydrodynamic time scale according to $\tau_{\mathrm{HD}} = 446\chi\rho_{\mathrm{peak}}^{-1/2}$ (see Lach et al. 2020 for details). The shaded area in Figure I.2.2 covers χ values from 1 to 10. Burning in the three regimes results in varying compositions.

In NSE the abundances of all isotopes, from proton (p) to IGEs, are in equilibrium. Forward and reverse reactions are in balance. However, high enough densities and temperatures to reach NSE are not present in the explosions of sub-$\mathrm{M_{Ch}}$ (see the discussions in Chapter IV, and Figures IV.2.2 and IV.2.3 therein). Only explosions of WDs with masses close to or above the $\mathrm{M_{Ch}}$ are able to reach NSE (see Lach et al. 2020). A detailed discussion of this burning regime is therefore omitted here and the reader is referred to Lach et al. (2020) instead.

In the α-rich freeze-out regime similarly high temperatures are present as in NSE. However, the peak densities are lower. The abundance of light particles, such as p and α-particles, originating from the photodissociation of ^{28}Si (Arnett 1996) is higher in this burning regime than in NSE. The reaction rates are slower at the lower densities (Arnett 1996) and the light particles react with other nuclei and cause the distribution to be out of equilibrium. The high α-particle density results in the freeze-out of forward reactions that take place in NSE. The name of this burning regime is coined by the high abundance of these α-particles.

At temperatures above about $5 \times 10^9\,\mathrm{K}$ Si is exhausted while Si burning can still take place at lower temperatures. In this temperature regime incomplete Si burning occurs. Two equilibria form located around the isotopes ^{28}Si and ^{56}Ni (Woosley et al. 1973). This is due to a bottleneck

at a mass number of 45. Elements with this mass number have a very low binding energy and, therefore, have a low abundance. The bottleneck is lifted at higher temperatures. In the α-rich freeze-out regime, this results in the burning of almost all material to ^{56}Ni.

The nucleosynthesis strongly depends on the density profile of the WD. Therefore, the WD mass is the leading parameter influencing the nucleosynthesis. Different to M_{Ch} WDs, sub-M_{Ch} WDs of about 1.05 $M_\odot$ have much lower densities (see Figure 1 of Seitenzahl and Townsley 2017). As a consequence the final abundances of sub-M_{Ch} WD explosions include less IGEs and more IMEs compared to explosions of M_{Ch} WDs. This coincides with the difference in burning regimes arising in the explosions.

I.2.7.2 Explosive He burning

Explosive He burning is in detail described by Khokhlov (1984) and Khokhlov and Érgma (1985). According to Khokhlov (1984) the burning covers a regime with temperatures above 10^9 K and densities higher than 10^5 g cm^{-3}. It is dominated by the triple-α reaction and α-captures. Both are in competition with each other, with the presiding reaction changing depending on the temperature. ^{12}C is formed in triple-α reactions. Following α-captures onto ^{12}C result in the production of heavier elements in the α-process (e.g. ^{24}Mg, ^{28}Si, ^{40}Ca, and ^{52}Fe). Eleven α-particles are needed to form ^{56}Ni from ^{12}C. It is the most abundant isotope at temperatures of 2×10^9 K and densities of 5×10^6 g cm^{-3} (Khokhlov 1984) which are met in He detonations as part of the double detonation scenario. The abundance can, however, be altered when including an admixture of C to the shell (see Section II.2.3.1) and by the metallicity of the main sequence progenitor star (see Chapter IV).

Once He is exhausted, a further burning regime is reached. It includes (α, γ) and (γ, α) reactions as well as $^{12}\mathrm{C} + {}^{12}\mathrm{C}$ reactions, among others, and leads to NSE. As stated in Khokhlov (1984), the regime requires densities above 10^7 g cm^{-3} and temperatures higher than 3×10^9 K. This regime is, however, not reached in the He shell detonations of the sub-M_{Ch} WD explosion models presented in this thesis (see Section IV.2).

I.2.7.3 SNe Ia as Fe source

During the SN explosion large amounts of ^{56}Ni are produced (Greggio and Renzini 1983). Heavy elements, like ^{56}Ni, are produced by nuclear fusion. As ^{56}Ni has the highest nuclear binding energy among the symmetric isotopes fusion is halted leading to a significant ^{56}Ni production (Audi et al. 2003). Fusion stops at an isotope with equal neutron and proton numbers due to the symmetric structure of the C and O fuel. This ^{56}Ni bottleneck exists as no energy would be gained from reactions to more massive elements.

Over time, ^{56}Ni decays to ^{56}Fe via ^{56}Co. The exact amount of ^{56}Ni produced in a SN Ia depends on the mass and density profile of the exploding WD. Maoz and Graur (2017) find a mean Fe yield from SNe Ia of 0.7 $M_\odot$, contrary to a mean value of 0.074 $M_\odot$ for core-collapse (CC) SNe. The relatively high amount originating from SNe Ia explains the rise in the Fe production found in galaxies (see also Section I.1.2.3). The consideration of a DTD for this type of SN improves the match.

I.3 Detonation simulations

Basics of hydrodynamics and the treatment of a WD in numerical codes are described in Sections I.3.1.1 and I.3.1.2, respectively. Section I.3.2 goes into detail on how these hydrodynamical principles are implemented in numerical hydrodynamic codes. Details on other codes used in connection with this thesis are given in Sections I.3.3 and I.3.4.

I.3.1 Theoretical basis

I.3.1.1 Hydrodynamics

Under the assumption that the mean free path of the particles is small compared to the length scale over which properties change, it is possible to treat matter as fluid (Müller 1998). This, however, only includes short range forces. Other forces are assumed to be external. In case of a fluid, a small mean free path results in only a small part of the particles being distributed to neighboring fluid elements. The fluid elements are in local thermal equilibrium and the fluid itself is described by the Euler equations.

As stated earlier (see Section I.2.2) WD matter can be described as fully ionized plasma of degenerate electrons. This fulfills the continuum assumption mentioned by Hillebrandt and Niemeyer (2000) which describes that matter comprised of particles behaves like a continuous fluid. The valid hydrodynamic equations are derived in Landau and Lifschitz (1983), and Shore (2007) and Landau and Lifschitz (2007) using two different approaches. A derivation is skipped here and the reader is referred to the above works instead.

The governing hydrodynamic equations are given by conservation laws (see LeVeque 1998) which can be deduced from the balance equation. The differential form of the balance equation is obtained by LeVeque (1998) as

$$\partial_t q(\boldsymbol{x}, t) + \nabla \cdot \boldsymbol{j}_q(\boldsymbol{x}, t) = S(\boldsymbol{x}, t) \tag{I.3.1}$$

with density q, flux density $\boldsymbol{j}$, and source density S taking a surface flux and the presence of sources or sinks into account. Time and spacial coordinates are given by t and $\boldsymbol{x}$. Based on this equation the following conservation laws are derived:
continuity equation for conservation of mass

$$\partial_t \rho + \nabla(\rho \boldsymbol{u}) = 0 \tag{I.3.2}$$

with mass density ρ and fluid velocity $\boldsymbol{u}$, **momentum equation**

$$\partial_t(\rho \boldsymbol{u}) + \nabla(\rho \boldsymbol{u} \otimes \boldsymbol{u}) + \nabla p = \rho \boldsymbol{f} \tag{I.3.3}$$

with external force $\boldsymbol{f}$ obtained from $\boldsymbol{f} = \nabla\Phi$ with gravitational potential Φ and pressure p, and the total **energy equation**

$$\partial_t(\rho e_{\text{tot}}) + \nabla(\rho e_{\text{tot}}\boldsymbol{u}) + \nabla(p\boldsymbol{u}) = \rho\boldsymbol{u}\cdot\boldsymbol{f} \tag{I.3.4}$$

with total energy e_{tot}. LeVeque (1998), however, neglects further source and external force terms in their calculations. The three equations (I.3.2) to (I.3.4) make up the Euler equations. If viscosity is incorporated as well, the governing equations are given by the Navier-Stokes equations. Their discussion is omitted here. The relation of inertial to viscous forces is described by the Reynolds number. Its value is rather large with 10^{14} for thermonuclear explosions of WDs (Woosley et al. 2009) which shows that viscosity can be neglected in the numerical treatment (Röpke 2017). Codes often apply a numerical viscosity to capture shock waves more accurately (Dolag et al. 2005). The employed Arepo code, however, does not require an artificial viscosity due to its adaptive mesh refinement capability (AMR) (see Springel 2010 and Section I.3.2.2).

I.3.1.2 WD in hydrostatic equilibrium

Prior to hydrodynamical explosion simulations a WD is set up to be in hydrostatic equilibrium. For this

$$\frac{\partial p}{\partial r} = -\frac{Gm\rho}{r^2} \tag{I.3.5}$$

has to hold (see Kippenhahn et al. 2012 for the derivation). It describes the equilibrium between gravity and pressure force with gravitational constant G. Further,

$$\frac{\partial m(r)}{\partial r} = 4\pi\rho r^2 \tag{I.3.6}$$

gives the relation between enclosed mass $m(r)$ and radius r with boundary condition $m(0) = 0$. A relation between total mass and radius is given by Equation (37.18) of Kippenhahn et al. (2012). Equations (I.3.5) and (I.3.6) give two equations for three variables (p, r, ρ). Therefore, further information is needed. It is given by the inclusion of the Helmholtz equation of state (Timmes and Swesty 2000).

I.3.1.3 Combustion

The composition of a fluid is coupled to the hydrodynamics which allows to examine individual species as well as nuclear reactions taking place. The relation is given by

$$\partial_t(\rho X_j) + \nabla(\rho\boldsymbol{u}X_j) = r_j(\rho, T, \boldsymbol{X}) \tag{I.3.7}$$

with mass fractions $\boldsymbol{X}$ and reaction rate r_j of species j with $\sum r_j = 0$ derived from mass conservation (see Equation I.3.2). The inclusion of different species also leads to an additional source term in the energy equation proportional to $\rho S(\boldsymbol{x})$ as nuclear energy is freed or consumed during burning.

The coupling of nuclear reactions to the hydrodynamic calculations permits to incorporate violent burning present in detonations as well as burning inside stars. The theory of burning fronts is described in Landau and Lifschitz (2007). The assumptions of a 1D wave front, a steady flow and a thin reaction zone allow to treat a burning front as shock.

A shock wave represents a weak (or discontinuous) solution of the Euler equations. At least one quantity is discontinuous in a shock serving as surface of discontinuity (Landau and Lifshitz 1987). The boundary conditions for the discontinuity are given by the Rankine-Hugoniot jump conditions for the mass, energy, and momentum flux (Landau and Lifshitz 1987):

$$\begin{aligned} [\rho v_x] &= 0, \\ [\frac{1}{2}v_x^2 + w] &= 0, \text{ and} \\ [p + \rho v_x^2] &= 0 \end{aligned}$$

with enthalpie w. The notation $[\rho v_x] = \rho_1 v_{1x} - \rho_2 v_{2x}$ constitutes the states before and after the shock front.

The conservation laws (Equations I.3.2 to I.3.4) allow to derive two further relations: the Hugoniot adiabatic and Rayleigh line (see Landau and Lifschitz 2007). Both are illustrated in Figure I.3.1. The Rayleigh line (blue) connects the unburnt to the burnt state while the Hugoniot adiabatic (red) describes the change in energy flux over the discontinuity. The burnt state can be to the left of point A or right of point A' in Figure I.3.1. In the two regimes combustion is described by two different processes: deflagrations (on the right) and detonations (on the left). The discussion here is limited to detonations. A physical solution for a self-sustained detonation is given in point O where the Hugoniot adiabatic and the tangent starting from the point of initial pressure and specific volume cross. The point lies in the regime of larger pressure ($p > p_0$) and smaller specific volume ($v < v_0$) relative to the initial values. It is a so-called Chapman-Jouguet solution (Landau and Lifschitz 2007). The respective point for a deflagration is O'. Landau and Lifschitz (2007) show that the region for a detonation is above point O with an initial velocity higher than the speed of sound in the unburnt material and below the sound speed in the burnt material. The burning front therefore propagates supersonically with respect to the unburnt matter. The change in velocity indicates that the material is compressed following its burning and that it propagates in the direction of the burning front. In a detonation the shock heats the fuel by compression which leads to an excess of the burning threshold allowing nuclear burning to set in. Figure 132 by Landau and Lifschitz (2007) illustrates that in this case the state of the matter changes and moves along the Rayleigh line.

The theory of Rankine-Hugoniot was first used in the context of SNe Ia by Khokhlov (1988). The Zeldovich-von Neumann-Döring theory (Zel'dovich 1940, von Neumann 1942, Döring 1943, but also see Fickett and Davis 1979) describes planar detonations taking only monotonic exothermic reactions into account and states that the shock compression results in a discontinuity in the pressure. Khokhlov (1989) are among the first to implement the theory in their SNe Ia models (see Röpke 2017 for a description).

I.3.2 Hydrodynamical simulations

In order to include the physics described in Section I.3.1, a discretisation is needed. Further, simulations of SN Ia explosions are multi-scale problems. Length scales go from the size of centimeters to the size of the WD and beyond. At the same time, different time scales are involved as well (e.g. nuclear burning time scale vs. time scale of hydrodynamic evolution). As an approximation nuclear reactions are therefore treated as instantaneous reactions at the flame discontinuity. An additional postprocessing step examines nuclear reactions in more detail (see Section I.3.3).

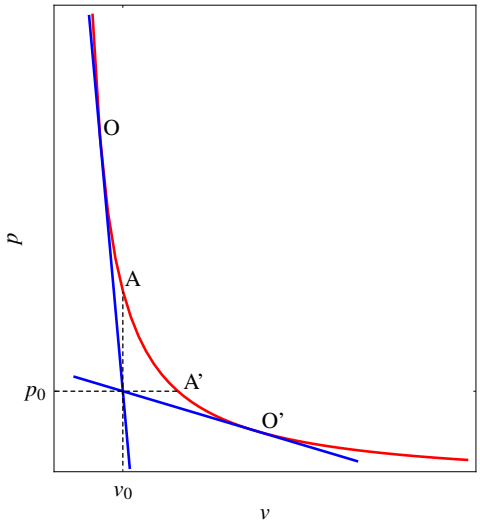

Figure I.3.1: Illustration of the jump conditions assuming a polytropic equation of state ($\gamma = 5/3$), shown are the Hugoniot adiabatic (red) and corresponding Rayleigh lines (blue), the Chapman-Jouguet points are O and O' (based on Figure 136 of Landau and Lifschitz 2007).

I.3.2.1 Discretisation

As part of the discretisation, the Euler equations (Equations I.3.2 to I.3.4) are solved instead of the Navier-Stokes equation (Müller 1998). LeVeque (1998) describes the effective conservation equations.

The finite volume method (LeVeque 1998) is used to solve the Euler equations. For this, the spatial and temporal variables are described by x_i, y_i, z_i and t_n with equal spacial ($h = \Delta x = \Delta y = \Delta z$) and temporal spacing ($k = \Delta t$). In this method the value of a quantity is calculated as the average of its function over a finite volume as given by

$$Q_i^n = \frac{1}{h} \int_{x_i}^{x_{i+1}} q(x, t^n) \mathrm{d}x. \tag{I.3.8}$$

This is different to an approximation of the function value itself. With this approach the balance equation becomes

$$Q_i^{n+1} = Q_i^n - \frac{k}{h}(J_{i+1}^n - J_i^n) \tag{I.3.9}$$

with

$$J_i^n \approx \frac{1}{k} \int_{t_n}^{t_{n+1}} j(q(x_i, t)) \mathrm{d}t. \tag{I.3.10}$$

A source term is neglected here (see LeVeque 1998).

The Godunov method (see LeVeque 1998) describes such a finite volume method and is used to solve the Riemann problem in the form of Equation (I.3.9). In this case q^n is interpreted as a value of a piecewise constant function $\tilde{q}^n(x_i, t)$ with a known exact solution in the interval $[t_n, t_{n+1}]$. Considering this, the Riemann problem only needs to be solved at the cell interfaces

and Equation (I.3.10) becomes

$$J_i^n = \frac{1}{k} \int_{t_n}^{t_{n+1}} j(\tilde{q}^n(x_i, t))\mathrm{d}t \tag{I.3.11}$$

which is used to solve Equation (I.3.9). For details on the resulting Riemann problem see LeVeque (1998). In numerical codes an appropriate Riemann solver needs to be chosen in addition to a time step size criterion. The described methods are used in the hydrodynamic Arepo code.

I.3.2.2 Arepo

Generally, numerical codes are based on the Eulerian mesh-based or Lagrangian Smoothed Particle Hydrodynamics (SPH) method. SPH codes employ a Monte-Carlo method to solve the above mentioned integrals. They are Galilean invariant and adaptive (Gingold and Monaghan 1977, LeVeque 1998, Springel 2010). In contrast to this, Eulerian codes enable a more accurate treatment of the contact discontinuity as it is grid-based enabling a high resolution of the shock (Stone and Norman 1992, Springel 2010). Agertz et al. (2007) and Mitchell et al. (2009) point out that the method can affect the result of the simulations to some degree. The Arepo code (Springel 2010) combines the advantages of both these methods. It is Eulerian mesh-based and permits the grid to move with the fluid flow (so-called moving-mesh). At the same time, it is also adaptive and Galilean invariant. In this work the Arepo code was used to carry out hydrodynamic explosion simulations while it was developed for cosmological simulations, such as Illustris (e.g. Vogelsberger et al. 2014). Adaptations were made in order to allow the simulation of sub-M_{Ch} CO WDs with a He shell in the context of this thesis.

The code is based on a Voronoi grid. This is implemented as a Delauney tesselation which is the topological dual and computationally less expensive. In order to create a Voronoi grid, mesh generating points are distributed in the computational domain. Tetrahedra are formed in 3D simulations using these points as corner points. Circumcircles of the tetrahedra do not enclose other mesh generating points. The cells in a Voronoi tessellation of space contain the volume that is closer to its mesh generating point than the one of another cell. The grid is adapted in each time step (LeVeque 1998). A Voronoi grid in 2D is shown in Figure I.3.2.

The Riemann problem is solved using a second order finite volume scheme (Springel 2010). The flux for each interface between cells is calculated separately. The Godunov method is employed with improvements made by Pakmor et al. (2016). In this context, averages of the quantities are calculated over the finite volume of a cell by

$$\boldsymbol{Q}_i = \int_{V_i} \begin{pmatrix} \rho \\ \rho \boldsymbol{v} \\ \rho e_{\mathrm{tot}} \end{pmatrix} \mathrm{d}V. \tag{I.3.12}$$

An evolution in time gives

$$\boldsymbol{Q}_{i+1} = \boldsymbol{Q}_i - k \sum_j A_{ij} \hat{\boldsymbol{F}}_{ij}^{n+1/2} \tag{I.3.13}$$

(see Pakmor et al. 2016). Here A_{ij} denotes the face area between cells i and j and a time-averaged approximation of the flux $\boldsymbol{F}_{ij}$ is given by $\hat{\boldsymbol{F}}_{ij}$. It is calculated similar to the MUSCL-Hancock scheme (van Leer 1984, Toro 2009) using the second order Runge-Kutta method by Heun while replacing temporal derivatives by spacial derivatives (Pakmor et al. 2016).

Coulomb corrections are included in the equation of state and self-gravity is treated as a source term in the Euler equations. A nuclear network solver (Pakmor et al. 2012a) was coupled

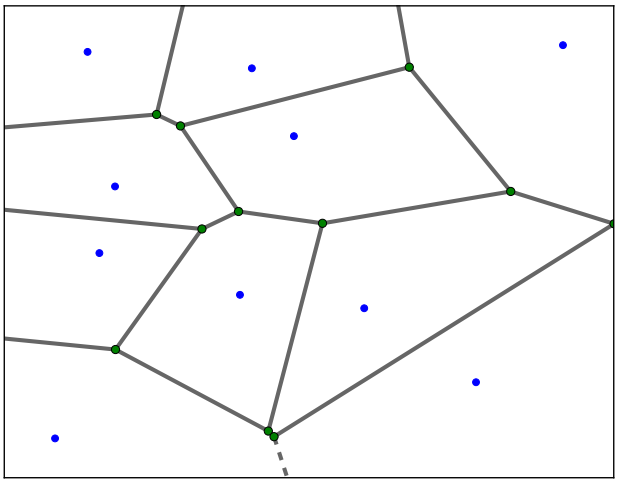

Figure I.3.2: Voronoi grid in 2D.

to the hydrodynamics code by Pakmor et al. (2013). The consideration of nuclear reactions adds an additional source term to the energy conservation equation and balance equations for the nuclear species as pointed out in Section I.3.1.3. The system of equations is closed by the Helmholtz equation of state (Timmes and Swesty 2000) which was implemented by Pakmor et al. (2013) and connects temperature, density, and pressure as well as composition with each other.

A burning limiter is implemented in the Arepo code as described in Gronow et al. (2020) and Gronow et al. (2021a). Burning is disabled if

$$\boldsymbol{\nabla} \cdot \boldsymbol{v} < 0 \,\text{and}\, \nabla p \cdot \frac{r_{\text{cell}}}{p_{\text{cell}}} > 0.66 \tag{I.3.14}$$

are fulfilled. Based on these relations it is determined whether a region is inside the shock or not. This method follows Fryxell et al. (1989) and Appendix A of Townsley et al. (2016). It differs from the one presented in Kushnir and Katz (2020). They introduce a scaling factor for a burning limiter in thermonuclear detonation waves. However, the scaling factor sensitively depends on the setup requiring a careful calibration for each model which goes beyond this work. The effect of their method on Arepo simulations of mergers involving hybrid HeCO WDs is investigated by Pakmor et al. (2021). Their results do not show a significant dependence on the burning limiter.

The AMR (see LeVeque 1998 for a description) capability of Arepo allows to increase the resolution in certain regions. This feature is used in order to reach a better resolution than found in previous works (e.g., Fink et al. 2007, Moll and Woosley 2013). Two additional levels of refinement are introduced in the framework of this thesis: First, the He shell has a higher resolution than the remaining WD to track the He detonation propagation more accurately. Second, the resolution at the location of the convergence point of the He detonation wave is increased. This region is located at $-2\times10^8\,\text{cm} < \text{x} < 2\times10^8\,\text{cm}$, $-2\times10^8\,\text{cm} < \text{y} < 2\times10^8\,\text{cm}$, and $-7\times10^8\,\text{cm} < \text{z} < -3\times10^8\,\text{cm}$, if not stated otherwise. The refinement criterion is defined as the mass of a cell. This is done in a similar way to Pakmor et al. (2013). An explicit refinement is used which splits a cell once its mass exceeds a reference mass (M_R) by a factor of two. The reference mass is set to $2\times10^{27}\,\text{g}$ in regions with the base resolution. In order to track the He shell location a passive scalar is added to the code. This is needed since He is also present in the background of the WD.

I.3.3 Nuclear network

In order to derive synthetic observables for the hydrodynamic simulations which can be compared to observations, it is necessary to determine detailed nucleosynthetic yields. The inclusion of different species and nuclear reactions taking place adds a set of non-linear, coupled, ordinary differential equations (see Section I.3.1.3) which need to be evaluated. The abundances of the individual isotopes are connected through nuclear reactions. The change in these isotopic abundances is described by Müller (1998) as

$$\dot{Y}_i = \sum_j c_i(j)\lambda_j Y_j + \sum_{j,k} c_i(j,k)\rho N_A \langle jk\rangle Y_j Y_k + \sum_{j,k,l} c_i(j,k,l)(\rho N_A)^2 \langle jkl\rangle Y_j Y_k Y_l \tag{I.3.15}$$

with $Y_i = X_i/A_i$, atomic number A_i, one-body reaction rate λ_j, and the average products of the cross section and relative velocity $\langle jk\rangle$ and $\langle jkl\rangle$, respectively. Müller (1998) defines

$$c_i(j) = \pm N_i, \qquad c_i(j,k) = \pm\frac{N_i}{N_j!N_k!}, \qquad \text{and} \qquad c_i(j,k,l) = \pm\frac{N_i}{N_j!N_k!N_l!} \tag{I.3.16}$$

to describe one-, two- and three-body interactions. N_i gives the total number of nuclei of a species taking part in a reaction. The signs represent production (+) or destruction (−).

I.3.3.1 Postprocessing

A calculation of detailed nucleosynthetic yields is computationally too expensive in combination with the hydrodynamic simulation. Instead only a small nuclear reaction network is considered in the Arepo simulations. This network is sufficient to capture the key reactions taking energy conservation into account (see Müller 1998).

Detailed nucleosynthetic yields are determined in a postprocessing step with the YANN code (Yet Another Nuclear Network, Pakmor et al. 2012b). The employed nuclear reaction network consists of 384 isotopes reaching up to ^{98}Mo and is first described in Pakmor et al. (2012b). The method is based on tracer particles which are added to the hydrodynamic simulation. These have no impact on gravity or the hydrodynamics and are advected passively in the simulation. The tracer particles are distributed in the WD to sample the initial density distribution. Each tracer represents a mass of 1×10^{27} g. The tracer particles record the density and temperature in the hydrodynamic simulation which are used as input for the postprocessing (see Travaglio et al. 2004). A similar method was already used by Thielemann et al. (1986).

Equation (I.3.15) is solved for these tracer trajectories to get detailed nucleosynthetic yields. The number of tracer particles needs to be chosen appropriately to account for the dimensionality of the problem. In this work two million tracer particles were used which permits an accurate representation of the WD structure in 3D.

Similar to Pakmor et al. (2012a), the 2014 JINA Reaclib database (Rauscher and Thielemann 2000) is used in combination with weak reaction rates taken from Langanke and Martínez-Pinedo (2001). A minimum temperature of 2×10^7 K is set in order to enable the nuclear reaction network only once this temperature is exceeded. The network further uses a solver for NSE at temperatures above 6×10^9 K. The nuclear reaction network makes use of a semi-implicit midpoint rule (Bader and Deuflhard 1983) using a Newton-Raphson method.

In order to account for a metallicity of the star the detailed solar composition given in Asplund et al. (2009) can be used as initial solar metallicity. These values can be scaled to the respective metallicity of the model. A more detailed description of the metallicity implementation is given in Sections III.1.2 and IV.1.

I.3.4 Radiative transfer calculations

Synthetic observables were calculated for sevveral models presented in this thesis. They enable a comparison of the models to observations of SNe Ia which can verify a model as potential SN Ia progenitor or indicate that an adjustment of the parameters is necessary. A discussion of these radiative transfer simulations is included here to allow a more comprehensive conclusion on whether the explosion models resemble SN Ia explosions. The radiative transfer calculations were carried out by Christine E. Collins formerly working at the Astrophysics Research Center (School of Mathematics and Physics, Queen's University Belfast, Northern Ireland, UK), now also affiliated with the GSI Helmholtzzentrum für Schwerionenforschung (Darmstadt, Germany). The radiative transfer code Artis (Sim 2007, Kromer and Sim 2009, based on methods of Lucy 2002, 2003, 2005) is used. It is a time-dependent multi-dimensional Monte-Carlo code.

The nucleosynthetic yields of the postprocessing step as well as the ejecta densities and velocities of the explosion simulations are used as initial parameters. These are mapped to a 50^3 Cartesian grid following the method described in Fink et al. (2014) (but also see Kromer et al. 2010). The grid expands in order to move with the trajectory of the ejecta over time (Kromer and Sim 2009). The total emitted γ-ray energy originating from the decays of ^{56}Ni and ^{56}Co to ^{56}Co and ^{56}Fe, respectively, is calculated and distributed on the grid in the form of energy packets based on the initial ^{56}Ni distribution (Kromer and Sim 2009). In the radiative transfer calculations, 2.56×10^7 indivisible energy packets are tracked for 111 logarithmically spaced time steps covering the time between 2 and 120 days after explosion while propagating through the ejecta. They are used as Monte Carlo quanta (Kromer and Sim 2009). As stated in Gronow et al. (2020), the atomic data set of Gall et al. (2012) is used along with a gray approximation that is applied in optically thick cells (Kromer and Sim 2009). Local thermodynamic equilibrium is assumed in the first 3 days since explosion (corresponding to the first ten time steps). For the radiative transfer calculations homologous expansion of the ejecta is assumed. In this case the radial position of the ejecta is directly linked to the velocity via $r = vt$ with time t since explosion. It allows to treat the radiative transfer independent of the hydrodynamic evolution. This state is reached after less than two minutes in the explosion models.

A line-of-sight dependence of the light curves is calculated similar to Kromer et al. (2010) by splitting the escaping photons into equal solid-angle bins. The employed method for line-of-sight dependent spectra is described in Bulla et al. (2015) and Gronow et al. (2020) reducing the Monte-Carlo noise in the angle-dependent spectrum.

Chapter II

Impact of core-shell mixing on the C detonation ignition mechanism

Introduction

The impact of an admixture of C into the He shell on the C detonation ignition mechanism is analysed in this part of the thesis. Hydrodynamic explosion simulations of sub-M_{Ch} WDs with a CO core and He shell were carried out. The work presented here is part of the paper published in the journal *Astronomy & Astrophysics*, Volume 635:A169 (2020, Gronow et al. 2020).

Previous work on double detonations of sub-M_{Ch} WDs has mostly been carried out in 1D or 2D (e.g., Woosley and Weaver 1994a, Bildsten et al. 2007). Moll and Woosley (2013) present results of 3D simulations, though only one quarter of the star is computed. 3D models are calculated by García-Senz et al. (2018) considering a rigid rotation. The work presented here follows up on these studies. A different numerical treatment compared to, for example, the SPH approach of García-Senz et al. (2018) is employed when using the Arepo code. The AMR capability of the code allows an increase in the resolution relative to previous models (e.g. Fink et al. 2007, Moll and Woosley 2013) as stated in Section I.3.2.2. This change in resolution leads to an improved tracking of the He detonation propagation and permits a focused study of the onset of the C detonation.

The effect a C admixture to the He shell has on the nucleosynthetic yields which stem from the shell detonation is discussed in Yoon et al. (2004) and Fink et al. (2010). The study presented here investigates the impact in more detail (Gronow et al. 2020). A previously neglected C detonation ignition mechanism is found, while work by Livne and Arnett (1995), García-Senz et al. (1999), Forcada (2007), and García-Senz et al. (2018) briefly mention a similar mechanism. However, a detailed description and dissection of the new found scissors mechanism is lacking in their works. The following sections present an explanation of the model setup (Section II.1), an interpretation of the hydrodynamic simulation (Section II.2), a description of the results of radiative transfer calculations (Section II.3), and a discussion of the results in the context of previous work (Section II.4).

II.1 Model setup

Nine different hydrodynamic models were set up to investigate the effect of core-shell mixing. The masses of the WDs were selected to reflect Models 1 and 3 of Fink et al. (2010) (Models FM1 and FM3 hereafter). Parameters of the models are listed in Table II.1.1 (see below for a description of the parameters). Model M2a was chosen to be the reference model with values listed in this chapter referring to it, if not stated differently.

A detailed analysis of the influence of a C admixture to the shell is carried out by the comparison of Models M1a and M2a. The dependence of the C detonation ignition mechanism on further parameters is investigated by considering varying WD masses (Models M2a and M3a), different nuclear reaction networks in the hydrodynamic simulations (Models M2a and M2a_i55), two locations of the He detonation ignition spot (Models M2a and b), and a change in resolution (Models M2a, M2a_13, M2a_21, M2a_36, and M2a_79).

The WD was initially set up to be in hydrostatic equilibrium in 1D following the procedure described in Section I.3.1.2 by integrating the valid equations. The total mass of the WD ($M_{\rm tot}$) and the density at the base of the He shell ($\rho_{\rm S}$) are initial parameters. The core temperature was set to be constant at 3×10^7 K and the temperature at the base of the He shell was 6×10^7 K. The temperature declines adiabatically beyond this region going further out. The initial mass of the shell ($M_{\rm iHeS}$) was only determined iteratively based on the input parameters $M_{\rm tot}$ and $\rho_{\rm S}$. Further, the central density ($\rho_{\rm C}$) is a variable being determined only via these input parameters. Table II.1.1 lists the parameters for each model. The He shell mass is determined under the assumption that all cells with an initial He mass fraction of at least 0.01 are part of the shell.

The WD core was set to consist of C and O in equal parts and the WD shell is made up of He. However, a small transition of 20 cells between core and shell was added to the 1D setup. This transition embodies a linear change in temperature and composition. The initial 1D density, temperature, and He mass fraction profiles of Model M2a are shown in Figure II.1.1 in blue. The black line in the density profile corresponds to the initial core radius of about 4×10^8 cm. The transition extends from 4.039×10^8 cm to 4.058×10^8 cm.

In order to carry out 3D hydrodynamic calculations, the 1D profile was mapped onto the Arepo grid using the HEALPix method (Górski et al. 2005) on concentric shells as described in Ohlmann et al. (2017).

II.1.1 Relaxation

Due to the mapping of the 1D profile on the unstructured Voronoi grid of Arepo a relaxation step needs to be carried out. The relaxation allows to take spurious velocities, which can originate from a discrepancy between gravity and the pressure gradient caused by the mapping, into account and it ensures that the model is in hydrostatic equilibrium at the beginning of the detonation simulation. This step is not carried out in most previous work, such as for example Fink et al. (2007, 2010), Moll and Woosley (2013), Shen et al. (2018a), and Townsley et al. (2019). Here,

Table II.1.1: Model parameters as listed in Gronow et al. (2020).

Model		M1a	M2a	M2b	M2a_i55	M3a
M_{tot}	$[\mathrm{M}_\odot]$	1.05	1.05	1.05	1.05	0.91
M_{iHeS}	$[\mathrm{M}_\odot]$	0.051	0.051	0.051	0.051	0.135
M_{pHeS}	$[\mathrm{M}_\odot]$	0.064	0.073	0.073	0.073	0.155
T_{S}	$[10^7\,\mathrm{K}]$	6	6	6	6	6
T_{C}	$[10^7\,\mathrm{K}]$	3	3	3	3	3
ρ_{S}	$[10^6\,\mathrm{g\,cm^{-3}}]$	1.2	1.2	1.2	1.2	1.5
ρ_{C}	$[10^7\,\mathrm{g\,cm^{-3}}]$	4.8	4.8	4.8	4.8	1.9
resolution	$[10^{-8}\,M_\odot]$	3.33	3.35	3.35	3.35	2.76
# isotopes		33	33	33	35	33
ignition spot		a	a	b	a	a

Model		M2a_79	M2a_36	M2a_21	M2a_13
M_{tot}	$[\mathrm{M}_\odot]$	1.05	1.05	1.05	1.05
M_{iHeS}	$[\mathrm{M}_\odot]$	0.051	0.051	0.051	0.051
M_{pHeS}	$[\mathrm{M}_\odot]$	0.073	0.073	0.073	0.073
T_{S}	$[10^7\,\mathrm{K}]$	6	6	6	6
T_{C}	$[10^7\,\mathrm{K}]$	3	3	3	3
ρ_{S}	$[10^6\,\mathrm{g\,cm^{-3}}]$	1.2	1.2	1.2	1.2
ρ_{C}	$[10^7\,\mathrm{g\,cm^{-3}}]$	4.8	4.8	4.8	4.8
resolution	$[10^{-8}\,M_\odot]$	79.18	36.27	21.44	12.71
# isotopes		33	33	33	33
ignition spot		a	a	a	a

the procedure of Ohlmann et al. (2017) is employed in the relaxation simulation.

The WD was relaxed in a hydrodynamic 3D simulation without the addition of nuclear reactions. The relaxation time is given by the time on which the stability of the star persists. The time scale is given by τ. It is fixed to ten dynamical time scales which describes the time on which a star contracts or expands if it is not in balance. The dynamical time scale is defined as

$$\tau_{\mathrm{dyn}} = \int_0^R \frac{\mathrm{d}r}{v_s(r)} \tag{II.1.1}$$

with radius R of the WD and $v_s(r)$ as local sound speed which depends on density and, therefore, radius. The velocities are damped for eight dynamical time scales with the damping being decreased over time. No damping is employed in the remaining time until ten dynamical time scales have passed in order to assure the stability of the setup. A source term is added to the momentum equation according to Equation (8) of Ohlmann et al. (2017) to enable damping. It is proportional to

$$\dot{\boldsymbol{v}} = -\frac{1}{\tau}\boldsymbol{v}.$$

After relaxation, five conditions have to be fulfilled as stated by Ohlmann et al. (2017). The models presented in this work fulfill these criteria:

- No large deviations to the initial pressure and density profiles developed.
- The pressure gradient and gravity balance each other.

- Mach numbers are small in comparison to expected Mach numbers of the problem, if the models are convectively stable.
- A steady state is reached, if the profiles are convectively unstable.
- The potential energy is constant to eliminate pulsations.

The relaxation introduces some mixing between core and shell. As a result the transition region broadens and the core radius decreases to 3.8×10^8 cm. At the same time the shell mass increases by about $0.02\,M_\odot$ as some C and O were mixed into the shell (approximately $0.01\,M_\odot$ each). The density, temperature, and He mass fraction profiles at the time of He detonation ignition are shown in Figure II.1.1 in red. The shell masses after relaxation (M_{pHeS}) are included in Table II.1.1. The green dotted and blue dashed lines in Figure II.1.1 indicate the location of the very base of the He shell and the outer edge of the transition region. It is apparent that some cells in the $[3.5 \times 10^8, 3.9 \times 10^8]$ cm regime show an unusual temperature increase. These are artifacts in the simulation, but do not influence the detonation simulation as the values are not high enough to trigger a detonation in the material.

It needs to be pointed out that the core-shell mixing observed in the models is set by the relaxation step with some contribution from the initial transition in the 1D profiles. The exact amount of mixing in WDs is not known to date as it is not well studied in progenitor evolution models. Simulations of rigidly rotating WDs are carried out by Neunteufel et al. (2017) in 1D. They consider dynamical shear instability, Goldreich-Schubert-Fricke instability, and secular shear instability (among others) to model the mixing process accurately (for details see Neunteufel et al. 2017). The degree of mixing in their models primarily depends on the total mass of the WD (massive systems showing less mixing than low mass systems). However, they point out that it depends on various parameters, such as the initial chemical profile.

II.1.2 Detonation

The final configurations of the relaxation simulations were used as initial profiles for the detonation simulations. In the double detonations simulated here, it was assumed that the He detonation is ignited by a thermal instability. This is different to dynamical ignition in the so-called D6 (dynamically driven double-degenerate double detonation) models of Shen et al. (2018a) and the violent mergers of Guillochon et al. (2010) and Pakmor et al. (2010, 2011, 2013). In this work, the ignition is realized by an artificial ignition in the simulations which is done by increasing the specific thermal energy to 5×10^{16} erg g^{-1} in selected cells. The value is high enough for a He detonation ignition while remaining physical. Simulations by Glasner et al. (2018) show comparable values. Due to spherical symmetry, the position of the He detonation ignition can be chosen somewhat freely. It was placed on the positive z-axis at $x = y = 0$ with a radial distance to the center of the WD corresponding to the peak in the temperature profile. A volume with radius ΔR was set to detonate with ΔR being 0.04 times the distance of the central ignition spot to the WD center. Glasner et al. (2018) find detonation ignition volumes of similar sizes in their simulations. The ignition volume was set up to be symmetric. However, small asymmetries can arise due to the Voronoi structure of the grid. The cells whose specific thermal energy is increased to trigger a He detonation are visible in the temperature profile of Figure II.1.1. They have a temperature of at least 7×10^8 K and are located around a radius of 4.04×10^8 cm.

In the detonation simulations a 33 isotope nuclear reaction network was used. This allows to keep an account of the key reactions. It consist of neutron (n), p, ^{4}He, ^{12}C, ^{13}N, ^{16}O, ^{20}Ne, ^{22}Na, ^{23}Na, ^{24}Mg, ^{25}Mg, ^{26}Mg, ^{27}Al, ^{28}Si, ^{29}Si, ^{30}Si, ^{31}P, ^{32}S, ^{36}Ar, ^{40}Ca, ^{44}Ti, ^{45}Ti, ^{46}Ti, ^{47}V,

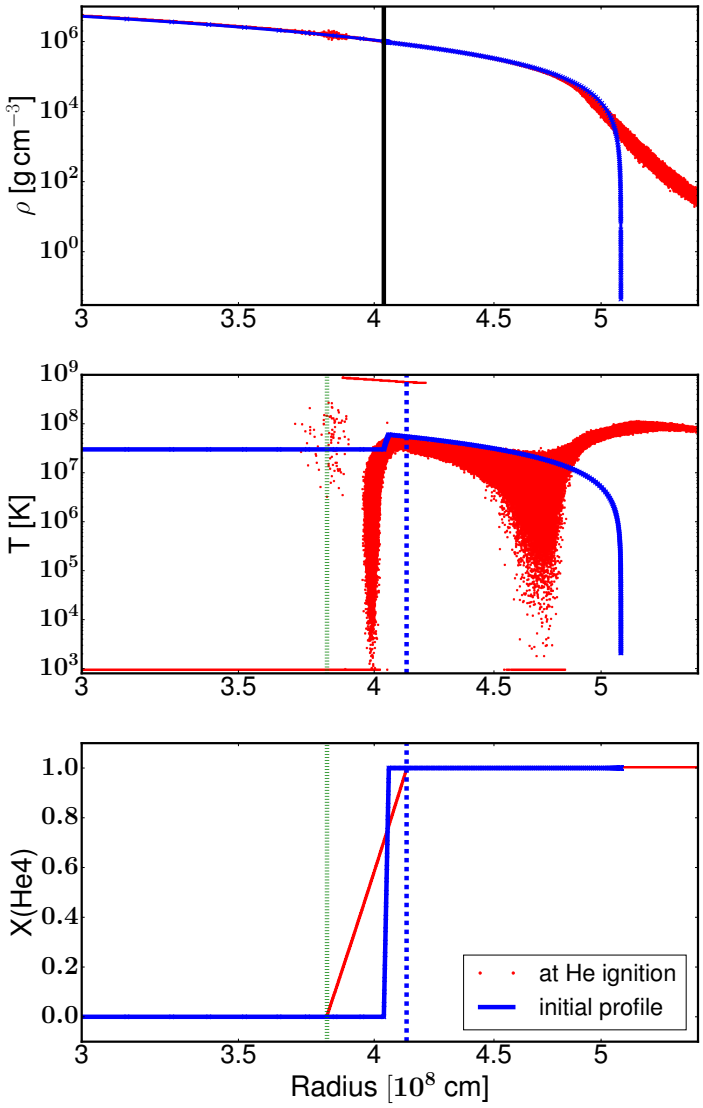

Figure II.1.1: Density, temperature, and helium mass fraction (*top to bottom*) over radius in the interval of 3 to 5.5 $\times$ 10^8 cm; shown are the initial profiles (blue) and at helium ignition (red) of Model M2a; the black solid, green dotted, and blue dashed lines represent the core-shell transition, base of the helium shell, and outer edge of the transition region, respectively; the He detonation cells have temperatures higher than 7×10^8 K at He ignition (from Gronow et al. 2020).

^{48}Cr, ^{49}Cr, ^{50}Cr, ^{51}Mn, ^{52}Fe, ^{53}Fe, ^{54}Fe, ^{55}Co, and ^{56}Ni. A list of the nuclear reactions is given in Table A.1 in Appendix A. Detailed nucleosynthetic yields are determined in a postprocessing step as described in Section I.3.3.

As mentioned earlier, the C detonation ignition mechanism was tested against a change in the location of the He detonation ignition spot. In addition to a He detonation ignition at the temperature peak (Model M2a), the He detonation was also ignited at the very base of the shell (Model M2b). A sketch of the locations is given in Figure II.1.2. The CO core is illustrated in yellow and the He shell in gray. The radial extend of the core and shell are not to scale.

The convergence of the He and C detonation is confirmed via additional simulations at varying

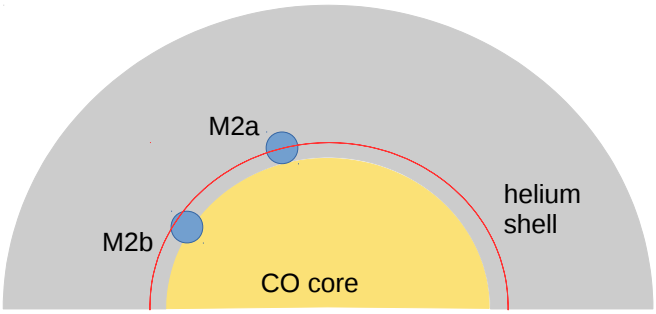

Figure II.1.2: Sketch of different ignition spots; the CO core is shown in yellow and the He shell in gray (from Gronow et al. 2020).

resolutions, Models M2a_79, M2a_36, M2a_21, and M2a_13. As pointed out in Section I.3.2.2 Arepo allows to increase the resolution in selected regions. For this the reference mass was decreased in each higher level of refinement. No additional refinement was used in Model M2a_79. Models M2a_36 and M2a_21 have references masses of 4×10^{26} g and 2×10^{26} g, respectively, as the He shell was additionally refined. A further refinement was added in the convergence region of the He detonation wave (see Section I.3.2.2) for Models M2a_13 and M2a which have a reference mass of 1.2×10^{26} g and 2×10^{25} g, respectively.

II.2 Explosion simulations

Explosion simulations were carried out for the nine models listed in Table II.1.1 until 100 s after He detonation ignition. At this time homologous expansion has set in. The focus of this and the next section is on the reference model M2a. As described in Section II.1.2, the He detonation was ignited artificially. In Model M2a, this resulted in an ignition that covers 4514 cells. In the following sections the evolution of the double detonation including the C detonation ignition mechanism is described (Section II.2.1) and an analysis of the abundances at 100 s (Section II.2.2) is given. The robustness of the C detonation ignition mechanism is investigated in Section II.2.3.

II.2.1 C detonation ignition mechanism

The double detonations presented here exhibit a C detonation ignition mechanism which, so far, received only little attention (see Section I.2.6). It is first fully presented in Gronow et al. (2020) (but also see Livne and Arnett 1995, García-Senz et al. 1999, Forcada 2007, García-Senz et al. 2018) and named 'scissors mechanism' based on the similarity of its process to closing scissors.

The evolution of the double detonation of Model M2a is shown in Figure II.2.1. The time evolution of the ^{12}C mass fraction, temperature, and density (left to right) are shown in a slice through the center of the WD with time since He detonation ignition increasing from top to bottom. The He detonation ignition is visible in the temperature profile in the top row of Figure II.2.1. A hotspot can be recognized on the positive z-axis. The propagation of the He detonation wave in the shell is illustrated in the ^{12}C mass fraction and temperature profiles of the second row in Figure II.2.1. The energy release in the burning front leads to a temperature increase in this region. Furthermore, it is apparent that some ^{12}C is burnt in the transition region between core and shell. At this point in time, 0.803 s after He detonation ignition, the propagation of the shock wave in the core is visible in the density profile. It has a much lower velocity than the detonation wave in the shell due to the higher densities present in the core. The third row of Figure II.2.1 shows the convergence of the He detonation wave at the antipode of its first ignition point on the negative z-axis. A C detonation is ignited at this point in time, 1.123 s after He detonation ignition. This can be confirmed by the profiles 1.282 s after He detonation ignition (bottom row of Figure II.2.1). The C detonation moves inward with a velocity of about 13.1×10^8cm s^{-1} developing into a core detonation that disrupts the WD. It is also visible that the newly formed detonation is about to overrun the shock wave in the core as it is about to converge off-center in the density profile. A successful C detonation is also confirmed by the profile of the ^{12}C mass fraction as ^{12}C is burnt in the core.

It should be pointed out that small asymmetries are visible in Figure II.2.1. These, however, are caused by the Voronoi structure of the computational grid. Further, an initial asymmetry in the He detonation ignition spot can lead to these asymmteries as well (see Section II.1.2).

A close-up on the propagation of the He detonation wave around its convergence point is shown in Figure II.2.2 in a zoom-in in time and space. The region plotted in Figure II.2.2 covers

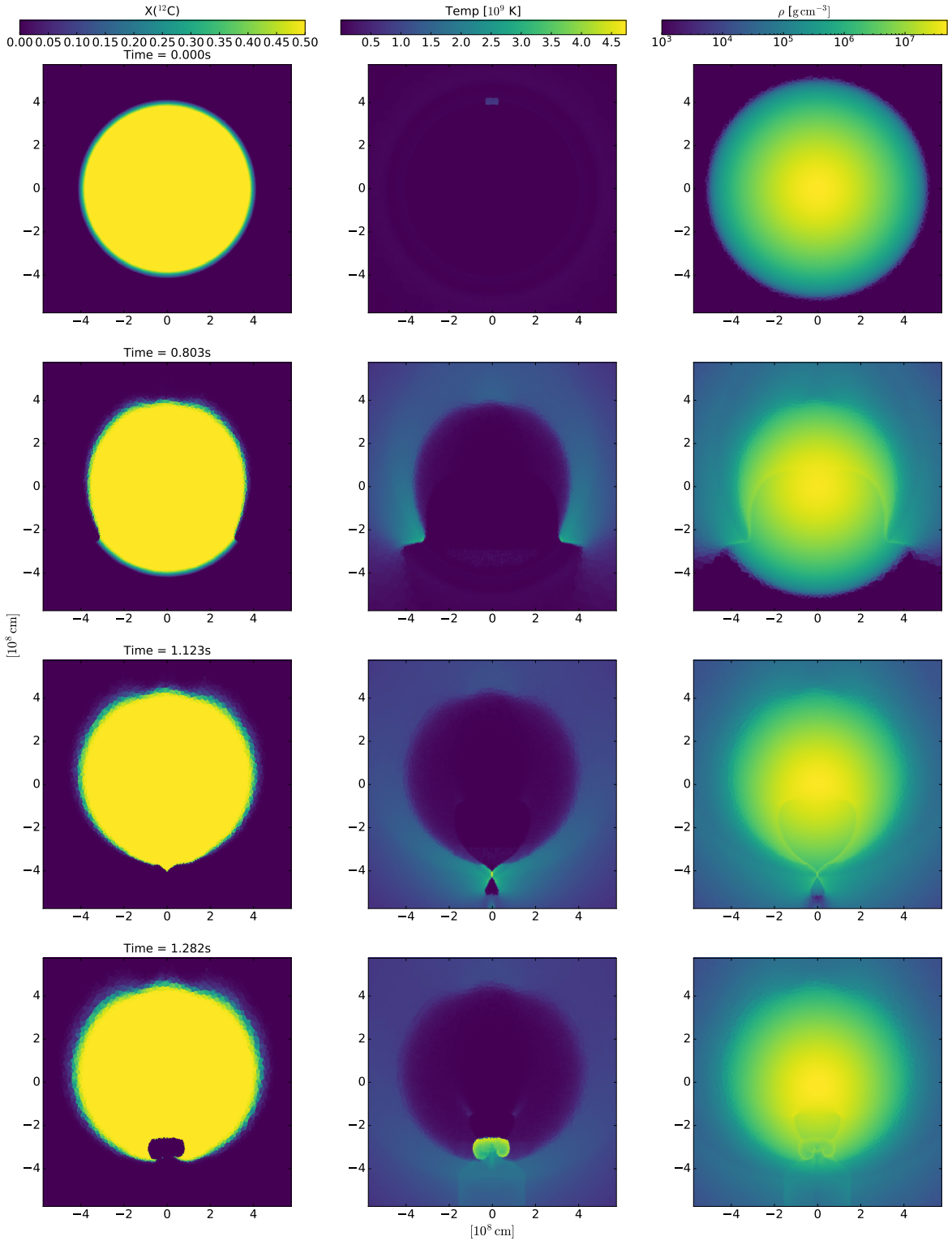

Figure II.2.1: Time evolution of Model M2a; carbon mass fraction, temperature in K, and density in g cm^{-3} (*left to right*) at times $t = 0\,\mathrm{s}$, $t = 0.803\,\mathrm{s}$, $t = 1.123\,\mathrm{s}$, and $t = 1.282\,\mathrm{s}$ *top to bottom)* plotted as slices through the center of the WD in the $x - z$ plane (from Gronow et al. 2020).

the range -2.5×10^8 cm $< x < 2.5 \times 10^8$ cm and -6.5×10^8 cm $< z < -2.5 \times 10^8$ cm for times between 1.080 s and 1.187 s of the temperature profile. The temperature at the burning front is about 3.6×10^9 K.

The convergence of the He detonation wave which corresponds to the point of C detonation ignition is illustrated in the central panel of Figure II.2.2. A comparison to the profile of the ^{12}C mass fraction in the third row of Figure II.2.1 shows that the point of convergence is located close to the base of the He shell where the material is enriched with ^{12}C. This mixing stems from the initial profile of the core-shell transition in 1D as well as the relaxation step (see Section II.1.1). The peak temperature at the convergence point is 2.7×10^9 K. However, temperature spikes of at least 2.4×10^9 K are high enough to ignite explosive C burning in cells with a ^{12}C mass fraction higher or equal to 0.2 at densities of about 3.0×10^6g cm^{-3}. The temperature in these cells increases to 2.8×10^9 K at 1.126 s after He detonation ignition supporting the C detonation. The detonating cells have an average volume of 3.22×10^{19} cm^3 which corresponds to a radius of about 20 km assuming a spherical structure of the cell. This does not correspond to a resolution high enough to resolve the C detonation ignition. Katz and Zingale (2019) state that a resolution of 1 km is needed. This is, however, not feasible in full 3D simulations and the C detonation ignition is therefore in part numerical.

In order to confirm that the C detonation ignition obtained in the simulations are physical, temperatures and densities at the C detonation ignition point are compared to critical values found in previous work (see Section I.2.6). These critical values are reached in all simulations presented here (see Table II.1.1) which allows to take the C detonation as physical.

II.2.2 Final abundances

Detailed nucleosynthetic yields are calculated in a postprocessing step as described in Section I.3.3. The abundances of ^{4}He, ^{12}C, ^{16}O, ^{28}Si, ^{32}S, ^{40}Ca, ^{44}Ti, and ^{56}Ni at 100 s after He detonation ignition for Models M1a, M2a, and M2a_i55 are listed in Table II.2.1 in solar masses ($M_\odot$). For comparison, the abundances of Model FM3 are included (from Fink et al. 2010 and Kromer et al. 2010). The nucleosynthetic yields are split into those obtained from the He detonation and those from the core detonation. This is based on the initial He mass fraction of the cell a tracer is associated with (see Section II.1).

The abundances of the models are in the expected range for a SN Ia. As such, the total ^{56}Ni yields correspond to the predictions of Stritzinger et al. (2006) and Scalzo et al. (2014) for normal SNe Ia. The nucleosynthetic yields of Model M2a can be compared to those of Model FM3 since both models have similar initial core and shell masses. However, Model FM3 does not exhibit mixing between core and shell. Their He shell is therefore not enriched with C which has an influence on the final abundances (see Section II.2.3.1 below). Furthermore, Fink et al. (2010) observe a C detonation ignition following the converging shock scenario and not the scissors mechanism as they assume the convergence of the He detonation wave not to be strong enough to trigger an ignition.

In the abundances originating from the He detonation, it is visible that both IMEs and IGEs are produced. The abundances of ^{32}S and ^{40}Ca are about the same (order of $10^{-3}\,M_\odot$). ^{16}O and ^{28}Si are slightly more abundant. Only little ^{12}C remains in the ejecta as it is burnt to heavier elements. The ^{44}Ti abundance is low with $7.0 \times 10^{-4}\,M_\odot$ which is expected to have an effect on the synthetic observables (see Kromer et al. 2010 and Section I.2.6.2). The relatively high amount of unburnt ^{4}He is caused by the expansion of the material during the burning. In this process the density decreases, the matter cools and burning stops.

Along with the high temperatures and densities in the He detonation, the C enrichment

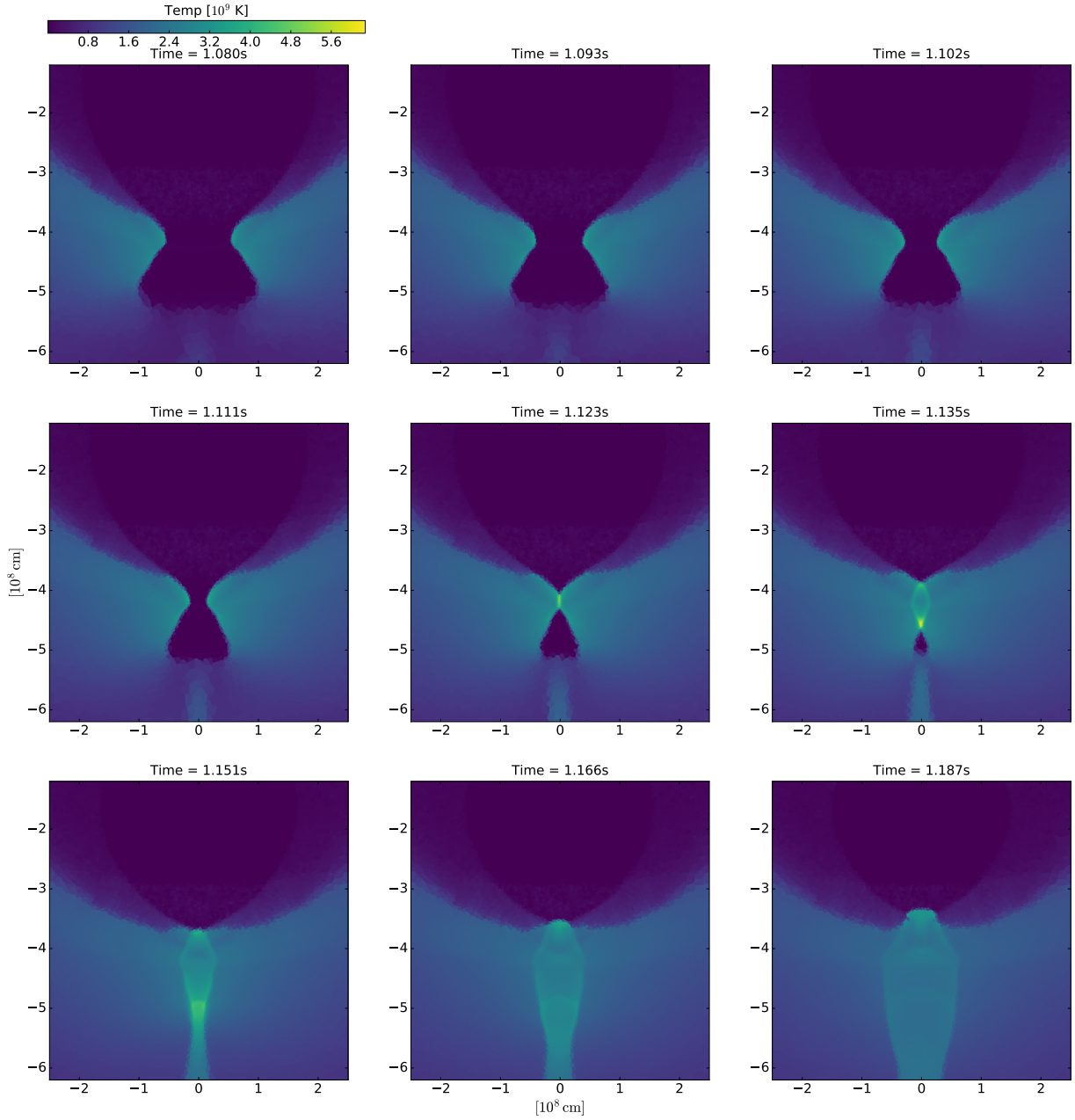

Figure II.2.2: Zoom-in of temperature profile in Fig. II.2.1; times are increasing from $t = 1.080\,\mathrm{s}$ (*top left*) to $t = 1.187\,\mathrm{s}$ (*bottom right*, from Gronow et al. 2020).

Table II.2.1: Abundances at $t = 100\,\mathrm{s}$ of Models M1a, FM3$^{(1),(2)}$, M2a, and M2a_i55 (from Gronow et al. 2020).

	He detonation			
	M1a	FM3$^{(1),(2)}$	M2a	M2a_i55
	[$M_\odot$]	[$M_\odot$]	[$M_\odot$]	[$M_\odot$]
^{4}He	2.5×10^{-2}	3.3×10^{-2}	2.3×10^{-2}	2.3×10^{-2}
^{12}C	3.6×10^{-4}	2.2×10^{-4}	1.0×10^{-4}	6.8×10^{-5}
^{16}O	5.0×10^{-3}	1.9×10^{-6}	7.4×10^{-3}	7.6×10^{-3}
^{28}Si	4.6×10^{-3}	1.4×10^{-4}	8.9×10^{-3}	9.1×10^{-3}
^{32}S	1.8×10^{-3}	7.8×10^{-4}	3.2×10^{-3}	3.3×10^{-3}
^{40}Ca	2.7×10^{-3}	2.2×10^{-3}	3.6×10^{-3}	3.5×10^{-3}
^{44}Ti	7.2×10^{-4}	3.4×10^{-3}	7.0×10^{-4}	6.9×10^{-4}
^{48}Cr	1.5×10^{-3}	4.4×10^{-3}	1.6×10^{-3}	1.6×10^{-3}
^{56}Ni	1.5×10^{-2}	1.7×10^{-3}	1.2×10^{-2}	1.2×10^{-2}

	core detonation			
	M1a	FM3$^{(1),(2)}$	M2a	M2a_i55
	[$M_\odot$]	[$M_\odot$]	[$M_\odot$]	[$M_\odot$]
^{4}He	4.2×10^{-3}		5.0×10^{-3}	5.4×10^{-3}
^{12}C	1.2×10^{-3}	2.7×10^{-3}	8.9×10^{-4}	8.2×10^{-4}
^{16}O	5.5×10^{-2}	8.0×10^{-2}	5.2×10^{-2}	5.2×10^{-2}
^{28}Si	1.7×10^{-1}	2.1×10^{-1}	1.6×10^{-1}	1.5×10^{-1}
^{32}S	1.1×10^{-1}	1.0×10^{-1}	1.1×10^{-1}	1.0×10^{-1}
^{40}Ca	2.4×10^{-2}	1.8×10^{-2}	2.3×10^{-2}	2.2×10^{-2}
^{44}Ti	2.8×10^{-5}	1.1×10^{-5}	2.8×10^{-5}	2.9×10^{-5}
^{48}Cr	4.9×10^{-4}	4.5×10^{-4}	4.8×10^{-4}	4.7×10^{-4}
^{56}Ni	5.6×10^{-1}	5.5×10^{-1}	5.7×10^{-1}	5.9×10^{-1}

References. (1) Fink et al. (2010), (2) Kromer et al. (2010)

leads to an increase in the production of ^{56}Ni compared to Model FM3. The presence of ^{12}C accelerates the α-capture processes (see Fink et al. 2010, Gronow et al. 2020, and Section II.2.3.1). Differences of one order of magnitude between Models M2a and FM3 can be found for most isotopes. The ^{12}C and ^{40}Ca abundances of Model FM3 are similar to those of Model M2a, and more ^{4}He is burnt in Model M2a than Model FM3. This in turn explains the higher ^{56}Ni production in Model M2a. These changes in the abundances are in part caused by the varying C enrichments of Models M2a and FM3. However, the modeling approach of Model FM3 is also different. Fink et al. (2010) use a level-set method. This does not enable a self-consistent calculation of the nuclear energy release involving nuclear burning. It is better suited to model the hydrodynamics in high density regimes such as the WD core. Further, the core detonation in Fink et al. (2010) is ignited by hand while the nuclear reaction network of Arepo registers a C detonation ignition self-consistently.

The nucleosynthetic yields of the core detonation are similar in Models M2a and FM3. The level-set method is more precise at these densities and the core masses of Models M2a and FM3 are a closer match than the shell masses. In Model M2a, ^{56}Ni is the most abundant isotope succeeded by ^{28}Si and ^{32}S. Because some ^{12}C is mixed into the shell of Model M2a, less ^{12}C remains unburnt in the core than in Model FM3. The production of other isotopes is of the same order of magnitude in both models. Small differences are explained by the different numerical

treatments.

II.2.3 Robustness of the C detonation ignition mechanism

The stability of the C detonation ignition mechanism is investigated regarding several parameters. The studies are presented in the following subsections.

II.2.3.1 Influence of core-shell mixing

As stated in Section II.1.1, details of the core-shell mixing are not yet known. The transition could be sharp or broad. Simulations are carried out by Neunteufel et al. (2017) showing that mixing takes place in the accretion process of rotating WDs. However, their simulations exhibit only relative little mixing and a comparison to the models presented here is difficult as they do not list mixing parameters (such as ^{12}C mass mixed into the shell). Core-shell mixing can be caused by several effects: A dredge-up of core material might occur caused by He shell burning, an accretion from a hybrid HeCO WD is possible or mixing might be due to accretion as in Neunteufel et al. (2017).

Work by Kromer et al. (2010) shows that an admixture of C into the shell can improve a match of synthetic observables to data compared to models without C admixture (see also Fink et al. 2010). In a simplified scheme, the effect of a C enrichment of the shell can be described examining matter that only consists of He and C. An admixture of metals other than ^{12}C is described in Shen and Moore (2014). The admixture of C into He has two effects: First, the burning rates increase. The triple-α reaction is a bottleneck as ^{12}C needs to be produced before burning along the α-chain sets in (starting with $^{12}\mathrm{C}(\alpha,\gamma)^{16}\mathrm{O}$). A seed abundance of ^{12}C reduces this need as α-captures are faster than the triple-α reaction at the temperatures present in He burning (see top panel in Figure II.2.3). The bottom panel of Figure II.2.3 shows that the effect is valid for temperatures higher than a cross-over temperature T_X for any ^{12}C mass fraction. Since temperatures in He burning are typically higher than T_X the burning rates are increased leading to stronger shocks by increasing the energy release.

Second, an over-pollution of the material with C has a different effect. It sets a limit to the mass number of the burnt material. Since the formation of ^{56}Ni from ^{12}C requires eleven α articles (see Section I.2.7), a so-called α-limited regime is entered if the ratio of He to C is lower than 11 : 1 and the α-chain stops at a nucleon number A smaller than 56. This point can be calculated adopting

$$12 + 4N = A, \tag{II.2.1}$$

with the number of α particles N that is needed to form a stagnation nucleus starting from ^{12}C, and

$$\frac{Y(^4\mathrm{He})}{Y(^{12}\mathrm{C})} = N = 3\frac{X(^4\mathrm{He})}{X(^{12}\mathrm{C})}. \tag{II.2.2}$$

Further,

$$X(^4\mathrm{He}) = 1 - X(^{12}\mathrm{C})$$

is derived from mass conservation involving only two isotopes. Equation (II.2.2) gives $N = 3/X(^{12}\mathrm{C}) - 3$ and with a substitution of N in Equation (II.2.1) the nucleon number of the stagnation nucleus is given by

$$A = \frac{12}{X(^{12}\mathrm{C})} \tag{II.2.3}$$

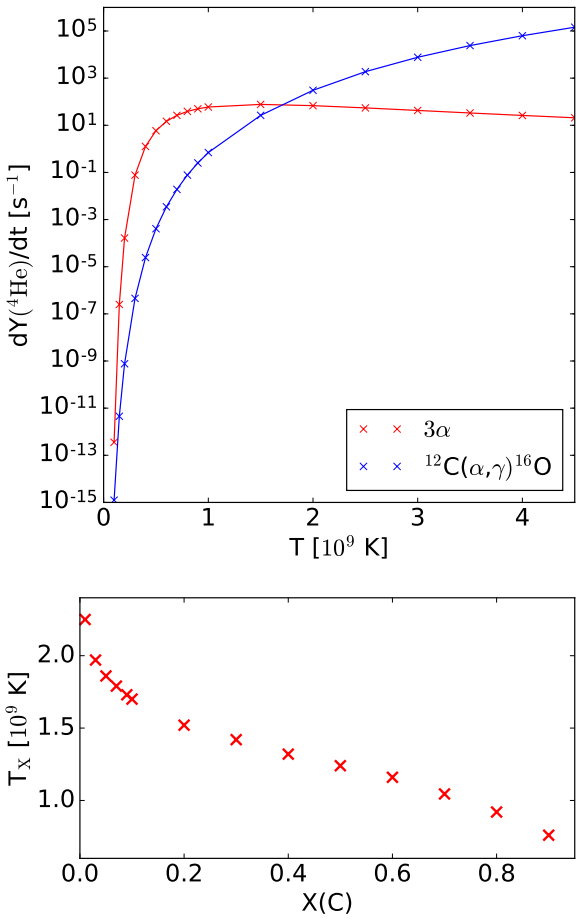

Figure II.2.3: *Top*: Rate of change in ^{4}He abundance dependent on temperature for the triple-α (red) and $^{12}\mathrm{C}(\alpha,\gamma)^{16}\mathrm{O}$ (blue) reactions and C mass fraction of 0.1. *Bottom*: cross-over temperature T_X dependent on the initial carbon abundance; both are at a density of $1.2 \times 10^6\,\mathrm{g\,cm^{-3}}$. Reaction rates are taken from the JINA Reaclib Database (Cyburt et al. 2010) in the same way as in Xu et al. (2013) for the α-capture and Fynbo et al. (2005) for the triple-α reaction (from Gronow et al. 2020).

(see also Gronow et al. 2020). According to Equation (II.2.3) the α-limited regime begins at a ^{12}C mass fraction of 0.21. Model 3m of Kromer et al. (2010), for example, exhibits a C enrichment corresponding to 34% which leads to a stagnation point around argon. The lower Ni production therefore has an influence on the synthetic observables. Different to Kromer et al. (2010) the C enrichment is not homogeneous in the models presented here. A gradient leading to a higher C enrichment at the base of the shell than at the outer edge of the transition region exists. This is more realistic based on simulations by Neunteufel et al. (2017).

A more detailed analysis of the mixing effect on the C detonation ignition mechanism is carried out in a comparison of Models M1a and M2a. While core-shell mixing in Model M2a originates from the relaxation step and the initial transition in 1D, the composition in Model M1a is reset after the relaxation to match the initial profile. Thus, almost no C is mixed into the shell of Model M1a. Only about $0.007\,M_\odot$ of ^{12}C and ^{16}O each are present in the shell. The abundances of Model M1a are included in Table II.2.1 for comparison. In this case the convergence of the He detonation wave at the antipode to its ignition spot is not strong enough to cause a C detonation ignition. This is the case because the transition region is much smaller compared to Model M2a

and the shell is not much enriched with C. Instead of the scissors mechanism, a core detonation is ignited following the converging shock scenario. The small differences in the final abundances of Models M1a and M2a are attributed to the degree of core-shell mixing. Differences of Models M1a and FM3 are explained by the different modeling approaches.

II.2.3.2 Resolution study

Table II.2.2: Reference mass M_{R} in the He shell and at the C detonation ignition point as well as energy release of the shell detonation and the C detonation ignition mechanism of Models M2a, M2a_13, M2a_21, M2a_36, and M2a_79 (from Gronow et al. 2020).

	M_{R} (He shell)	$\mathrm{E}_{\mathrm{He\ shell}}$	M_{R} (C ign. spot)	scissors mechanism
	$[10^{26}\,\mathrm{g}]$	[erg]	$[10^{26}\,\mathrm{g}]$	
M2a_79	20.0	9.78×10^{49}		
M2a_36	4.0	9.93×10^{49}		
M2a_21	2.0	9.97×10^{49}	2.0	no
M2a_13	2.0		1.2	yes
M2a	2.0		0.2	yes

A convergence study was carried out for the shell and core detonation. The respective reference masses (M_{R}, see Sections I.3.2.2 and II.1.2) are listed in Table II.2.2.

The level of refinement is changed for Models M2a_79, M2a_36, and M2a_21, with increasing resolution going from Model M2a_79 to Model M2a_21. The energy release of the He detonation is listed in Table II.2.2. Since the difference between the simulations with a high resolution (Models M2a_36 and M2a_21) is smaller than between those with a low resolution (Models M2a_79 and M2a_36), convergence of the He detonation is presumed.

For a study on the convergence of the C detonation ignition mechanism Model M2a_21 is used as basis since it has the highest resolution in the He shell. A further refinement around the He detonation wave convergence point for Models M2a_13 and M2a is added. As both models with the higher resolution than Model M2a_21 show a C detonation following the scissors mechanism, it is the converged numerical solution.

II.2.3.3 Sensitivity to ignition spot

The sensitivity of the C detonation ignition mechanism to the location of the He detonation ignition spot is studied by moving the He detonation ignition spot further in. A sketch of the two locations incorporated here is shown in Figure II.1.2. The models are labeled M2a and M2b. While the He detonation in Model M2a is set to the location of the temperature peak, it is at the very base of the He shell in Model M2b. Both models show the same propagation of the He detonation wave and the same C detonation ignition mechanism, while changes in the abundances are very small. The C detonation ignition mechanism is therefore regarded to be robust against small changes in the ignition spot.

II.2.3.4 Different core and shell masses

In order to include a core-shell mass configuration different from Model M2a, Model M3a was chosen to be similar to Model FM1 (Fink et al. 2010). Its total mass is about $0.9\,M_\odot$ and has a He shell about twice as massive as Model M2a. The He detonation ignition spot of Model M3a covers a smaller volume than the one of Model M2a as ΔR is set to 0.02. The resolution is, however, similar (see Table II.1.1). The convergence of the He detonation wave in Model M3a is strong enough to trigger a C detonation 1.251 s after He detonation ignition. The densities in this region are at least 5.8×10^6 g cm^{-3} and temperatures are above 3.2×10^9 K which is sufficient for a physical C detonation ignition (see Section I.2.6). The C mass fraction in these cells is at least 0.32.

Table II.2.3: Abundances at $t = 100$ s of Models M3a and FM1$^{(1),(2)}$ (from Gronow et al. 2020).

	He detonation		core detonation	
	M3a [M$_\odot$]	FM1$^{(1),(2)}$ [M$_\odot$]	M3a [M$_\odot$]	FM1$^{(1),(2)}$ [M$_\odot$]
^{4}He	4.2×10^{-2}	8.3×10^{-2}	1.4×10^{-3}	
^{12}C	7.6×10^{-5}	1.2×10^{-3}	4.0×10^{-4}	6.6×10^{-3}
^{16}O	1.7×10^{-2}	3.2×10^{-6}	6.8×10^{-2}	1.4×10^{-1}
^{28}Si	2.7×10^{-2}	4.8×10^{-4}	1.8×10^{-1}	2.7×10^{-1}
^{32}S	5.0×10^{-3}	2.2×10^{-3}	1.2×10^{-1}	1.3×10^{-1}
^{40}Ca	4.2×10^{-3}	4.7×10^{-3}	2.3×10^{-2}	2.0×10^{-2}
^{44}Ti	1.3×10^{-3}	7.9×10^{-3}	1.9×10^{-5}	7.2×10^{-6}
^{48}Cr	2.5×10^{-3}	1.1×10^{-2}	4.4×10^{-4}	3.9×10^{-4}
^{56}Ni	3.1×10^{-2}	8.4×10^{-4}	3.1×10^{-1}	1.7×10^{-1}

References. (1) Fink et al. (2010), (2) Kromer et al. (2010)

The final abundances of Models M3a and FM1 are listed in Table II.2.3. The shell of Model M3a is about $0.03\,M_\odot$ more massive than the one of Model FM1. This causes a higher ^{56}Ni production in the He detonation of Model M3a. The abundances originating from the core detonation are about the same in both models. More ^{16}O is burnt in Model M3a producing more ^{56}Ni. The observed differences in the nucleosynthetic yields are attributed to the numerical treatments used in both models as pointed out in Section II.2.2.

For a more detailed study on the robustness of the C detonation ignition mechanism regarding different WD masses, simulations involving a broader range of core and shell masses is needed (see Chapter III).

II.2.3.5 Influence of the nuclear network

Shen and Moore (2014) state that only a large nuclear reaction network allows to treate burning accurately in hydrodynamic simulations. Townsley et al. (2019) state that their 55 isotope nuclear reaction network is sufficient to capture the energy release accurately as it matches the energy release when using a 495 isotope nuclear reaction network within a few percent. The nuclear reaction network of Townsley et al. (2019) is best suited to follow He burning while the 33 isotope nuclear reaction network used in the hydrodynamic simulations presented here best captures C burning.

A sensitivity of the simulation to the nuclear reaction network is tested using a nuclear reaction network consisting of 55 isotopes to match that of Townsley et al. (2019), Model M2a_i55. It comprises n, p, ^{4}He, ^{11}B, $^{12-13}$C, $^{13-15}$N, $^{15-17}$O, ^{18}F, $^{19-22}$Ne, $^{22-23}$Na, $^{23-26}$Mg, $^{25-27}$Al, $^{28-30}$Si, $^{29-31}$P, $^{31-33}$S, $^{33-35}$Cl, $^{36-39}$Ar, ^{39}K, ^{40}Ca, ^{43}Sc, ^{44}Ti, ^{47}V, ^{48}Cr, ^{51}Mn, ^{52,56}Fe, ^{55}Co, and $^{56,58-59}$Ni. The nuclear reactions are given by Table A.3 in Appendix A. The final abundances of Model M2a_i55 are included in Table II.2.1 and the energy release of the shell and core detonation of Models M2a and M2a_i55 are listed in Table II.2.4. They are within a few percent of each other. The C detonation ignition mechanism further does not change with a larger nuclear reaction network in the hydrodynamic explosion simulation.

Table II.2.4: Energy release of Models M2a and M2a_i55 (from Gronow et al. 2020).

	He detonation [erg]	core detonation [erg]
M2a	9.93×10^{49}	1.35×10^{51}
M2a_i55	1.01×10^{50}	1.34×10^{51}

II.3 Radiative transfer calculations

Radiative transfer calculations were carried out by Christine E. Collins to obtain synthetic observables following the description in Section I.3.4. A detailed analysis of the synthetic light curves and spectra is given in Gronow et al. (2020). This section only points out the main findings.

In order to investigate the influence of the scissors mechanism on the observables, light curves and spectra were calculated for Models M1a, M2a, and M2a_i55. Radiative transfer calculations were also carried out for Model FM3 to ensure that any differences are only due to the hydrodynamic models and not changes in the setup of the model in Artis. The examination of the four models allows to look into the effect of mixing and the nuclear reaction network in the hydrodynamic simulation as well as a comparison to Model FM3.

II.3.1 Angle-averaged synthetic observables

II.3.1.1 Light curves

Angle-averaged light curves in the U-, B-, and I-band for Models M1a, M2a, M2a_i55, and FM3 are shown in Figure II.3.1 and parameters of all light curves are given in Table II.3.1. It is apparent that the shapes of the light curves are very similar. This is also visible in the parameters. The luminosity peak in the B-band of Model M2a is 0.3 mag brighter than in Model FM3 and occurs about 1 day earlier while the decay is slower. This is caused by the higher ^{56}Ni abundance in the nucleosynthetic yields coming from the shell detonation in Model M2a.

Table II.3.1: Observational parameters of Models M1a, M2a, M2a_i55, and FM3 (from Gronow et al. 2020).

	M2a	FM3	M1a	M2a_i55
Δm_{15}(B) (mag)	1.82	2.00	1.62	1.83
t_{max}(B) (d)	16.6	17.7	16.4	16.6
$M_{U,max}$ (mag)	-18.7	-18.4	-18.5	-18.7
$M_{B,max}$ (mag)	-18.9	-18.6	-18.7	-18.9
$M_{V,max}$ (mag)	-19.8	-19.7	-19.8	-19.8
$M_{R,max}$ (mag)	-19.6	-19.6	-19.6	-19.6
$M_{I,max}$ (mag)	-19.2	-19.2	-19.2	-19.2
$(U - B)_{B,max}$ (mag)	0.24	0.24	0.36	0.26
$(B - V)_{B,max}$ (mag)	0.81	0.95	0.92	0.82
$(V - R)_{B,max}$ (mag)	-0.099	-0.016	-0.099	-0.093
$(V - I)_{B,max}$ (mag)	-0.44	-0.39	-0.42	-0.47

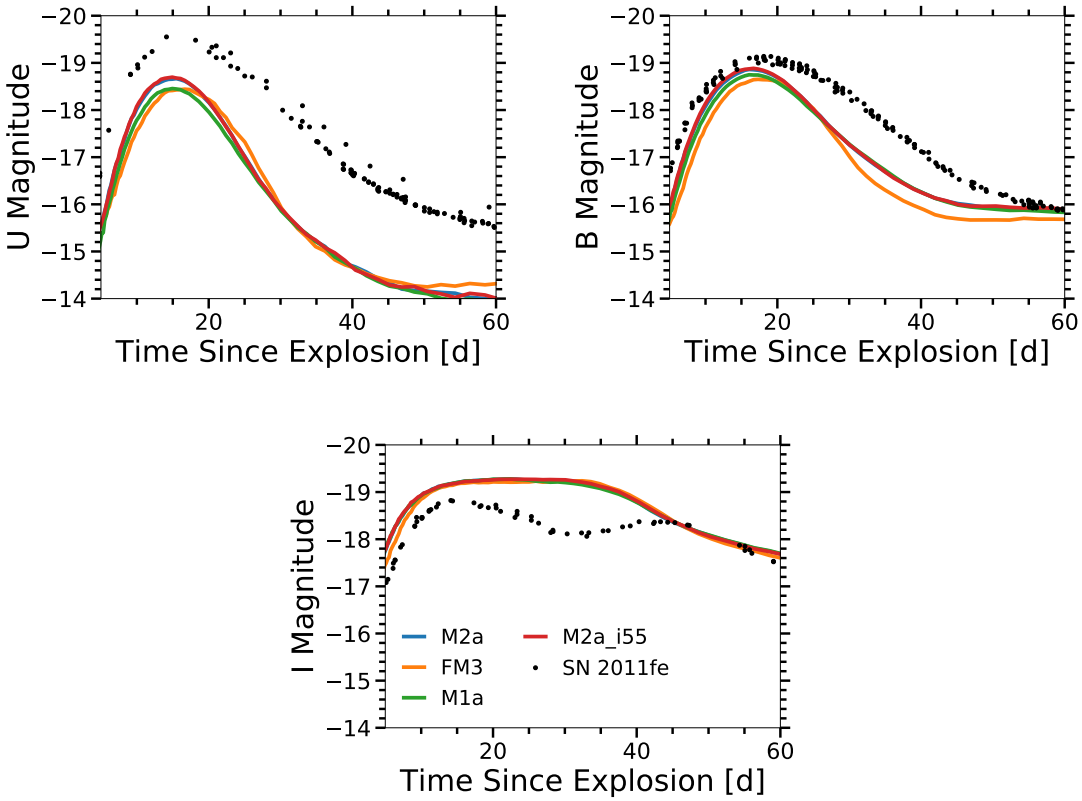

Figure II.3.1: Angle-averaged U-, B-, and I-band limited light curves of Models M1a, M2a, M2a_i55, and FM3 compared normal SN Ia SN 2011fe (Nugent et al. 2011) (from Gronow et al. 2020).

Differences between Models M2a and M2a_i55 are even smaller than those to Model FM3. Therefore, the use of a 55 isotope nuclear reaction network has no significant effect on the light curves. If the mixing is reset (Model M1a), the B-band peak occurs about 0.2 days earlier which is due to the thinner shell in Model M1a compared to Model M2a. Further, the peak magnitude of Model M1a is 0.2 mag fainter as less ^{56}Ni is produced during the shell detonation. However, the differences between all models are small compared to those to data (see Section II.4.2).

II.3.1.2 Spectra

The angle-averaged spectrum of Model M2a at 18 days after explosion is shown in Figure II.3.2 and the total emission spectrum is shown in black. The elemental contribution to the spectrum was calculated as described in Gronow et al. (2020) and is color coded in the volume under the emission spectrum. The key absorption processes are shown under the spectrum confirming a strong imprint of the ejecta originating from the He detonation in the bluer wavelength region (see also Kromer et al. 2010).

The synthetic spectra of Models M1a, M2a, M2a_i55, and FM3 at 10 days (top) and 18 days (bottom) after explosion are compared in Figure II.3.3. As expected from the comparison of the light curves, no significant differences appear. Gronow et al. (2020) point out that the Si II emission line at $\sim$ 6400 Å and the Ca II emission at $\sim$ 8500 Å of Model FM3 are weaker at 10 days while the Ti II absorption is stronger than for Model M2a.

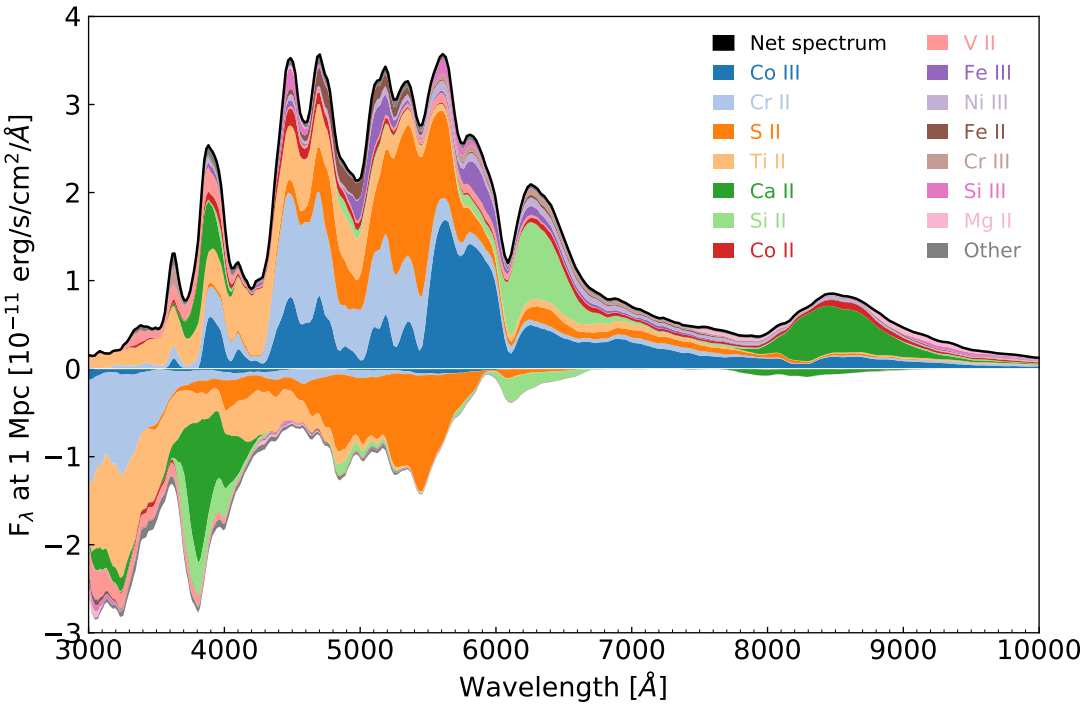

Figure II.3.2: Angle-averaged emission and absorption spectrum of Model M2a at 18 days after explosion. The total emission spectrum is shown in black and the colors indicate the contribution of ions to the emission and absorption. The ions are listed in the legend in order of greatest contribution of flux (from Gronow et al. 2020).

II.3.2 Angle-dependent observables

Due to the far off-center location of the C detonation ignition spot, it is expected that the observables have a strong viewing angle-dependency. Kromer et al. (2010) point out that a spectrum might be redder or bluer when viewed from a polar direction than observed from the equator. This is caused by the asymmetric distribution of the ejecta which is visible in Figure II.3.4 showing the mass fractions of ^{4}He, ^{32}S, ^{40}Ca, and ^{56}Ni color coded in velocity space in a slice along the x-axis for Model M2a. Figure II.3.4 illustrates that more IMEs and IGEs are present along the positive z-axis which causes a strong viewing angle effect. The asymmetries in the other models are similar as stated by Gronow et al. (2020).

Angle-dependent light curves of Model M2a are visible in Figure II.3.5 for the g- and r-band. An angle of $\theta = 0°$ points to the north pole and an angle of $\theta = 180°$ to the south pole. The g-band light curves show a stronger angle-dependency and have a difference in the peak luminosities of about 1 mag. In both bands the equatorial viewing angles ($\theta = 90°$) match the angle-average light curve well. The angle-dependent spectra show a much stronger dependence than the light curves. Figure II.3.6 illustrates this for Model M2a at 12 days after explosion.

II.3.2.1 Comparison to observations

Figures II.3.5 and II.3.6 include observational data (redshift corrected) for SN 2016jhr (Jiang et al. 2017) and SN 2018byg (De et al. 2019) which are used as comparison objects for the models in this chapter. SN 2016jhr and SN 2018byg were suggested to originate from double detonations.

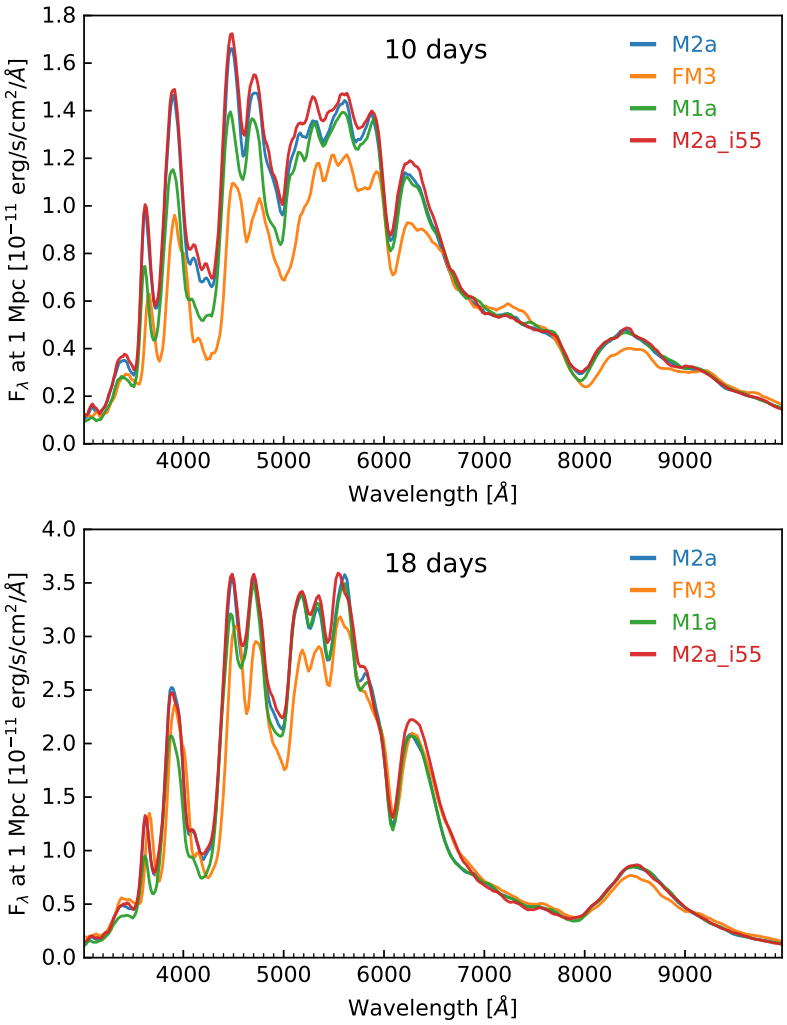

Figure II.3.3: Spectra of Models M1a, M2a, M2a_i55, and FM3 at 10 days (*top*) and 18 days (*bottom*) after maximum luminosity (from Gronow et al. 2020).

SN 2016jhr has a prominent early optical flash at 0.5 days after explosion. It has an early red and fast color evolution and has a normal brightness. The early flash is attributed to the decay of ^{56}Ni originating from the He detonation by Jiang et al. (2017). SN 2018byg is a faint SN Ia, but is included here as suggested double detonation. It shows broad Ti and IGE absorption features and near peak a high velocity (about 25.000 km/s) Ca II triplet which is found to be typical for SNe Ia. It has an early fast rise in r-band (see Figure II.3.5) attributed to the radioactive decay of the outer ejecta by De et al. (2019). For the comparison the observational data is corrected for reddening by Galactic extinction as listed by Jiang et al. (2017) (E(B-V)$_{\rm MW}$ = 0.0263 mag) and De et al. (2019) (AV= 0.032 mag).

The models presented here are too bright to match SN 2018byg. However, a spectral comparison can be carried out. A strong absorption is necessary to account for the strong line blanketing observed in SN 2018byg. This is not found in the angle-averaged spectra. It is, however, reproduced by the most extreme lines-of-sight ($\theta = 0°$ and $\theta = 45°$) of Model M2a (see Figure II.3.6). The higher abundance of heavy elements along the positive z-axis causes the strong absorption. The spectra also show significant line blanketing in the blue wavelength region and a deep Ca II absorption feature. The angle-dependent spectrum comparison of Model M2a with SN 2018byg illustrates well why multi-dimensional simulations are needed.

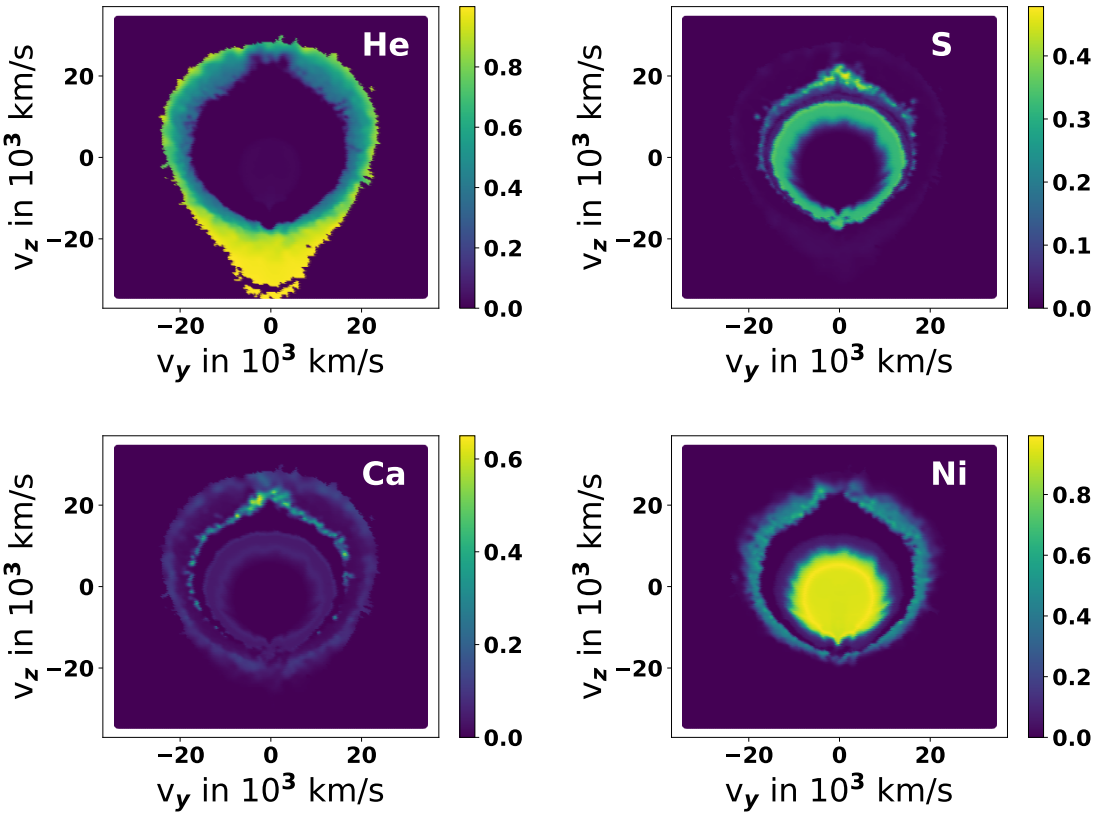

Figure II.3.4: Mass fractions of He, S, Ca, and Ni for Model M2a in a slice along the x-axis and in velocity space (from Gronow et al. 2020).

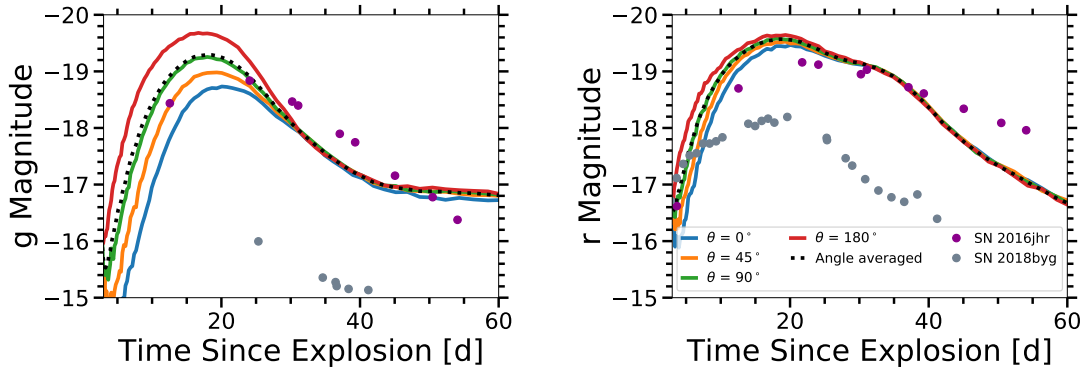

Figure II.3.5: Viewing angle-dependent g- and r-band limited and angle-averaged (black dots) light curves of Model M2a are compared to SN 2016jhr and SN 2018byg (from Gronow et al. 2020).

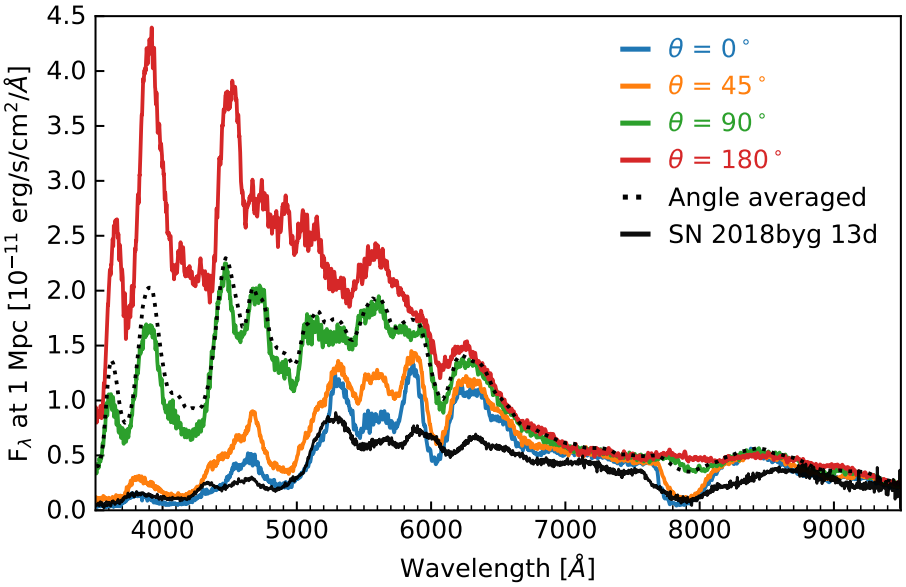

Figure II.3.6: Viewing angle-dependent spectra of Model M2a at 12 days after explosion, angles are $\theta = 0°$, 45°, 90°, and 180°, as well as the angle-averaged spectrum. The spectrum of SN 2018byg at 13 days after explosion is added for comparison (de-reddened and redshift corrected) (from Gronow et al. 2020).

II.4 Discussion

II.4.1 In the context of previous hydrodynamic simulations

A C detonation ignition mechanism similar to the scissors mechanism presented here is found by Livne and Arnett (1995), García-Senz et al. (1999), Forcada et al. (2006), and Forcada (2007). A detailed description of the mechanism and other hydrodynamic results is, however, missing in large parts which makes a comparison difficult. Livne and Arnett (1995) and García-Senz et al. (1999), for example, look into different masses than covered in Models M1a to M3a. Livne and Arnett (1995) cover a range of masses between $0.7\,M_\odot$ and $1.1\,M_\odot$, but the core-shell mass configurations differ from the ones of Models M1a, M2a, and M3a. A WD with a total mass of $1.02\,M_\odot$ is looked at by García-Senz et al. (1999). The model presented in Forcada et al. (2006) and Forcada (2007) has a total mass of $0.9\,M_\odot$ which is similar to Model M3a. However, the shell mass in their model is higher with $0.2\,M_\odot$. A similar C detonation ignition mechanism is also found by García-Senz et al. (2018) for rotating WDs of different masses in 3D simulations of a quarter of the star. All these different models confirm that the C detonation ignition mechanism is robust and is not only valid for a WD of a specific core-shell mass configuration.

Forcada (2007) point out that the location of the He detonation spot is important for a C detonation ignition in the scissors mechanism. However, the study presented in Section II.2.3.3 shows that it is robust against small changes in the position. On the contrary, the size of the transition region is important (Section II.2.3.1).

Many previous simulations (e.g. Fink et al. 2010) do not regard a C detonation ignition at the convergence point of the He detonation wave as feasible. Fink et al. (2010), however, state that a core detonation is ignited in the converging shock scenario if it is not triggered earlier. The C detonation is not triggered self-consistently in their level-set approach, but ignited artificially which causes the convergence point not to be investigated further.

II.4.2 Comparison to observations

A comparison of the angle-dependent observables with SN 2016jhr and SN 2018byg is given in Section II.3.2.1. This section focuses on a comparison of the angle-averaged light curves. For this, data of SN 2011fe (Nugent et al. 2011) is included in Figures II.3.1 and II.4.1 as it represents a SN Ia of normal brightness. Nugent et al. (2011) find that the total galactic extinction in SN 2011fe is negligible and that a correction is not needed for a comparison to models.

The models presented here have a similar peak brightness as SN 2011fe in the B-band (Figure II.3.1) while the decline is too fast compared to data. Further, the U-band brightness is too low. This is caused by the absorption from the He detonation ashes. SN 2016jhr is found to have a brightness similar to Model M2a (see Gronow et al. 2020) with the peak brightness being at 20 days which differs from Model M2a by 3.4 days (see Figure II.3.5).

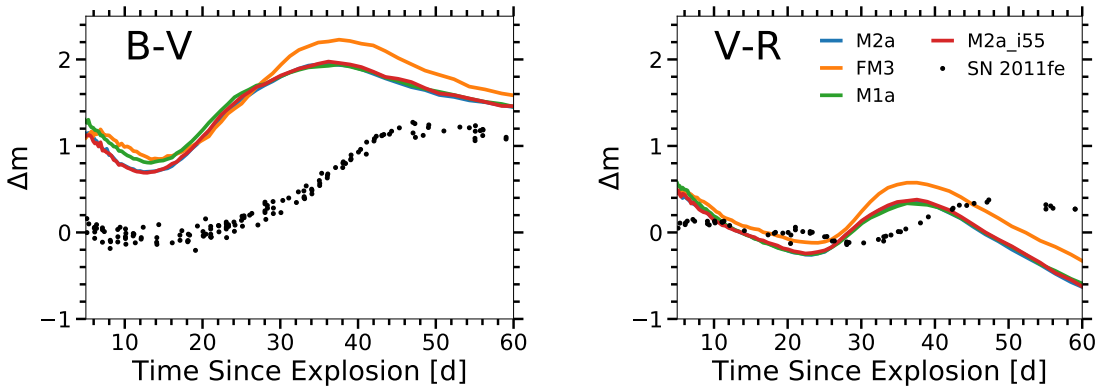

Figure II.4.1: Angle-averaged B-V and V-R color curves of Models M1a,M2a, M2a_i55, and FM3. The colors of SN 2011fe (Nugent et al. 2011) are included for comparison (from Gronow et al. 2020).

The angle-averaged time evolution of the models is shown in Figure II.4.1. Data of SN 2011fe is included for comparison. The B-V color points out that the models are too red at early times in relation to data. This is also found by Kromer et al. (2010) who attribute it to the ejecta of the He detonation.

Chapter III

Can different core and He shell masses explain variations of Type Ia supernovae?

Introduction

Observations of SNe Ia show a relation between the peak brightness of the B-band light curve and the decline rate as pointed out by Phillips (1993) and Phillips et al. (1999) (see Section I.1.2.1). Previous work found that models of M_{Ch} WDs are not able to reproduce the relation while simulations of sub-M_{Ch} show a relatively good match (see Section I.2). The study presented in this chapter follows up on those works: A parameter study was carried out involving a range of core and shell masses. Since the mass of the WD is the leading parameter for the production of ^{56}Ni (Sim et al. 2010, predicted by Pinto and Eastman 2000) and therefore brightness of the light curve, the models are expected to generate a broad range of luminosities possibly explaining the observational trend.

Similar parameter studies have been carried out by, for example, Fink et al. (2007, 2010), Polin et al. (2019), and Leung and Nomoto (2020). Those are, however, carried out in 1D (Polin et al. 2019) and 2D (Fink et al. 2007, 2010, Leung and Nomoto 2020), and omit the inclusion of a metallicity of the zero-age main sequence progenitor star (e.g. Polin et al. 2019). The simulations presented here are calculated in 3D (see Sections II.1 and III.1 for a description of the setup) and assume a solar metallicity of the zero-age main sequence progenitor star. The bulk of the work presented here is part of a paper accepted to be published by the journal *Astronomy & Astrophysics* (Gronow et al. 2021a).

III.1 Models of the parameter study

III.1.1 Model setup

The models in this parameter study were set up in the same way as described in Section II.1 for the models presented in Chapter II: A WD with CO core and He shell was constructed to be in hydrostatic equilibrium in 1D. For this, the total mass ($M_{\rm tot}$) and density at the base of the He shell ($\rho_{\rm s}$) were set as initial parameters along side the core temperature (T_c) and temperature at the base of the He shell (T_s). The shell mass ($M_{\rm s}$) and central density ($\rho_{\rm c}$) were derived from these. The 1D structure was mapped to the 3D computational Arepo grid (see Section II.1 for details). The refinement capability of Arepo is used to increase the resolution in selected regions (see Section I.3.2.2). Parameters of the models including the resolution at 1 s after He detonation ignition are given in Tables III.1.1, III.1.2, and III.1.3.

The parameter study consists of 14 WDs with varying mass configurations covering a range of different shell and core masses. The core mass ranges from $0.8\,M_\odot$ to $1.1\,M_\odot$ and the shell mass is between $0.02\,M_\odot$ and $0.1\,M_\odot$. These limits allow to include models with expected low and high luminosities (see e.g. Sim et al. 2010, Fink et al. 2010). WDs with low mass He shells are thought to better match observables (e.g. Fink et al. 2010, Townsley et al. 2019) as they show fewer imprints originating from the He detonation (Höflich et al. 1996, Fink et al. 2010, Kromer et al. 2010). The parameter study also includes WDs with the highest expected He shell mass (Woosley and Kasen 2011, Neunteufel et al. 2016). The He shell mass range found by Neunteufel et al. (2016) in their binary evolution models is in part covered in this study. However, the accretion process, and therefore the resulting shell mass, is sensitive to the donor mass, orbital period (Neunteufel et al. 2016) as well as details of the progenitor evolution.

The core and shell masses of the initial profiles ($M_{\rm c,\,ini}$ and $M_{\rm s,\,ini}$) are listed in Tables III.1.1, III.1.2, and III.1.3. The split is based on the initial He mass fraction with cells having a value of at least 0.01 being associated with the shell. The model names are based on the initial core and shell masses fixing the first two and subsequent two digits, respectively. A model of a WD with initial core mass of $1.1\,M_\odot$ and shell mass of $0.05\,M_\odot$ is therefore named M11_05.

III.1.2 Metallicity implementation

Different to the models discussed in Chapter II, the models in this part assume a solar metallicity of the zero-age main sequence progenitor star. This introduces metallicity as a further parameter to those of the core and shell masses, and C enrichment of the shell. The metallicity is set by adding ^{14}N and ^{22}Ne to the composition. These isotopes are chosen as they are most abundant following the reactions described below and determine the electron fraction $Y_{\rm e}$, defined as

$$Y_{\rm e} = \frac{n_{\rm e}}{n_{\rm B}} \tag{III.1.1}$$

Table III.1.1: Parameters of models with core masses of $0.8\,M_\odot$ (from Gronow et al. 2021a).

		M08_10_r	M08_10	M08_05	M08_03
$M_{\mathrm{c,\,ini}}$	$[M_\odot]$	0.795	0.795	0.803	0.803
$M_{\mathrm{s,\,ini}}$	$[M_\odot]$	0.109	0.109	0.053	0.028
$M_{\mathrm{s,\,det}}$	$[M_\odot]$	0.109	0.127	0.075	0.040
M_{tot}	$[M_\odot]$	0.910	0.910	0.856	0.830
T_{s}	$[10^7\,\mathrm{K}]$	6	6	6	6
T_{c}	$[10^7\,\mathrm{K}]$	3	3	3	3
ρ_{c}	$[10^7\,\mathrm{g\,cm^{-3}}]$	1.864	1.887	1.413	1.224
ρ_{s}	$[10^6\,\mathrm{g\,cm^{-3}}]$	0.730	1.034	0.390	0.356
r_{det}	$[10^8\,\mathrm{cm}]$	4.40	4.48	5.32	5.56
He det ign vol	$[10^{23}\,\mathrm{cm^3}]$	0.12	0.43	1.52	6.36
$M(^4\mathrm{He}_{\mathrm{det,\,s}})$	$[M_\odot]$	0.083	0.082	0.051	0.027
$M(^{12}\mathrm{C}_{\mathrm{det,\,s}})$	$[M_\odot]$	0.013	0.023	0.012	0.006
$M(^{14}\mathrm{N}_{\mathrm{det,\,s}})$	$[M_\odot]$	2.7e−4	2.6e−4	1.6e−4	7.7e−5
$M(^{16}\mathrm{O}_{\mathrm{det,\,s}})$	$[M_\odot]$	0.012	0.022	0.012	0.006
$M(^{22}\mathrm{Ne}_{\mathrm{det,\,s}})$	$[M_\odot]$	3.4e−4	6.1e−4	3.2e−4	1.7e−4
$M(^{12}\mathrm{C}_{\mathrm{det,\,c}})$	$[M_\odot]$	0.401	0.392	0.393	0.398
$M(^{16}\mathrm{O}_{\mathrm{det,\,c}})$	$[M_\odot]$	0.390	0.381	0.383	0.387
$M(^{22}\mathrm{Ne}_{\mathrm{det,\,c}})$	$[M_\odot]$	0.011	0.010	0.011	0.011
resolution	$[10^{-8}\,M_\odot]$	1.47	2.08	3.95	37.10
ignition mechn.		s		(s,) cs	cs
core ign. time		1.33	1.102	2.05	2.65

with electron and baryon number densities n_{e} and n_{B}, respectively. The electron fraction is 0.5 if the WD only consists of He, C, and O. The value decreases with increasing metallicity. The code was changed in order to integrate this in the 1D setup.

During CNO burning in the progenitor star and its companion the available ^{12}C and ^{16}O are transformed into ^{14}N which represents the metallicity in the WD shell. In a subsequent burning step taking place in the core of the progenitor star, the material is converted to ^{22}Ne via $^{14}\mathrm{N}(\alpha,\gamma)^{18}\mathrm{F}(\beta^+,\nu_e)^{18}\mathrm{O}(\alpha,\gamma)^{22}\mathrm{Ne}$ (Gronow et al. 2021b). Based on these processes and using the solar abundances of Asplund et al. (2009), the shell composition is set to be $X(^4\mathrm{He}) = 0.997$ and $X(^{14}\mathrm{N}) = 0.003$ in mass fractions in the initial profile. A small transition region between shell and core is succeeded by a core comprised of $X(^{12}\mathrm{C}) = 0.5$, $X(^{16}\mathrm{O}) = 0.49$ and $X(^{22}\mathrm{Ne}) = 0.01$. This results in a homogeneous distribution of the isotopes in the WD which is chosen assuming that it originates from a homogeneous production during the evolution of the zero-age main sequence progenitor star. The sedimentation of ^{22}Ne can be neglected in the models as it does not cause large changes in the ^{22}Ne distribution in the somewhat extended sub-$\mathrm{M_{Ch}}$ WDs (Bildsten and Hall 2001, Deloye and Bildsten 2002, García-Berro et al. 2008). It is to be noted that the effect on the electron fraction Y_{e} due to its metallicity-dependence is included only after the mapping of the 1D profile to the 3D computational grid. In greater detail, ^{20}Ne is used in the setup of the initial 1D profile and changed to depict ^{22}Ne in the mapping step. This has a minimal effect on the hydrostatic equilibrium of the WD and a more consistent treatment would include the consideration of ^{22}Ne already in the initial setup. Nevertheless, perturbations in the hydrostatic equilibrium originating from this procedure are compensated in the relaxation step. The WD is therefore in hydrostatic equilibrium at He detonation ignition.

In order to incorporate the inclusion of metallicity the nuclear reaction network of the hydrodynamic simulations is extended to 35 isotopes so that it includes ^{14}N and ^{22}Ne (see Section II.1.2

Table III.1.2: Parameters of models with a core mass of 0.9 $M_\odot$ and 1.1 $M_\odot$ (from Gronow et al. 2021a).

		M11_05	M09_10_r	M09_10	M09_05	M09_03
$M_{\mathrm{c,\,ini}}$	$[M_\odot]$	1.100	0.888	0.888	0.899	0.905
$M_{\mathrm{s,\,ini}}$	$[M_\odot]$	0.054	0.108	0.108	0.053	0.026
$M_{\mathrm{s,\,det}}$	$[M_\odot]$	0.123	0.108	0.142	0.074	0.043
M_{tot}	$[M_\odot]$	1.159	1.001	1.001	0.952	0.931
T_{s}	$[10^7\,\mathrm{K}]$	6	6	6	6	6
T_{c}	$[10^7\,\mathrm{K}]$	3	3	3	3	3
ρ_{c}	$[10^7\,\mathrm{g\,cm^{-3}}]$	10.213	3.219	3.273	2.471	2.170
ρ_{s}	$[10^6\,\mathrm{g\,cm^{-3}}]$	2.000	1.303	2.261	0.781	0.493
r_{det}	$[10^8\,\mathrm{cm}]$	3.53	4.21	4.21	4.59	5.02
He det ign vol	$[10^{23}\,\mathrm{cm^3}]$	0.22	0.40	0.26	1.32	1.26
$M(^4\mathrm{He}_{\mathrm{det,s}})$	$[M_\odot]$	0.049	0.085	0.085	0.053	0.026
$M(^{12}\mathrm{C}_{\mathrm{det,s}})$	$[M_\odot]$	0.037	0.012	0.029	0.011	0.009
$M(^{14}\mathrm{N}_{\mathrm{det,s}})$	$[M_\odot]$	1.5e−4	2.8e−4	2.8e−4	1.7e−4	7.1e−5
$M(^{16}\mathrm{O}_{\mathrm{det,s}})$	$[M_\odot]$	0.036	0.011	0.028	0.010	0.009
$M(^{22}\mathrm{Ne}_{\mathrm{det,s}})$	$[M_\odot]$	0.001	3.1e−4	7.7e−4	2.8e−4	2.3e−4
$M(^{12}\mathrm{C}_{\mathrm{det,c}})$	$[M_\odot]$	0.518	0.446	0.429	0.442	0.446
$M(^{16}\mathrm{O}_{\mathrm{det,c}})$	$[M_\odot]$	0.504	0.434	0.418	0.430	0.434
$M(^{22}\mathrm{Ne}_{\mathrm{det,c}})$	$[M_\odot]$	0.014	0.012	0.011	0.012	0.012
resolution	$[10^{-8}\,M_\odot]$	27.36	1.38	4.89	2.26	4.34
ignition mechn.		edge	s		(s,) cs	(s,) cs
core ign. time		0.006	1.17	0.50	1.71	2.14

for a list of the remaining 33 isotopes). The nuclear reactions included in the hydrodynamic simulations are given by Tables A.1 and A.2 in Appendix A. Two models with a particularly thin He shell, Models M10_02 and M10_02T, are calculated involving a 55 isotope nuclear reaction network (see Section II.2.3.5 for details) following work by Shen and Moore (2014) and Townsley et al. (2019). In the postprocessing step (see Section I.3.3) a more complete set of isotopes is included to represent metallicity based on the solar values of Asplund et al. (2009).

III.1.3 Relaxation

Before a detonation simulation was started, a relaxation step was carried out as described in Section II.1.1. This is necessary to account for spurious velocities originating from the mapping on the unstructured 3D grid. During the relaxation some ^{22}Ne is mixed into the shell along with ^{12}C. It is apparent that models with a similar initial shell mass agree well in the composition of the shell after relaxation. The composition of the shell and core after relaxation are given in Tables III.1.1, III.1.2, and III.1.3 by $M(^4\mathrm{He}_{\mathrm{det,s}})$, $M(^{12}\mathrm{C}_{\mathrm{det,s}})$, $M(^{14}\mathrm{N}_{\mathrm{det,s}})$, $M(^{16}\mathrm{O}_{\mathrm{det,s}})$, and $M(^{22}\mathrm{Ne}_{\mathrm{det,s}})$, and $M(^{12}\mathrm{C}_{\mathrm{det,c}})$, $M(^{16}\mathrm{O}_{\mathrm{det,c}})$, and $M(^{22}\mathrm{Ne}_{\mathrm{det,c}})$, respectively.

The transition region between core and shell broadens during the relaxation step in the same way as described in Section II.1 leading to a decrease of the core radius. Figure III.1.1 shows the ^{4}He and ^{12}C mass fraction profiles in the radial span from 3×10^8 cm to 5×10^8 cm for Models M10_10, M10_05, and M10_03 (top to bottom). The initial profiles are in red and blue, and profiles after relaxation in black and magenta.

The degree of mixing between core and shell is primarily set by the relaxation step and only

Table III.1.3: Parameters of models with a core mass of 1.0 $M_\odot$ (data of Models M10_10, M10_05, M10_03, and M10_02 from Gronow et al. 2021a).

		M10_10	M10_05	M10_03	M10_02	M10_02T
$M_{\mathrm{c,\,ini}}$	$[M_\odot]$	1.015	1.002	1.028	1.005	1.009
$M_{\mathrm{s,\,ini}}$	$[M_\odot]$	0.090	0.052	0.027	0.020	0.020
$M_{\mathrm{s,\,det}}$	$[M_\odot]$	0.133	0.074	0.047	0.028	0.027
M_{tot}	$[M_\odot]$	1.105	1.055	1.055	1.025	1.029
T_{s}	$[10^7\,\mathrm{K}]$	6	6	6	6	50
T_{c}	$[10^7\,\mathrm{K}]$	3	3	3	3	3
ρ_{c}	$[10^7\,\mathrm{g\,cm^{-3}}]$	6.847	4.777	4.777	3.904	4.068
ρ_{s}	$[10^6\,\mathrm{g\,cm^{-3}}]$	2.460	1.094	0.850	0.510	0.469
r_{det}	$[10^8\,\mathrm{cm}]$	3.47	4.20	4.25	4.36	4.58
He det ign vol	$[10^{23}\,\mathrm{cm^3}]$	0.63	0.15	0.77	0.95	0.82
$M(^4\mathrm{He}_{\mathrm{det,\,s}})$	$[M_\odot]$	0.084	0.050	0.026	0.020	0.018
$M(^{12}\mathrm{C}_{\mathrm{det,\,s}})$	$[M_\odot]$	0.024	0.012	0.010	0.004	0.003
$M(^{14}\mathrm{N}_{\mathrm{det,\,s}})$	$[M_\odot]$	2.7e−4	1.5e−4	7.3e−5	5.2e−5	1.3e−4
$M(^{16}\mathrm{O}_{\mathrm{det,\,s}})$	$[M_\odot]$	0.023	0.012	0.010	0.004	0.005
$M(^{22}\mathrm{Ne}_{\mathrm{det,\,s}})$	$[M_\odot]$	6.4e−4	3.3e−4	2.8e−4	1.1e−4	1.5e−4
$M(^{12}\mathrm{C}_{\mathrm{det,\,c}})$	$[M_\odot]$	0.489	0.493	0.506	0.501	0.403
$M(^{16}\mathrm{O}_{\mathrm{det,\,c}})$	$[M_\odot]$	0.475	0.479	0.493	0.487	0.584
$M(^{22}\mathrm{Ne}_{\mathrm{det,\,c}})$	$[M_\odot]$	0.013	0.013	0.014	0.013	0.020
resolution	$[10^{-8}\,M_\odot]$	78.11	3.38	3.61	47.71	
ignition mechn.		edge	s	(s,) cs	art cs	shell
core ign. time		0.005	1.17	1.62	1.96	0.005

in part by the initial transition region of the 1D profile. A change in the transition region after the relaxation step allows to investigate the effect of mixing on the double detonation simulation and its results (see also Section II.2.3.1). In this parameter study the effect of core-shell mixing is analysed by a change in the transition of Models M08_10 and M09_10: The composition of both models was reset to match the profiles before relaxation in Models M08_10_r and M09_10_r. This is done as a first step for a further study on different transition structures since the core-shell mixing obtained after relaxation might overestimate the actual mixing in CO WDs with a He shell.

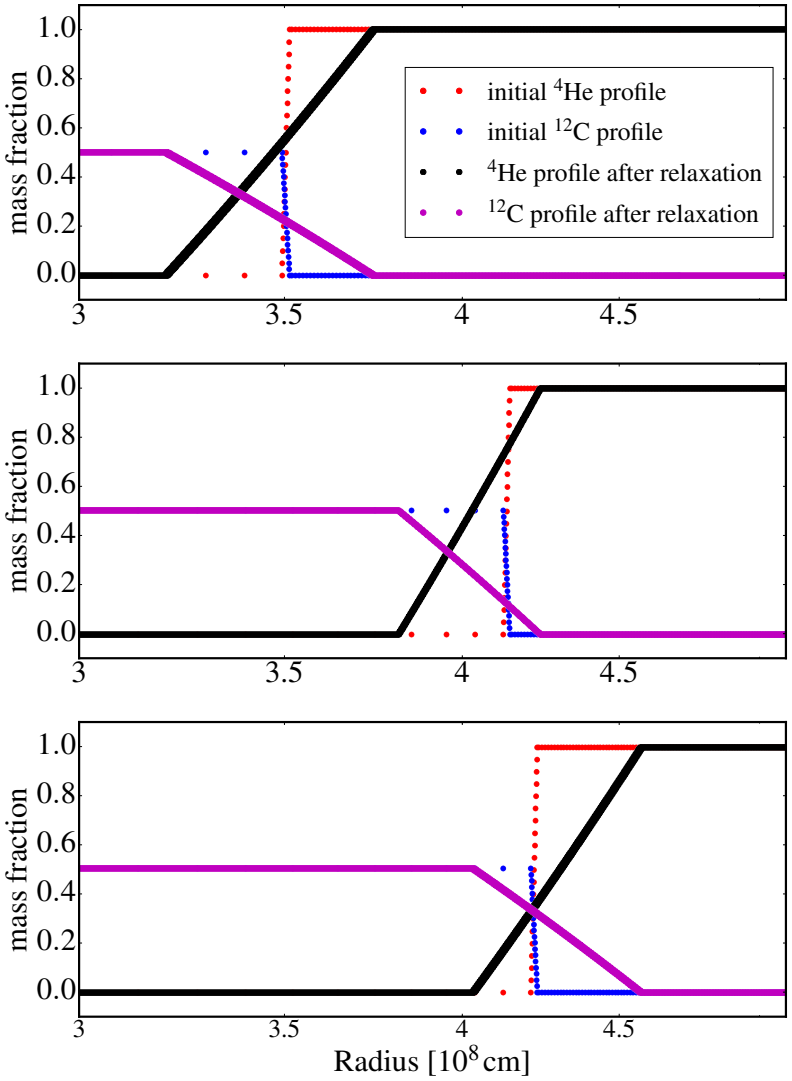

Figure III.1.1: Radial abundance profiles of ^{4}He and ^{12}C of Models M10_10, M10_05 and M10_03 *(top to bottom)*; the initial profiles are shown in red and blue, and the profiles after relaxation in black and magenta (from Gronow et al. 2021a).

III.2 Simulation results

Hydrodynamic explosion simulations were carried out for all models introduced in Section III.1. The He detonation was ignited in the same way as in the models presented in Chapter II: the specific thermal energy was artificially increased in selected cells around the peak in the temperature profile (for details see Section II.1.2). The radial position of the He detonation ignition spot on the positive z-axis and its volume are given in Tables III.1.1, III.1.2, and III.1.3.

III.2.1 C detonation ignition mechanism

Varying C detonation ignition mechanisms are observed in the simulations. The exact C detonation ignition mechanism of a model depends on many parameters of the WD setup (also see the discussion in Chapter II). The edge-lit mechanism is, for example, sensitive to the density at the base of the He shell, while details of the transition region between core and shell, and especially its C enrichment, are important for a C detonation ignition following the scissors mechanism. The individual C detonation ignition mechanism the models exhibit are given in Tables III.1.1, III.1.2, and III.1.3: the edge-lit, scissors and converging shock mechanisms are marked as 'edge', 's', and 'cs', respectively.

Due to the high dimensionality of the simulations (3D) it is not feasible to reach a resolution necessary to resolve the C detonation in detail. Nevertheless, the C detonation ignition mechanisms found in the simulations are regarded as physical if critical values for a C detonation ignition are met. These values were determined in previous work by Röpke et al. (2007b) and Seitenzahl et al. (2009) (see Section I.2.6). A C detonation is triggered in all but one model. The model with the lightest shell mass, Model M10_02, does not show a numerical ignition in the Arepo code. A C detonation is ignited artificially in this model once densities of 2.5×10^7 g cm^{-3} are reached and the temperature exceeds 8.0×10^8 K. Cells fulfilling these criteria are located off-center in the core much like where a C detonation would be ignited in the converging shock scenario. The artificial detonation ignition is carried out in order to allow a comparison of the model to the model presented in Townsley et al. (2019) which has a very similar setup. They observe a C detonation ignition in the converging shock scenario. This cannot be confirmed for Model M10_02 which might be caused by a lack of resolution. Since the criteria for the artificial ignition listed above for the temperature and density correspond well with those found for a C detonation ignition by Röpke et al. (2007b) and Seitenzahl et al. (2009) a detonation ignition may be physical. The values at hand, however, are not sufficient to trigger a numerical C detonation ignition in the Arepo code.

A time evolution of the different C detonation ignition scenarios is shown in Figure III.2.1. The most massive models, Models M10_10 and M11_05, show a C detonation ignition following the edge-lit scenario. This is illustrated for Model M10_10 in the top row of Figure III.2.1. In these models the density at the base of the shell is high, with a value of 2.2×10^6 g cm^{-3} for Model M10_10, and allows a direct C detonation ignition. This is visible in the first two panels:

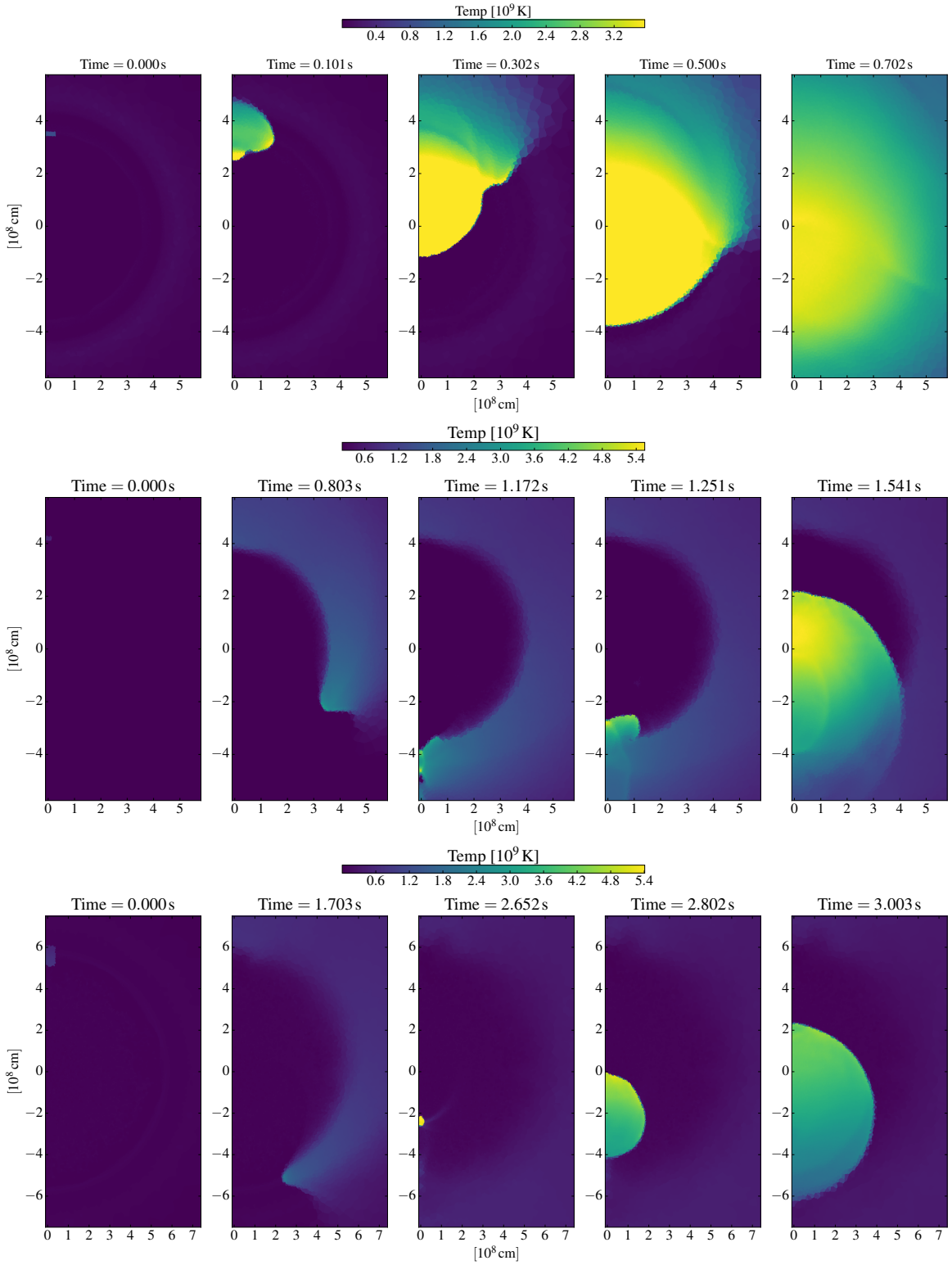

Figure III.2.1: Time evolution of Models M10_10, M10_05, and M08_03 (*top to bottom*); visible are the edge-lit, scissors, and converging shock mechanism, respectively; the temperature is given in K at different times increasing from left to right in a slice along the y-axis showing only the positive x-axis (from Gronow et al. 2021a).

A He detonation was ignited in a temperature hotspot in the left most panel by increasing the temperature to about 7.0×10^8 K in Model M10_10 which triggered a C detonation shortly after. At 0.1 s after He detonation ignition it is visible that a strong C detonation developed propagating into the core. The right most panel shows that the C detonation moves through the whole WD in 0.7 s. For a C detonation to be ignited successfully in the edge-lit scenario, Livne and Glasner (1990) point out that the He detonation needs to be ignited at some distance from the core so that the detonation develops enough strength. This is not confirmed in Models M10_10 and M11_05 as the He detonation is ignited around the temperature peak in the initial temperature profile which corresponds to a location close to the base of the He shell. However, the distance of the He detonation ignition spot to the very base of the shell is 2.7×10^7 cm in Model M10_10. A significantly larger distance to the base of the shell would not allow the ignition of a C detonation. In this case the densities are too low and a He detonation would fade out.

The densities at the base of the shell are much lower in Models M10_05, M09_10_r, and M08_10_r. In these models the scissors mechanism is found. In the three models the densities and temperatures at the convergence point of the He detonation wave are high enough to trigger a C detonation in the C enriched transition region. In Model M10_05 densities of at least 5.0×10^6 g cm^{-3} and temperatures of 2.5×10^9 K are reached while having a C mass fraction higher than 0.28. The evolution of Model M10_05 is shown in the middle row of Figure III.2.1. This is very similar to the evolution shown in Figure II.2.1 for Model M2a (see also Gronow et al. 2020). A description of the scissors mechanism can be found in Section II.2.1. Both models, Models M10_05 and M2a, have a related setup. The differences are described in Section III.1. However, they are in most part attributed to the metallicity implementation in Model M10_05.

In Models M08_05, M09_05, M09_03, and M10_03 some burning can be observed at the convergence point of the He detonation wave. The convergence is, however, not strong enough to ignite a C detonation successfully. Instead a C detonation is triggered in the converging shock scenario. This is marked as '(s,) cs' in Tables III.1.1, III.1.2, and III.1.3. The densities at the convergence point are too low for a C detonation ignition. Critical values for the density and temperature are not met, except in two cells of Model M10_03. This, however, is not sufficient for the ignition of a C detonation. It should also be pointed out that the critical values referred to in this work are the lowest values found by Röpke et al. (2007b) and Seitenzahl et al. (2009) which are shown not to be adequate for Model M10_03.

The described behavior is not found in Model M08_03. Being the model with the lowest total mass, it burns at the lowest density. Due to this, conditions for a C detonation ignition are not met at the core-shell interface, either in the edge-lit or scissors mechanism. Instead, the convergence of the shock wave in the core is strong enough to ignite C in the converging shock scenario. This is shown in the bottom row of Figure III.2.1. After the He detonation is ignited (first panel) and propagates through the shell (second panel), a C detonaiton is ignited off-center in the core (third panel). Subsequently the whole core is burnt.

Similar to the discussion presented in Chapter II, the mixing effect is analysed by a comparison of Models M08_10 and M08_10_r as well as Models M09_10 and M09_10_r (see Section III.1.3 for a description of the setups). As pointed out earlier, the composition of models with the same shell mass are similar after relaxation. The compositions of Models M08_10 and M09_10 therefore closely resemble that of Model M10_10. However, since the densities in Models M08_10 and M09_10 are lower than in Model M10_10, due to the lower total mass, a C detonation is not ignited in the edge-lit scenario. In Models M08_10 and M09_10 the He detonation also burns at the very base of the shell. The shallow transition region between core ad shell enables the detonation to move into matter that is more enriched in C. A C detonation is ignited in this region when the He detonation has only propagated around two thirds of the WD core in Model

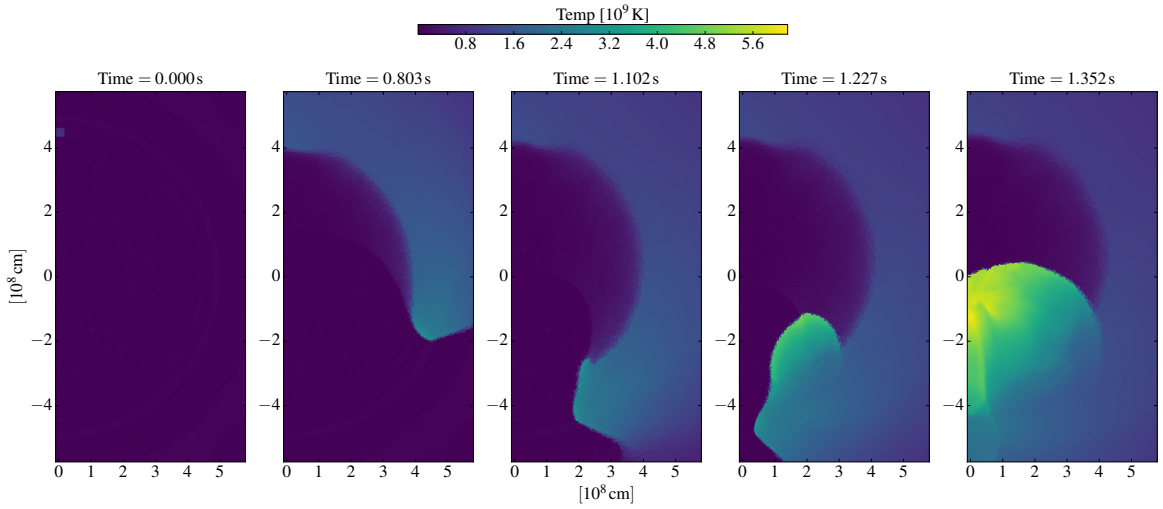

Figure III.2.2: Time evolution of Model M08_10; the temperature is given in K at different times increasing from left to right in a slice along the y-axis showing only the positive x-axis.

M08_10 (see Figure III.2.2). In order to investigate whether this kind of detonation is physical or only a numerical artifact due to, for example, the limited resolution, a detailed study needs to be carried out. An investigation involving different transition regions, varying C enrichment and a higher resolution will be conducted in the future.

The composition in Models M08_10_r and M09_10_r was reset after relaxation to match the initial profiles leading to a steeper transition region. This prevents the ignition of a C detonation as found for Models M08_10 and M09_10, and a C detonation is ignited at the convergence point of the He detonation wave following the scissors mechanism as stated above.

III.2.2 Nucleosynthetic yields

Table III.2.1: Abundances at $t = 100\,\mathrm{s}$ of Models M08_10 and M08_10_r (from Gronow et al. 2021a).

	He detonation		core detonation	
	M08_10 $[M_\odot]$	M08_10_r $[M_\odot]$	M08_10 $[M_\odot]$	M08_10_r $[M_\odot]$
^{4}He	3.1×10^{-2}	3.6×10^{-2}	1.9×10^{-3}	1.4×10^{-3}
^{12}C	8.5×10^{-5}	1.2×10^{-4}	3.0×10^{-4}	1.1×10^{-3}
^{16}O	1.7×10^{-2}	9.3×10^{-3}	7.9×10^{-2}	8.1×10^{-2}
^{28}Si	2.3×10^{-2}	1.3×10^{-2}	1.9×10^{-1}	1.9×10^{-1}
^{32}S	9.1×10^{-3}	5.5×10^{-3}	1.1×10^{-1}	1.1×10^{-1}
^{40}Ca	8.1×10^{-3}	6.2×10^{-3}	1.6×10^{-2}	1.7×10^{-2}
^{44}Ti	1.9×10^{-3}	1.8×10^{-3}	1.4×10^{-5}	1.4×10^{-5}
^{48}Cr	4.5×10^{-3}	3.8×10^{-3}	3.0×10^{-4}	3.3×10^{-4}
^{52}Fe	8.1×10^{-3}	7.5×10^{-3}	6.5×10^{-3}	7.3×10^{-3}
^{55}Mn	6.5×10^{-8}	6.4×10^{-8}	7.9×10^{-8}	6.8×10^{-8}
^{55}Co	8.7×10^{-4}	9.4×10^{-4}	3.9×10^{-3}	3.8×10^{-3}
^{56}Ni	1.1×10^{-2}	1.5×10^{-2}	3.0×10^{-1}	3.1×10^{-1}

Table III.2.2: Abundances at $t = 100\,\mathrm{s}$ of Models M08_05 and M08_03 (from Gronow et al. 2021a).

	He detonation		core detonation	
	M08_05 $[M_\odot]$	M08_03 $[M_\odot]$	M08_05 $[M_\odot]$	M08_03 $[M_\odot]$
^{4}He	2.7×10^{-2}	1.8×10^{-2}	8.2×10^{-5}	3.2×10^{-6}
^{12}C	2.3×10^{-3}	3.3×10^{-3}	7.5×10^{-3}	1.2×10^{-2}
^{16}O	6.3×10^{-3}	2.6×10^{-3}	1.2×10^{-1}	1.4×10^{-1}
^{28}Si	9.3×10^{-3}	4.2×10^{-3}	2.3×10^{-1}	2.6×10^{-1}
^{32}S	4.7×10^{-3}	2.4×10^{-3}	1.3×10^{-1}	1.4×10^{-1}
^{40}Ca	8.0×10^{-3}	3.1×10^{-3}	1.9×10^{-2}	1.9×10^{-2}
^{44}Ti	2.7×10^{-3}	2.2×10^{-4}	1.2×10^{-5}	1.2×10^{-5}
^{48}Cr	2.6×10^{-3}	7.2×10^{-6}	3.1×10^{-4}	2.9×10^{-4}
^{52}Fe	8.0×10^{-4}	8.8×10^{-7}	6.8×10^{-3}	5.6×10^{-3}
^{55}Mn	1.0×10^{-7}	1.8×10^{-7}	9.9×10^{-8}	2.0×10^{-7}
^{55}Co	3.1×10^{-5}	2.8×10^{-7}	3.5×10^{-3}	2.8×10^{-3}
^{56}Ni	6.7×10^{-5}	9.9×10^{-7}	2.0×10^{-1}	1.3×10^{-1}

Detailed nucleosynthetic yields for all models were calculated in a postprocessing step (see Section I.3.3). The abundances at 100 s after He detonation ignition for ^{4}He, ^{12}C, ^{16}O, ^{28}Si, ^{32}S, ^{40}Ca, ^{44}Ti, ^{48}Cr, ^{52}Fe, ^{55}Mn, ^{55}Co, and ^{56}Ni are listed in Tables III.2.1 to III.2.6. The abundances originating from the core and shell detonation are split in the same way as in Table II.2.1 based on the initial He mass fraction of 0.01. The individual nucleosynthetic yields of the models strongly depend on the WD core and shell masses. The total yields of ^{56}Ni of all models are, nevertheless, found to be in the expected range for SNe Ia (e.g. Stritzinger et al. 2006).

The discussion here focuses on the abundances given in Tables III.2.1 to III.2.6. Detailed nucleosynthetic yields are given in the Appendix (Section B.1). They are calculated in the same way as in Seitenzahl et al. (2013b). Tables B.1 to B.4 list the abundances at 100 s after He detonation ignition for stable nuclides and radioactive nuclides with lifetime less than 2 Gyr decayed to stability. Nuclides with a longer lifetime are specified with the yields at 100 s. The nucleosynthetic yields of some radioactive nuclides at 100 s after He detonation ignition are given in Tables B.5 to B.8.

In all models the nucleosynthetic yields originating from the shell detonation are dominated by IMEs. The C enrichment influences the yields as described in Section II.2.3.1 (also see Yoon et al. 2004, Gronow et al. 2020). Generally, WDs with massive He shells are disfavored by observations due to the strong imprints they leave on the observables (Höflich et al. 1996, Fink et al. 2010, Kromer et al. 2010). Models with a low He shell mass are therefore part of this study and represented by Models M10_03, M10_02, M09_03, and M08_03. In these models the ^{56}Ni production in the shell detonation is in the range of $9.9 \times 10^{-7}\,M_\odot$ (Model M08_03) and $6.0 \times 10^{-5}\,M_\odot$ (Model M10_03). The final abundance of ^{44}Ti is between $2.3 \times 10^{-4}\,M_\odot$ (Model M08_03) and $2.7 \times 10^{-3}\,M_\odot$ (Model M08_05). As pointed out in Section I.2.6.2, Ti and Cr are too prominent in most synthetic spectra leading to color light curves that are too red (Kromer et al. 2010) with these low values resulting in a potentially better match with observations.

The models of the parameter study show that the ^{56}Ni production increases with core mass. This is the case as the densities are higher for higher mass WDs allowing burning to produce more heavy elements. Further, it needs to be noted that models with a similar shell mass burn at different densities which has an influence on the nucleosynthetic yields of the shell detonation.

The effect mixing has on the final abundances is visible in the comparison of the nucleosyn-

Table III.2.3: Abundances at $t = 100\,\mathrm{s}$ of Models M09_10 and M09_10_r (from Gronow et al. 2021a).

	He detonation		core detonation	
	M09_10 $[M_\odot]$	M09_10_r $[M_\odot]$	M09_10 $[M_\odot]$	M09_10_r $[M_\odot]$
^{4}He	2.6×10^{-2}	3.2×10^{-2}	3.2×10^{-3}	3.9×10^{-3}
^{12}C	3.1×10^{-5}	3.9×10^{-5}	2.0×10^{-6}	1.3×10^{-4}
^{16}O	1.5×10^{-2}	8.5×10^{-3}	2.7×10^{-2}	5.5×10^{-2}
^{28}Si	3.9×10^{-2}	1.3×10^{-2}	1.5×10^{-1}	1.6×10^{-1}
^{32}S	1.1×10^{-2}	4.3×10^{-3}	9.4×10^{-2}	9.2×10^{-2}
^{40}Ca	7.9×10^{-3}	4.7×10^{-3}	1.7×10^{-2}	1.6×10^{-2}
^{44}Ti	8.5×10^{-4}	8.9×10^{-4}	1.6×10^{-5}	1.6×10^{-5}
^{48}Cr	2.5×10^{-3}	1.9×10^{-3}	3.7×10^{-4}	3.4×10^{-4}
^{52}Fe	5.1×10^{-3}	4.0×10^{-3}	8.2×10^{-3}	7.5×10^{-3}
^{55}Mn	7.6×10^{-8}	6.2×10^{-8}	1.8×10^{-8}	4.5×10^{-8}
^{55}Co	4.5×10^{-4}	3.7×10^{-4}	4.9×10^{-3}	3.9×10^{-3}
^{56}Ni	2.2×10^{-2}	2.6×10^{-2}	4.7×10^{-1}	4.8×10^{-1}

Table III.2.4: Abundances at $t = 100\,\mathrm{s}$ of Models M09_05 and M09_03 (from Gronow et al. 2021a).

	He detonation		core detonation	
	M09_05 $[M_\odot]$	M09_03 $[M_\odot]$	M09_05 $[M_\odot]$	M09_03 $[M_\odot]$
^{4}He	2.5×10^{-2}	1.5×10^{-2}	1.9×10^{-3}	5.8×10^{-4}
^{12}C	4.3×10^{-4}	3.5×10^{-3}	2.6×10^{-3}	4.9×10^{-3}
^{16}O	7.3×10^{-3}	3.9×10^{-3}	7.8×10^{-2}	9.2×10^{-2}
^{28}Si	1.0×10^{-2}	5.8×10^{-3}	1.9×10^{-1}	2.2×10^{-1}
^{32}S	4.4×10^{-3}	2.8×10^{-3}	1.1×10^{-1}	1.3×10^{-1}
^{40}Ca	5.1×10^{-3}	4.0×10^{-3}	1.8×10^{-2}	2.0×10^{-2}
^{44}Ti	2.0×10^{-3}	7.2×10^{-4}	1.5×10^{-5}	1.4×10^{-5}
^{48}Cr	4.6×10^{-3}	1.0×10^{-4}	3.7×10^{-4}	3.9×10^{-4}
^{52}Fe	5.1×10^{-3}	4.1×10^{-6}	8.1×10^{-3}	8.8×10^{-3}
^{55}Mn	6.8×10^{-8}	1.3×10^{-7}	5.7×10^{-8}	7.6×10^{-8}
^{55}Co	4.1×10^{-4}	4.3×10^{-7}	4.2×10^{-3}	4.5×10^{-3}
^{56}Ni	2.0×10^{-3}	1.0×10^{-6}	3.8×10^{-1}	3.3×10^{-1}

Table III.2.5: Abundances at $t = 100\,\mathrm{s}$ of Models M10_10 and M10_05 (from Gronow et al. 2021a).

	He detonation		core detonation	
	M10_10 $[M_\odot]$	M10_05 $[M_\odot]$	M10_10 $[M_\odot]$	M10_05 $[M_\odot]$
^{4}He	2.1×10^{-2}	2.0×10^{-2}	6.5×10^{-3}	4.6×10^{-3}
^{12}C	1.1×10^{-5}	4.0×10^{-5}	1.7×10^{-5}	4.4×10^{-4}
^{16}O	3.1×10^{-3}	9.3×10^{-3}	2.7×10^{-3}	6.1×10^{-2}
^{28}Si	3.7×10^{-2}	1.3×10^{-2}	7.3×10^{-2}	1.6×10^{-1}
^{32}S	1.6×10^{-2}	4.9×10^{-3}	5.4×10^{-2}	9.6×10^{-2}
^{40}Ca	3.4×10^{-3}	4.3×10^{-3}	1.3×10^{-2}	1.7×10^{-2}
^{44}Ti	2.7×10^{-4}	7.9×10^{-4}	1.8×10^{-5}	2.1×10^{-5}
^{48}Cr	5.5×10^{-4}	2.1×10^{-3}	3.8×10^{-4}	3.6×10^{-4}
^{52}Fe	2.0×10^{-3}	4.1×10^{-3}	8.7×10^{-3}	7.8×10^{-3}
^{55}Mn	6.1×10^{-8}	5.9×10^{-8}	9.1×10^{-8}	4.4×10^{-8}
^{55}Co	2.7×10^{-4}	4.8×10^{-4}	4.4×10^{-3}	4.0×10^{-3}
^{56}Ni	3.9×10^{-2}	8.2×10^{-3}	7.2×10^{-1}	5.4×10^{-1}

Table III.2.6: Abundances at $t = 100\,\mathrm{s}$ of Models M11_05, M10_03, and M10_02 (from Gronow et al. 2021a).

	He detonation			core detonation		
	M11_05 $[M_\odot]$	M10_03 $[M_\odot]$	M10_02 $[M_\odot]$	M11_05 $[M_\odot]$	M10_03 $[M_\odot]$	M10_02 $[M_\odot]$
^{4}He	1.0×10^{-2}	1.3×10^{-2}	1.3×10^{-2}	8.4×10^{-3}	5.1×10^{-3}	3.8×10^{-3}
^{12}C	5.7×10^{-6}	7.6×10^{-4}	1.7×10^{-3}	2.5×10^{-6}	1.2×10^{-3}	1.9×10^{-3}
^{16}O	3.8×10^{-3}	6.8×10^{-3}	1.9×10^{-3}	7.5×10^{-4}	4.9×10^{-2}	5.7×10^{-2}
^{28}Si	5.6×10^{-2}	8.9×10^{-3}	2.9×10^{-3}	4.6×10^{-2}	1.5×10^{-1}	1.7×10^{-1}
^{32}S	2.4×10^{-2}	3.7×10^{-3}	1.6×10^{-3}	3.7×10^{-2}	9.1×10^{-2}	1.0×10^{-1}
^{40}Ca	5.7×10^{-3}	3.3×10^{-3}	2.4×10^{-3}	1.0×10^{-2}	1.6×10^{-2}	1.8×10^{-2}
^{44}Ti	1.6×10^{-4}	1.1×10^{-3}	5.7×10^{-4}	1.7×10^{-5}	1.8×10^{-5}	1.8×10^{-5}
^{48}Cr	7.4×10^{-4}	1.7×10^{-3}	2.3×10^{-4}	3.2×10^{-4}	3.7×10^{-4}	3.9×10^{-4}
^{52}Fe	2.1×10^{-3}	6.5×10^{-4}	2.5×10^{-5}	7.3×10^{-3}	8.1×10^{-3}	8.8×10^{-3}
^{55}Mn	6.4×10^{-8}	7.3×10^{-8}	9.9×10^{-8}	5.7×10^{-8}	3.8×10^{-8}	4.4×10^{-8}
^{55}Co	2.2×10^{-4}	1.7×10^{-5}	1.5×10^{-6}	3.7×10^{-3}	4.2×10^{-3}	4.5×10^{-3}
^{56}Ni	1.2×10^{-2}	6.0×10^{-5}	1.9×10^{-6}	8.3×10^{-1}	5.9×10^{-1}	5.4×10^{-1}

thetic yields of Models M08_10_r and M08_10 as well as Models M09_10_r and M09_10. The different degrees of mixing do not have a big influence on the core mass or structure in general. Therefore, the final abundances agree well. More ^{12}C remains unburnt in Model M08_10_r which is due to the higher initial ^{12}C mass in the core. In the nucleosynthetic yields originating from the He detonation it is apparent that less IMEs are produced in Model M08_10_r which is due to a lower C enrichment. The presence of C in Model M08_10 stops the α-chain at a lower mass number (Section II.2.3.1). However, the influence of mixing on the observables is expected to be small since about equal masses of ^{44}Ti are produced. Only a slightly lower ^{48}Cr production in Model M08_10_r might have an impact.

The spatial distribution of ^{56}Ni is shown in Figure III.2.3 for Models M08_03 (a), M10_05 (b), and M10_10 (c). It is visible that the ejecta distribution is affected by the C detonation ignition mechanism. Model M08_03 is the lightest model of the parameter study and a C detonation is ignited in the converging shock scenario as described in Section III.2.1. The low densities in the model only allow a production of ^{56}Ni in the very center of the WD and at the shock convergence point.

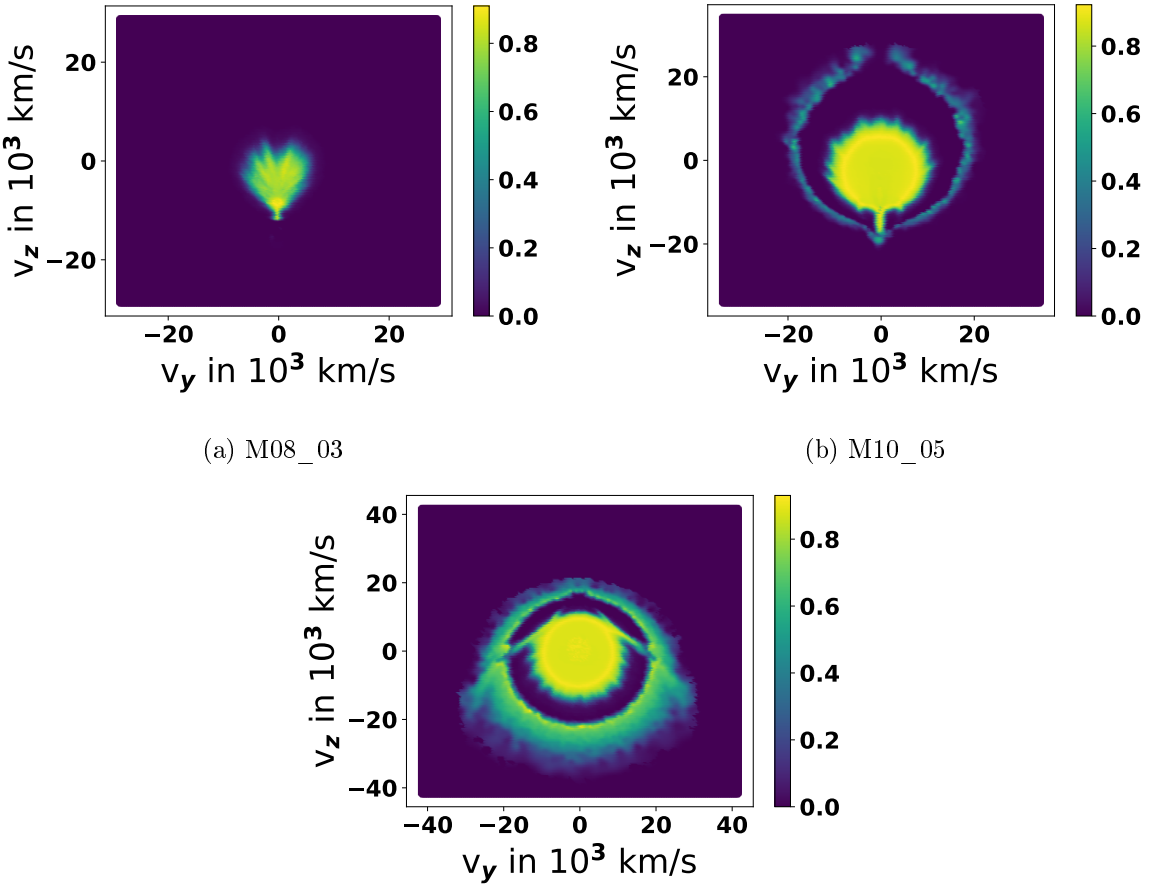

(a) M08_03

(b) M10_05

(c) M10_10

Figure III.2.3: ^{56}Ni mass fractions of Models M08_03 (*top left*), M10_05 (*top right*), and M10_10 (*bottom*) in a slice along the x-axis in velocity space (from Gronow et al. 2021a).

Contrary to this, some ^{56}Ni is produced in the He detonation in Model M10_05 which detonates following the scissors mechanism. Most ^{56}Ni is, however, produced in the core. The distribution presented in Figure III.2.3b very closely resembles the ^{56}Ni distribution in Fig-

ure II.3.4. The density at the convergence point in Model M10_05 is slightly higher than the one in Model M2a (1.2×10^7 g cm^{-3} and 8.3×10^6 g cm^{-3}, respectively). This higher density in Model M10_05 allows for some ^{56}Ni to be synthesized at the convergence point of the He detonation wave as well. The edge-lit mechanism shows a more symmetric ^{56}Ni distribution than the other two mechanisms (see Figure III.2.3c for Model M10_10). ^{56}Ni is produced in the whole core and in the shell. An impact of the C detonation ignition mechanism is visible since ^{56}Ni is located closer to the base of the shell on the positive z-axis and spread in a broader volume on the negative z-axis. The 'wings' are an artifact that can potentially be resolved in a higher resolution simulation: As the He detonation propagates around the core it reaches the base of the He shell and causes a core detonation. However, since a C detonation was previously ignited this does not have a substantial effect on the nucleosynthesis. A similar effect is discussed in Section III.2.1 for Models M08_10 and M09_10. The choice of a smaller He detonation ignition spot, a change in the details of the transition region or an increase in the resolution might prevent the behavior.

The total yields of ^{56}Ni are plotted over the total mass of the models in Figure III.2.4. It illustrates the expected upward trend. Data from Scalzo et al. (2019) is included for comparison. Different to the total mass of the models the total ejected mass is derived from observations. Both data sets cover a similar range in the parameter space which serves as some validation of the models.

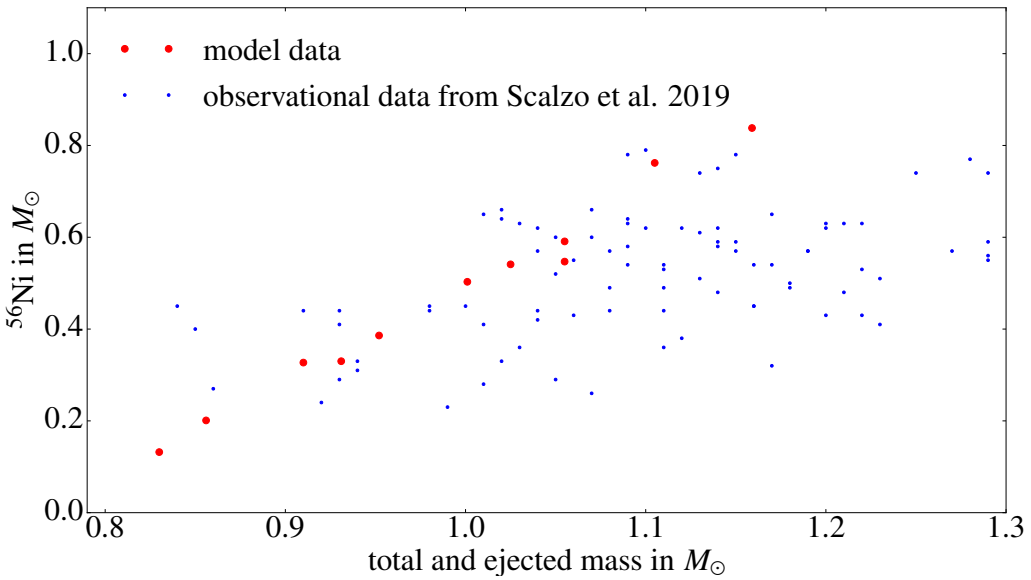

Figure III.2.4: Total ^{56}Ni yields over total mass for all models, observational data of the ejected ^{56}Ni mass and total ejected mass are taken from Scalzo et al. (2019).

III.3 Comparison to previous hydrodynamic models

Due to different setups of the WDs, a comparison with previous work on explosion simulations of sub-M_{Ch} WDs is difficult. It also needs to be taken into account that the dimensionality of the studies often differs. The simulations presented here are among the first in 3D (but also see Moll and Woosley 2013, Tanikawa et al. 2018).

The similar setup of Models M10_05 and M2a enables a comparison of the two models. Only the metallicity of the zero-age main sequence progenitor star was changed (from zero to solar) in the initial profile of Model M2a (also see Section III.1). This does, nevertheless, have a small impact on the composition after relaxation (Section II.1 and Section III.1.1). In addition to ^{22}Ne being present in the core, ^{14}N and ^{22}Ne are in the shell as well with ^{22}Ne being mixed into the shell during the relaxation. The metallicity implementation in the postprocessing comprises a more accurate representation of isotopes (Section III.1.2). As stated in Section III.2.1, both models show the same C detonation ignition mechanism. The nucleosynthetic yields coming from the He detonation show a higher IME abundance in Model M10_05 as more ^{4}He and ^{12}C is burnt, while the final ^{44}Ti abundance is a very close match in Models M10_05 and M2a. The abundances obtained in the core detonation are in good agreement as well. However, in Model M10_05 a total of $0.04\,M_{\odot}$ ^{56}Ni are produced less compared to Model M2a. The abundances are instead shifted to stable Ni isotopes (Timmes et al. 2003, Kasen et al. 2009, Shen et al. 2018b). A detailed discussion of the nucleosynthetic yields of Model M10_05 and in part of Model M2a is given in Lach et al. (2020) (Models M2a$_{\odot}$ and M2a in Lach et al. 2020, respectively).

The similarity of Models M10_05 and M2a allows a subsequent comparison to Model FM3 (Fink et al. 2010) since the initial setup of Model M2a was chosen to resemble that of Model FM3. Differences of Models M2a and FM3 are described in Section II.2. Similar to Model M2a, Model FM3 differs from Model M10_05 as it is calculated at zero metallicity. A comparison of the yields (Tables II.2.1 and III.2.5) shows that those of ^{44}Ti and ^{48}Cr originating from the shell detonation deviate. This is, however, due to the different numerical treatments as pointed out in the comparison of Models M1a and M2a with Model FM3 (see Section II.2.2). Trends in the comparison of the nucleosynthetic abundances of other isotopes resemble those found in Section II.2.2 with similar values found in the abundances originating from the core detonation in Models M10_05 and FM3 taking a small shift to stable IGEs into account due to the metallicity of Model M10_05.

Tanikawa et al. (2018) present an explosion simulation of a WD with $0.95\,M_{\odot}$ core and a $0.05\,M_{\odot}$ shell. This can be crudely compared to Model M10_05. Tanikawa et al. (2018) carry out a 3D simulation using an SPH code while employing a 13 isotopes nuclear reaction network in the hydrodynamic simulation. This number might be too low to capture the energy release accurately (Shen and Moore 2014, Townsley et al. 2019). Their model accounts for some mixing taking place between core and shell, but is calculated at zero metallicity. Generally, the nucleosynthetic yields of ^{56}Ni and IMEs are in good agreement with Model M10_05. The

amount of ^{56}Ni synthesized in the shell detonation is lower in their model which can be explained by the lower shell mass of the WD.

Neunteufel et al. (2016) present a set of models showing that on average 0.163 $M_\odot$ are accreted onto a WD until a detonation is ignited. Woosley and Kasen (2011) argue against this saying that less mass should be accumulated. Since more massive WDs with thin shells have light curves of normal SNe Ia, a set of models is found by Neunteufel et al. (2016) that potentially resembles classical SNe Ia. Their 1D models show that more mass is accreted onto a WD if the core mass is lower. In addition, hot WDs are found to have lower shell masses than cold WDs. The models presented here (Section III.1.1) are in part covered in the study of Woosley and Kasen (2011). Comparison models calculated at zero metallicity are their Models 10D, 8A, 10HB, 10HD, 9B, and 8HBC (for details see Woosley and Kasen 2011).

Generally, it is found that the total amount of synthesized ^{56}Ni in the detonations are a good match in models with similar masses. The mass configurations of Models 10B and 10HD are similar to Model M10_05. The final IME abundances of the models are in good agreement with each other. A lower production of ^{44}Ti, ^{48}Cr, and ^{52}Fe in Model M10_05 indicates that it might better match observations as the color is less red (Section I.2.6.2). However, the ^{55}Co production is slightly higher in Model M10_05 which influences the amount of manganese after its decay (see Lach et al. 2020, Gronow et al. 2021b and Chapter IV for a discussion on the importance of manganese in GCE).

Model M08_10_r can be compared to Models 8A and 8HBC. Both models by Woosley and Kasen (2011) differ in luminosity, but otherwise have the same setup. Model 8A shows a better match to Model M08_10_r in the ^{56}Ni yields. However, the ^{44}Ti, ^{48}Cr, and ^{55}Co abundances are higher in Model M08_10_r. In contrast, more ^{44}Ti and ^{56}Ni is produced in Model 8HC. The differences between the models presented here and those of Woosley and Kasen (2011) are in most part caused by discrepancies in the setups. Further, Woosley and Kasen (2011) carry out 1D simulations. Transferring the setup to 3D results in a He detonation ignition in a shell and not just one spot. This influences the expansion of matter behind the shock.

A further parameter study has been carried out by Polin et al. (2019) in 1D covering part of the same parameter space as the models presented in this thesis. Their models have zero metallicity, while core-shell mixing is incorporated. The different mixing setups of the models by Polin et al. (2019) and the ones presented here cannot be compared in detail as Polin et al. (2019) only give the radial extend and do not list the composition of the transition region. Similar to Tanikawa et al. (2018), the nuclear reaction network they use in the hydrodynamic simulation (21 isotopes) is not appropriate for models with low shell masses. Nevertheless, a good agreement in the mass configurations of the models presented here with some models of Polin et al. (2019) is found. These include models with large He shells (a 0.8 $M_\odot$ or 0.9 $M_\odot$ core with a 0.08 $M_\odot$ shell, or a 1.0 $M_\odot$ with a 0.10 $M_\odot$ shell) and thin He shells (a 1.0 $M_\odot$ core with a 0.02 $M_\odot$ shell). Generally, the IME yields are higher in their models while the models presented here show a much lower abundance of ^{56}Ni originating from the shell detonation. Similar to Woosley and Kasen (2011), the differences in the nucleosynthetic yields are explained by the different metallicities and masses of the models, dimensionality, and numerical treatments.

As pointed out in Section III.2.1, Model M10_02 has a mass configuration that closely resembles that of the model presented in Townsley et al. (2019). However, not all model parameters are listed in Townsley et al. (2019) making a comparison difficult in some aspects. Due to core-shell mixing in Model M10_02, the core is slightly less massive than in the model of Townsley et al. (2019). Townsley et al. (2019) assume a 'modest' C enrichment. However, its details are not provided. This difference is visible in the initial composition of the two models. Both models are calculated at solar metallicity using ^{14}N and ^{22}Ne for the metallicity representation in the explosion simulation. Due to a different initial temperature profile the densities in Model

M10_02 are slightly higher. This leads to a higher production of ^{56}Ni originating from the He detonation in Model M10_02 compared to Townsley et al. (2019). At the same time, a higher C enrichment in Model M10_02 increases the ^{44}Ti yields. The abundances obtained from the core detonation are in good agreement, with the difference in ^{56}Ni being explained by a lower core mass of Model M10_02 due to core-shell mixing.

An additional simulation was carried out with the mass configuration of Model M10_02, but an increased temperature at the base of the He shell to match the value of the model by Townsley et al. (2019). This model, M10_02T, has a minimally different setup than Model M10_02 as can be seen in Table III.1.3. The resolution is not listed as the simulation is stopped at an earlier point. The simulation shows a He detonation ignition in a narrow shell at the base of the He shell (given as 'shell' in Table III.1.3). This detonation quickly burns the whole He shell and triggers a C detonation at the core-shell interface burning the core in less than one second. This detonation ignition mechanism is different to the one found by Townsley et al. (2019). It is caused by the higher temperature at the base of the He shell. A simulation of a model with the same setup as Model M10_02T, but involving a 35 isotope nuclear reaction network in the hydrodynamic simulation is carried out as well, named M10_02T_35. A C detonation is ignited in the same way as in Model M10_02. A comparison of Models M10_02T and M10_02T_35 therefore shows that the temperature at the base of the He shell is sufficiently high in Model M10_02T to trigger explosive burning via additional reactions that are included in the 55 isotope nuclear reaction network (compare Tables A.1 to A.3 in Appendix A). Further studies are necessary for a reliable conclusion on whether an accretion of matter from a companion leads to a temperature of about 5×10^8 K at the base of the He shell and a subsequent He detonation ignition in a shell, and not one hotspot.

III.4 Synthetic observables

Similar to Section II.3, radiative transfer calculations were carried out by Christine E. Collins for the models discussed in this chapter. A part of the analysis of the synthetic observables (Gronow et al. 2021a) is included here to allow a more complete study of the models and an extended comparison to data. A detailed description of the synthetic observables is presented in Gronow et al. (2021a) and part of a follow-up paper (C. E. Collins in preparation).

III.4.1 Angle-averaged light curves

Table III.4.1: Parameters of the angle-averaged bolometric light curves, including Model M2a (Gronow et al. 2020) for comparison (from Gronow et al. 2021a).

	$M_{bol,max}$	$t_{bol,max}$ [days]	Δm_{15}(bol)	mechanism
M08_03	-17.57	17.4	0.93	cs
M08_05	-17.92	18.1	0.85	(s,) cs
M08_10_r	-18.35	17.9	0.83	s
M09_03	-18.42	18.1	0.86	(s,) cs
M09_05	-18.54	18.1	0.81	(s,) cs
M09_10_r	-18.82	17.2	0.89	s
M10_02	-18.91	17.4	0.86	art cs
M10_03	-18.99	17.1	0.86	(s,) cs
M10_05	-18.92	17.4	0.88	s
M10_10	-19.17	16.6	0.82	edge
M11_05	-19.28	16.1	0.81	edge
M2a	-18.93	17.4	0.71	s

As stated in Section III.2 a range of ^{56}Ni masses is produced in the double detonations of the different models. Since the ^{56}Ni mass is directly linked to the brightness of a light curve, various luminosities are found matching values for sub-luminous to normal SNe Ia. The bolometric light curves are obtained as described in Gronow et al. (2021a) via an integration of the model spectra at wavelengths between 600 Å and 30000 Å. Parameters of the angle-averaged light curves are given in Table III.4.1. The peak brightness lies between −17.57 mag and −19.28 mag. It is apparent that the brightness increases with model mass. Model M10_05 is an exception in this trend showing that the C detonation ignition mechanism is important in addition to the core and shell masses. The angle-averaged bolometric light curves of the models are presented in Figure III.4.1 with those of Models M2a and FM3 added for comparison. Model M2a has a similar peak brightness as Model M10_05 (values of −18.93 and −18.92). However, the decline rate over 15 days, Δm_{15}(bol), is lower in Model M2a than in Model M10_05 (0.71 and 0.88, respectively). This change reveals that a higher metallicity of the zero-age main sequence

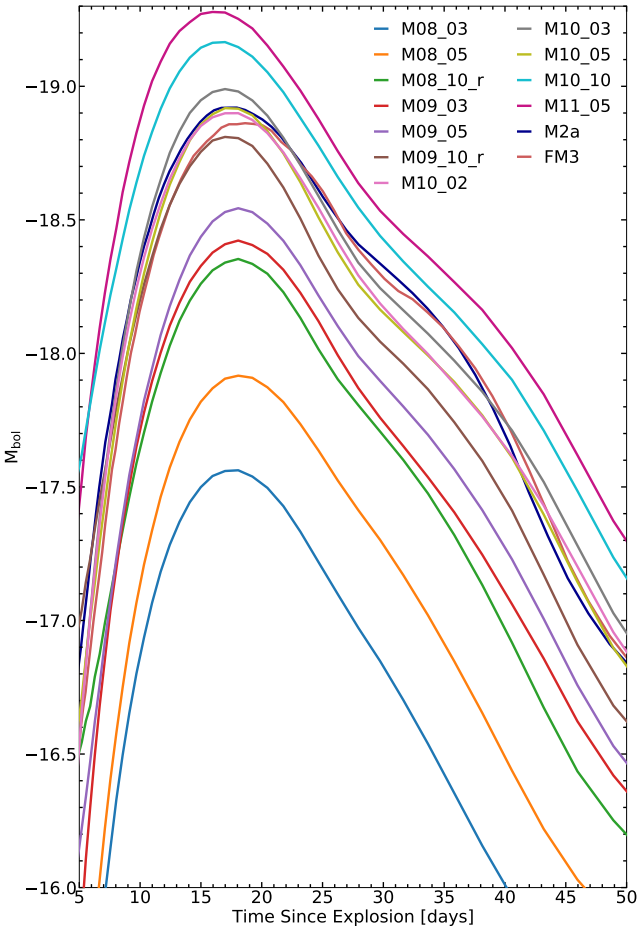

Figure III.4.1: Angle-averaged bolometric light curves for all models introduced in Section III.1, including Models M2a (Gronow et al. 2020) and FM3 (Fink et al. 2010) for comparison (from Gronow et al. 2021a).

progenitor star causes an increase in the decline rate after maximum while the peak brightness is unchanged. The metallicity likely results in a lower opacity and therefore faster decline rate. This is supported by the fact that the decline rate of Model M2a is the slowest of the models included in Table III.4.1. In the models of the parameter study it is found that those with similar peak luminosities also have similar decline rates.

III.4.2 Angle-dependent light curves

Angle-dependent light curves illustrate the effect of the different C detonation ignition mechanisms and multi-dimensionality of a double detonation (see also Section II.3.2). The asymmetric ^{56}Ni distribution of Models M08_03, M10_05, and M10_10 is shown in Figure III.2.3. Line-of-sight dependent light curves of those models are illustrated in Figure III.4.2. An angle of $\theta = 0°$ corresponds to a view in direction of the north pole, $\theta = 90°$ in equatorial direction, and $\theta = 180°$ in direction of the south pole. A strong angle-dependence is visible at maximum brightness which decreases over time as the ejecta become optically thinner. The brightest lines-of-sight are at $\theta = 180°$ for Models M08_03 and M10_05. In the converging shock and scissor mechanism these models exhibit the highest amount of ^{56}Ni located close to the surface at this angle. In

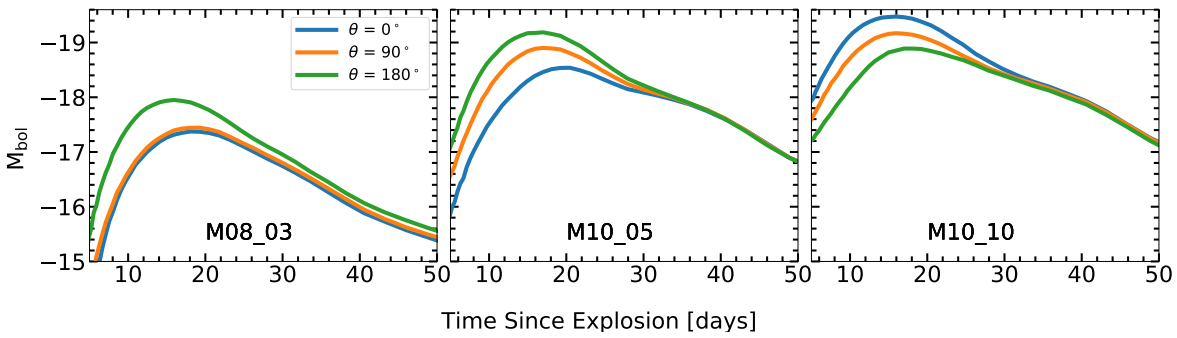

Figure III.4.2: Bolometric angle-dependent light curves of Models M08_03, M10_05, and M10_10 (from Gronow et al. 2021a).

Model M08_03 the light curves at $\theta = 0°$ and 90° are very similar which can be inferred from Figure III.2.3a. In contrast to this, ^{56}Ni is closer to the surface at $\theta = 90°$ than 0° in Model M10_05. The light curves of Model M10_10 show the opposite behavior than those of Model M10_05. This is due to the fact that the C detonation is ignited in the edge-lit scenario which results in an enhanced ^{56}Ni abundance close to the surface in direction of the north pole.

III.4.3 Bolometric width-luminosity relation and comparison to data

The dependence of the peak bolometric brightness on the decline rate Δm_{15}(bol) is shown in the top panel of Figure III.4.3. Values for 100 different viewing angles are included to demonstrate the high angle-dependency of the parameters. Errors for the angle-averaged values are calculated as standard deviation of the viewing angle distribution. A comparison of the angle-average to the viewing angle-dependent values shows that angle-averages do not well represent the full range. The angle-dependent values show an increase in decline rate with higher peak brightness. This is due to the fact that ^{56}Ni is closer to the surface in these cases enabling a faster decline.

Due to high uncertainties associated with band limited light curves of hydrodynamic models, bolometric data points are calculated from observations in order to allow a comparison as initial test. Data provided by Scalzo et al. (2019) is included in Figure III.4.3. A weak width-luminosity dependence is found by Scalzo et al. (2019) (see also Section I.1.2.1). The brighter models of the parameter study cover a similar parameter space as the observations. They loosely follow the same trend. However, the viewing angle-dependent data points span a wider range than found in observations. Further, the model with the lowest luminosity, Model M08_03, has a brightness about 0.8 mag lower than the faintest observation and declines too slow on average. A similar behavior is found by Shen et al. (2018b) attributing the difference to a minimum WD mass (see Shen and Bildsten 2014).

Scalzo et al. (2019) found a strong correlation between Δm_{15}(bol) and the decline rate over 40 days, Δm_{40}(bol). A weak trend is visible in the angle-averaged values of the models. The addition of viewing angle-dependent values makes the trend clearer (see bottom panel in Figure III.4.3). There is, however, a significant offset from data. Δm_{40}(bol) is too fast which indicates that the optical depth might be too low. This would be explained by a mass that is too low or ejecta velocities that are in disagreement with SNe Ia. Kushnir et al. (2020) and Sharon and Kushnir (2020) argue that models do not match the γ-ray escape time t_0 to ^{56}Ni mass re-

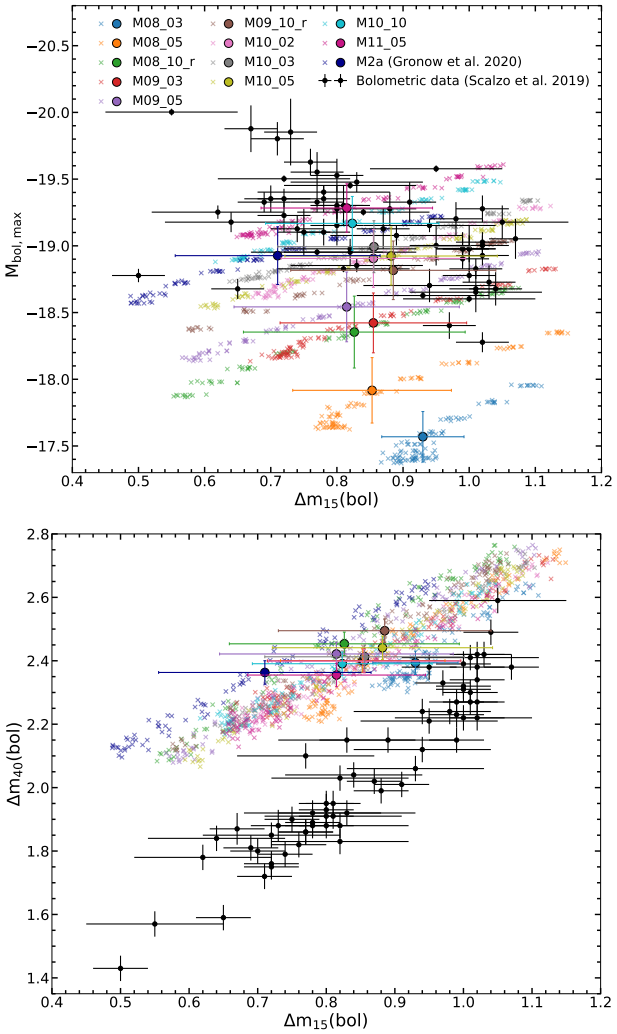

Figure III.4.3: *Top*: peak bolometric magnitude over Δm_{15}(bol). *Bottom*: bolometric decline rate over 40 days, Δm_{40}(bol), over Δm_{15}(bol). Angle-averaged light curve values (circles) and 100 different viewing angles (crosses) are shown. Model M2a (Gronow et al. 2020) and bolometric data of Scalzo et al. (2019) are included for comparison. The errors are calculated as standard deviation of the viewing angle distributions (from Gronow et al. 2021a).

lation, with a light curve being driven by the γ-ray opacity at 40 days after explosion. Wygoda et al. (2019) nevertheless state that sub-M_{Ch} models are in better agreement with observations than models of M_{Ch} WDs.

Chapter IV

Metallicity-dependent nucleosynthetic yields

Introduction

The previous studies presented in this thesis have shown that the nucleosynthetic yields of an exploding sub-M_{Ch} WD depend in some aspects on the C enrichment of the He shell (Chapter II) and the respective core and shell masses (Chapter III). A further parameter having an influence on the isotopic abundances obtained after explosion is the metallicity of the zero-age main sequence progenitor star. Its effect is discussed in the following sections. It is one of the first studies being carried out examining sub-M_{Ch} CO WDs with a He shell (but see also Leung and Nomoto 2020). The work presented here is submitted for publication in the journal *Astronomy & Astrophysics* (Gronow et al. 2021b).

An effect of the metallicity on the nucleosynthetic yields is suggested by observations. According to Höflich et al. (1998) and Timmes et al. (2003) some variations found in observational spectra are potentially explained by it. A derivation of the metallicity of a SN Ia from observations is, however, difficult. Lentz et al. (2000) and Taubenberger et al. (2008) deduce values which have large inaccuracies due to the uncertainties in the observations themselves. In addition, some of the variations found in observations could also be explained by parameters other than the metallicity.

Studies by, for example, Shigeyama et al. (1992), Umeda et al. (1999), Iwamoto et al. (1999), Timmes et al. (2003), Sim et al. (2010), and Shen et al. (2018b) have shown that the consideration of a non-zero metallicity shifts the isotopic production to stable IGE isotopes. Umeda et al. (1999) and Iwamoto et al. (1999) point out that the nucleosynthetic yields of ^{54}Fe, ^{56}Ni, and ^{58}Ni are affected. A relation between the ^{56}Ni production and metallicity is derived by Timmes et al. (2003). Their 1D study of M_{Ch} WD explosions involving metallicities between $1/3\,Z_{\odot}$ and $3\,Z_{\odot}$ shows a decrease by 25% going from lowest to highest metallicity. Further, Seitenzahl et al. (2013a) suggests that the Mn production is heavily affected.

The influence of the metallicity of the zero-age main sequence progenitor star on the nucleosynthetic yields stems from a resulting neutronization. A neutron excess can be obtained in different ways. In a M_{Ch} WD it is caused by electron captures at high densities in the core and from the initial metallicity of its progenitor star. In sub-M_{Ch} WDs only the initial metallicity is important. Electron captures do not take place in the core as the densities are not high enough. The neutron excess influences the electron fraction Y_e. A lower Y_e value indicates that the production of neutron-rich IGEs is increased (Thielemann et al. 1986).

As already mentioned in Section I.1.2.3, SNe Ia are important for GCE. The nucleosynthetic yields obtained from explosion models are input parameters for GCE models. The results of these models in turn help to constrain the explosion mechanism by a comparison to galaxy observations. Work by Seitenzahl et al. (2013a), Cescutti and Kobayashi (2017), Kobayashi et al. (2020), and Eitner et al. (2020) suggests that multiple explosion channels contribute to the Mn production. Further, GCE models involving metallicity-dependent nucleosynthetic yields better reproduced trends found in chemical evolution from observations (Seitenzahl et al. 2013a, Kobayashi et al. 2020, Eitner et al. 2020).

The representation of metallicity in the hydrodynamic simulations is described in Section III.1.

In the postprocessing step (Section I.3.3) a larger number of isotopes is included (see Section III.1). In this study the hydrodynamic explosion models of Chapter III (Gronow et al. 2021a) are used as basis. Only the postprocessing step is re-calculated employing different metallicities. This is possible as the energetics and therefore explosion dynamics only very weakly depend on the metallicity (see Section IV.1).

IV.1 Models

As stated above, eleven hydrodynamic models of Chapter III (Gronow et al. 2021a) are used as basis for the metallicity study (parameters are given in Tables II.1.1, III.1.1, and III.1.3). This allows to investigate the metallicity effect on WDs with core masses between $0.8\,M_\odot$ and $1.1\,M_\odot$, and shell masses of $0.02\,M_\odot$ to $0.1\,M_\odot$. The temperature and density evolution of the two million tracer particles (see Section I.3.3 for a description of the method) of the hydrodynamic simulations are used in re-calculations of the postprocessing taking different metallicities into account. The study in Chapter III assumes a solar metallicity of the zero-age main sequence progenitor star. The solar abundances (Asplund et al. 2009) are scaled in order to permit the calculation of detailed nucleosynthetic yields at $0.01\,Z_\odot$, $0.1\,Z_\odot$, and $3\,Z_\odot$. The full data set included in the metallicity study therefore consists of 44 models. Following Prantzos et al. (2018), the abundance ratios of α-elements are fixed at sub-solar metallicity. This gives [C/Fe]=0.18, [O/Fe]=0.47, [Mg/Fe]=0.27, [Si/Fe]=0.37, [S/Fe]=0.35, [Ar/Fe]=0.35, [Ca/Fe]=0.33, and [Ti/Fe]=0.23 based on observations of low metallicity stars. Since SNe Ia are expected to have contributed to the chemical enrichment on only small scales at early times, the α-elements (which originate from CC SNe) are increased compared to IGEs. This is realised by setting the α-elemental abundances to the listed values and scaling down those of IGEs at early times. The scaled solar abundances of Asplund et al. (2009) are used as input parameters in the postprocessing along with the initial composition profiles. Some ^{12}C and ^{22}Ne were mixed into the He shell during the relaxation step of the hydrodynamic models (see Section III.1.3) which has an influence on the nucleosynthesis and is incorporated in the initial profiles of the composition. The reaction rates listed in Section I.3.3 are employed as in all postprocessing simulations carried out in the framework of this thesis.

The omission of a calculation of the explosion simulation for the models at the various metallicities is possible as the energy release is not significantly affected by a change in metallicity. A comparison of Models M2a (Gronow et al. 2020), M2a_pp, and M10_05_1 (Model M10_05 in Chapter III and Gronow et al. 2021a) validates the approach. The nucleosynthetic yields are given in Tables IV.2.1 and IV.2.2. Model M2a_pp is based on the same explosion model as Model M2a. In the postprocessing step, the metallicity is changed from zero to solar in order to match that of Model M10_05_1. The differences in the total and shell masses of the models is less than 1%. It is caused by the change in the setup as described in Section III.1.1. Differences in the abundances originating from the core detonations of Models M2a_pp and M10_05_1 amount to about 10% while those produced in the shell detonation differ by about 50% (neglecting ^{12}C in both cases). As the nucleosynthetic yields originating from the shell detonation contribute only little to the total yields, the computational approach described here allows a good enough treatment of the nucleosynthetic yields for the goal of this study. However, an impact on synthetic observables might be more prominent as the spectra and light curves are sensitive to the shell ejecta.

As indicated above, the models of Chapter III are renamed for the parameter study on the metallicity in order to incorporate the metallicity of the various models in the name. For this

the previous model names (Section III.1.1) are extended by a number corresponding to the metallicity of the model (e.g. _01 for $0.1\,Z_{\odot}$). Names such as Model M10_03 are instead used to refer to all models with a $1.0\,M_{\odot}$ core and $0.03\,M_{\odot}$ shell, thus combining four models at different metallicities into one notation.

IV.2 Metallicity-dependent nucleosynthesis

A comparison of the hydrodynamic models that are the basis of this study was carried out in Chapter III. Relations found in the nucleosynthetic yields of the models at solar metallicity are the same at the other metallicities. In the following, the focus is on the influence of a change in metallicity on the abundances. In addition, Shen and Moore (2014) present a study on the metallicity effect on the detonation speed. The nucleosynthetic yields of the models are given in Tables IV.2.1 to IV.2.23. The abundances of Model M2a are taken from Table II.2.1 (see also Gronow et al. 2020) and expanded by ^{52}Fe, ^{54}Fe, ^{55}Fe, ^{55}Mn, ^{55}Co, and ^{58}Ni. Those of the models at solar metallicity (taken from Tables III.2.1 to III.2.6, Gronow et al. 2021a) are extended by ^{54}Fe, ^{55}Fe, and ^{58}Ni. Detailed nucleosynthetic yields of the models are given in Appendix B.2 in the same way as described in Section III.2.2.

The nucleosynthesis taking place in double detonations of sub-M_{Ch} WDs is described by explosive He and Si burning (see Section I.2.7). Explosive He burning takes place in the shell (Khokhlov 1984, Khokhlov and Érgma 1985). A comparison of the models presented here and Figure 1 of Khokhlov (1984) shows that NSE is not reached in the burning. The abundances are influenced by the presence of ^{14}N as seed nucleus. It frees p via ^{14}N(α,γ)^{18}F(α,p)^{21}Ne. The free p can then be used to form ^{16}O in a reaction faster than α-capture on ^{12}C, ^{12}C(p,γ)^{13}N(α,p)^{16}O (Shen and Bildsten 2009).

Explosive Si burning occurs in the WD core with C and O serving as fuel. Woosley et al. (1973) describe it in three different burning regimes as described in Section I.2.7. They are separated by gray areas in Figures IV.2.1, IV.2.2, and IV.2.3.

For the nucleosynthesis the generally low density in sub-M_{Ch} WDs compared to M_{Ch} WDs is important. As mentioned in the introduction to this chapter, no electron captures take place in the cores of sub-M_{Ch} WDs due to the low density. Further, NSE is not reached as densities of at least 7×10^7 g cm^{-3} are necessary (see e.g. Figure IV.2.2 for comparison). Instead, IGEs are produced in the α-rich freeze-out regime and in incomplete Si burning.

IV.2.1 Low and intermediate mass elements

At high densities the metallicity affects the nucleosynthetic yields via a neutron excess. However, in lower density regimes, such as the shell and outer region of the core, the isotopes which compose the metallicity (e.g. ^{14}N and ^{22}Ne) serve as seed nuclei. This influence is important for the production of IMEs as they are in most part produced in these lower density regions of incomplete Si burning with peak densities of up to 2.5×10^7 g cm^{-3}. As such ^{14}N(α,p)^{17}O reactions allow a speedup of the burning (Gronow et al. 2021b).

In the nucleosynthetic yields originating from the He detonation little to no influence of the metallicity is detected for elements lighter or equal to ^{44}Ti. This also applies to the abundances

Table IV.2.1: Abundances at $t = 100\,\mathrm{s}$ of Models M2a$^{(3)}$ and M2a_pp (from Gronow et al. 2021b).

	He detonation		core detonation	
	M2a$^{(3)}$ [$M_\odot$]	M2a_pp [$M_\odot$]	M2a$^{(3)}$ [$M_\odot$]	M2a_pp [$M_\odot$]
^{4}He	2.3×10^{-2}	2.2×10^{-2}	5.0×10^{-3}	4.2×10^{-3}
^{12}C	1.0×10^{-4}	1.0×10^{-4}	8.9×10^{-4}	8.6×10^{-4}
^{16}O	7.4×10^{-3}	6.8×10^{-3}	5.2×10^{-2}	5.6×10^{-2}
^{28}Si	8.9×10^{-3}	9.6×10^{-3}	1.6×10^{-1}	1.7×10^{-1}
^{32}S	3.2×10^{-3}	3.6×10^{-3}	1.1×10^{-1}	1.0×10^{-1}
^{40}Ca	3.6×10^{-3}	3.5×10^{-3}	2.3×10^{-2}	1.8×10^{-2}
^{44}Ti	7.0×10^{-4}	7.1×10^{-4}	2.8×10^{-5}	2.2×10^{-5}
^{48}Cr	1.6×10^{-3}	1.6×10^{-3}	4.8×10^{-4}	3.7×10^{-4}
^{52}Fe	3.2×10^{-3}	3.2×10^{-3}	1.0×10^{-2}	8.0×10^{-3}
^{54}Fe	2.6×10^{-5}	3.2×10^{-5}	9.2×10^{-5}	2.4×10^{-2}
^{55}Fe	5.3×10^{-7}	5.7×10^{-7}	6.0×10^{-7}	4.9×10^{-5}
^{55}Mn	1.6×10^{-7}	5.8×10^{-8}	6.4×10^{-10}	4.3×10^{-8}
^{55}Co	3.8×10^{-4}	3.9×10^{-4}	1.1×10^{-4}	4.1×10^{-3}
^{56}Ni	1.2×10^{-2}	1.2×10^{-2}	5.7×10^{-1}	5.3×10^{-1}
^{58}Ni	2.3×10^{-4}	2.4×10^{-4}	8.9×10^{-4}	1.7×10^{-2}

References. (3) Gronow et al. (2020)

Table IV.2.2: Abundances at $t = 100\,\mathrm{s}$ of Models M10_05_1$^{(4)}$ and M10_05_3 (from Gronow et al. 2021b).

	He detonation		core detonation	
	M10_05_1$^{(4)}$ [$M_\odot$]	M10_05_3 [$M_\odot$]	M10_05_1$^{(4)}$ [$M_\odot$]	M10_05_3 [$M_\odot$]
^{4}He	2.0×10^{-2}	1.9×10^{-2}	4.6×10^{-3}	3.3×10^{-3}
^{12}C	4.0×10^{-5}	4.0×10^{-5}	4.4×10^{-4}	4.3×10^{-4}
^{16}O	9.3×10^{-3}	9.7×10^{-3}	6.1×10^{-2}	6.1×10^{-2}
^{28}Si	1.3×10^{-2}	1.3×10^{-2}	1.6×10^{-1}	1.6×10^{-1}
^{32}S	4.9×10^{-3}	4.9×10^{-3}	9.6×10^{-2}	8.4×10^{-2}
^{40}Ca	4.3×10^{-3}	4.3×10^{-3}	1.7×10^{-2}	1.3×10^{-2}
^{44}Ti	7.9×10^{-4}	8.1×10^{-4}	2.1×10^{-5}	1.4×10^{-5}
^{48}Cr	2.1×10^{-3}	2.1×10^{-3}	3.6×10^{-4}	2.8×10^{-4}
^{52}Fe	4.1×10^{-3}	4.4×10^{-3}	7.8×10^{-3}	6.4×10^{-3}
^{54}Fe	4.2×10^{-5}	5.0×10^{-5}	2.2×10^{-2}	5.4×10^{-2}
^{55}Fe	7.6×10^{-7}	1.1×10^{-6}	5.0×10^{-5}	3.5×10^{-4}
^{55}Mn	5.9×10^{-8}	8.7×10^{-8}	4.4×10^{-8}	3.3×10^{-7}
^{55}Co	4.8×10^{-4}	4.9×10^{-4}	4.0×10^{-3}	6.4×10^{-3}
^{56}Ni	8.2×10^{-3}	8.1×10^{-3}	5.4×10^{-1}	4.8×10^{-1}
^{58}Ni	1.2×10^{-4}	1.4×10^{-4}	1.8×10^{-2}	4.9×10^{-2}

References. (4) Gronow et al. (2021a)

Table IV.2.3: Abundances at $t = 100\,\mathrm{s}$ of Models M10_05_001 and M10_05_01 (from Gronow et al. 2021b).

	He detonation		core detonation	
	M10_05_001 [$M_\odot$]	M10_05_01 [$M_\odot$]	M10_05_001 [$M_\odot$]	M10_05_01 [$M_\odot$]
^{4}He	2.0×10^{-2}	2.0×10^{-2}	5.0×10^{-3}	5.0×10^{-3}
^{12}C	4.0×10^{-5}	4.0×10^{-5}	4.4×10^{-4}	4.4×10^{-4}
^{16}O	9.2×10^{-3}	9.2×10^{-3}	6.0×10^{-2}	6.0×10^{-2}
^{28}Si	1.3×10^{-2}	1.3×10^{-2}	1.6×10^{-1}	1.6×10^{-1}
^{32}S	5.0×10^{-3}	5.0×10^{-3}	9.9×10^{-2}	9.9×10^{-2}
^{40}Ca	4.3×10^{-3}	4.3×10^{-3}	1.8×10^{-2}	1.8×10^{-2}
^{44}Ti	7.8×10^{-4}	7.8×10^{-4}	2.4×10^{-5}	2.4×10^{-5}
^{48}Cr	2.1×10^{-3}	2.1×10^{-3}	4.0×10^{-4}	4.0×10^{-4}
^{52}Fe	4.0×10^{-3}	4.0×10^{-3}	8.4×10^{-3}	8.4×10^{-3}
^{54}Fe	3.5×10^{-5}	3.5×10^{-5}	1.2×10^{-2}	1.2×10^{-2}
^{55}Fe	4.1×10^{-7}	4.2×10^{-7}	1.8×10^{-5}	1.7×10^{-5}
^{55}Mn	3.3×10^{-10}	2.9×10^{-9}	4.2×10^{-9}	7.4×10^{-9}
^{55}Co	4.8×10^{-4}	4.8×10^{-4}	3.0×10^{-3}	2.9×10^{-3}
^{56}Ni	8.3×10^{-3}	8.3×10^{-3}	5.6×10^{-1}	5.6×10^{-1}
^{58}Ni	1.0×10^{-4}	1.0×10^{-4}	9.6×10^{-3}	9.4×10^{-3}

Table IV.2.4: Abundances at $t = 100\,\mathrm{s}$ of Models M10_10_001 and M10_10_01 (from Gronow et al. 2021b).

	He detonation		core detonation	
	M10_10_001 [$M_\odot$]	M10_10_01 [$M_\odot$]	M10_10_001 [$M_\odot$]	M10_10_01 [$M_\odot$]
^{4}He	2.1×10^{-2}	2.1×10^{-2}	7.1×10^{-3}	7.1×10^{-3}
^{12}C	7.4×10^{-6}	7.3×10^{-6}	2.5×10^{-6}	2.5×10^{-6}
^{16}O	3.0×10^{-3}	3.0×10^{-3}	2.7×10^{-3}	2.7×10^{-3}
^{28}Si	3.7×10^{-2}	3.7×10^{-2}	7.3×10^{-2}	7.3×10^{-2}
^{32}S	1.6×10^{-2}	1.6×10^{-2}	5.6×10^{-2}	5.6×10^{-2}
^{40}Ca	3.4×10^{-3}	3.4×10^{-3}	1.4×10^{-2}	1.4×10^{-2}
^{44}Ti	2.7×10^{-4}	2.7×10^{-4}	2.0×10^{-5}	2.0×10^{-5}
^{48}Cr	5.3×10^{-4}	5.3×10^{-4}	4.1×10^{-4}	4.1×10^{-4}
^{52}Fe	2.0×10^{-3}	2.0×10^{-3}	9.3×10^{-3}	9.3×10^{-3}
^{54}Fe	9.4×10^{-4}	9.5×10^{-4}	1.0×10^{-2}	1.0×10^{-2}
^{55}Fe	1.8×10^{-6}	1.8×10^{-6}	3.2×10^{-6}	3.0×10^{-6}
^{55}Mn	9.9×10^{-10}	3.6×10^{-9}	1.5×10^{-9}	1.4×10^{-9}
^{55}Co	2.5×10^{-4}	2.5×10^{-4}	3.2×10^{-3}	3.1×10^{-3}
^{56}Ni	4.0×10^{-2}	3.9×10^{-2}	7.4×10^{-1}	7.5×10^{-1}
^{58}Ni	5.7×10^{-4}	5.7×10^{-4}	1.4×10^{-2}	1.4×10^{-2}

Table IV.2.5: Abundances at $t = 100\,\mathrm{s}$ of Models M10_10_1$^{(4)}$ and M10_10_3 (from Gronow et al. 2021b).

	He detonation		core detonation	
	M10_10_1$^{(4)}$ [$M_\odot$]	M10_10_3 [$M_\odot$]	M10_10_1$^{(4)}$ [$M_\odot$]	M10_10_3 [$M_\odot$]
^{4}He	2.1×10^{-2}	2.0×10^{-2}	6.5×10^{-3}	4.5×10^{-3}
^{12}C	1.1×10^{-5}	7.5×10^{-6}	1.7×10^{-5}	1.1×10^{-6}
^{16}O	3.1×10^{-3}	3.2×10^{-3}	2.7×10^{-3}	2.7×10^{-3}
^{28}Si	3.7×10^{-2}	3.8×10^{-2}	7.3×10^{-2}	7.3×10^{-2}
^{32}S	1.6×10^{-2}	1.6×10^{-2}	5.4×10^{-2}	4.8×10^{-2}
^{40}Ca	3.4×10^{-3}	3.5×10^{-3}	1.3×10^{-2}	1.1×10^{-2}
^{44}Ti	2.7×10^{-4}	2.8×10^{-4}	1.8×10^{-5}	1.2×10^{-5}
^{48}Cr	5.5×10^{-4}	6.0×10^{-4}	3.8×10^{-4}	3.0×10^{-4}
^{52}Fe	2.0×10^{-3}	2.0×10^{-3}	8.7×10^{-3}	7.2×10^{-3}
^{54}Fe	1.1×10^{-3}	1.1×10^{-3}	2.3×10^{-2}	4.9×10^{-2}
^{55}Fe	3.1×10^{-6}	3.7×10^{-6}	8.0×10^{-6}	8.6×10^{-5}
^{55}Mn	6.1×10^{-8}	8.6×10^{-8}	9.1×10^{-8}	9.2×10^{-8}
^{55}Co	2.7×10^{-4}	2.7×10^{-4}	4.4×10^{-3}	7.2×10^{-3}
^{56}Ni	3.9×10^{-2}	3.9×10^{-2}	7.2×10^{-1}	6.5×10^{-1}
^{58}Ni	5.7×10^{-4}	5.4×10^{-4}	3.2×10^{-2}	6.8×10^{-2}

References. (4) Gronow et al. (2021a)

Table IV.2.6: Abundances at $t = 100\,\mathrm{s}$ of Models M10_03_001 and M10_03_01 (from Gronow et al. 2021b).

	He detonation		core detonation	
	M10_03_001 [$M_\odot$]	M10_03_01 [$M_\odot$]	M10_03_001 [$M_\odot$]	M10_03_01 [$M_\odot$]
^{4}He	1.3×10^{-2}	1.3×10^{-2}	5.5×10^{-3}	5.5×10^{-3}
^{12}C	7.7×10^{-4}	7.7×10^{-4}	1.2×10^{-3}	1.2×10^{-3}
^{16}O	6.6×10^{-3}	6.6×10^{-3}	4.8×10^{-2}	4.8×10^{-2}
^{28}Si	8.9×10^{-3}	8.9×10^{-3}	1.5×10^{-1}	1.5×10^{-1}
^{32}S	3.7×10^{-3}	3.7×10^{-3}	9.4×10^{-2}	9.4×10^{-2}
^{40}Ca	3.2×10^{-3}	3.2×10^{-3}	1.8×10^{-2}	1.8×10^{-2}
^{44}Ti	1.0×10^{-3}	1.0×10^{-3}	2.0×10^{-5}	2.0×10^{-5}
^{48}Cr	1.7×10^{-3}	1.7×10^{-3}	4.0×10^{-4}	4.0×10^{-4}
^{52}Fe	7.3×10^{-4}	7.2×10^{-4}	8.7×10^{-3}	8.7×10^{-3}
^{54}Fe	4.7×10^{-6}	4.7×10^{-6}	1.2×10^{-2}	1.2×10^{-2}
^{55}Fe	5.6×10^{-8}	6.2×10^{-8}	1.7×10^{-5}	1.7×10^{-5}
^{55}Mn	3.4×10^{-10}	3.4×10^{-9}	3.5×10^{-9}	4.4×10^{-9}
^{55}Co	1.7×10^{-5}	1.7×10^{-5}	3.1×10^{-3}	3.0×10^{-3}
^{56}Ni	6.9×10^{-5}	6.8×10^{-5}	6.1×10^{-1}	6.1×10^{-1}
^{58}Ni	2.3×10^{-6}	2.6×10^{-6}	1.0×10^{-2}	1.1×10^{-2}

Table IV.2.7: Abundances at $t = 100\,\mathrm{s}$ of Models M10_03_1$^{(4)}$ and M10_03_3 (from Gronow et al. 2021b).

	He detonation		core detonation	
	M10_03_1$^{(4)}$ [$M_\odot$]	M10_03_3 [$M_\odot$]	M10_03_1$^{(4)}$ [$M_\odot$]	M10_03_3 [$M_\odot$]
^{4}He	1.3×10^{-2}	1.2×10^{-2}	5.1×10^{-3}	3.6×10^{-3}
^{12}C	7.6×10^{-4}	7.5×10^{-4}	1.2×10^{-3}	1.2×10^{-3}
^{16}O	6.8×10^{-3}	7.1×10^{-3}	4.9×10^{-2}	4.9×10^{-2}
^{28}Si	8.9×10^{-3}	9.0×10^{-3}	1.5×10^{-1}	1.5×10^{-1}
^{32}S	3.7×10^{-3}	3.7×10^{-3}	9.1×10^{-2}	8.0×10^{-2}
^{40}Ca	3.3×10^{-3}	3.5×10^{-3}	1.6×10^{-2}	1.3×10^{-2}
^{44}Ti	1.1×10^{-3}	1.2×10^{-3}	1.8×10^{-5}	1.2×10^{-5}
^{48}Cr	1.7×10^{-3}	1.5×10^{-3}	3.7×10^{-4}	2.8×10^{-4}
^{52}Fe	6.5×10^{-4}	5.1×10^{-4}	8.1×10^{-3}	6.7×10^{-3}
^{54}Fe	6.2×10^{-6}	5.3×10^{-6}	2.7×10^{-2}	5.4×10^{-2}
^{55}Fe	2.1×10^{-7}	3.3×10^{-7}	4.8×10^{-5}	3.3×10^{-4}
^{55}Mn	7.3×10^{-8}	1.1×10^{-7}	3.8×10^{-8}	2.7×10^{-7}
^{55}Co	1.7×10^{-5}	1.4×10^{-5}	4.2×10^{-3}	6.6×10^{-3}
^{56}Ni	6.0×10^{-5}	4.2×10^{-5}	5.9×10^{-1}	5.3×10^{-1}
^{58}Ni	1.4×10^{-5}	2.2×10^{-5}	2.5×10^{-2}	5.5×10^{-2}

References. (4) Gronow et al. (2021a)

Table IV.2.8: Abundances at $t = 100\,\mathrm{s}$ of Models M10_02_001 and M10_02_01 (from Gronow et al. 2021b).

	He detonation		core detonation	
	M10_02_001 [$M_\odot$]	M10_02_01 [$M_\odot$]	M10_02_001 [$M_\odot$]	M10_02_01 [$M_\odot$]
^{4}He	1.4×10^{-2}	1.4×10^{-2}	4.2×10^{-3}	4.2×10^{-3}
^{12}C	1.7×10^{-3}	1.7×10^{-3}	2.0×10^{-3}	2.0×10^{-3}
^{16}O	1.8×10^{-3}	1.8×10^{-3}	5.7×10^{-2}	5.7×10^{-2}
^{28}Si	2.9×10^{-3}	2.9×10^{-3}	1.7×10^{-1}	1.7×10^{-1}
^{32}S	1.6×10^{-3}	1.6×10^{-3}	1.1×10^{-1}	1.1×10^{-1}
^{40}Ca	2.3×10^{-3}	2.3×10^{-3}	2.0×10^{-2}	2.0×10^{-2}
^{44}Ti	5.7×10^{-4}	5.7×10^{-4}	2.0×10^{-5}	2.0×10^{-5}
^{48}Cr	2.5×10^{-4}	2.5×10^{-4}	4.3×10^{-4}	4.3×10^{-4}
^{52}Fe	2.9×10^{-5}	2.9×10^{-5}	9.5×10^{-3}	9.5×10^{-3}
^{54}Fe	5.0×10^{-7}	5.3×10^{-7}	1.4×10^{-2}	1.4×10^{-2}
^{55}Fe	1.1×10^{-8}	1.4×10^{-8}	1.9×10^{-5}	1.8×10^{-5}
^{55}Mn	4.6×10^{-10}	4.7×10^{-9}	3.8×10^{-9}	4.7×10^{-9}
^{55}Co	1.3×10^{-6}	1.3×10^{-6}	3.3×10^{-3}	3.3×10^{-3}
^{56}Ni	1.8×10^{-6}	1.8×10^{-6}	5.6×10^{-1}	5.6×10^{-1}
^{58}Ni	9.2×10^{-8}	2.5×10^{-7}	8.9×10^{-3}	8.7×10^{-3}

Table IV.2.9: Abundances at $t = 100\,\mathrm{s}$ of Models M10_02_1$^{(4)}$ and M10_02_3 (from Gronow et al. 2021b).

	He detonation		core detonation	
	M10_02_1$^{(4)}$ [$M_\odot$]	M10_02_3 [$M_\odot$]	M10_02_1$^{(4)}$ [$M_\odot$]	M10_02_3 [$M_\odot$]
^{4}He	1.3×10^{-2}	1.3×10^{-2}	3.8×10^{-3}	2.7×10^{-3}
^{12}C	1.7×10^{-3}	1.6×10^{-3}	1.9×10^{-3}	1.9×10^{-3}
^{16}O	1.9×10^{-3}	2.0×10^{-3}	5.7×10^{-2}	5.8×10^{-2}
^{28}Si	2.9×10^{-3}	3.0×10^{-3}	1.7×10^{-1}	1.7×10^{-1}
^{32}S	1.6×10^{-3}	1.7×10^{-3}	1.0×10^{-1}	9.0×10^{-2}
^{40}Ca	2.4×10^{-3}	2.5×10^{-3}	1.8×10^{-2}	1.4×10^{-2}
^{44}Ti	5.7×10^{-4}	5.5×10^{-4}	1.8×10^{-5}	1.3×10^{-5}
^{48}Cr	2.3×10^{-4}	1.9×10^{-4}	3.9×10^{-4}	3.1×10^{-4}
^{52}Fe	2.5×10^{-5}	1.9×10^{-5}	8.8×10^{-3}	7.2×10^{-3}
^{54}Fe	1.3×10^{-6}	1.6×10^{-6}	2.5×10^{-2}	6.0×10^{-2}
^{55}Fe	9.2×10^{-8}	1.5×10^{-7}	5.3×10^{-5}	3.7×10^{-4}
^{55}Mn	9.9×10^{-8}	1.4×10^{-7}	4.4×10^{-8}	3.1×10^{-7}
^{55}Co	1.5×10^{-6}	1.3×10^{-6}	4.5×10^{-3}	7.1×10^{-3}
^{56}Ni	1.9×10^{-6}	1.8×10^{-6}	5.4×10^{-1}	4.9×10^{-1}
^{58}Ni	5.8×10^{-6}	9.7×10^{-6}	1.7×10^{-2}	4.6×10^{-2}

References. (4) Gronow et al. (2021a)

Table IV.2.10: Abundances at $t = 100\,\mathrm{s}$ of Models M09_10_r_001 and M09_10_r_01 (from Gronow et al. 2021b).

	He detonation		core detonation	
	M09_10_r_001 [$M_\odot$]	M09_10_r_01 [$M_\odot$]	M09_10_r_001 [$M_\odot$]	M09_10_r_01 [$M_\odot$]
^{4}He	3.2×10^{-2}	3.2×10^{-2}	4.2×10^{-3}	4.2×10^{-3}
^{12}C	3.8×10^{-5}	3.8×10^{-5}	1.4×10^{-4}	1.3×10^{-4}
^{16}O	8.4×10^{-3}	8.4×10^{-3}	5.5×10^{-2}	5.5×10^{-2}
^{28}Si	1.3×10^{-2}	1.3×10^{-2}	1.5×10^{-1}	1.5×10^{-1}
^{32}S	4.4×10^{-3}	4.3×10^{-3}	9.5×10^{-2}	9.5×10^{-2}
^{40}Ca	4.7×10^{-3}	4.7×10^{-3}	1.7×10^{-2}	1.7×10^{-2}
^{44}Ti	8.7×10^{-4}	8.7×10^{-4}	1.8×10^{-5}	1.8×10^{-5}
^{48}Cr	1.9×10^{-3}	1.9×10^{-3}	3.7×10^{-4}	3.7×10^{-4}
^{52}Fe	4.0×10^{-3}	4.0×10^{-3}	8.1×10^{-3}	8.1×10^{-3}
^{54}Fe	4.0×10^{-5}	4.1×10^{-5}	1.2×10^{-2}	1.2×10^{-2}
^{55}Fe	3.7×10^{-7}	3.9×10^{-7}	1.7×10^{-5}	1.7×10^{-5}
^{55}Mn	3.5×10^{-10}	3.0×10^{-9}	7.8×10^{-9}	1.4×10^{-8}
^{55}Co	3.7×10^{-4}	3.7×10^{-4}	2.9×10^{-3}	2.8×10^{-3}
^{56}Ni	2.6×10^{-2}	2.6×10^{-2}	4.9×10^{-1}	4.9×10^{-1}
^{58}Ni	6.7×10^{-4}	6.7×10^{-4}	8.2×10^{-3}	8.0×10^{-3}

Table IV.2.11: Abundances at $t = 100\,\mathrm{s}$ of Models M09_10_r_1[(4)] and M09_10_r_3 (from Gronow et al. 2021b).

	He detonation		core detonation	
	M09_10_r_1[(4)] [$M_\odot$]	M09_10_r_3 [$M_\odot$]	M09_10_r_1[(4)] [$M_\odot$]	M09_10_r_3 [$M_\odot$]
^{4}He	3.2×10^{-2}	3.1×10^{-2}	3.9×10^{-3}	2.8×10^{-3}
^{12}C	3.9×10^{-5}	3.8×10^{-5}	1.3×10^{-4}	1.3×10^{-4}
^{16}O	8.5×10^{-3}	8.8×10^{-3}	5.5×10^{-2}	5.6×10^{-2}
^{28}Si	1.3×10^{-2}	1.3×10^{-2}	1.6×10^{-1}	1.5×10^{-1}
^{32}S	4.3×10^{-3}	4.3×10^{-3}	9.2×10^{-2}	8.1×10^{-2}
^{40}Ca	4.7×10^{-3}	4.8×10^{-3}	1.6×10^{-2}	1.3×10^{-2}
^{44}Ti	8.9×10^{-4}	9.1×10^{-4}	1.6×10^{-5}	1.2×10^{-5}
^{48}Cr	1.9×10^{-3}	2.0×10^{-3}	3.4×10^{-4}	2.6×10^{-4}
^{52}Fe	4.0×10^{-3}	4.1×10^{-3}	7.5×10^{-3}	6.1×10^{-3}
^{54}Fe	5.0×10^{-5}	6.0×10^{-5}	2.2×10^{-2}	5.2×10^{-2}
^{55}Fe	8.5×10^{-7}	1.2×10^{-6}	4.7×10^{-5}	3.3×10^{-4}
^{55}Mn	6.2×10^{-8}	9.0×10^{-8}	4.5×10^{-8}	3.0×10^{-7}
^{55}Co	3.7×10^{-4}	3.8×10^{-4}	3.9×10^{-3}	6.2×10^{-3}
^{56}Ni	2.6×10^{-2}	2.6×10^{-2}	4.8×10^{-1}	4.3×10^{-1}
^{58}Ni	6.6×10^{-4}	6.4×10^{-4}	1.6×10^{-2}	4.1×10^{-2}

References. (4) Gronow et al. (2021a)

Table IV.2.12: Abundances at $t = 100\,\mathrm{s}$ of Models M09_05_001 and M09_05_01 (from Gronow et al. 2021b).

	He detonation		core detonation	
	M09_05_001 [$M_\odot$]	M09_05_01 [$M_\odot$]	M09_05_001 [$M_\odot$]	M09_05_01 [$M_\odot$]
^{4}He	2.6×10^{-2}	2.6×10^{-2}	2.1×10^{-3}	2.1×10^{-3}
^{12}C	4.4×10^{-4}	4.4×10^{-4}	2.7×10^{-3}	2.7×10^{-3}
^{16}O	7.1×10^{-3}	7.1×10^{-3}	7.7×10^{-2}	7.7×10^{-2}
^{28}Si	1.0×10^{-2}	1.0×10^{-2}	1.9×10^{-1}	1.9×10^{-1}
^{32}S	4.5×10^{-3}	4.5×10^{-3}	1.1×10^{-1}	1.1×10^{-1}
^{40}Ca	5.1×10^{-3}	5.1×10^{-3}	2.0×10^{-2}	2.0×10^{-2}
^{44}Ti	2.0×10^{-3}	2.0×10^{-3}	1.7×10^{-5}	1.7×10^{-5}
^{48}Cr	4.5×10^{-3}	4.5×10^{-3}	4.0×10^{-4}	4.0×10^{-4}
^{52}Fe	5.1×10^{-3}	5.1×10^{-3}	8.8×10^{-3}	8.8×10^{-3}
^{54}Fe	8.3×10^{-5}	8.3×10^{-5}	1.4×10^{-2}	1.4×10^{-2}
^{55}Fe	1.1×10^{-6}	1.1×10^{-6}	2.2×10^{-5}	2.1×10^{-5}
^{55}Mn	3.3×10^{-10}	3.2×10^{-9}	4.4×10^{-9}	5.9×10^{-9}
^{55}Co	4.1×10^{-4}	4.1×10^{-4}	3.1×10^{-3}	3.1×10^{-3}
^{56}Ni	2.1×10^{-3}	2.1×10^{-3}	4.0×10^{-1}	4.0×10^{-1}
^{58}Ni	7.3×10^{-5}	7.4×10^{-5}	5.5×10^{-3}	5.4×10^{-3}

Table IV.2.13: Abundances at $t = 100\,\mathrm{s}$ of Models M09_05_1$^{(4)}$ and M09_05_3 (from Gronow et al. 2021b).

	He detonation		core detonation	
	M09_05_1$^{(4)}$ [$M_\odot$]	M09_05_3 [$M_\odot$]	M09_05_1$^{(4)}$ [$M_\odot$]	M09_05_3 [$M_\odot$]
^{4}He	2.5×10^{-2}	2.5×10^{-2}	1.9×10^{-3}	1.3×10^{-3}
^{12}C	4.3×10^{-4}	4.3×10^{-4}	2.6×10^{-3}	2.6×10^{-3}
^{16}O	7.3×10^{-3}	7.6×10^{-3}	7.8×10^{-2}	7.9×10^{-2}
^{28}Si	1.0×10^{-2}	1.0×10^{-2}	1.9×10^{-1}	1.9×10^{-1}
^{32}S	4.4×10^{-3}	4.5×10^{-3}	1.1×10^{-1}	9.7×10^{-2}
^{40}Ca	5.1×10^{-3}	5.2×10^{-3}	1.8×10^{-2}	1.4×10^{-2}
^{44}Ti	2.0×10^{-3}	2.1×10^{-3}	1.5×10^{-5}	1.1×10^{-5}
^{48}Cr	4.6×10^{-3}	5.0×10^{-3}	3.7×10^{-4}	2.8×10^{-4}
^{52}Fe	5.1×10^{-3}	5.3×10^{-3}	8.1×10^{-3}	6.6×10^{-3}
^{54}Fe	9.1×10^{-5}	9.7×10^{-5}	2.5×10^{-2}	5.9×10^{-2}
^{55}Fe	1.4×10^{-6}	1.6×10^{-6}	6.1×10^{-5}	4.2×10^{-4}
^{55}Mn	6.8×10^{-8}	1.0×10^{-7}	5.7×10^{-8}	3.9×10^{-7}
^{55}Co	4.1×10^{-4}	3.9×10^{-4}	4.2×10^{-3}	6.5×10^{-3}
^{56}Ni	2.0×10^{-3}	1.7×10^{-3}	3.8×10^{-1}	3.4×10^{-1}
^{58}Ni	1.0×10^{-4}	1.1×10^{-4}	1.0×10^{-2}	2.7×10^{-2}

References. (4) Gronow et al. (2021a)

Table IV.2.14: Abundances at $t = 100\,\mathrm{s}$ of Models M09_03_001 and M09_03_01 (from Gronow et al. 2021b).

	He detonation		core detonation	
	M09_03_001 [$M_\odot$]	M09_03_01 [$M_\odot$]	M09_03_001 [$M_\odot$]	M09_03_01 [$M_\odot$]
^{4}He	1.5×10^{-2}	1.5×10^{-2}	6.7×10^{-4}	6.8×10^{-4}
^{12}C	3.5×10^{-3}	3.5×10^{-3}	4.9×10^{-3}	4.9×10^{-3}
^{16}O	3.8×10^{-3}	3.8×10^{-3}	9.2×10^{-2}	9.2×10^{-2}
^{28}Si	5.8×10^{-3}	5.8×10^{-3}	2.2×10^{-1}	2.2×10^{-1}
^{32}S	2.7×10^{-3}	2.7×10^{-3}	1.3×10^{-1}	1.3×10^{-1}
^{40}Ca	3.9×10^{-3}	4.0×10^{-3}	2.2×10^{-2}	2.2×10^{-2}
^{44}Ti	7.5×10^{-4}	7.5×10^{-4}	1.6×10^{-5}	1.6×10^{-5}
^{48}Cr	1.3×10^{-4}	1.2×10^{-4}	4.3×10^{-4}	4.3×10^{-4}
^{52}Fe	5.2×10^{-6}	5.1×10^{-6}	9.5×10^{-3}	9.5×10^{-3}
^{54}Fe	1.5×10^{-7}	1.9×10^{-7}	1.6×10^{-2}	1.5×10^{-2}
^{55}Fe	3.6×10^{-9}	7.9×10^{-9}	2.5×10^{-5}	2.5×10^{-5}
^{55}Mn	6.1×10^{-10}	6.2×10^{-9}	9.6×10^{-9}	8.0×10^{-9}
^{55}Co	2.6×10^{-7}	2.6×10^{-7}	3.3×10^{-3}	3.3×10^{-3}
^{56}Ni	7.5×10^{-7}	7.5×10^{-7}	3.4×10^{-1}	3.4×10^{-1}
^{58}Ni	5.0×10^{-8}	2.4×10^{-7}	3.8×10^{-3}	3.7×10^{-3}

Table IV.2.15: Abundances at $t = 100\,\mathrm{s}$ of Models M09_03_1[(4)] and M09_03_3 (from Gronow et al. 2021b).

	He detonation		core detonation	
	M09_03_1[(4)] [$M_\odot$]	M09_03_3 [$M_\odot$]	M09_03_1[(4)] [$M_\odot$]	M09_03_3 [$M_\odot$]
^{4}He	1.5×10^{-2}	1.4×10^{-2}	5.8×10^{-4}	3.3×10^{-4}
^{12}C	3.5×10^{-3}	3.4×10^{-3}	4.9×10^{-3}	4.7×10^{-3}
^{16}O	3.9×10^{-3}	4.2×10^{-3}	9.2×10^{-2}	9.3×10^{-2}
^{28}Si	5.8×10^{-3}	5.9×10^{-3}	2.2×10^{-1}	2.2×10^{-1}
^{32}S	2.8×10^{-3}	2.9×10^{-3}	1.3×10^{-1}	1.1×10^{-1}
^{40}Ca	4.0×10^{-3}	4.1×10^{-3}	2.0×10^{-2}	1.6×10^{-2}
^{44}Ti	7.2×10^{-4}	6.5×10^{-4}	1.4×10^{-5}	1.1×10^{-5}
^{48}Cr	1.0×10^{-4}	7.4×10^{-5}	3.9×10^{-4}	3.0×10^{-4}
^{52}Fe	4.1×10^{-6}	2.7×10^{-6}	8.8×10^{-3}	7.1×10^{-3}
^{54}Fe	1.0×10^{-6}	1.4×10^{-6}	2.8×10^{-2}	6.6×10^{-2}
^{55}Fe	1.3×10^{-7}	2.3×10^{-7}	7.2×10^{-5}	4.9×10^{-5}
^{55}Mn	1.3×10^{-7}	1.9×10^{-7}	7.6×10^{-8}	4.8×10^{-7}
^{55}Co	4.3×10^{-7}	5.3×10^{-7}	4.5×10^{-3}	7.0×10^{-3}
^{56}Ni	1.0×10^{-6}	1.3×10^{-6}	3.3×10^{-1}	2.9×10^{-1}
^{58}Ni	7.4×10^{-6}	1.3×10^{-5}	7.0×10^{-3}	1.8×10^{-2}

References. (4) Gronow et al. (2021a)

Table IV.2.16: Abundances at $t = 100\,\mathrm{s}$ of Models M08_10_r_001 and M08_10_r_01 (from Gronow et al. 2021b).

	He detonation		core detonation	
	M08_10_r_001 [$M_\odot$]	M08_10_r_01 [$M_\odot$]	M08_10_r_001 [$M_\odot$]	M08_10_r_01 [$M_\odot$]
^{4}He	3.6×10^{-2}	3.6×10^{-2}	1.5×10^{-3}	1.5×10^{-3}
^{12}C	1.2×10^{-4}	1.2×10^{-4}	1.1×10^{-3}	1.1×10^{-3}
^{16}O	9.1×10^{-3}	9.1×10^{-3}	8.0×10^{-2}	8.0×10^{-2}
^{28}Si	1.3×10^{-2}	1.2×10^{-2}	1.9×10^{-1}	1.9×10^{-1}
^{32}S	5.6×10^{-3}	5.6×10^{-3}	1.1×10^{-1}	1.1×10^{-1}
^{40}Ca	6.2×10^{-3}	6.2×10^{-3}	1.9×10^{-2}	1.9×10^{-2}
^{44}Ti	1.8×10^{-3}	1.8×10^{-3}	1.5×10^{-5}	1.5×10^{-5}
^{48}Cr	3.8×10^{-3}	3.8×10^{-3}	3.7×10^{-4}	3.7×10^{-4}
^{52}Fe	7.3×10^{-3}	7.4×10^{-3}	7.9×10^{-3}	7.9×10^{-3}
^{54}Fe	6.3×10^{-5}	6.3×10^{-5}	1.3×10^{-2}	1.3×10^{-2}
^{55}Fe	9.7×10^{-7}	9.9×10^{-7}	2.2×10^{-5}	2.1×10^{-5}
^{55}Mn	3.3×10^{-10}	3.3×10^{-9}	3.3×10^{-8}	3.6×10^{-8}
^{55}Co	9.2×10^{-4}	9.2×10^{-4}	2.8×10^{-3}	2.8×10^{-3}
^{56}Ni	1.5×10^{-2}	1.5×10^{-2}	3.2×10^{-1}	3.2×10^{-1}
^{58}Ni	1.7×10^{-4}	1.8×10^{-4}	4.2×10^{-3}	4.1×10^{-3}

Table IV.2.17: Abundances at $t = 100\,\mathrm{s}$ of Models M08_10_r_1[(4)] and M08_10_r_3 (from Gronow et al. 2021b).

	He detonation		core detonation	
	M08_10_r_1[(4)] [$M_\odot$]	M08_10_r_3 [$M_\odot$]	M08_10_r_1[(4)] [$M_\odot$]	M08_10_r_3 [$M_\odot$]
^{4}He	3.6×10^{-2}	3.4×10^{-2}	1.4×10^{-3}	9.9×10^{-4}
^{12}C	1.2×10^{-4}	1.2×10^{-4}	1.1×10^{-3}	1.0×10^{-3}
^{16}O	9.3×10^{-3}	9.6×10^{-3}	8.1×10^{-2}	8.2×10^{-2}
^{28}Si	1.3×10^{-2}	1.3×10^{-2}	1.9×10^{-1}	1.9×10^{-1}
^{32}S	5.5×10^{-3}	5.6×10^{-3}	1.1×10^{-1}	9.6×10^{-2}
^{40}Ca	6.2×10^{-3}	6.3×10^{-3}	1.7×10^{-2}	1.4×10^{-2}
^{44}Ti	1.8×10^{-3}	1.8×10^{-3}	1.4×10^{-5}	1.0×10^{-5}
^{48}Cr	3.8×10^{-3}	3.9×10^{-3}	3.3×10^{-4}	2.6×10^{-4}
^{52}Fe	7.5×10^{-3}	7.9×10^{-3}	7.3×10^{-3}	6.0×10^{-3}
^{54}Fe	7.3×10^{-5}	8.7×10^{-5}	2.3×10^{-2}	5.6×10^{-2}
^{55}Fe	1.4×10^{-6}	1.7×10^{-6}	6.1×10^{-5}	4.3×10^{-4}
^{55}Mn	6.4×10^{-8}	9.3×10^{-8}	6.8×10^{-8}	4.4×10^{-7}
^{55}Co	9.4×10^{-4}	9.7×10^{-4}	3.8×10^{-3}	5.9×10^{-3}
^{56}Ni	1.5×10^{-2}	1.5×10^{-2}	3.1×10^{-1}	2.8×10^{-1}
^{58}Ni	2.1×10^{-4}	2.5×10^{-4}	7.8×10^{-3}	2.0×10^{-2}

References. (4) Gronow et al. (2021a)

Table IV.2.18: Abundances at $t = 100\,\mathrm{s}$ of Models M08_05_001 and M08_05_01 (from Gronow et al. 2021b).

	He detonation		core detonation	
	M08_05_001 [$M_\odot$]	M08_05_01 [$M_\odot$]	M08_05_001 [$M_\odot$]	M08_05_01 [$M_\odot$]
^{4}He	2.8×10^{-2}	2.8×10^{-2}	9.8×10^{-5}	9.8×10^{-5}
^{12}C	2.3×10^{-3}	2.3×10^{-3}	7.5×10^{-3}	7.5×10^{-3}
^{16}O	6.1×10^{-3}	6.1×10^{-3}	1.2×10^{-1}	1.2×10^{-1}
^{28}Si	9.2×10^{-3}	9.2×10^{-3}	2.3×10^{-1}	2.3×10^{-1}
^{32}S	4.7×10^{-3}	4.7×10^{-3}	1.3×10^{-1}	1.3×10^{-1}
^{40}Ca	7.8×10^{-3}	7.9×10^{-3}	2.0×10^{-2}	2.0×10^{-2}
^{44}Ti	2.6×10^{-3}	2.6×10^{-3}	1.3×10^{-5}	1.3×10^{-5}
^{48}Cr	2.7×10^{-3}	2.7×10^{-3}	3.5×10^{-4}	3.5×10^{-4}
^{52}Fe	8.9×10^{-4}	8.8×10^{-4}	7.4×10^{-3}	7.4×10^{-3}
^{54}Fe	8.7×10^{-6}	8.8×10^{-6}	1.4×10^{-2}	1.3×10^{-2}
^{55}Fe	1.5×10^{-7}	1.6×10^{-7}	2.6×10^{-5}	2.6×10^{-5}
^{55}Mn	4.7×10^{-10}	4.7×10^{-9}	5.5×10^{-9}	8.2×10^{-9}
^{55}Co	3.0×10^{-5}	3.0×10^{-5}	2.6×10^{-3}	2.6×10^{-3}
^{56}Ni	7.5×10^{-5}	7.4×10^{-5}	2.1×10^{-1}	2.1×10^{-1}
^{58}Ni	2.6×10^{-6}	3.0×10^{-6}	1.8×10^{-3}	1.8×10^{-3}

Table IV.2.19: Abundances at $t = 100\,\mathrm{s}$ of Models M08_05_1$^{(4)}$ and M08_05_3 (from Gronow et al. 2021b).

	He detonation		core detonation	
	M08_05_1$^{(4)}$ [$M_\odot$]	M08_05_3 [$M_\odot$]	M08_05_1$^{(4)}$ [$M_\odot$]	M08_05_3 [$M_\odot$]
^{4}He	2.7×10^{-2}	2.6×10^{-2}	8.2×10^{-5}	4.6×10^{-5}
^{12}C	2.3×10^{-3}	2.3×10^{-3}	7.5×10^{-3}	7.2×10^{-3}
^{16}O	6.3×10^{-3}	6.6×10^{-3}	1.2×10^{-1}	1.2×10^{-1}
^{28}Si	9.3×10^{-3}	9.4×10^{-3}	2.3×10^{-1}	2.3×10^{-1}
^{32}S	4.7×10^{-3}	4.8×10^{-3}	1.3×10^{-1}	1.1×10^{-1}
^{40}Ca	8.0×10^{-3}	8.5×10^{-3}	1.9×10^{-2}	1.4×10^{-2}
^{44}Ti	2.7×10^{-3}	2.9×10^{-3}	1.2×10^{-5}	9.3×10^{-6}
^{48}Cr	2.6×10^{-3}	2.4×10^{-3}	3.1×10^{-4}	2.4×10^{-4}
^{52}Fe	8.0×10^{-4}	6.4×10^{-4}	6.8×10^{-3}	5.4×10^{-3}
^{54}Fe	1.1×10^{-5}	1.1×10^{-5}	2.4×10^{-2}	5.7×10^{-2}
^{55}Fe	4.4×10^{-7}	6.4×10^{-7}	7.5×10^{-5}	5.2×10^{-4}
^{55}Mn	1.0×10^{-7}	1.5×10^{-7}	9.9×10^{-8}	5.8×10^{-7}
^{55}Co	3.1×10^{-5}	2.7×10^{-5}	3.5×10^{-3}	5.2×10^{-3}
^{56}Ni	6.7×10^{-5}	5.0×10^{-5}	2.0×10^{-1}	1.8×10^{-1}
^{58}Ni	1.9×10^{-5}	3.3×10^{-5}	3.3×10^{-3}	7.8×10^{-3}

References. (4) Gronow et al. (2021a)

Table IV.2.20: Abundances at $t = 100\,\mathrm{s}$ of Models M08_03_001 and M08_03_01 (from Gronow et al. 2021b).

	He detonation		core detonation	
	M08_03_001 [$M_\odot$]	M08_03_01 [$M_\odot$]	M08_03_001 [$M_\odot$]	M08_03_01 [$M_\odot$]
^{4}He	1.9×10^{-2}	1.9×10^{-2}	3.5×10^{-6}	3.5×10^{-6}
^{12}C	3.4×10^{-3}	3.4×10^{-3}	1.3×10^{-2}	1.3×10^{-2}
^{16}O	2.5×10^{-3}	2.5×10^{-3}	1.4×10^{-1}	1.4×10^{-1}
^{28}Si	4.2×10^{-3}	4.2×10^{-3}	2.6×10^{-1}	2.6×10^{-1}
^{32}S	2.3×10^{-3}	2.3×10^{-3}	1.4×10^{-1}	1.4×10^{-1}
^{40}Ca	3.1×10^{-3}	3.1×10^{-3}	2.2×10^{-2}	2.2×10^{-2}
^{44}Ti	2.3×10^{-4}	2.2×10^{-4}	1.3×10^{-5}	1.3×10^{-5}
^{48}Cr	8.2×10^{-6}	8.1×10^{-6}	3.2×10^{-4}	3.2×10^{-4}
^{52}Fe	8.6×10^{-7}	8.6×10^{-7}	6.2×10^{-3}	6.2×10^{-3}
^{54}Fe	2.2×10^{-8}	7.5×10^{-8}	1.3×10^{-2}	1.3×10^{-2}
^{55}Fe	6.4×10^{-10}	4.0×10^{-9}	3.0×10^{-5}	2.9×10^{-5}
^{55}Mn	8.4×10^{-10}	8.5×10^{-9}	6.3×10^{-9}	2.0×10^{-8}
^{55}Co	1.1×10^{-7}	1.1×10^{-7}	2.2×10^{-3}	2.1×10^{-3}
^{56}Ni	8.0×10^{-7}	8.1×10^{-7}	1.4×10^{-1}	1.4×10^{-1}
^{58}Ni	4.3×10^{-8}	1.9×10^{-7}	1.1×10^{-3}	1.1×10^{-3}

Table IV.2.21: Abundances at $t = 100\,\mathrm{s}$ of Models M08_03_1[(4)] and M08_03_3 (from Gronow et al. 2021b).

	He detonation		core detonation	
	M08_03_1[(4)] [$M_\odot$]	M08_03_3 [$M_\odot$]	M08_03_1[(4)] [$M_\odot$]	M08_03_3 [$M_\odot$]
^{4}He	1.8×10^{-2}	1.8×10^{-2}	3.2×10^{-6}	2.5×10^{-6}
^{12}C	3.3×10^{-3}	3.3×10^{-3}	1.2×10^{-2}	1.2×10^{-2}
^{16}O	2.6×10^{-3}	2.8×10^{-3}	1.4×10^{-1}	1.5×10^{-1}
^{28}Si	4.2×10^{-3}	4.4×10^{-3}	2.6×10^{-1}	2.5×10^{-1}
^{32}S	2.4×10^{-3}	2.6×10^{-3}	1.4×10^{-1}	1.2×10^{-1}
^{40}Ca	3.1×10^{-3}	3.0×10^{-3}	1.9×10^{-2}	1.5×10^{-2}
^{44}Ti	2.2×10^{-4}	1.9×10^{-4}	1.2×10^{-5}	8.9×10^{-6}
^{48}Cr	7.2×10^{-6}	6.0×10^{-6}	2.9×10^{-4}	2.1×10^{-4}
^{52}Fe	8.8×10^{-7}	9.6×10^{-7}	5.6×10^{-3}	4.5×10^{-3}
^{54}Fe	1.3×10^{-6}	1.9×10^{-6}	2.4×10^{-2}	5.4×10^{-2}
^{55}Fe	9.5×10^{-8}	1.7×10^{-7}	8.6×10^{-5}	5.9×10^{-4}
^{55}Mn	1.8×10^{-7}	2.6×10^{-7}	2.0×10^{-7}	8.1×10^{-7}
^{55}Co	2.8×10^{-7}	4.3×10^{-7}	2.8×10^{-3}	4.0×10^{-3}
^{56}Ni	9.9×10^{-7}	1.2×10^{-6}	1.3×10^{-1}	1.1×10^{-1}
^{58}Ni	5.5×10^{-6}	9.2×10^{-6}	2.0×10^{-3}	4.6×10^{-3}

References. (4) Gronow et al. (2021a)

Table IV.2.22: Abundances at $t = 100\,\mathrm{s}$ of Models M11_05_001 and M11_05_01 (from Gronow et al. 2021b).

	He detonation		core detonation	
	M11_05_001 [$M_\odot$]	M11_05_01 [$M_\odot$]	M11_05_001 [$M_\odot$]	M11_05_01 [$M_\odot$]
^{4}He	1.1×10^{-2}	1.1×10^{-2}	9.2×10^{-3}	9.2×10^{-3}
^{12}C	5.2×10^{-6}	5.3×10^{-6}	3.1×10^{-6}	3.1×10^{-6}
^{16}O	3.7×10^{-3}	3.7×10^{-3}	7.5×10^{-4}	7.5×10^{-4}
^{28}Si	5.5×10^{-2}	5.6×10^{-2}	4.5×10^{-2}	4.5×10^{-2}
^{32}S	2.5×10^{-2}	2.4×10^{-2}	3.8×10^{-2}	3.8×10^{-2}
^{40}Ca	5.7×10^{-3}	5.7×10^{-3}	1.1×10^{-2}	1.1×10^{-2}
^{44}Ti	1.5×10^{-4}	1.5×10^{-4}	2.0×10^{-5}	2.1×10^{-5}
^{48}Cr	7.2×10^{-4}	7.2×10^{-4}	3.5×10^{-4}	3.5×10^{-4}
^{52}Fe	2.0×10^{-3}	2.0×10^{-3}	7.8×10^{-3}	7.8×10^{-3}
^{54}Fe	1.5×10^{-3}	1.5×10^{-3}	8.0×10^{-3}	7.8×10^{-3}
^{55}Fe	4.5×10^{-6}	4.6×10^{-6}	1.8×10^{-6}	1.9×10^{-6}
^{55}Mn	1.6×10^{-9}	4.1×10^{-9}	3.3×10^{-10}	7.4×10^{-10}
^{55}Co	2.1×10^{-4}	2.1×10^{-4}	2.6×10^{-3}	2.6×10^{-3}
^{56}Ni	1.2×10^{-2}	1.2×10^{-2}	8.5×10^{-1}	8.5×10^{-1}
^{58}Ni	1.9×10^{-4}	1.9×10^{-4}	1.8×10^{-2}	1.8×10^{-2}

Table IV.2.23: Abundances at $t = 100\,\mathrm{s}$ of Models M11_05_1$^{(4)}$ and M11_05_3 (from Gronow et al. 2021b).

	He detonation		core detonation	
	M11_05_1$^{(4)}$ [$M_\odot$]	M11_05_3 [$M_\odot$]	M11_05_1$^{(4)}$ [$M_\odot$]	M11_05_3 [$M_\odot$]
^{4}He	1.0×10^{-2}	9.9×10^{-3}	8.4×10^{-3}	5.7×10^{-3}
^{12}C	5.7×10^{-6}	5.7×10^{-6}	2.5×10^{-6}	1.2×10^{-6}
^{16}O	3.8×10^{-3}	4.0×10^{-3}	7.5×10^{-4}	7.6×10^{-4}
^{28}Si	5.6×10^{-2}	5.6×10^{-2}	4.6×10^{-2}	4.4×10^{-2}
^{32}S	2.4×10^{-2}	2.5×10^{-2}	3.7×10^{-2}	3.4×10^{-2}
^{40}Ca	5.7×10^{-3}	5.8×10^{-3}	1.0×10^{-2}	9.1×10^{-3}
^{44}Ti	1.6×10^{-4}	1.7×10^{-4}	1.7×10^{-5}	1.2×10^{-5}
^{48}Cr	7.4×10^{-4}	8.0×10^{-4}	3.2×10^{-4}	2.6×10^{-4}
^{52}Fe	2.1×10^{-3}	2.2×10^{-3}	7.3×10^{-3}	6.1×10^{-3}
^{54}Fe	1.7×10^{-3}	1.8×10^{-3}	1.5×10^{-2}	3.8×10^{-2}
^{55}Fe	6.9×10^{-6}	8.0×10^{-6}	4.5×10^{-6}	3.4×10^{-5}
^{55}Mn	6.4×10^{-8}	9.2×10^{-8}	5.7×10^{-8}	6.6×10^{-8}
^{55}Co	2.2×10^{-4}	2.2×10^{-4}	3.7×10^{-3}	6.1×10^{-3}
^{56}Ni	1.2×10^{-2}	1.1×10^{-2}	8.3×10^{-1}	7.5×10^{-1}
^{58}Ni	2.0×10^{-4}	2.1×10^{-4}	3.0×10^{-2}	8.1×10^{-2}

References. (4) Gronow et al. (2021a)

of ^{12}C, ^{16}O, and ^{28}Si produced in the core detonation. It is apparent in the yields obtained from the core detonation that an increase in metallicity decreases the amount of unburnt ^{4}He which is a product of the α-rich freeze-out. A higher neutronization supports the reaction ^{4}He(αn,γ)^{9}Be(α,n)^{12}C causing it to dominate the triple-α reaction (Howard et al. 1993, Hix and Thielemann 1999) and resulting in the effect on the ^{4}He abundance.

IV.2.2 Iron group elements

The metallicity effect on the abundances of heavy elements is stronger as they are mostly produced in high density regions. In the He detonation IGEs are produced via α-captures as NSE is not reached. In the core detonation, these isotopes are formed in the regimes of incomplete Si burning and α-rich freeze-out. A focus of the analysis is on elements which are in most part produced in SNe Ia (Timmes et al. 1995, McWilliam 1997, Kobayashi et al. 2020), and those which are a main product of a SN Ia, Mn, Fe, and Ni.

IV.2.2.1 Manganese

Mn is an element of interest in many studies (Seitenzahl et al. 2013a, Cescutti and Kobayashi 2017, Kobayashi et al. 2020, Eitner et al. 2020, Lach et al. 2020). It is in large parts produced in SNe Ia (Timmes et al. 1995, McWilliam 1997, Kobayashi et al. 2020). Its only stable isotope is ^{55}Mn which is formed in incomplete Si burning. Mn is, however, mostly produced by the decay of ^{55}Co via ^{55}Fe. The nucleosynthetic yields of both isotopes are higher than that of ^{55}Mn directly after explosion, with the abundance of ^{55}Co being significantly higher making the Mn production predominantly dependent on it (Truran et al. 1967). Lach et al. (2020) describe

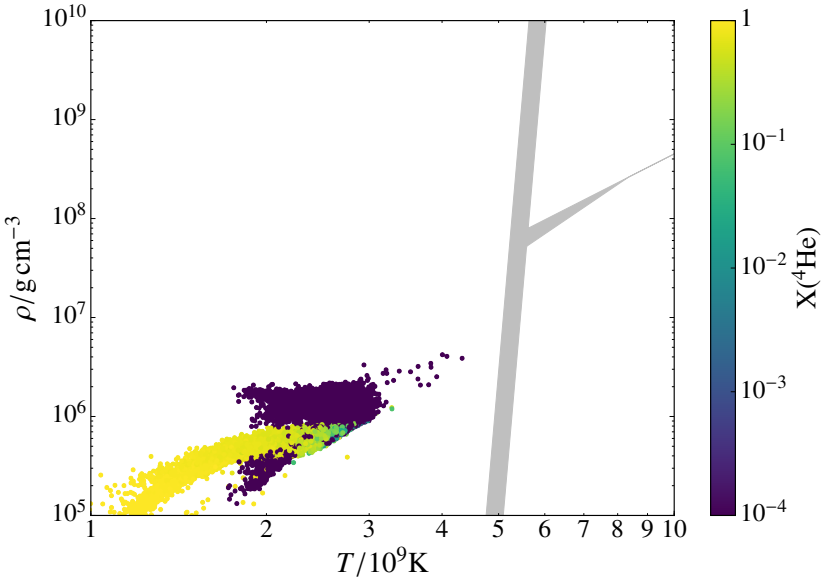

Figure IV.2.1: Tracer particle distribution of the shell detonation in the $T_{\mathrm{peak}} - \rho_{\mathrm{peak}}$–plane for Model M10_03_001 at $t = 100\,\mathrm{s}$ with color coded ^{4}He mass fraction (from Gronow et al. 2021b).

how the shell-core mass ratio and density of the He shell in a sub-M_{Ch} WD influence the Mn production. The dependence on metallicity is discussed here.

The nucleosynthetic yields produced in the He detonation show that ^{55}Fe and ^{55}Co only weakly depend on metallicity. On the contrary, the ^{55}Mn production increases by one order of magnitude with each metallicity increase (from 0.01 $Z_\odot$ to 0.1 $Z_\odot$ to 1 $Z_\odot$ to 3 $Z_\odot$). Nevertheless, the values only almost match those of ^{55}Co for Models M09_03_3 and M08_03_3. The change is caused by ^{14}N, ^{22}Ne (mixed into the shell during relaxation) and other isotopes composing the metallicity as they serve as seed nuclei. Additional reactions are enabled which support the nucleosynthesis of neutron-rich isotopes. The tracer particles of the He detonation are shown in Figure IV.2.1 in the $T_{\mathrm{peak}} - \rho_{\mathrm{peak}}$–plane for Model M10_03_001. They can subsequently be identified in Figures IV.2.2 and IV.2.3.

Figure IV.2.2 illustrates the tracer particle distribution similar to Figure IV.2.1 for all tracers of Model M10_03. The metallicity increases from left to right and color coded are the mass fractions of ^{55}Mn (top) and ^{55}Co (bottom). Previously mentioned trends in the yields produced in the He detonation are visible in the figure. Figure IV.2.2 also shows that both isotopes are produced in incomplete Si burning. The different orders of magnitude found in the produced amounts of ^{55}Mn and ^{55}Co is found in the range of the different color bars.

In the yields originating from the core detonation it is visible that the ^{55}Co abundance doubles going from lowest to highest metallicity. The increase can be found in the incomplete Si burning regime of the bottom panel of Figure IV.2.2. In contrast to incomplete Si burning, ^{55}Co is destroyed in the α-rich freeze-out regime via ^{55}Co(p,γ)^{56}Ni (Seitenzahl et al. 2013a). A steeper increase in the ^{55}Mn production in the incomplete Si burning regime can be seen as well. This was already suggested by Seitenzahl et al. (2013a).

Mn is produced in SNe Ia as well as CC SNe. A raise in [Mn/Fe] at [Fe/H] ≥ -1 is found in observations (Gratton and Sneden 1988, 1991) reaching solar values (Matteucci and Greggio 1986, Cescutti and Kobayashi 2017, Eitner et al. 2020, Kobayashi et al. 2020). The origin of the increase is undetermined to date. According to Seitenzahl et al. (2013a) a source with super-solar Mn is required. They conclude that 50% of SNe Ia originate from M_{Ch} WD explosions using CC SN yields of Woosley and Weaver (1995) as the high densities in M_{Ch} WDs are needed for

the production of sufficient ^{55}Co, as well as to reach NSE. The study by Seitenzahl et al. (2013a), however, neglects to take the contribution of Mn produced in the He detonation into account. Lach et al. (2020) show that [Mn/Fe] is significantly higher in the shell, reaching super-solar values, than in the core increasing the total value. This can be confirmed by the nucleosynthetic yields obtained in this study (see Tables IV.2.1 to IV.2.23). Further, the contribution of the yields originating from the He detonation become more important at higher shell masses.

Seitenzahl et al. (2013a) argue that a metallicity effect on the yields can be neglected in sub-M_{Ch} WDs as gravitational settling is needed in order for sufficient ^{22}Ne to be present in a high density regime. The models presented here exhibit a homogeneous distribution of the metallicity in the core coming from a homogeneous production during the evolution of the progenitor star. As a result isotopes of the metallicity implementation are sufficiently abundant at high densities and alter the abundances accordingly. This leads to a higher ^{55}Mn production with increasing metallicity. All models reach super-solar values of [Mn/Fe] at $3\,Z_{\odot}$. However, it needs to be pointed out that a contribution of WDs with super-solar metallicity to the solar [Mn/Fe] at [Fe/H]$= 0$ is excluded in one-zone GCE models while the actual contribution is unknown. Further, the CC SN yields have a strong impact on the GCE model. Using CC SN yields different from those by Woosley and Weaver (1995) in the model of Seitenzahl et al. (2013a) potentially results in a less stiff demand for explosions of M_{Ch} WDs. A more detailed description is given in Section IV.4.

IV.2.2.2 Iron and nickel

The nucleosynthesis of Ni is of particular interest as it is the main product of a SN Ia. After its decay, the abundance of Fe is high as well. The isotopes ^{54}Fe and ^{58}Ni represent the next stable isotopes to ^{52}Fe and ^{56}Ni which are produced in the burning along the α-chain. In addition, observations allow the determination of the ^{57}Ni abundance via its decay to ^{57}Co. A comparison to model data is therefore anticipated.

The increase found in the abundances of ^{54}Fe and ^{58}Ni with increasing metallicity is not as strong as the one of ^{55}Mn. Nevertheless, it is apparent that the production of stable isotopes increases with metallicity, or in other words with neutronization (Shigeyama et al. 1992, Umeda et al. 1999, Iwamoto et al. 1999, Timmes et al. 2003, Sim et al. 2010, Shen et al. 2018b). This is well visible in the nucleosynthetic yields of the models at $3\,Z_{\odot}$ obtained from the core detonation in which the amount of ^{54}Fe and ^{58}Ni increase to four times their values at $0.01\,Z_{\odot}$. Additional neutrons are present originating from the reaction ^{22}Ne(α,n)^{25}Mg in α-rich freeze-out (Shigeyama et al. 1992). This enables the production of neutron-rich isotopes via (α,n) and (n,γ) reactions, for example ^{25}Mg(n,γ)^{26}Mg. The neutron freed in the reaction of ^{22}Ne with an α-particle can further support the production of C isotopes via reactions with ^{20}Ne (Gronow et al. 2021b). These reactions are ^{20}Ne(n,α)^{17}O(n,α)^{14}C and ^{20}Ne(n,γ)^{21}Ne(n,α)^{18}O(p,α)^{15}N(p,α)^{12}C (Chamulak et al. 2007). Chamulak et al. (2007) describe that α-particles are freed in this process while p are captured.

Both, ^{54}Fe and ^{58}Ni have two neutrons more than their counterparts on the α-chain, ^{52}Fe and ^{56}Ni. Contrary to the impact of the neutron excess, the yields produced in the He detonation are in most part influenced by the isotopes of the metallicity implementation as seed nuclei. Nevertheless, some ^{22}Ne was mixed into the shell during the relaxation step which causes a small neutron excess. This only leads to a minor enhancement of neutron-rich isotopes as the admixed mass is small.

The tracer particle distribution of Model M10_03 is shown at $0.01\,Z_{\odot}$ (left) and $3\,Z_{\odot}$ (right) in Figure IV.2.3. The color coded mass fractions correspond to ^{56}Ni (top) and ^{58}Ni (bottom). It is visible that less ^{56}Ni is produced in the low density regime of incomplete Si burning at higher

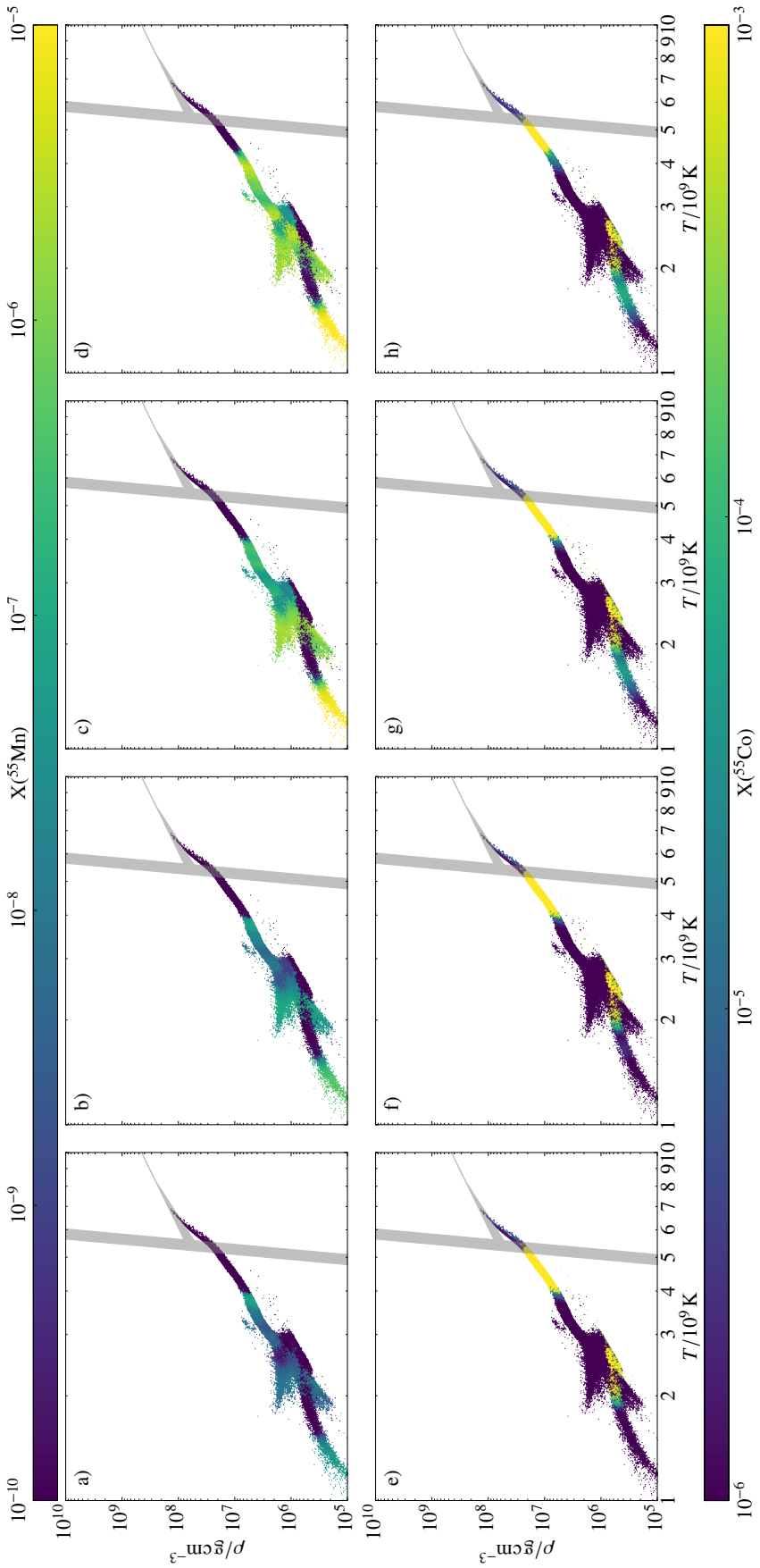

Figure IV.2.2: Tracer particle distribution of Model M10_03 at 0.01, 0.1, 1, and $3\,Z_\odot$ (*left to right*) in the $T_{\mathrm{peak}} - \rho_{\mathrm{peak}}$–plane, mass fractions of ^{55}Mn (*top*) and ^{55}Co (*bottom*) at $t = 100\,\mathrm{s}$ are color coded (from Gronow et al. 2021b).

metallicity. This also applies to the nucleosynthetic yields obtained form the He detonation. The change in the ^{58}Ni abundances is best seen in the density regime below 3×10^6 g cm^{-3}. A small increase in the abundance is also visible in the α-rich freeze-out regime.

Curtis et al. (2018) point out that the production of ^{57}Ni, which is slightly more neutron-rich than ^{56}Ni, increases with higher metallicity affecting the ^{57}Ni to ^{56}Ni ratio. The dependence of both Ni isotopes is illustrated in Figure IV.2.4. Models with the same mass configuration have the same color and are connected by lines. The metallicity of the models increases to the top left and the total mass of the models to the top right. However, due to the individual mass configurations some models do not follow the overall trend of an increase in the total ^{56}Ni abundance with higher total mass. As such, the large shell mass of Model M08_10_r leads to a ^{56}Ni production of the order of $10^{-2}\,M_\odot$. This is sufficient to balance the difference in the ^{56}Ni abundance produced in the core detonations of Models M08_10_r and M09_03. Figure IV.2.4 shows that the ^{56}Ni production decreases with higher metallicity while the one of ^{57}Ni increases. The values of the models at $0.01\,Z_\odot$ and $0.1\,Z_\odot$ are almost the same which makes a distinction in the figure difficult.

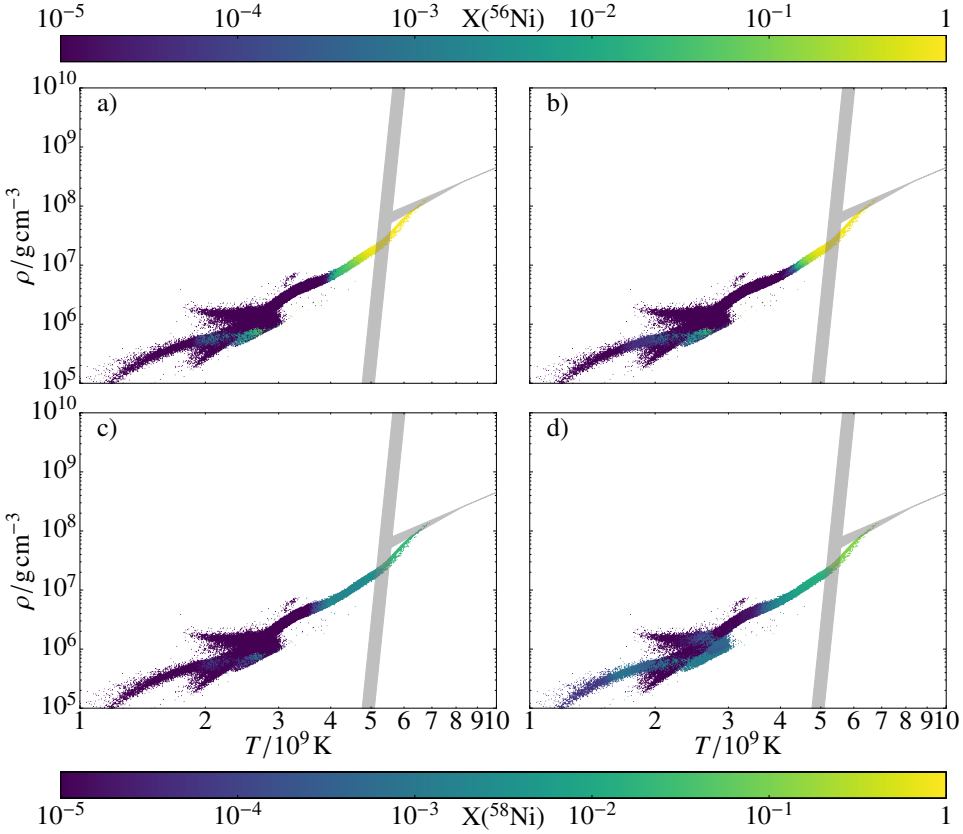

Figure IV.2.3: Tracer particle distribution in the $T_{\rm peak} - \rho_{\rm peak}$–plane for Models M10_03_001 (*left*) and M10_03_3 (*right*) with color coded mass fractions of ^{56}Ni (*top*) and ^{58}Ni (*bottom*) at $t = 100$ s (from Gronow et al. 2021b).

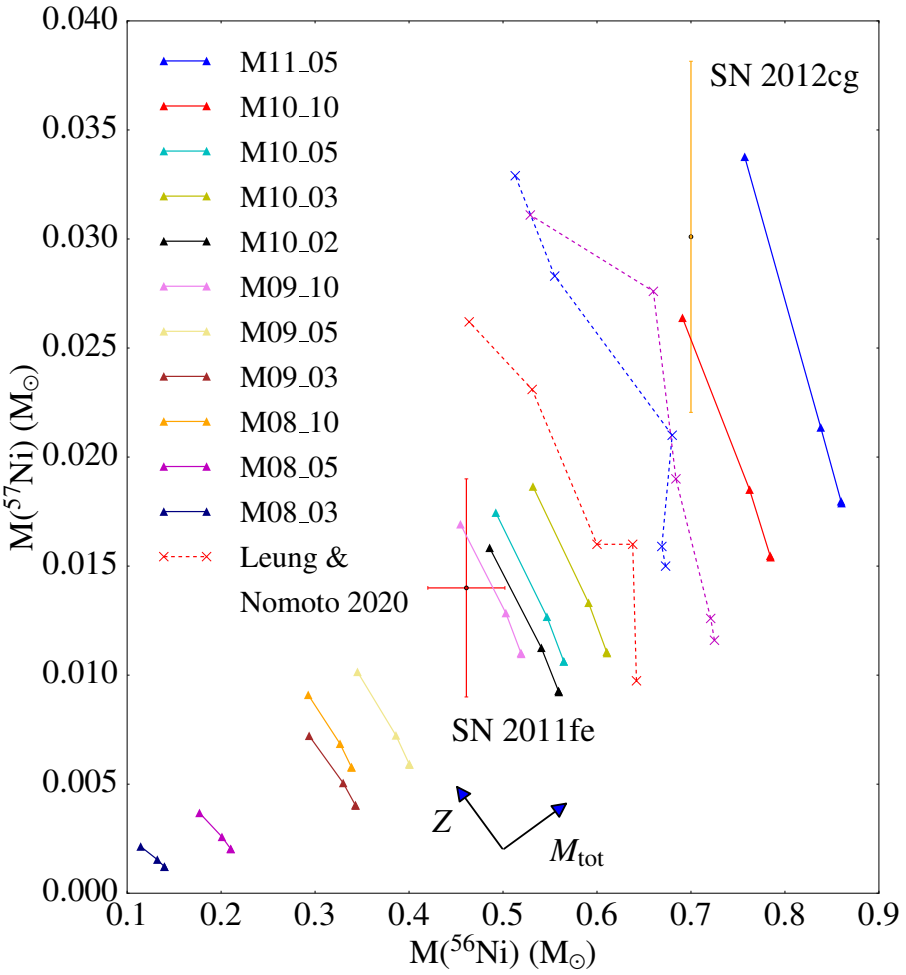

Figure IV.2.4: $M(^{57}\mathrm{Ni})$ plotted against $M(^{56}\mathrm{Ni})$ (solid lines). For comparison models of Leung and Nomoto (2020) (dashed lines) and data for SN 2011fe (Dimitriadis et al. 2017, case 1) and SN 2012cg (Graur et al. 2016) is included (from Gronow et al. 2021b).

IV.2.3 Elemental ratios relative to Fe

The elemental ratios relative to Fe are compared to solar values in Figures IV.2.5 and IV.2.6. The ratios are defined similar to Equation (I.1.4) by

$$[\mathrm{X/Fe}] = \log\left(\frac{X(\mathrm{X})}{X(\mathrm{Fe})}\right) - \log\left(\frac{X_\odot(\mathrm{X})}{X_\odot(\mathrm{Fe})}\right). \tag{IV.2.1}$$

Figure IV.2.5 shows the elemental ratios of selected elements for Models M08_03 (top) and M10_03 (bottom) at the different metallicities. The elemental ratios of all models are sorted by metallicity in Figure IV.2.6 with increasing metallicity from top to bottom.

Figure IV.2.5 illustrates well how the metallicity influences the elemental ratios of a model. The models shown here exhibit the same trends. These also apply to the other models. Some of the trends were already mentioned above. This includes the increase in Mn with higher metallicity. A (small) decrease in Ti and Cr with increasing metallicity indicates that explosions of WDs with higher metallicity progenitor stars are able to match observations better (see Section I.2.6.2). However, the decrease in the abundances is associated with the yields obtained in the core and not the shell detonation. Strong imprints caused by Ti and Cr might therefore persist. Super-solar values of Ti, vanadium (V), and Cr originate in large part from the He detonation. The elemental ratios are, however, almost solar for Models M08_03, M09_03, and M10_03. Out of these Model M10_03 is the best fit at all metallicities. In addition, an odd-even effect is visible in the production of IMEs. The effect gives an account of stable isotopes with even numbers of neutrons and protons being favored against those with odd numbers which is caused by the different binding energies of such isotopes. The pairing effect leads to a stable structure of elements with an even atomic number as the nuclear binding energy is high. These elements are in most part produced in the burning along the α-chain. Furthermore, the production of elements with an odd atomic number is influenced by the neutron excess of the WD (Wheeler et al. 1989). This can be seen in Figures IV.2.5 and IV.2.6 and results from the fact that these elements tend to only have stable isotopes that are neutron-rich.

A drop-off is visible for copper (Cu), zinc (Zn), and cobalt (Co). It decreases with higher metallicity. Figure IV.2.6 shows that models with larger shell masses produce more Co, Cu, and Zn. This confirms that the He detonation is the main production site for Cu and Zn. Sub-solar values of these elements are typical for pure detonations of WDs as pointed out by Lach et al. (2020). These features are visible in all models (see Figure IV.2.6). The influence of the He detonation on the elemental ratios can be deducted by a comparison of all models. This is carried out in Lach et al. (2020) whose findings are confirmed in this study.

The models illustrate that [Mn/Fe] decreases with increasing core mass (see Figure IV.2.6). This is the case because a high ratio stems from the Mn production in the shell detonation (see Section IV.2.2.1). The relative contribution to the total ratio therefore decreases with increasing mass. In addition, the Fe production in the core increases with higher core mass. Only three models, Models M09_05_1, M09_10_r_1, and M10_05_1, have a total mass high enough for a normal SN Ia and about solar [Mn/Fe]. Nevertheless, all models have super-solar values at $3\,Z_\odot$.

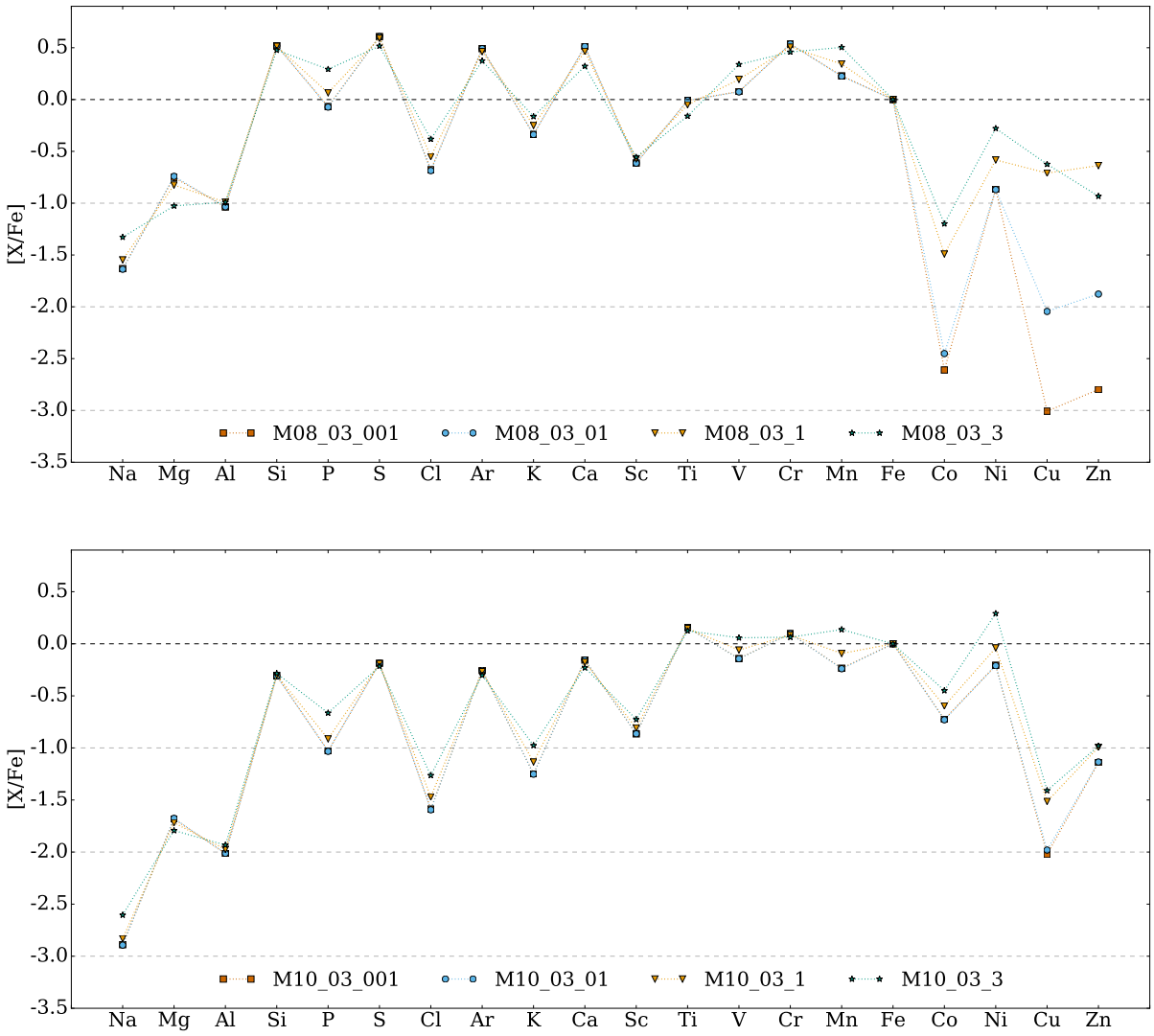

Figure IV.2.5: Elemental ratios relative to Fe compared to solar ratios of Models M08_03 (*top*) and M10_03 (*bottom*) at four different metallicities (from Gronow et al. 2021b).

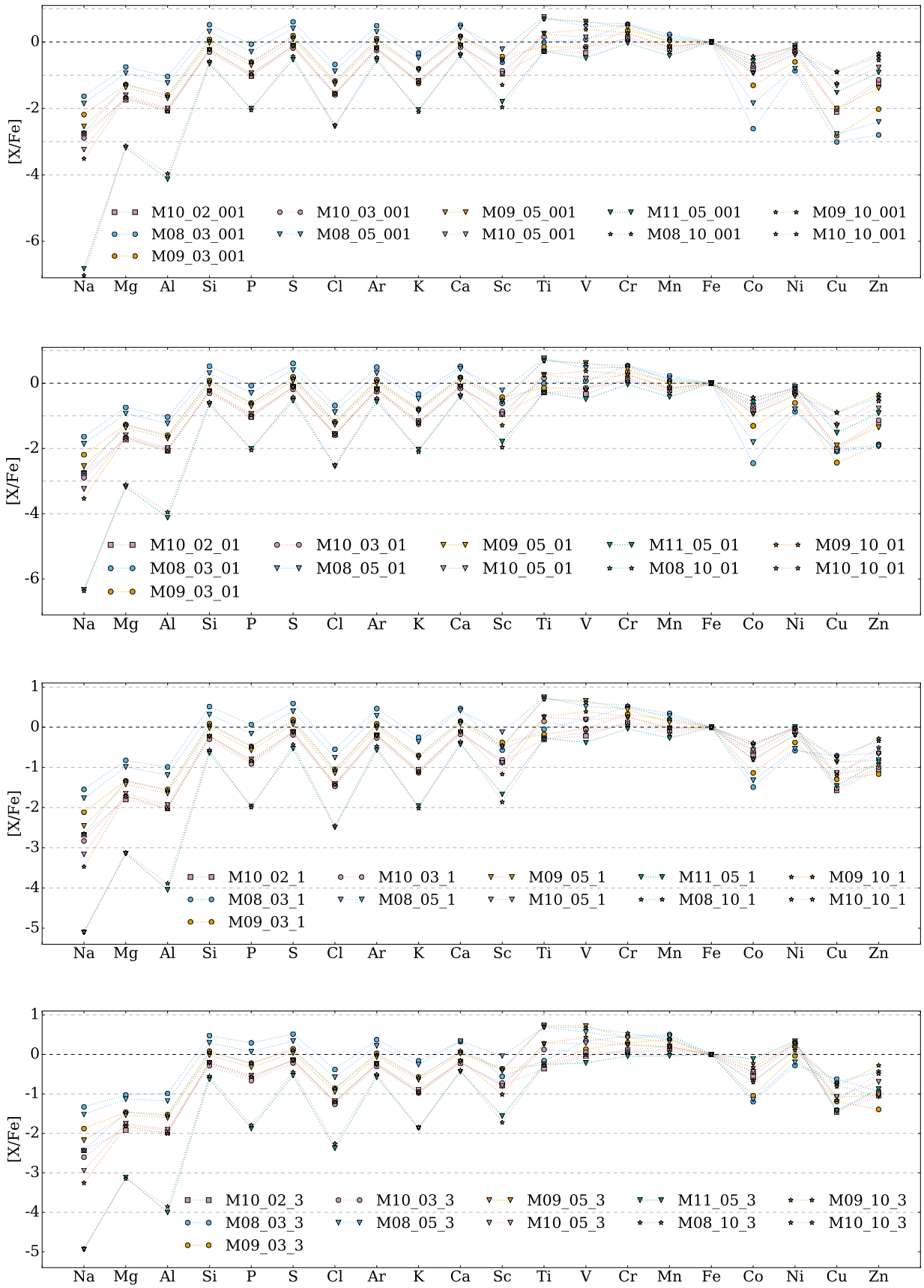

Figure IV.2.6: Elemental ratios relative to Fe compared to solar ratios of all models at metallicities of 0.01 $Z_\odot$, 0.1 $Z_\odot$, 1 $Z_\odot$ and 3 $Z_\odot$ (*top to bottom*) (from Gronow et al. 2021b).

IV.3 Discussion

Parameter studies involving sub-M_{Ch} WDs at non-zero metallicity are carried out by Shigeyama et al. (1992), Timmes et al. (2003), Sim et al. (2010), Shen et al. (2018b), and Leung and Nomoto (2020). Most of these studies, however, look into a WD without He shell. Only Leung and Nomoto (2020) study the effect of metallicity on WDs with CO core and He shell.

As discussed in Section IV.2.2.1, the metallicity has an important effect on the Mn production. This is also stated in Seitenzahl et al. (2013a) and Lach et al. (2020). Lach et al. (2020) further analyse the nucleosynthetic yields of various explosion channels involving M_{Ch} and sub-M_{Ch} WDs focusing on Mn, Zn, and Cu as well as a GCE model. The models presented here confirm that an increase in metallicity results in a higher Cu production as stated in Lach et al. (2020). Nevertheless, it is still sub-solar, even in the models with high total masses such as Model M11_05.

Lach et al. (2020) point out that a distinction between M_{Ch} and sub-M_{Ch} WD progenitors based on super-solar values of Mn and Ni is difficult. This is confirmed here as models with a $1.0\,M_\odot$ core are able to produce super-solar values of both elements. This method is, however, used by Flörs et al. (2019) in nebular spectra. The work presented here (see also Gronow et al. 2021b) and by Lach et al. (2020) indicate that the criterion needs to be applied carefully.

Sim et al. (2010) and Shen et al. (2018b) investigate sub-M_{Ch} CO WD explosions. Shen et al. (2018b) look into metallicities of $0\,Z_\odot$, $0.5\,Z_\odot$, $1\,Z_\odot$, and $2\,Z_\odot$ using ^{22}Ne and ^{56}Fe to represent metallicity in the explosion simulation. A concrete comparison is difficult in both cases (Sim et al. 2010 and Shen et al. 2018b) due to different initial setups. However, all models (including the ones presented here, Gronow et al. 2021b) show the same trends. The models of Shen et al. (2018b) show a decreasing trend in the ^{56}Ni production toward more stable isotopes. Their models further match those of Shigeyama et al. (1992) relatively well at $2\,Z_\odot$.

As mentioned in the introduction to this chapter, a relation between the ^{56}Ni production and metallicity is found by Timmes et al. (2003). Their study shows a decrease in ^{56}Ni by 25% going from $0.3\,Z_\odot$ to $3\,Z_\odot$. Shen et al. (2018b) find the same trend. However, the decrease is higher with 50% for models with a mass of $0.8\,M_\odot$ than for those with masses of $1.0\,M_\odot$ who show a decrease by 10%. The ^{56}Ni abundance experiences a decrease by 12% in most models presented here. Only the model with the lowest total mass, Model M08_03, shows a decrease by 21%. Ohkubo et al. (2006) find a similar value of 15% in their study involving metallicities between $0.001\,Z_\odot$ and $0.05\,Z_\odot$. Timmes et al. (2003) derive a linear relation between the ^{56}Ni mass and metallicity. For this, they assume a fixed value of $0.6\,M_\odot$ ^{56}Ni produced in a normal SN Ia. However, the ^{56}Ni abundance changes with the total mass of the exploding WD. As listed in Tables IV.2.1 to IV.2.23 WDs with lower total masses produce significantly less ^{56}Ni. In this case, the relative change of the ^{56}Ni mass with metallicity is larger than for more massive WDs.

A parameter study involving core and shell masses similar to the ones presented here is carried out by Leung and Nomoto (2020). The models of this thesis, however, include lower masses for both, the core and shell. The 2D simulations of Leung and Nomoto (2020) do not include core-shell mixing which influences the nucleosynthesis obtained from the shell detonation as described

in Section II.2.3.1. Their study covers metallicities of $0\,Z_{\odot}$ to $5\,Z_{\odot}$. Their model groups H, I, and J investigate the effect of metallicity on the nucleosynthetic yields. Out of these the models in group I best resemble Model M10_10. Similar to the abundances discussed in Section IV.2, they find an increase in the yields of stable isotopes. A decrease in the ^{56}Ni production by 20% is found as well while the absolute values are higher in the models of this work. The increase in the Mn production is similar in their work and in the study presented here. However, the abundances of neutron-rich isotopes differ by up to four orders of magnitude. The abundances of ^{30}Si and ^{34}S are one order of magnitude higher in their study. Differences can also be found in the abundances of ^{44}Ti, ^{55}Mn, and ^{64}Zn. In all three cases the nucleosynthetic yields presented in Section IV.2 are a better match to solar values. The discrepancies in the nucleosynthetic yields can be explained by the different setups as described above. In addition, Leung and Nomoto (2020) only employ a seven isotope nuclear reaction network in the hydrodynamic simulations which is not optimal to capture the energy release in WDs with thin shells (Shen et al. 2018b, Townsley et al. 2019). Their code further employs a level-set method which is not best suited at the low densities in a He shell or in sub-M_{Ch} WDs in general.

Leung and Nomoto (2020) point out that the detonation position, detonation channel, time of C detonation ignition, explosion energy, and total energy are only weakly affected by the metallicity. This supports the computational approach chosen in this study, namely the omission of a full re-calculation of the explosion simulations at all metallicities (see Section IV.1). Three models of Leung and Nomoto (2020) are added to Figure IV.2.4 for comparison. All models show the same trends as the models of this study. However, the models by Leung and Nomoto (2020) have higher abundances of ^{57}Ni due to the described differences. Data points for SN 2011fe (Dimitriadis et al. 2017, case 1) and SN 2012cg (Graur et al. 2016) are included in the figure as well. The observational data lies in the same parameter space as the models of the metallicity study. Based on the location of the data for SN 2011fe its progenitor is potentially similar to Model M09_10_r_3. A WD similar to Model M10_10 can be the progenitor of SN 2012cg.

IV.4 Galactic chemical evolution model

GCE calculations using models of this metallicity study were carried out in collaboration with Benoit Côté. He is affiliated with the Konkoly Observatory (Research Centre for Astronomy and Earth Sciences, Eötvös Loránd Research Network (ELKH), Budapest, Hungary), ELTE Eötvös Loránd University (Institute of Physics, Budapest, Hungary), and the Joint Institute for Nuclear Astrophysics - Center for the Evolution of the Elements (USA). The GCE models are included here to discuss the impact of sub-M_{Ch} WD explosions on the Mn enrichment of the MW and are part of the work to be published by Gronow et al. (2021b).

The GCE model was calculated using the OMEGA+ code (Côté et al. 2018). It is a two-zone model describing a central galaxy encircled by a large gas reservoir. Star formation ($\dot{M}_{\star}$), chemical enrichment processes, and galactic in- and outflows to the gas reservoir ($\dot{M}_{in,gal}$ and $\dot{M}_{out,gal}$) are taken into account. The chemical composition can be calculated as a function of time. The evolution of the mass in the two zones is given by

$$\dot{M}_{gal} = \dot{M}_{in,gal} + \dot{M}_{ej} - \dot{M}_{\star} - \dot{M}_{out,gal} \tag{IV.4.1}$$

for the galaxy and

$$\dot{M}_{gas} = \dot{M}_{in,gas} + \dot{M}_{out,gal} - \dot{M}_{in,gal} - \dot{M}_{out,gas} \tag{IV.4.2}$$

for the gas reservoir with the combined mass loss rate $\dot{M}_{ej}$ and in- and outflow rates from the external medium to the gas reservoir ($\dot{M}_{in,gas}$ and $\dot{M}_{out,gas}$, Côté et al. 2018). It is further possible to track individual elements. The code is calibrated to match properties of the MW (e.g. current star formation rate). A more detailed description of the code and how it is used as part of this study is given in Côté et al. (2018) and Gronow et al. (2021b).

In this work only low- and intermediate-mass stars (LIMS), CC SNe and SNe Ia are included as astrophysical sites. While the ejecta are assumed to mix homogeneously, a DTD is included for SNe Ia which allows to take the lifetime of stars into account (details are given in Ritter et al. 2018). All SNe Ia are assumed to originate from sub-M_{Ch} WD explosions. This permits to investigate in which way this explosion channel contributes to the Mn evolution in the solar neighborhood (see also Lach et al. 2020).

The metallicity-dependent nucleosynthetic yields of Model M10_03 are used in this first test case with the DTD of Ruiter et al. (2014) employed at all metallicities. It is normalized in order to account for the SN Ia rate observed in nearby galaxies (see Côté et al. 2016). In the DTD about 10^{-3} SNe Ia are to emerge per unit of stellar mass formed in total.

Mass- and metallicity-dependent nucleosynthetic yields of LIMS are taken from Cristallo et al. (2015). Two different data sets for mass- and metallicity-dependent yields of CC SNe are employed: those of Limongi and Chieffi (2018 , LC18) and Nomoto et al. (2013 , N13). The yields of LC18 are used for massive stars from 8 to 100 $M_{\odot}$ assuming a mixture of rotation velocities (Prantzos et al. 2018). In case the yields of N13 are applied, it is considered that 50% of stars with an initial mass higher than 20 $M_{\odot}$ end in hypernovae. The yields are therefore adopted for

massive stars from 8 to 50 $M_{\odot}$. This limit was selected to prevent an overproduction of metals produced by CC SNe.

The evolution of [Mn/Fe] over [Fe/H] in the solar neighborhood as obtained from the GCE model is shown in Figure IV.4.1. The use of different CC SN yields and SN Ia treatments is included. The necessary contribution of SN Ia to [Mn/Fe] to reach solar values at [Fe/H]= 0 depends on the employed CC SN yields (gray solid lines in the figure). The yields of LC18 account for a significant increase in [Mn/Fe] at [Fe/H] > -0.5 (top panel in Figure IV.4.1). The CC SN yields of N13 show a different evolution (bottom panel).

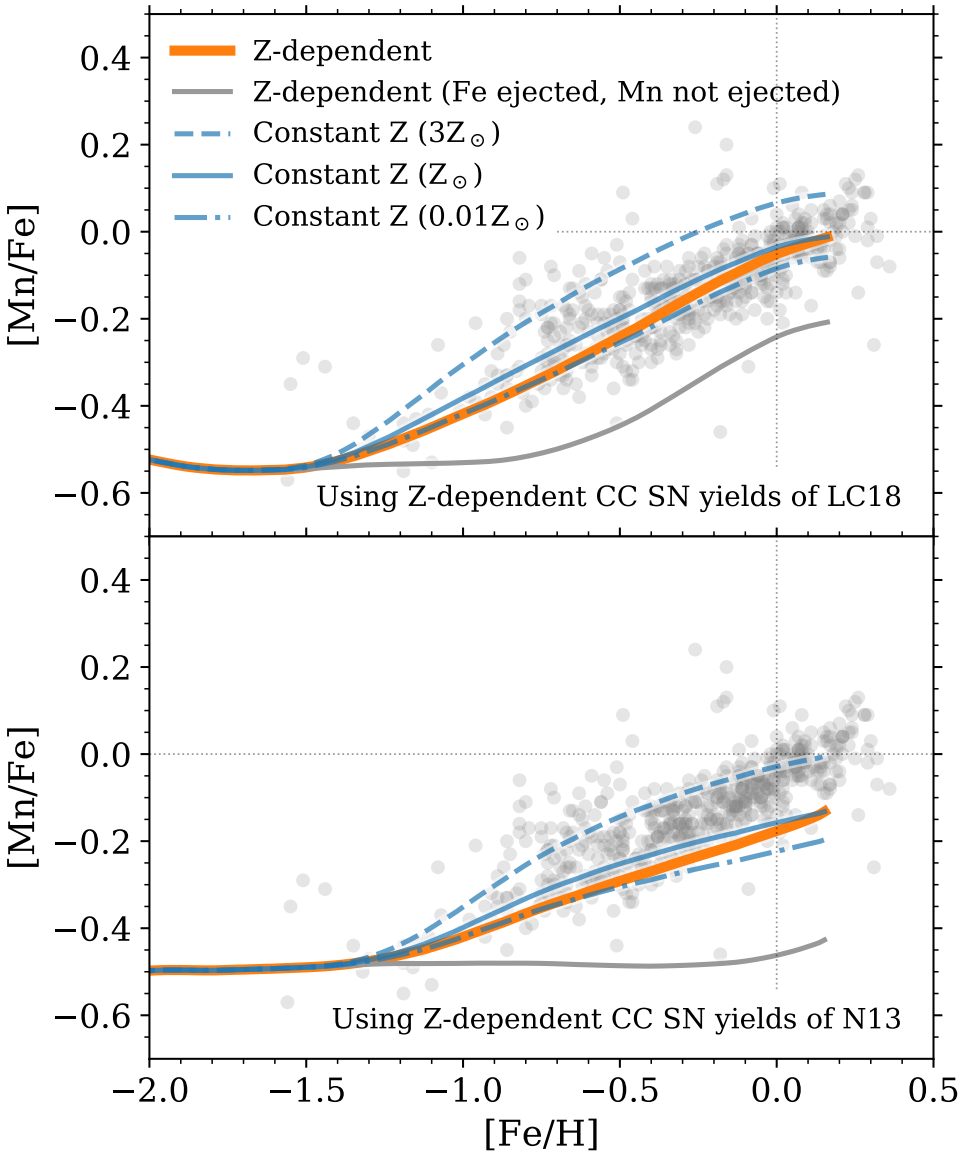

Figure IV.4.1: Model evolution of Mn in the solar neighborhood (lines) compared to the evolution derived from stellar spectroscopy (dots, Battistini and Bensby 2015). The CC SNe yields of LC18 are used in the top and those of N13 in the bottom panel. Blue lines show the predictions using nucleosynthetic yields at constant metallicity and orange lines the predictions using metallicity-dependent SN Ia yields. The metallicity-dependent case assuming SNe Ia only eject Fe while CC SNe eject Fe and Mn is shown as gray line. (from Gronow et al. 2021b).

The Mn evolution taking metallicity-dependent SN Ia yields into account is shown in orange. Using the LC18 yields results in a good agreement with data (Battistini and Bensby 2015). Since the CC SN yields employed by Seitenzahl et al. (2013a) are similar to N13, their predicted Mn production resembles that presented in the bottom panel of Figure IV.4.1 using the N13 yields. As stated in Section IV.2.2.1, a less stiff requirements for M_{Ch} WD explosions is obtained when incorporating CC SN yields of LC18. The impact of metallicity-dependent SN Ia nucleosynthetic yields is visible in a comparison of the blue lines in Figure IV.4.1. While the Mn production at constant metallicities of $0.01\,Z_{\odot}$ and $1\,Z_{\odot}$ matches that of the metallicity-dependent curve rather well, the consideration of metallicity-dependent yields is necessary to explain the trend at [Fe/H] > 0 to higher [Mn/Fe] values.

Figure IV.4.2 illustrates the predicted solar elemental abundances of selected elements given the use of metallicity-dependent SN Ia yields. CC SN yields of LC18 are employed in the top and the ones of N13 in the bottom panel of Figure IV.4.2. The contribution of CC SNe to Mn is significant when using the LC18 yields. It lowers the need for M_{Ch} WD explosions to take place. With the assumption used here that sub-M_{Ch} WD explosions are the dominant SN Ia channel, 80% of the Mn production can be accounted for. Employing other CC SN yields, like those of N13, however, requires a contribution by M_{Ch} WD explosions as the Mn production in CC SNe is assumed to be much lower. It should also be stated that the model involves some uncertainties such as the number of SNe Ia that occured in the MW before Solar System formation.

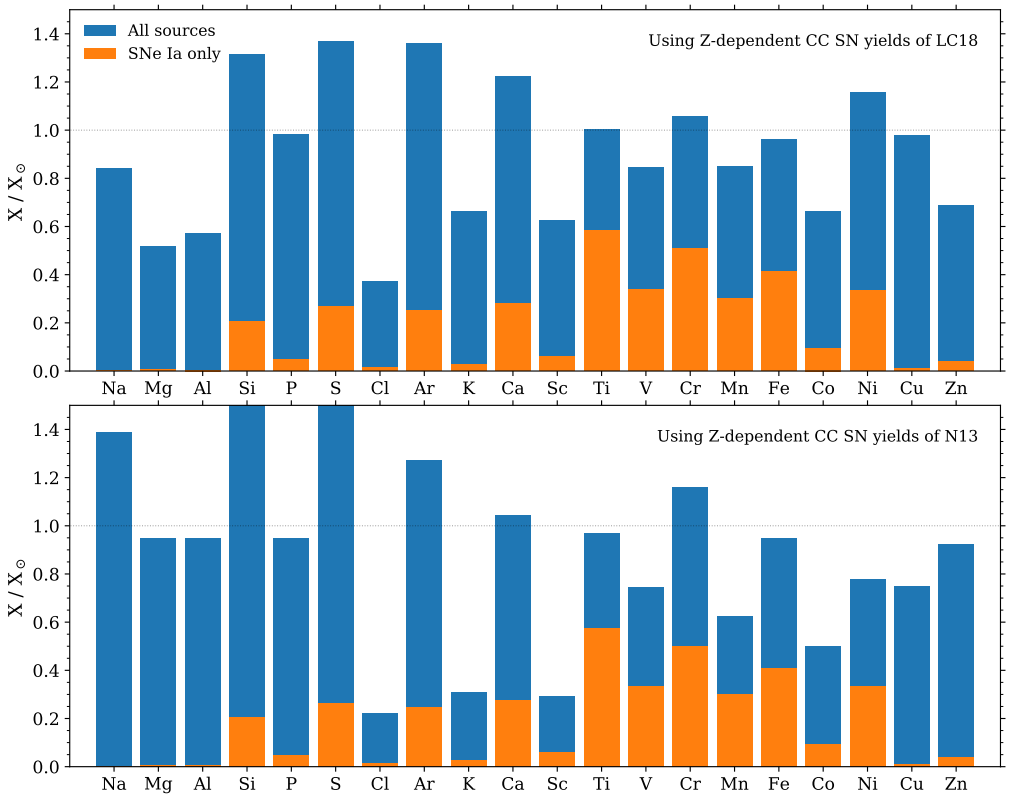

Figure IV.4.2: Model solar elemental distribution normalized to solar abundances (Asplund et al. 2009). Blue bars indicate predictions combining the contribution of CC SNe (*top:* Limongi and Chieffi 2018, *bottom:* Nomoto et al. 2013), LIMS (Cristallo et al. 2015), and metallicity-dependent yields for SNe Ia. Orange bands show the share of SNe Ia within the total predicted abundances (from Gronow et al. 2021b).

A limit on the contribution of SNe Ia to the Mn production is set by other elements (see Figure IV.4.2). Critical amounts of Ti and Cr are produced applying LC18 yields for CC SNe filling the solar composition. Modifying the GCE model to account for all the solar Mn would therefore result in an overproduction of Ti and Cr. Ca and Ni are already overproduced in the current model using LC18 yields while this is not the case when those of N13 are included.

Chapter V

Summary

V.1 Conclusions

In the framework of this thesis several parameter studies were carried out involving double detonations of sub-M_{Ch} WDs. The aims are to provide more detailed explosion models for a possible progenitor channel of SNe Ia than provided by previous work (e.g. Nomoto 1982b, Shigeyama et al. 1992, Woosley and Weaver 1994b, Livne and Arnett 1995, Nugent et al. 1997, Bildsten et al. 2007, Fink et al. 2007, 2010, Moll and Woosley 2013) (see Chapters II and III), and to investigate the contribution of such explosions to the chemical enrichment of the MW (see Chapter IV).

In order to achieve these goals a new modeling approach for double detonations was introduced which allows to reach higher resolutions than those of work by, for example, Fink et al. (2007) and Moll and Woosley (2013). The numerical treatment was used to simulate explosions of sub-M_{Ch} WDs covering a wide parameter space of different core and shell masses as well as metallicities. The following sections give a detailed summary of the findings in each study.

V.1.1 Impact of core-shell mixing

The double detonation scenario is a favored explosion mechanism for sub-M_{Ch} WDs to produce SNe Ia (e.g. Nomoto 1982a,b, Livne 1990, Livne and Glasner 1990, Woosley and Weaver 1994b, Livne and Arnett 1995, Fink et al. 2007, 2010, Woosley et al. 2011, Moll and Woosley 2013, Shen and Bildsten 2014, Blondin et al. 2017a, Shen et al. 2018a, Tanikawa et al. 2018, Shen et al. 2018a, Polin et al. 2019, Leung and Nomoto 2020). Some details of this scenario are, however, not well studied to date and leave some questions unanswered. Two of these question concern the exact ignition mechanism of the He detonation and its propagation in the He shell. Due to a lack of resolution details of the C detonation ignition remain uncertain as well (see Section I.2.6.2 for a discussion of the open questions). This thesis tackles the uncertainties involving the propagation of the He detonation in the shell and the C detonation ignition mechanism by carrying out full 3D simulations of non-rotating WDs using the moving-mesh code Arepo. On the one hand, the chosen dimensionality permits to accurately model the problem. Simulations carried out in 1D or 2D (e.g., Woosley and Weaver 1994a, Bildsten et al. 2007, Fink et al. 2010) assume symmetries which are not given under all circumstances. As an example, the ignition of the He detonation in one spot in 1D corresponds to a ring or shell detonation ignition in 2D and 3D, respectively (Section III.3). Only simulations by Moll and Woosley (2013) and Tanikawa et al. (2018) are in 3D, with Moll and Woosley (2013) simulating a quarter of the WD. On the other hand, the Arepo code permits the use of AMR. With this the resolution in selected regions such as the He shell and around the convergence point of the He detonation wave is increased. This enables a more accurate treatment of the He detonation propagation compared to earlier work (e.g. Fink et al. 2007, Moll and Woosley 2013). Nevertheless, a sufficiently high resolution to fully resolve the C detonation ignition is not reached.

A focus of the first study (Chapter II) is on the influence of core-shell mixing on the C

detonation ignition mechanism. The results are presented and discussed in Sections II.2, II.3, and II.4. A C detonation ignition mechanism is found which received little to no attention to this point. In this scissors mechanism a C detonation is ignited at the convergence point of the He detonation wave. It is located opposite to the first ignition spot of the He detonation. The ignition mechanism is mentioned in work by Livne and Arnett (1995), García-Senz et al. (1999), Forcada (2007), and García-Senz et al. (2018). However, a detailed description, analysis and discussion are omitted. Other work (e.g. Fink et al. 2007, 2010, Moll and Woosley 2013, Shen and Bildsten 2014) does not regard the convergence of the He detonation wave to be strong enough and neglects the possibility of a C detonation ignition at this point. Instead a C detonation ignition following the converging shock scenario is investigated.

The robustness of the scissors mechanism is analysed regarding different parameters (Section II.2.3). It was shown that small changes in the location of the He detonation ignition spot do not affect a successful C detonation ignition. The mechanism is further stable toward the application of larger nuclear reaction networks in the explosion simulation which are more accurate for the modeling of explosions in thin shells according to Shen et al. (2018b) and Townsley et al. (2019).

The C detonation ignition mechanism was found in WDs of two different mass configurations in this initial study. Along with work by García-Senz et al. (1999), Forcada (2007), and García-Senz et al. (2018), it confirms that the mechanism is not limited to a specific setup. However, details of the transition region between core and shell are important. If the shell is not enriched with C, C is absent at the convergence point of the He detonation wave and a C detonation cannot be ignited. The C detonation ignition mechanism is nonetheless the converged solution based on the resolution study carried out and discussed in Section II.2.3.2. García-Senz et al. (2018) point out that rotation induces a symmetry axis. If the He detonation is ignited far off from this axis, it can smear out the convergence point of the He detonation wave which affects the C detonation ignition. García-Senz et al. (2018) nevertheless find that a core detonation is likely.

Despite the increased resolution in the simulations compared to previous studies, the C detonation cannot be fully resolved as it takes place on much smaller scales. The C detonations of the models are therefore in part numerical. However, a comparison of the density, temperature, and composition of the detonating regions with critical values for a C detonation ignition found in literature (Röpke et al. 2007b, Seitenzahl et al. 2009) confirms that a physical detonation is reasonable in all models.

The final yields of the models and especially the ^{56}Ni yields are in the expected range for normal SNe Ia (Stritzinger et al. 2006, Scalzo et al. 2014). The two initial mass configurations presented in Chapter II are chosen to resemble Models FM1 and FM3 (Fink et al. 2010). Due to the different transition regions and degrees of mixing, the final abundances produced in the shell detonation of Models M2a and FM3 show discrepancies. These also impact the C detonation ignition mechanism, with Model FM3 exhibiting a core detonation following the converging shock mechanism. As pointed out in Section II.2.1, the level-set approach used by Fink et al. (2010) is not best suited for low densities present in, for example, the He shell.

Radiative transfer calculations were carried out by Christine E. Collins using Artis for Models M1a, M2a M2a_i55, and FM3 (re-calculation). A comparison of the models to Model FM3 shows no significant differences. Similar to models by Kromer et al. (2010), the color is too red compared to a spectroscopically normal SN, like SN 2011fe, which is a general problem of double detonation simulations. However, several spectral features, like a strong Si II line, are met. It is shown that Model M2a matches spectral features of SN 2016hjr rather well. The model is not able to reproduce the extreme line blanketing found in SN 2018byg around peak brightness. Nevertheless, the most extreme lines-of-sight match this level (see Figure II.3.6).

The study has shown that details of the transition region are important for the C detonation ignition. A C enrichment of the shell further impacts the nucleosynthetic yields produced in the He detonation. While the models indicate that a C detonation is ignited in the converging shock scenario if the scissors mechanism is not successful, the detected C detonation ignition mechanism should not be disregarded in the future. The simulations further illustrate well that multi-dimensional simulations are needed to treat the double detonation appropriately.

V.1.2 A possible explanation for variations in SNe Ia

A second parameter study (Chapter III) investigates whether different core and shell masses of a sub-M_{Ch} WD can explain observed variations found in SNe Ia. Core masses of $0.8\,M_\odot$ to $1.1\,M_\odot$ and shell masses in the range of $0.02\,M_\odot$ and $0.1\,M_\odot$ are covered. Thin He shells are of particular interest as their imprints on the early observables are weaker than those of massive shells (Höflich et al. 1996, Kromer et al. 2010). This is taken into account in this study with shell masses below or equal to $0.03\,M_\odot$. These models show significant lower abundances of ^{44}Ti and ^{56}Ni produced in the shell detonation than other models.

The total ^{56}Ni mass produced in the double detonation increases with core mass. This is the case as more material is available to be burnt and because the densities increase with higher mass allowing to burn to heavier elements. The products of the shell detonation are generally dominated by IMEs which are synthesised in large amounts due to the low densities in the shell compared to those in the core. The C enrichment of the shell has an influence on the nucleosynthetic yields obtained in the shell detonation in the same way as in the previous study (see Section II.2.3.1). Different degrees of mixing are studied in order to gain further insights into its effect on the explosion. The models show that it can alter the C detonation ignition mechanism while differences in the final abundances are relatively low. Independent of the C detonation ignition mechanism, large asymmetries are found in the ejecta structure. The details of those, however, depend on the mechanism (Section III.2). A comparison of Models M10_05 and M2a illustrates the effect metallicity has on the final abundances in a first step showing that the production is shifted to more stable Ni isotopes.

Besides the C enrichment of the shell, other parameters such as the dimensionality of the study, the numerical treatment, and nuclear reaction network of the explosion simulation (Shen et al. 2018b, Townsley et al. 2019) influence the nucleosynthetic yields in some respects. Differences in these quantities affect a comparison to work by others (e.g. Bildsten et al. 2007, Fink et al. 2007, 2010, Polin et al. 2019, Leung and Nomoto 2020). Discrepancies are in addition caused by varying initial profiles mostly involving the mass configurations of the core and shell. It is to be noted that the mass configurations of all models presented in this thesis are in most part set by the relaxation step. Despite the differences, a comparison can be carried out in some cases. As such, a match to models by Woosley and Kasen (2011) and Polin et al. (2019) is found (Section III.3). The nucleosynthetic yields indicate that the new models of this work are a potential better match to observations than the models of, for example, Polin et al. (2019).

The models show a range of peak luminosities in the light curves (Section III.4). The values are associated with sub-luminous to normal SNe Ia. A comparison of all models shows that the brightness increases with ^{56}Ni mass as expected. The introduced solar metallicity increases the decline rate, which is visible examining Models M10_05 and M2a.

The asymmetry found in the ejecta structure results in strong angle-dependencies of the observables. The distribution of ^{56}Ni in the ejecta has the strongest influence on this. The models loosely follow the width-luminosity relation found for SNe Ia (see Sections III.4). While the fainter models decline too slow compared to data (Scalzo et al. 2019), brighter models cover

the same parameter space as observations. Both, data and models show a strong correlation between the decline rates over 15 days, Δm_{15}(bol), and over 40 days, Δm_{40}(bol). However, the models have an offset to data. This might indicate a generic problem of the progenitor channel, namely that the masses are too low or the ejecta velocities do not match those in observations. Nevertheless, explosions of sub-M_{Ch} WDs remain a promising candidate for lower luminosity SNe Ia and peculiar events.

V.1.3 Metallicity-dependent nucleosynthetic yields and GCE

A follow-up study to the models of Chapter III was carried out assuming varying metallicities of the zero-age main sequence progenitor star. A re-calculation of the postprocessing at the respective metallicties is found to be sufficient as the energetics only weakly depend on the metallicity. The nucleosynthetic yields obtained this way are in good agreement with a full re-calculation of the hydrodynamic model (Section IV.1).

The impact of the metallicity on the nucleosythetic yields is stronger at higher densities which are present in the core. Here, the neutron excess leads to an increase in the abundances of stable isotopes. As such, the yields of ^{54}Fe and ^{58}Ni increase to four times the value at $0.01\,Z_\odot$ if the metallicity is $3\,Z_\odot$. The influence on the Mn production is even stronger as discussed in Section IV.2.2.1 and stated by Seitenzahl et al. (2013a). In the He detonation the isotopes of the metallicity implementation serve as seed nuclei enabling additional reactions to take place. The abundances of isotopes lighter than or equally massive as ^{44}Ti is minimal. However, the production of ^{55}Mn increases by one order of magnitude with each step of increasing metallicity (from $0.01\,Z_\odot$ to $0.1\,Z_\odot$ to $Z_\odot$ to $3\,Z_\odot$). The ^{54}Fe and ^{58}Ni production in the He detonation is increased as well.

Changes in the elemental ratios relative to Fe compared to solar values are discussed in Section IV.2.3. The same trends are visible in all models. A comparison of the models leads to the derivation that Cu and Zn are mostly produced in the He detonation (see also Lach et al. 2020). Sub-solar values of these elements as well as Co are features of pure detonations as pointed out by Lach et al. (2020). Super-solar values of Ti originate from the He detonation. However, solar values are also produced in some models.

Only Leung and Nomoto (2020) carry out a parameter study for sub-M_{Ch} CO WDs with a He shell covering different metallicities. Other studies (e.g. Sim et al. 2010, Shen et al. 2018b) omit a He shell. The final abundances of the models by Leung and Nomoto (2020) show the same trends as the models of this work. Discrepancies found in the yields originate in most part from the different numerical treatments while the small size of the nuclear reaction network of the explosion simulations in Leung and Nomoto (2020) is expected to have an impact as well.

The models confirm a decreasing abundance of ^{56}Ni with increasing metallicity as found by Timmes et al. (2003) and Shen et al. (2018b), among others. The dependence is found to be not as strong in the models of this study showing a decrease by 13% on average whereas Timmes et al. (2003) detect a decrease in ^{56}Ni by 25%. However, a reduction of the ^{56}Ni yields by 15% found by Ohkubo et al. (2006) is in agreement with the outcome of this study. It further needs to be taken into account that the decrease depends on the WD mass as discussed in Section IV.3.

The study further shows that super-solar values of Mn can be reached in a double detonation of sub-M_{Ch} WDs. For this, the contribution of the He detonation is important as its Mn production is significantly super-solar. Assuming double detonations to be the dominant explosion channel for a SN Ia, it significantly contributes to the observed increase of [Mn/Fe] at [Fe/H] > -1 in the solar neighborhood. A necessary contribution of M_{Ch} WD explosions of 50% to SNe Ia as suggested by Seitenzahl et al. (2013a) is not required taking this into account. When

using the CC SN yields of LC18 (Limongi and Chieffi 2018), the presented GCE model is able to account for 80% of the Mn production omitting any contribution from M_{Ch} WD explosions (Section IV.4). The metallicity study includes this GCE model (carried out by Benoit Côté) as a test case.

V.1.4 Implications for SN Ia modeling and outlook

This thesis presents a comprehensive overview of various parameter studies, involving different core and shell masses as well as metallicities in particular. The metallicity-dependent nucleosynthetic yields obtained in the parameter study of Chapter IV provide the basis for future GCE studies. They enable a detailed analysis of the contribution to the chemical enrichment of the MW by double detonations of sub-M_{Ch} WDs.

The 3D simulations of this thesis highlight well that multi-dimensional models are needed to treat the problem accurately. Current 1D and 2D simulations conceal some angle-dependent aspects of the problem. As a first step, a 3D simulation at significantly higher resolution will give more insights into the evolution of a double detonation. Due to the high computational cost the setup has to be chosen carefully. In further steps, the accretion process from the companion star onto the CO WD should be included in the hydrodynamical simulation leading to a more precise modeling of the He shell mass and core-shell mixing. In addition, the rotation of a WD can influence the C detonation ignition mechanism as stated in García-Senz et al. (2018) and should be incorporated in simulations according to Neunteufel et al. (2017). It also needs to be taken into account that the reaction rates used in the framework of this thesis have some uncertainties (see Cyburt et al. 2010). These are neglected here. Future updates of the JINA Reaclib database are planned to include data on them as stated by Cyburt et al. (2010). This will allow the calculation of resulting inaccuracies in the final abundances.

More detailed radiative transfer calculations covering the early peak found in observed SN Ia light curves should be carried out. The code used in connection with the models of this thesis, Artis, is not best suited at these early times (Gronow et al. 2020). Calculations by Noebauer et al. (2017), however, find such an early peak for Model FM3 indicating it might be present in models such as Model M2a as well, based on the similarity of the models. Further studies involving radiative transfer calculations of the models presented here are currently being carried out. The treatment of non-local thermodynamic equilibrium in these calculations can result in a decrease of the He detonation imprints on the observables improving a match to data. Generally, explosions of sub-M_{Ch} WDs in the double detonation scenario remain a promising candidate for SNe Ia. This study has shown that many characteristics, like varying luminosities and spectral features, can be reproduced.

Additional notes: As is evident from the publications Gronow et al. (2020) and Gronow et al. (2021a), the radiative transfer calculations included in Chapters II and III have been done in collaboration with Christine E. Collins and Stuart S. Sim. The galactic chemical evolution models were calculated in collaboration with Benoit Côté as stated in Section IV.4 (see also Gronow et al. 2021b).

The work was supported by the Deutsche Forschungsgemeinschaft (DFG, German Research Foundation) – Project-ID 138713538 – SFB 881 ('The Milky Way System", subproject A10), by the ChETEC COST Action (CA16117) via COST (European Cooperation in Science and Technology), and by the National Science Foundation under Grant No. OISE-1927130 (IReNA). Computing time was provided by the Gauss Centre for Supercomputing e.V. (www.gauss-centre.eu) on the GCS Supercomputer JUWELS (Jülich Supercomputing Centre 2019) at Jülich Super-

computing Centre (JSC) which is gratefully acknowledged. Radiative transfer calculations were performed using the DiRAC Data Intensive service at Leicester, operated by the University of Leicester IT Services, which forms part of the STFC DiRAC HPC Facility (www.dirac.ac.uk). The equipment was funded by BEIS capital funding via STFC capital grants ST/K000373/1 and ST/R002363/1 and STFC DiRAC Operations grant ST/R001014/1. The work also used the Cambridge Service for Data Driven Discovery (CSD3), part of which is operated by the University of Cambridge Research Computing on behalf of the STFC DiRAC HPC Facility (www.dirac.ac.uk). The DiRAC component of CSD3 was funded by BEIS capital funding via STFC capital grants ST/P002307/1 and ST/R002452/1 and STFC operations grant ST/R00689X/1. DiRAC is part of the National e-Infrastructure. Further, the work was supported by computational resources provided by the Australian Government through the National Computational Infrastructure (NCI) under the National Computational Merit Allocation Scheme.

Software including NumPy and SciPy (Oliphant 2007), IPython (Pérez and Granger 2007), and Matplotlib (Hunter 2007) were used for data analysis and visualization.

Publications by Sabrina Gronow

S. Gronow, C. Collins, S. T. Ohlmann, R. Pakmor, M. Kromer, I. R. Seitenzahl, S. A. Sim, and F. K. Röpke. SNe Ia from double detonations: Impact of core-shell mixing on the carbon ignition mechanism. *A&A*, 635:A169, Mar. 2020.

S. Gronow, C. E. Collins, S. A. Sim, and F. K. Röpke. Double detonations of sub-Chandrasekhar mass CO white dwarfs: Can different core and He shell masses explain variations of Type Ia supernovae? *arXiv e-prints*, art. arXiv:2102.06719, Feb. 2021a. accepted by *A&A*.

S. Gronow, B. Côté, F. Lach, I. R. Seitenzahl, C. E. Collins, S. A. Sim, and F. K. Roepke. Metallicity-dependent nucleosynthetic yields of Type Ia supernovae originating from double detonations of sub-M_{Ch} white dwarfs. *arXiv e-prints*, art. arXiv:2103.14050, Mar. 2021b. submitted to *A&A*.

F. Lach, F. K. Roepke, I. R. Seitenzahl, B. Coté, S. Gronow, and A. J. Ruiter. Nucleosynthesis imprints from different Type Ia Supernova explosion scenarios and implications for galactic chemical evolution. *A&A*, 644:A118, Dec. 2020.

Bibliography

O. Agertz, B. Moore, J. Stadel, D. Potter, et al. Fundamental differences between SPH and grid methods. *MNRAS*, 380(3):963–978, Sept. 2007.

L. G. Althaus, P. G. Pons, A. H. Córsico, M. Miller Bertolami, et al. The formation of ultra-massive carbon-oxygen core white dwarfs and their evolutionary and pulsational properties. *A&A*, 646:A30, Feb. 2021.

S. P. S. Anand. On Chandrasekhar's Limiting Mass for Rotating White Dwarf Stars. *Proceedings of the National Academy of Science*, 54:23–26, July 1965.

D. Arnett. *Supernovae and Nucleosynthesis: An Investigation of the History of Matter from the Big Bang to the Present.* 1996.

W. D. Arnett. A Possible Model of Supernovae: Detonation of ^{12}C. *Ap&SS*, 5:180–212, Oct. 1969.

W. D. Arnett, J. W. Truran, and S. E. Woosley. Nucleosynthesis in Supernova Models. II. The ^{12}C Detonation Model. *ApJ*, 165:87–103, Apr. 1971.

M. Asplund, N. Grevesse, A. J. Sauval, and P. Scott. The Chemical Composition of the Sun. *ARA&A*, 47:481–522, Sept. 2009.

G. Audi, A. H. Wapstra, and C. Thilbault. The AME2003 atomic mass evaluation. *Nuclear Physics A*, 729:337–676, 2003.

W. Baade. No. 675. Nova Ophiuchi of 1604 as a supernova. *Contributions from the Mount Wilson Observatory / Carnegie Institution of Washington*, 675:1–9, Jan. 1943.

W. Baade and F. Zwicky. On Super-novae. *Proceedings of the National Academy of Science*, 20: 254–259, May 1934.

G. Bader and P. Deuflhard. A semi-implicit mid-point rule for stiff systems of ordinary differential equations. *Numerische Mathematik*, 41(3):373–398, Oct. 1983.

C. Battistini and T. Bensby. The origin and evolution of the odd-Z iron-peak elements Sc, V, Mn, and Co in the Milky Way stellar disk. *A&A*, 577:A9, May 2015.

K. Belczynski, T. Bulik, and A. J. Ruiter. New Constraints on Type Ia Supernova Progenitor Models. *ApJ*, 629:915–921, Aug. 2005.

W. Benz. Three-dimensional simulations of core ignition in sub-Chandrasekhar mass models. In P. Ruiz-Lapuente, R. Canal, and J. Isern, editors, *Thermonuclear Supernovae*, volume 486 of *NATO ASIC Proc.*, pages 457–474, Dordrecht, 1997. Kluwer Academic Publishers.

L. Bildsten and D. M. Hall. Gravitational Settling of ^{22}NE in Liquid White Dwarf Interiors. *ApJ*, 549:L219–L223, Mar. 2001.

L. Bildsten, K. J. Shen, N. N. Weinberg, and G. Nelemans. Faint Thermonuclear Supernovae from AM Canum Venaticorum Binaries. *ApJ*, 662:L95–L98, June 2007.

S. I. Blinnikov and A. M. Khokhlov. Development of Detonations in Degenerate Stars. *Soviet Astronomy Letters*, 12:131–136, Apr. 1986.

T. Blöcker. Stellar evolution of low and intermediate-mass stars. I. Mass loss on the AGB and its consequences for stellar evolution. *A&A*, 297:727, May 1995.

S. Blondin, L. Dessart, and D. J. Hillier. The detonation of a sub-Chandrasekhar-mass white dwarf at the origin of the low-luminosity Type Ia supernova 1999by. *Monthly Notices of the Royal Astronomical Society*, 474(3):3931–3953, 11 2017a. ISSN 0035-8711.

S. Blondin, L. Dessart, D. J. Hillier, and A. M. Khokhlov. Evidence for sub-Chandrasekhar-mass progenitors of Type Ia supernovae at the faint end of the width-luminosity relation. *MNRAS*, 470:157–165, Sept. 2017b.

J. S. Bloom, D. Kasen, K. J. Shen, P. E. Nugent, et al. A Compact Degenerate Primary-star Progenitor of SN 2011fe. *ApJ*, 744:L17, Jan. 2012.

D. Bodansky, D. D. Clayton, and W. A. Fowler. Nuclear Quasi-Equilibrium during Silicon Burning. *ApJS*, 16:299–+, Nov. 1968.

H. E. Bond, G. H. Schaefer, R. L. Gilliland, J. B. Holberg, et al. The Sirius System and Its Astrophysical Puzzles: Hubble Space Telescope and Ground-based Astrometry. *ApJ*, 840(2): 70, May 2017.

J. Botyánszki, D. Kasen, and T. Plewa. Multidimensional Models of Type Ia Supernova Nebular Spectra: Strong Emission Lines from Stripped Companion Gas Rule Out Classic Single-degenerate Systems. *ApJ*, 852(1):L6, Jan 2018.

A. Boyle, S. A. Sim, S. Hachinger, and W. Kerzendorf. Helium in double-detonation models of type Ia supernovae. *A&A*, 599:A46, Mar. 2017.

T. Brahe. *De nova et nullius ævi memoria prius visa Stella, iam pridem anno á nato CHRISTO 1572, mense Novembri primum Conspecta, contemplatio mathematica.* Laurentius Benedictus, Kopenhagen, 1573.

D. Branch and G. A. Tammann. Type Ia supernovae as standard candles. *ARA&A*, 30:359–389, 1992.

D. Branch and J. C. Wheeler. *Supernova Explosions.* Springer-Verlag, 2017.

D. Branch, P. Garnavich, T. Matheson, E. Baron, et al. Optical Spectra of the Type Ia Supernova 1998aq. *AJ*, 126(3):1489–1498, Sept. 2003.

E. Bravo. Sensitivity of Type Ia supernovae to electron capture rates. *A&A*, 624:A139, Apr 2019.

E. Bravo, C. Badenes, and H. Martínez-Rodríguez. SNR-calibrated Type Ia supernova models. *MNRAS*, 482(4):4346–4363, Feb. 2019.

M. Bulla, S. A. Sim, and M. Kromer. Polarization spectral synthesis for Type Ia supernova explosion models. *MNRAS*, 450:967–981, June 2015.

G. Cescutti and C. Kobayashi. Manganese spread in Ursa Minor as a proof of sub-classes of type Ia supernovae. *Astronomy & Astrophysics*, 607:A23, 2017.

D. A. Chamulak, E. F. Brown, and F. X. Timmes. The Laminar Flame Speedup by ^{22}Ne Enrichment in White Dwarf Supernovae. *ApJ*, 655:L93–L96, Feb. 2007.

S. Chandrasekhar. The Maximum Mass of Ideal White Dwarfs. *ApJ*, 74:81, July 1931.

S. Chandrasekhar. The Density of White Dwarf Stars. *Journal of Astrophysics and Astronomy*, 15:105, June 1994.

S. A. Colgate and C. McKee. Early Supernova Luminosity. *ApJ*, 157:623–643, Aug. 1969.

G. Contardo, B. Leibundgut, and W. D. Vacca. Epochs of maximum light and bolometric light curves of type Ia supernovae. *A&A*, 359:876–886, July 2000.

R. J. Cooke, M. Pettini, and R. A. Jorgenson. The Most Metal-poor Damped Lyα Systems: An Insight into Dwarf Galaxies at High-redshift. *ApJ*, 800(1):12, Feb. 2015.

B. Côté, C. Ritter, B. W. O'Shea, F. Herwig, et al. Uncertainties in Galactic Chemical Evolution Models. *ApJ*, 824:82, June 2016.

B. Côté, D. W. Silvia, B. W. O'Shea, B. Smith, et al. Validating Semi-analytic Models of High-redshift Galaxy Formation Using Radiation Hydrodynamical Simulations. *ApJ*, 859(1): 67, May 2018.

S. Cristallo, O. Straniero, L. Piersanti, and D. Gobrecht. Evolution, Nucleosynthesis, and Yields of AGB Stars at Different Metallicities. III. Intermediate-mass Models, Revised Low-mass Models, and the ph-FRUITY Interface. *ApJS*, 219(2):40, Aug. 2015.

S. Curtis, K. Ebinger, C. Fröhlich, M. Hempel, et al. PUSHing Core-collapse Supernovae to Explosions in Spherical Symmetry. III. Nucleosynthesis Yields. *The Astrophysical Journal*, 870(1):2, dec 2018.

R. H. Cyburt, A. M. Amthor, R. Ferguson, Z. Meisel, et al. THE JINA REACLIB DATABASE: ITS RECENT UPDATES AND IMPACT ON TYPE-I X-RAY BURSTS. *The Astrophysical Journal Supplement Series*, 189(1):240–252, jun 2010.

U. Das and B. Mukhopadhyay. New Mass Limit for White Dwarfs: Super-Chandrasekhar Type Ia Supernova as a New Standard Candle. *Physical Review Letters*, 110(7):071102, Feb. 2013.

P. Dave, R. Kashyap, R. Fisher, F. Timmes, et al. Constraining the Single-degenerate Channel of Type Ia Supernovae with Stable Iron-group Elements in SNR 3C 397. *ApJ*, 841(1):58, May 2017.

K. De, M. M. Kasliwal, A. Polin, P. E. Nugent, et al. ZTF 18aaqeasu (SN2018byg): A Massive Helium-shell Double Detonation on a Sub-Chandrasekhar-mass White Dwarf. *ApJ*, 873(2): L18, mar 2019.

T. J. L. de Boer, V. Belokurov, T. C. Beers, and Y. S. Lee. The α-element knee of the Sagittarius stream. *MNRAS*, 443(1):658–663, Sept. 2014.

C. J. Deloye and L. Bildsten. Gravitational Settling of ^{22}Ne in Liquid White Dwarf Interiors: Cooling and Seismological Effects. *ApJ*, 580(2):1077–1090, Dec. 2002.

G. Dimitriadis, M. Sullivan, W. Kerzendorf, A. J. Ruiter, et al. The late-time light curve of the Type Ia supernova SN 2011fe. *MNRAS*, 468(4):3798–3812, July 2017.

K. Dolag, F. Vazza, G. Brunetti, and G. Tormen. Turbulent gas motions in galaxy cluster simulations: the role of smoothed particle hydrodynamics viscosity. *MNRAS*, 364(3):753–772, Dec. 2005.

W. Döring. Über den Detonationsvorgang in Gasen. *Annalen der Physik*, 435:421–436, 1943.

P. Eitner, M. Bergemann, C. J. Hansen, G. Cescutti, et al. Observational constraints on the origin of the elements-III. Evidence for the dominant role of sub-Chandrasekhar SN Ia in the chemical evolution of Mn and Fe in the Galaxy. *Astronomy & Astrophysics*, 635:A38, 2020.

E. Farag, F. X. Timmes, M. Taylor, K. M. Patton, et al. On Stellar Evolution in a Neutrino Hertzsprung-Russell Diagram. *ApJ*, 893(2):133, Apr. 2020.

W. Fickett and C. Davis. *Detonation*. Los Alamos Series in Basic and Applied Sciences. University of California Press, 1979.

A. V. Filippenko. Optical Spectra of Supernovae. *ARA&A*, 35:309–355, 1997.

M. Fink, W. Hillebrandt, and F. K. Röpke. Double-detonation supernovae of sub-Chandrasekhar mass white dwarfs. *A&A*, 476:1133–1143, Dec. 2007.

M. Fink, F. K. Röpke, W. Hillebrandt, I. R. Seitenzahl, et al. Double-detonation sub-Chandrasekhar supernovae: can minimum helium shell masses detonate the core? *A&A*, 514:A53, May 2010.

M. Fink, F. K. Röpke, S. A. Sim, M. Kromer, et al. Sub-Chandrasekhar models for Type Ia supernovae and astrophysical transients. In *Proceedings of Science*, page PoS(NIC XII)050, 2013.

M. Fink, M. Kromer, I. R. Seitenzahl, F. Ciaraldi-Schoolmann, et al. Three-dimensional pure deflagration models with nucleosynthesis and synthetic observables for Type Ia supernovae. *MNRAS*, 438:1762–1783, Feb. 2014.

R. Fisher and K. Jumper. Single-degenerate Type Ia Supernovae Are Preferentially Overluminous. *ApJ*, 805(2):150, June 2015.

A. Flörs, J. Spyromilio, S. Taubenberger, S. Blondin, et al. Sub-Chandrasekhar progenitors favoured for Type Ia supernovae: evidence from late-time spectroscopy. *Monthly Notices of the Royal Astronomical Society*, 491(2):2902–2918, 11 2019. ISSN 0035-8711.

R. J. Foley, P. J. Challis, R. Chornock, M. Ganeshalingam, et al. Type Iax Supernovae: A New Class of Stellar Explosion. *ApJ*, 767:57, Apr. 2013.

R. Forcada. Edge-lit double detonation in Subchandrasekhar-mass models for Type Ia supernovae. In *Supernovae: lights in the darkness*, 2007.

R. Forcada, D. Garcia-Senz, and J. José. Single point off-center helium ignitions as origin of some Type Ia supernovae. In *International Symposium on Nuclear Astrophysics - Nuclei in the Cosmos*, 2006.

B. A. Fryxell, E. Müller, and W. D. Arnett. Hydrodynamics and nuclear burning. MPA Green Report 449, Max-Planck-Institut für Astrophysik, Garching, 1989.

H. O. U. Fynbo, C. A. Diget, U. C. Bergmann, M. J. G. Borge, et al. Revised rates for the stellar triple-α process from measurement of ^{12}C nuclear resonances. *Nature*, 433(7022):136–139, Jan 2005.

Gaia Collaboration, T. Prusti, J. H. J. de Bruijne, A. G. A. Brown, et al. The Gaia mission. *A&A*, 595:A1, Nov. 2016.

Gaia Collaboration, A. G. A. Brown, A. Vallenari, T. Prusti, et al. Gaia Data Release 2. Summary of the contents and survey properties. *A&A*, 616:A1, Aug. 2018.

L. Galbany, C. Ashall, P. Höflich, S. González-Gaitán, et al. Evidence for a Chandrasekhar-mass explosion in the Ca-strong 1991bg-like type Ia supernova 2016hnk. *A&A*, 630:A76, Oct 2019.

E. E. E. Gall, S. Taubenberger, M. Kromer, S. A. Sim, et al. Interpreting the near-infrared spectra of the 'golden standard' Type Ia supernova 2005cf. *MNRAS*, 427:994–1003, Dec. 2012.

V. N. Gamezo, A. M. Khokhlov, E. S. Oran, A. Y. Chtchelkanova, et al. Thermonuclear Supernovae: Simulations of the Deflagration Stage and Their Implications. *Science*, 299:77–81, Jan. 2003.

V. N. Gamezo, A. M. Khokhlov, and E. S. Oran. Three-dimensional Delayed-Detonation Model of Type Ia Supernovae. *ApJ*, 623:337–346, Apr. 2005.

E. García-Berro, L. G. Althaus, A. H. Córsico, and J. Isern. Gravitational Settling of ^{22}Ne and White Dwarf Evolution. *ApJ*, 677(1):473–482, Apr. 2008.

D. García-Senz and E. Bravo. Type Ia Supernova models arising from different distributions of igniting points. *A&A*, 430:585–602, Feb. 2005.

D. García-Senz, E. Bravo, and S. E. Woosley. Single and multiple detonations in white dwarfs. *A&A*, 349:177–188, Sept. 1999.

D. García-Senz, R. M. Cabezón, and I. Domínguez. Surface and Core Detonations in Rotating White Dwarfs. *ApJ*, 862(1):27, Jul 2018.

A. Gautschy. Helium Ignition in the Cores of Low-Mass Stars. *arXiv e-prints*, art. arXiv:1208.3870, Aug. 2012.

R. A. Gingold and J. J. Monaghan. Smoothed particle hydrodynamics - Theory and application to non-spherical stars. *MNRAS*, 181:375–389, Nov. 1977.

S. A. Glasner, E. Livne, E. Steinberg, A. Yalinewich, et al. Ignition of detonation in accreted helium envelopes. *MNRAS*, 476(2):2238–2248, May 2018.

G. Goldhaber, D. E. Groom, A. Kim, G. Aldering, et al. Timescale Stretch Parameterization of Type Ia Supernova B-Band Light Curves. *ApJ*, 558:359–368, Sept. 2001.

K. M. Górski, E. Hivon, A. J. Banday, B. D. Wandelt, et al. HEALPix: A Framework for High-Resolution Discretization and Fast Analysis of Data Distributed on the Sphere. *ApJ*, 622:759–771, Apr. 2005.

R. G. Gratton and C. Sneden. Light element and NI abundance in field disk and halo stars. *A&A*, 178:179–193, May 1987.

R. G. Gratton and C. Sneden. Abundances in extremely metal-poor stars. *A&A*, 204:193–218, Oct. 1988.

R. G. Gratton and C. Sneden. Abundances of elements of the Fe-group in metal-poor stars. *A&A*, 241:501–525, Jan. 1991.

O. Graur and T. E. Woods. Progenitor constraints on the Type Ia supernova SN 2014J from Hubble Space Telescope H β and [O III] observations. *MNRAS*, 484(1):L79–L84, Mar. 2019.

O. Graur, D. Zurek, M. M. Shara, A. G. Riess, et al. Late-time Photometry of Type Ia Supernova SN 2012cg Reveals the Radioactive Decay of ^{57}Co. *ApJ*, 819:31, Mar. 2016.

D. A. Green and F. R. Stephenson. Historical Supernovae. In K. W. Weiler, editor, *Supernovae and Gamma-Ray Bursters*, volume 598 of *Lecture Notes in Physics*, pages 7–19, Berlin Heidelberg New York, 2003. Springer-Verlag.

L. Greggio and A. Renzini. The binary model for type I supernovae - Theoretical rates. *A&A*, 118:217–222, Feb. 1983.

S. Gronow, C. Collins, S. T. Ohlmann, R. Pakmor, et al. SNe Ia from double detonations: Impact of core-shell mixing on the carbon ignition mechanism. *A&A*, 635:A169, Mar. 2020.

S. Gronow, C. E. Collins, S. A. Sim, and F. K. Röpke. Double detonations of sub-Chandrasekhar mass CO white dwarfs: Can different core and He shell masses explain variations of Type Ia supernovae? *arXiv e-prints*, art. arXiv:2102.06719, Feb. 2021a. accepted by *A&A*.

S. Gronow, B. Côté, F. Lach, I. R. Seitenzahl, et al. Metallicity-dependent nucleosynthetic yields of Type Ia supernovae originating from double detonations of sub-M_{Ch} white dwarfs. *arXiv e-prints*, art. arXiv:2103.14050, Mar. 2021b. submitted to *A&A*.

J. Guillochon, M. Dan, E. Ramirez-Ruiz, and S. Rosswog. Surface Detonations in Double Degenerate Binary Systems Triggered by Accretion Stream Instabilities. *ApJ*, 709:L64–L69, Jan. 2010.

C. Hayashi and R. C. Cameron. The Evolution of Massive Stars. III. Hydrogen Exhaustion Through the Onset of Carbon-Burning. *ApJ*, 136:166, July 1962.

B. Hendricks, A. Koch, G. A. Lanfranchi, C. Boeche, et al. The Metal-poor Knee in the Fornax Dwarf Spheroidal Galaxy. *ApJ*, 785(2):102, Apr. 2014.

W. Hillebrandt and J. C. Niemeyer. Type Ia Supernova Explosion Models. *ARA&A*, 38:191–230, 2000.

W. R. Hix and F. Thielemann. Silicon Burning. II. Quasi-Equilibrium and Explosive Burning. *ApJ*, 511:862–875, Feb. 1999.

P. Hoeflich, J. C. Wheeler, and A. Khokhlov. Hard X-Rays and Gamma Rays from Type IA Supernovae. *ApJ*, 492:228, Jan. 1998.

P. Höflich and A. Khokhlov. Explosion Models for Type Ia Supernovae: A Comparison with Observed Light Curves, Distances, H_0, and q_0. *ApJ*, 457:500–528, Feb. 1996.

P. Höflich, A. Khokhlov, J. C. Wheeler, M. M. Phillips, et al. Maximum Brightness and Post-maximum Decline of Light Curves of Type IA Supernovae: A Comparison of Theory and Observations. *ApJ*, 472:L81–L84, Dec. 1996.

P. Höflich, J. C. Wheeler, and F. K. Thielemann. Type Ia Supernovae: Influence of the Initial Composition on the Nucleosynthesis, Light Curves, and Spectra and Consequences for the Determination of Omega M and Lambda. *ApJ*, 495:617–629, Mar. 1998.

C. Holcomb, J. Guillochon, F. De Colle, and E. Ramirez-Ruiz. Conditions for Successful Helium Detonations in Astrophysical Environments. *ApJ*, 771:14, July 2013.

W. M. Howard, S. Goriely, M. Rayet, and M. Arnould. Nuclear statistical equilibrium, neutron-rich α-rich freeze out and the r-process. In *Nuclei in the Cosmos 2*, pages 607–612, Jan. 1993.

D. A. Howell, M. Sullivan, P. E. Nugent, R. S. Ellis, et al. The type Ia supernova SNLS-03D3bb from a super-Chandrasekhar-mass white dwarf star. *Nature*, 443:308–311, Sept. 2006.

F. Hoyle and W. A. Fowler. Nucleosynthesis in Supernovae. *ApJ*, 132:565–590, Nov. 1960.

J. D. Hunter. Matplotlib: A 2D Graphics Environment. *Computing in Science & Engineering*, 9(3):90–95, 2007.

I. Iben, Jr. and A. V. Tutukov. Supernovae of type I as end products of the evolution of binaries with components of moderate initial mass (M not greater than about 9 solar masses). *ApJS*, 54:335–372, Feb. 1984.

I. Iben, Jr., K. Nomoto, A. Tornambe, and A. V. Tutukov. On interacting helium star-white dwarf pairs as supernova precursors. *ApJ*, 317:717–723, June 1987.

J. Iben, I. and A. Renzini. Asymptotic giant branch evolution and beyond. *ARA&A*, 21:271–342, Jan. 1983.

J. Iben, Icko. Stellar Evolution Within and off the Main Sequence. *ARA&A*, 5:571, Jan. 1967.

K. Iwamoto, F. Brachwitz, K. Nomoto, N. Kishimoto, et al. Nucleosynthesis in Chandrasekhar Mass Models for Type Ia Supernovae and Constraints on Progenitor Systems and Burning-Front Propagation. *ApJS*, 125:439–462, Dec. 1999.

J.-A. Jiang, M. Doi, K. Maeda, T. Shigeyama, et al. A hybrid type Ia supernova with an early flash triggered by helium-shell detonation. *Nature*, 550:80–83, Oct. 2017.

F. M. Jiménez-Esteban, S. Torres, A. Rebassa-Mansergas, G. Skorobogatov, et al. A white dwarf catalogue from Gaia-DR2 and the Virtual Observatory. *MNRAS*, 480(4):4505–4518, Nov. 2018.

G. C. Jordan, IV, H. B. Perets, R. T. Fisher, and D. R. van Rossum. Failed-detonation Supernovae: Subluminous Low-velocity Ia Supernovae and their Kicked Remnant White Dwarfs with Iron-rich Cores. *ApJ*, 761:L23, Dec. 2012.

Jülich Supercomputing Centre. JUWELS: Modular Tier-0/1 Supercomputer at the Jülich Supercomputing Centre. *Journal of large-scale research facilities*, 5(A135), 2019.

D. Kasen, F. K. Röpke, and S. E. Woosley. The diversity of type Ia supernovae from broken symmetries. *Nature*, 460:869–872, Aug. 2009.

R. Kashyap, R. Fisher, E. García-Berro, G. Aznar-Siguán, et al. Spiral Instability Can Drive Thermonuclear Explosions in Binary White Dwarf Mergers. *ApJ*, 800:L7, Feb. 2015.

M. P. Katz and M. Zingale. Numerical Stability of Detonations in White Dwarf Simulations. *ApJ*, 874(2):169, Apr. 2019.

S. J. Kenyon, M. Livio, J. Mikolajewska, and C. A. Tout. On Symbiotic Stars and Type IA Supernovae. *ApJ*, 407:L81, Apr. 1993.

A. M. Khokhlov. Explosive Helium Burning in White Dwarfs. *Soviet Astronomy Letters*, 10: 123–126, Feb. 1984.

A. M. Khokhlov. Hugoniot adiabates for the waves of combustion in degenerate matter of supernovae. *Ap&SS*, 149:91–106, Nov. 1988.

A. M. Khokhlov. The structure of detonation waves in supernovae. *MNRAS*, 239:785–808, Aug. 1989.

A. M. Khokhlov. Delayed detonation model for type Ia supernovae. *A&A*, 245:114–128, May 1991.

A. M. Khokhlov and É. V. Érgma. Explosive He^4 burning: I - Kinetics of burning at constant temperature and density. *Astrofizika*, 23:605–619, Nov. 1985.

R. Kippenhahn, A. Weigert, and A. Weiss. *Stellar Structure and Evolution*. Springer-Verlag, Berlin Heidelberg, 2012. ISBN 978-3-642-30255-8.

S. J. Kleinman, S. O. Kepler, D. Koester, I. Pelisoli, et al. SDSS DR7 White Dwarf Catalog. *ApJS*, 204(1):5, Jan. 2013.

C. Kobayashi, S.-C. Leung, and K. Nomoto. New Type Ia Supernova Yields and the Manganese and Nickel Problems in the Milky Way and Dwarf Spheroidal Galaxies. *ApJ*, 895(2):138, June 2020.

D. Koester and G. Chanmugam. Physics of white dwarf stars. *Reports on Progress in Physics*, 53:837–915, July 1990.

K. Krisciunas, N. B. Suntzeff, P. Candia, J. Arenas, et al. Optical and Infrared Photometry of the Nearby Type Ia Supernova 2001el. *AJ*, 125:166–180, Jan. 2003.

M. Kromer and S. A. Sim. Time-dependent three-dimensional spectrum synthesis for Type Ia supernovae. *MNRAS*, 398:1809–1826, Aug. 2009.

M. Kromer, S. A. Sim, M. Fink, F. K. Röpke, et al. Double-detonation Sub-Chandrasekhar Supernovae: Synthetic Observables for Minimum Helium Shell Mass Models. *ApJ*, 719:1067–1082, Aug. 2010.

M. Kromer, M. Fink, V. Stanishev, S. Taubenberger, et al. 3D deflagration simulations leaving bound remnants: a model for 2002cx-like Type Ia supernovae. *MNRAS*, 429:2287–2297, Mar. 2013.

D. Kushnir and B. Katz. An accurate and efficient numerical calculation of detonation waves in multidimensional supernova simulations using a burning limiter and adaptive quasi-statistical equilibrium. *MNRAS*, 493(4):5413–5433, Apr. 2020.

D. Kushnir, N. Wygoda, and A. Sharon. Sub-Chandrasekhar-mass detonations are in tension with the observed t_0-M_{Ni56} relation of type Ia supernovae. *MNRAS*, 499(4):4725–4747, Oct. 2020.

F. Lach, F. K. Roepke, I. R. Seitenzahl, B. Coté, et al. Nucleosynthesis imprints from different Type Ia Supernova explosion scenarios and implications for galactic chemical evolution. *A&A*, 644:A118, Dec. 2020.

L. Landau and E. M. Lifschitz. Lehrbuch der Theoretischen Physik, Band X.: Physikalische Kinetik. *Berlin: Akademie-Verlag*, 1983.

L. Landau and E. M. Lifschitz. Lehrbuch der theoretischen Physik, Vol. 6, Hydrodynamik. *Frankfurt am Main: Harri Deutsch Verlag*, 2007.

L. D. Landau and E. M. Lifshitz. *Fluid Mechanics (Course of Theoretical Physics: Volume 6)*. Butterworth-Heinemann, Oxford, 2 edition, January 1987. ISBN 0750627670.

K. Langanke and G. Martínez-Pinedo. Rate Tables for the Weak Processes of pf-SHELL Nuclei in Stellar Environments. *Atomic Data and Nuclear Data Tables*, 79:1–46, Sept. 2001.

E. J. Lentz, E. Baron, D. Branch, P. H. Hauschildt, et al. Metallicity Effects in Non-LTE Model Atmospheres of Type IA Supernovae. *ApJ*, 530:966–976, Feb. 2000.

S.-C. Leung and K. Nomoto. Explosive Nucleosynthesis in Sub-Chandrasekhar-mass White Dwarf Models for Type Ia Supernovae: Dependence on Model Parameters. *The Astrophysical Journal*, 888(2):80, jan 2020.

R. J. LeVeque. Nonlinear Conservation Laws and Finite Volume Methods. In O. Steiner and A. Gautschy, editors, *Computational Methods for Astrophysical Flows*, Saas-Fee Advanced Course 27, pages 1–159. Springer, Berlin Heidelberg New York, 1998.

C.-J. Li, W. E. Kerzendorf, Y.-H. Chu, T.-W. Chen, et al. Search for Surviving Companions of Progenitors of Young LMC SN Ia Remnants. *ApJ*, 886(2):99, Dec. 2019a.

W. Li, A. V. Filippenko, R. Chornock, E. Berger, et al. SN 2002cx: The Most Peculiar Known Type Ia Supernova. *PASP*, 115:453–473, Apr. 2003.

W. Li, R. Chornock, J. Leaman, A. V. Filippenko, et al. Nearby supernova rates from the Lick Observatory Supernova Search - III. The rate-size relation, and the rates as a function of galaxy Hubble type and colour. *MNRAS*, 412:1473–1507, Apr. 2011a.

W. Li, J. Leaman, R. Chornock, A. V. Filippenko, et al. Nearby supernova rates from the Lick Observatory Supernova Search – II. The observed luminosity functions and fractions of supernovae in a complete sample. *MNRAS*, 412:1441–1472, Apr. 2011b.

W. Li, X. Wang, M. Hu, Y. Yang, et al. Observations of Type Ia Supernova 2014J for Nearly 900 Days and Constraints on Its Progenitor System. *ApJ*, 882(1):30, Sept. 2019b.

M. Limongi and A. Chieffi. Presupernova Evolution and Explosive Nucleosynthesis of Rotating Massive Stars in the Metallicity Range$-3 \leq [Fe/H] \leq 0$. *The Astrophysical Journal Supplement Series*, 237(1):13, 2018.

P. Lira, N. B. Suntzeff, M. M. Phillips, M. Hamuy, et al. Optical light curves of the Type IA supernovae SN 1990N and 1991T. *AJ*, 115:234–+, Jan. 1998.

D. Liu, B. Wang, and Z. Han. The double-degenerate model for the progenitors of Type Ia supernovae. *MNRAS*, 473(4):5352–5361, Feb. 2018.

M. Livio and P. Mazzali. On the progenitors of Type Ia supernovae. *Phys. Rep.*, 736:1–23, Mar. 2018.

E. Livne. Successive detonations in accreting white dwarfs as an alternative mechanism for type I supernovae. *ApJ*, 354:L53–L55, May 1990.

E. Livne. Numerical simulations of the convective flame in white dwarfs. *ApJ*, 406:L17–L20, Mar. 1993.

E. Livne and D. Arnett. Explosions of Sub-Chandrasekhar Mass White Dwarfs in Two Dimensions. *ApJ*, 452:62–74, Oct. 1995.

E. Livne and A. S. Glasner. Geometrical effects in off-center detonation of helium shells. *ApJ*, 361:244–250, Sept. 1990.

E. Livne and A. S. Glasner. Numerical simulations of off-center detonations in helium shells. *ApJ*, 370:272–281, Mar. 1991.

M. Long, I. Jordan, George C., D. R. van Rossum, B. Diemer, et al. Three-dimensional Simulations of Pure Deflagration Models for Thermonuclear Supernovae. *ApJ*, 789(2):103, July 2014.

L. B. Lucy. Monte Carlo transition probabilities. *A&A*, 384:725–735, Mar. 2002.

L. B. Lucy. Monte Carlo transition probabilities. II. *A&A*, 403:261–275, May 2003.

L. B. Lucy. Monte Carlo techniques for time-dependent radiative transfer in 3-D supernovae. *A&A*, 429:19–30, Jan. 2005.

P. Magain. The chemical composition of the extreme halo stars. I. Blue spectra of 20 dwarfs. *A&A*, 209:211–225, Jan. 1989.

D. Maoz and O. Graur. Star Formation, Supernovae, Iron, and α: Consistent Cosmic and Galactic Histories. *ApJ*, 848:25, Oct. 2017.

D. Maoz, F. Mannucci, and G. Nelemans. Observational Clues to the Progenitors of Type Ia Supernovae. *ARA&A*, 52:107–170, Aug. 2014.

K. S. Marquardt, S. A. Sim, A. J. Ruiter, I. R. Seitenzahl, et al. Type Ia supernovae from exploding oxygen-neon white dwarfs. *A&A*, 580:A118, Aug. 2015.

R. E. Marshak. The Internal Temperature of White Dwarf Stars. *ApJ*, 92:321, Nov. 1940.

T. Matheson, R. P. Kirshner, P. Challis, S. Jha, et al. Optical Spectroscopy of Type ia Supernovae. *AJ*, 135(4):1598–1615, Apr. 2008.

F. Matteucci. The evolution of the alpha-elements in galaxies. *Mem. Soc. Astron. Italiana*, 63 (2):301–314, Jan. 1992.

F. Matteucci and L. Greggio. Relative roles of type I and II supernovae in the chemical enrichment of the interstellar gas. *A&A*, 154:279–287, Jan. 1986.

C. McCully, S. W. Jha, R. J. Foley, L. Bildsten, et al. A luminous, blue progenitor system for the type Iax supernova 2012Z. *Nature*, 512:54–56, Aug. 2014.

A. McWilliam. Abundance Ratios and Galactic Chemical Evolution. *ARA&A*, 35:503–556, 1997.

R. Minkowski. Spectra of Supernovae. *PASP*, 53:224–225, Aug. 1941.

N. L. Mitchell, I. G. McCarthy, R. G. Bower, T. Theuns, et al. On the origin of cores in simulated galaxy clusters. *MNRAS*, 395(1):180–196, May 2009.

R. Moll and S. E. Woosley. Multi-dimensional Models for Double Detonation in Sub-Chandrasekhar Mass White Dwarfs. *ApJ*, 774:137, Sept. 2013.

C. J. Moore, R. H. Cole, and C. P. L. Berry. Gravitational-wave sensitivity curves. *Classical and Quantum Gravity*, 32(1):015014, Jan. 2015.

E. Müller. Simulation of Astrophysical Fluid Flow. In O. Steiner and A. Gautschy, editors, *Computational Methods for Astrophysical Flows*, Saas-Fee Advanced Course 27, pages 343–494. Springer, Berlin Heidelberg New York, 1998.

R. Napiwotzki. The galactic population of white dwarfs. In *Journal of Physics Conference Series*, volume 172 of *Journal of Physics Conference Series*, page 012004, June 2009.

P. Neunteufel, S. C. Yoon, and N. Langer. Models for the evolution of close binaries with He-star and white dwarf components towards Type Ia supernova explosions. *A&A*, 589:A43, May 2016.

P. Neunteufel, S.-C. Yoon, and N. Langer. Helium ignition in rotating magnetized CO white dwarfs leading to fast and faint rather than classical Type Ia supernovae. *A&A*, 602:A55, June 2017.

J. C. Niemeyer and W. Hillebrandt. Turbulent Nuclear Flames in Type Ia Supernovae. *ApJ*, 452:769–778, Oct. 1995.

U. M. Noebauer, M. Kromer, S. Taubenberger, P. Baklanov, et al. Early light curves for Type Ia supernova explosion models. *MNRAS*, 472:2787–2799, Dec. 2017.

K. Nomoto. Accreting white dwarf models for type I supernovae. I. Presupernova evolution and triggering mechanisms. *ApJ*, 253:798–810, Feb. 1982a.

K. Nomoto. Accreting white dwarf models for type I supernovae. II. Off-center detonation supernovae. *ApJ*, 257:780–792, June 1982b.

K. Nomoto, D. Sugimoto, and S. Neo. Carbon deflagration supernova, an alternative to carbon detonation. *Ap&SS*, 39:L37–L42, Feb. 1976.

K. Nomoto, F.-K. Thielemann, and K. Yokoi. Accreting white dwarf models of Type I supernovae. III. Carbon deflagration supernovae. *ApJ*, 286:644–658, Nov. 1984.

K. Nomoto, C. Kobayashi, and N. Tominaga. Nucleosynthesis in Stars and the Chemical Enrichment of Galaxies. *ARA&A*, 51(1):457–509, Aug. 2013.

P. Nugent, E. Baron, D. Branch, A. Fisher, et al. Synthetic Spectra of Hydrodynamic Models of Type IA Supernovae. *ApJ*, 485:812–819, Aug. 1997.

P. E. Nugent, M. Sullivan, S. B. Cenko, R. C. Thomas, et al. Supernova SN 2011fe from an exploding carbon-oxygen white dwarf star. *Nature*, 480:344–347, Dec. 2011.

T. Ohkubo, H. Umeda, K. Nomoto, and T. Yoshida. Nucleosynthesis by Type Ia Supernova for different Metallicity. In S. Kubono, W. Aoki, T. Kajino, T. Motobayashi, et al., editors, *Origin of Matter and Evolution of Galaxies*, volume 847 of *American Institute of Physics Conference Series*, pages 458–460, July 2006.

S. T. Ohlmann, M. Kromer, M. Fink, R. Pakmor, et al. The white dwarf's carbon fraction as a secondary parameter of Type Ia supernovae. *A&A*, 572:A57, 2014.

S. T. Ohlmann, F. K. Röpke, R. Pakmor, and V. Springel. Constructing stable 3D hydrodynamical models of giant stars. *A&A*, 599:A5, Mar. 2017.

T. E. Oliphant. Python for Scientific Computing. *Computing in Science & Engineering*, 9(3): 10–20, 2007.

R. Pakmor, M. Kromer, F. K. Röpke, S. A. Sim, et al. Sub-luminous type Ia supernovae from the mergers of equal-mass white dwarfs with mass ~0.9$M_\odot$. *Nature*, 463:61–64, Jan. 2010.

R. Pakmor, S. Hachinger, F. K. Röpke, and W. Hillebrandt. Violent mergers of nearly equal-mass white dwarf as progenitors of subluminous Type Ia supernovae. *A&A*, 528:A117+, Apr. 2011.

R. Pakmor, P. Edelmann, F. K. Röpke, and W. Hillebrandt. Stellar GADGET: a smoothed particle hydrodynamics code for stellar astrophysics and its application to Type Ia supernovae from white dwarf mergers. *MNRAS*, 424:2222–2231, Aug. 2012a.

R. Pakmor, M. Kromer, S. Taubenberger, S. A. Sim, et al. Normal Type Ia Supernovae from Violent Mergers of White Dwarf Binaries. *ApJ*, 747:L10, Mar. 2012b.

R. Pakmor, M. Kromer, S. Taubenberger, and V. Springel. Helium-ignited Violent Mergers as a Unified Model for Normal and Rapidly Declining Type Ia Supernovae. *ApJ*, 770:L8, June 2013.

R. Pakmor, V. Springel, A. Bauer, P. Mocz, et al. Improving the convergence properties of the moving-mesh code AREPO. *MNRAS*, 455(1):1134–1143, Jan 2016.

R. Pakmor, Y. Zenati, H. B. Perets, and S. Toonen. Thermonuclear explosion of a massive hybrid HeCO white-dwarf triggered by a He-detonation on a companion. *MNRAS*, Mar. 2021.

B. Paxton, L. Bildsten, A. Dotter, F. Herwig, et al. Modules for Experiments in Stellar Astrophysics (MESA). *ApJS*, 192:3, Jan. 2011.

B. Paxton, M. Cantiello, P. Arras, L. Bildsten, et al. Modules for Experiments in Stellar Astrophysics (MESA): Planets, Oscillations, Rotation, and Massive Stars. *ApJS*, 208:4, Sept. 2013.

B. Paxton, P. Marchant, J. Schwab, E. B. Bauer, et al. Modules for Experiments in Stellar Astrophysics (MESA): Binaries, Pulsations, and Explosions. *ApJS*, 220:15, Sept. 2015.

B. Paxton, J. Schwab, E. B. Bauer, L. Bildsten, et al. Modules for Experiments in Stellar Astrophysics (MESA): Convective Boundaries, Element Diffusion, and Massive Star Explosions. *ApJS*, 234:34, feb 2018.

B. Paxton, R. Smolec, J. Schwab, A. Gautschy, et al. Modules for Experiments in Stellar Astrophysics (MESA): Pulsating Variable Stars, Rotation, Convective Boundaries, and Energy Conservation. *ApJS*, 243(1):10, Jul 2019.

R. Pereira, R. C. Thomas, G. Aldering, P. Antilogus, et al. Spectrophotometric time series of SN 2011fe from the Nearby Supernova Factory. *A&A*, 554:A27, June 2013.

F. Pérez and B. E. Granger. IPython: A System for Interactive Scientific Computing. *Computing in Science & Engineering*, 9(3):21–29, 2007.

S. Perlmutter and B. P. Schmidt. *Measuring Cosmology with Supernovae*, volume 598, pages 195–217. 2003.

S. Perlmutter, G. Aldering, G. Goldhaber, R. A. Knop, et al. Measurements of Omega and Lambda from 42 High-Redshift Supernovae. *ApJ*, 517:565–586, June 1999.

M. M. Phillips. The absolute magnitudes of Type Ia supernovae. *ApJ*, 413:L105–L108, Aug. 1993.

M. M. Phillips, P. Lira, N. B. Suntzeff, R. A. Schommer, et al. The Reddening-Free Decline Rate Versus Luminosity Relationship for Type Ia Supernovae. *AJ*, 118:1766–1776, Oct. 1999.

P. A. Pinto and R. G. Eastman. The Physics of Type Ia Supernova Light Curves. I. Analytic Results and Time Dependence. *ApJ*, 530:744–756, Feb. 2000.

A. L. Piro, T. A. Thompson, and C. S. Kochanek. Reconciling ^{56}Ni production in Type Ia supernovae with double degenerate scenarios. *MNRAS*, 438(4):3456–3464, Mar. 2014.

A. Polin, P. Nugent, and D. Kasen. Observational Predictions for Sub-Chandrasekhar Mass Explosions: Further Evidence for Multiple Progenitor Systems for Type Ia Supernovae. *ApJ*, 873(1):84, Mar. 2019.

O. R. Pols, C. A. Tout, J. C. Lattanzio, and A. I. Karakas. Thermal Pulses and Dredge-up in AGB Stars. In P. Podsiadlowski, S. Rappaport, A. R. King, F. D'Antona, et al., editors, *Evolution of Binary and Multiple Star Systems*, volume 229 of *Astronomical Society of the Pacific Conference Series*, page 31, Jan. 2001.

N. Prantzos, C. Abia, M. Limongi, A. Chieffi, et al. Chemical evolution with rotating massive star yields–I. The solar neighbourhood and the s-process elements. *Monthly Notices of the Royal Astronomical Society*, 476(3):3432–3459, 2018.

T. Rauscher and F.-K. Thielemann. Astrophysical Reaction Rates From Statistical Model Calculations. *Atomic Data and Nuclear Data Tables*, 75:1–2, May 2000.

A. Rebassa-Mansergas, S. Toonen, V. Korol, and S. Torres. Where are the double-degenerate progenitors of Type Ia supernovae? *MNRAS*, 482(3):3656–3668, Jan. 2019.

M. Reinecke, W. Hillebrandt, and J. C. Niemeyer. Three-dimensional simulations of type Ia supernovae. *A&A*, 391:1167–1172, Sept. 2002.

A. G. Riess, A. V. Filippenko, P. Challis, A. Clocchiatti, et al. Observational Evidence from Supernovae for an Accelerating Universe and a Cosmological Constant. *AJ*, 116:1009–1038, Sept. 1998.

A. G. Riess, A. V. Filippenko, W. Li, R. R. Treffers, et al. The Rise Time of Nearby Type Ia Supernovae. *AJ*, 118:2675–2688, Dec. 1999.

C. Ritter, B. Côté, F. Herwig, J. F. Navarro, et al. SYGMA: Stellar Yields for Galactic Modeling Applications. *ApJS*, 237(2):42, Aug. 2018.

F. K. Röpke. Multi-dimensional numerical simulations of type Ia supernova explosions. In S. Röser, editor, *Reviews in Modern Astronomy*, volume 19 of *Reviews in Modern Astronomy*, pages 127–156, Jan. 2006.

F. K. Röpke. Flame-driven Deflagration-to-Detonation Transitions in Type Ia Supernovae? *ApJ*, 668:1103–1108, Oct. 2007.

F. K. Röpke. Combustion in thermonuclear supernova explosions. In A. Alsabti and P. Murdin, editors, *Handbook of Supernovae*, pages 1185–1209. Springer, Mar. 2017.

F. K. Röpke and J. C. Niemeyer. Delayed detonations in full-star models of type Ia supernova explosions. *A&A*, 464:683–686, Mar. 2007.

F. K. Röpke, W. Hillebrandt, W. Schmidt, J. C. Niemeyer, et al. A Three-Dimensional Deflagration Model for Type Ia Supernovae Compared with Observations. *ApJ*, 668:1132–1139, Oct. 2007a.

F. K. Röpke, S. E. Woosley, and W. Hillebrandt. Off-Center Ignition in Type Ia Supernovae. I. Initial Evolution and Implications for Delayed Detonation. *ApJ*, 660:1344–1356, May 2007b.

A. J. Ruiter, K. Belczynski, and C. Fryer. Rates and Delay Times of Type Ia Supernovae. *ApJ*, 699:2026–2036, July 2009.

A. J. Ruiter, K. Belczynski, S. A. Sim, W. Hillebrandt, et al. Delay times and rates for Type Ia supernovae and thermonuclear explosions from double-detonation sub-Chandrasekhar mass models. *MNRAS*, 417:408–419, Oct. 2011.

A. J. Ruiter, K. Belczynski, S. A. Sim, I. R. Seitenzahl, et al. The effect of helium accretion efficiency on rates of Type Ia supernovae: double detonations in accreting binaries. *MNRAS*, 440:L101–L105, 2014.

R. Scalzo, G. Aldering, P. Antilogus, C. Aragon, et al. Type Ia supernova bolometric light curves and ejected mass estimates from the Nearby Supernova Factory. *MNRAS*, 440:1498–1518, May 2014.

R. A. Scalzo, E. Parent, C. Burns, M. Childress, et al. Probing type Ia supernova properties using bolometric light curves from the Carnegie Supernova Project and the CfA Supernova Group. *MNRAS*, 483(1):628–647, Feb. 2019.

E. M. Schlegel. A new subclass of type II supernovae ? *MNRAS*, 244:269–271, May 1990.

B. P. Schmidt, N. B. Suntzeff, M. M. Phillips, R. A. Schommer, et al. The High-Z Supernova Search: Measuring Cosmic Deceleration and Global Curvature of the Universe Using Type IA Supernovae. *ApJ*, 507:46–63, Nov. 1998.

I. R. Seitenzahl and D. M. Townsley. *Nucleosynthesis in Thermonuclear Supernovae*, page 1955. 2017.

I. R. Seitenzahl, C. A. Meakin, D. M. Townsley, D. Q. Lamb, et al. Spontaneous Initiation of Detonations in White Dwarf Environments: Determination of Critical Sizes. *ApJ*, 696: 515–527, May 2009.

I. R. Seitenzahl, G. Cescutti, F. K. Röpke, A. J. Ruiter, et al. Solar abundance of manganese: a case for near Chandrasekhar-mass Type Ia supernova progenitors. *A&A*, 559:L5, Nov. 2013a.

I. R. Seitenzahl, F. Ciaraldi-Schoolmann, F. K. Röpke, M. Fink, et al. Three-dimensional delayed-detonation models with nucleosynthesis for Type Ia supernovae. *MNRAS*, 429:1156–1172, Feb. 2013b.

A. Sharon and D. Kushnir. All Known SN Ia Models Fail to Reproduce the Observed t_0-M_{NI56} Correlation. *Research Notes of the American Astronomical Society*, 4(9):158, Sept. 2020.

K. J. Shen and L. Bildsten. Unstable Helium Shell Burning on Accreting White Dwarfs. *ApJ*, 699:1365–1373, July 2009.

K. J. Shen and L. Bildsten. The Ignition of Carbon Detonations via Converging Shock Waves in White Dwarfs. *ApJ*, 785:61, Apr. 2014.

K. J. Shen and K. Moore. The Initiation and Propagation of Helium Detonations in White Dwarf Envelopes. *ApJ*, 797:46, Dec. 2014.

K. J. Shen, D. Kasen, N. N. Weinberg, L. Bildsten, et al. Thermonuclear .Ia Supernovae from Helium Shell Detonations: Explosion Models and Observables. *ApJ*, 715:767–774, June 2010.

K. J. Shen, D. Boubert, B. T. Gänsicke, S. W. Jha, et al. Three Hypervelocity White Dwarfs in Gaia DR2: Evidence for Dynamically Driven Double-degenerate Double-detonation Type Ia Supernovae. *ApJ*, 865:15, Sept. 2018a.

K. J. Shen, D. Kasen, B. J. Miles, and D. M. Townsley. Sub-Chandrasekhar-mass White Dwarf Detonations Revisited. *ApJ*, 854(1):52, Feb. 2018b.

T. Shigeyama, K. Nomoto, H. Yamaoka, and F. Thielemann. Possible models for the type IA supernova 1990N. *ApJ*, 386:L13–L16, Feb. 1992.

H. L. Shipman. Masses and Radii of White Dwarfs. *ApJ*, 177:723, Nov. 1972.

S. N. Shore. *Astrophysical hydrodynamics: an introduction.* WILEY-VCH Verlag, Weinheim, 2 edition, 2007.

S. A. Sim. Multidimensional simulations of radiative transfer in Type Ia supernovae. *MNRAS*, 375:154–162, Feb. 2007.

S. A. Sim, F. K. Röpke, W. Hillebrandt, M. Kromer, et al. Detonations in Sub-Chandrasekhar-mass C+O White Dwarfs. *ApJ*, 714:L52–L57, May 2010.

S. A. Sim, M. Fink, M. Kromer, F. K. Röpke, et al. 2D simulations of the double-detonation model for thermonuclear transients from low-mass carbon–oxygen white dwarfs. *MNRAS*, 420: 3003–3016, Mar. 2012.

S. A. Sim, F. K. Röpke, M. Kromer, M. Fink, et al. Type Ia Supernovae from Sub-Chandrasekhar Mass White Dwarfs. In R. Di Stefano, M. Orio, and M. Moe, editors, *IAU Symposium*, volume 281 of *IAU Symposium*, pages 267–274, Jan. 2013a.

S. A. Sim, I. R. Seitenzahl, M. Kromer, F. Ciaraldi-Schoolmann, et al. Synthetic light curves and spectra for three-dimensional delayed-detonation models of Type Ia supernovae. *MNRAS*, 436:333–347, Nov. 2013b.

V. Springel. E pur si muove: Galilean-invariant cosmological hydrodynamical simulations on a moving mesh. *MNRAS*, 401:791–851, Jan. 2010.

J. M. Stone and M. L. Norman. ZEUS-2D: A Radiation Magnetohydrodynamics Code for Astrophysical Flows in Two Space Dimensions. II. The Magnetohydrodynamic Algorithms and Tests. *ApJS*, 80:791–+, June 1992.

M. Stritzinger, P. A. Mazzali, J. Sollerman, and S. Benetti. Consistent estimates of ^{56}Ni yields for type Ia supernovae. *A&A*, 460:793–798, Dec. 2006.

N. Takanashi, M. Doi, and N. Yasuda. Light-curve studies of nearby Type Ia supernovae with a Multiband Stretch method. *MNRAS*, 389(4):1577–1592, Oct. 2008.

G. A. Tammann, W. Loeffler, and A. Schroeder. The Galactic Supernova Rate. *ApJS*, 92:487, June 1994.

A. Tanikawa, K. Nomoto, and N. Nakasato. Three-dimensional Simulation of Double Detonations in the Double-degenerate Model for Type Ia Supernovae and Interaction of Ejecta with a Surviving White Dwarf Companion. *ApJ*, 868(2):90, Dec. 2018.

S. Taubenberger. The Extremes of Thermonuclear Supernovae. In A. Alsabti and P. Murdin, editors, *Handbook of Supernovae*, pages 317–373. Springer, Mar. 2017.

S. Taubenberger, S. Hachinger, G. Pignata, P. A. Mazzali, et al. The underluminous Type Ia supernova 2005bl and the class of objects similar to SN 1991bg. *MNRAS*, 385:75–96, Mar. 2008.

F.-K. Thielemann, K. Nomoto, and K. Yokoi. Explosive nucleosynthesis in carbon deflagration models of Type I supernovae. *A&A*, 158:17–33, Apr. 1986.

F. K. Thielemann, F. Brachwitz, P. Höflich, G. Martinez-Pinedo, et al. The physics of type Ia supernovae. *NAR*, 48(7-8):605–610, May 2004.

F. X. Timmes and F. D. Swesty. The Accuracy, Consistency, and Speed of an Electron-Positron Equation of State Based on Table Interpolation of the Helmholtz Free Energy. *ApJS*, 126: 501–516, Feb. 2000.

F. X. Timmes, S. E. Woosley, and T. A. Weaver. Galactic chemical evolution: Hydrogen through zinc. *ApJS*, 98:617–658, June 1995.

F. X. Timmes, E. F. Brown, and J. W. Truran. On Variations in the Peak Luminosity of Type Ia Supernovae. *ApJ*, 590:L83–L86, June 2003.

S. Toonen, G. Nelemans, and S. Portegies Zwart. Supernova Type Ia progenitors from merging double white dwarfs. Using a new population synthesis model. *A&A*, 546:A70, Oct. 2012.

E. F. Toro. *Riemann Solvers and Numerical Methods for Fluid Dynamics: A Practical Introduction*. Springer, Berlin Heidelberg, 2009. ISBN 9783540498346.

D. M. Townsley, K. Moore, and L. Bildsten. Laterally Propagating Detonations in Thin Helium Layers on Accreting White Dwarfs. *ApJ*, 755:4, Aug. 2012.

D. M. Townsley, B. J. Miles, F. X. Timmes, A. C. Calder, et al. A Tracer Method for Computing Type Ia Supernova Yields: Burning Model Calibration, Reconstruction of Thickened Flames, and Verification for Planar Detonations. *ApJS*, 225:3, July 2016.

D. M. Townsley, B. J. Miles, K. J. Shen, and D. Kasen. Double Detonations with Thin, Modestly Enriched Helium Layers can Make Normal Type Ia Supernovae. *ApJ*, 878(2):L38, June 2019.

C. Travaglio, W. Hillebrandt, M. Reinecke, and F.-K. Thielemann. Nucleosynthesis in multi-dimensional SN Ia explosions. *A&A*, 425:1029–1040, Oct. 2004.

J. W. Truran, W. D. Arnett, and A. G. W. Cameron. Nucleosynthesis in supernova shock waves. *Can. J. Phys.*, 45:2315–2332, 1967.

A. Tutukov and L. Yungelson. Double-degenerate semidetached binaries with helium secondaries: cataclysmic variables, supersoft X-ray sources, supernovae and accretion-induced collapses. *MNRAS*, 280:1035–1045, June 1996.

H. Umeda, K. Nomoto, H. Yamaoka, and S. Wanajo. Evolution of 3-9 M_solar Stars for Z=0.001-0.03 and Metallicity Effects on Type Ia Supernovae. *ApJ*, 513:861–868, Mar. 1999.

S. van den Bergh and K. W. Kamper. The remnant of Kepler's supernova. *ApJ*, 218:617, Dec. 1977.

B. van Leer. On the Relation Between the Upwind-Differencing Schemes of Godunov, Enguist, Osher and Roe. *SIAM J. Sci. Stat. Comput.*, 5:1, Oct. 1984.

M. Vogelsberger, S. Genel, V. Springel, P. Torrey, et al. Introducing the Illustris Project: simulating the coevolution of dark and visible matter in the Universe. *MNRAS*, 444:1518–1547, Oct. 2014.

J. von Neumann. Theory of detonation waves. Prog. Rept. No. 238; O.S.R.D. Rept. No. 549, Ballistic Research Laboratory File No. X-122, Aberdeen Proving Ground, MD, Aberdeen Proving Ground, MD, 1942.

R. Waldman, D. Sauer, E. Livne, H. Perets, et al. Helium Shell Detonations on Low-mass White Dwarfs as a Possible Explanation for SN 2005E. *ApJ*, 738:21, Sept. 2011.

R. F. Webbink. Double white dwarfs as progenitors of R Coronae Borealis stars and Type I supernovae. *ApJ*, 277:355–360, Feb. 1984.

G. Wegner and S. R. Swanson. Early spectra of the supernova 1987F. *MNRAS*, 278(1):22–38, Jan. 1996.

J. C. Wheeler, C. Sneden, and J. Truran, James W. Abundance ratios as a function of metallicity. *ARA&A*, 27:279–349, Jan. 1989.

J. Whelan and I. J. Iben. Binaries and Supernovae of Type I. *ApJ*, 186:1007–1014, Dec. 1973.

K. D. Wilk, D. J. Hillier, and L. Dessart. Ejecta mass diagnostics of Type Ia supernovae. *MNRAS*, 474(3):3187–3211, Mar 2018.

S. E. Woosley and D. Kasen. Sub-Chandrasekhar Mass Models for Supernovae. *ApJ*, 734:38, June 2011.

S. E. Woosley and T. A. Weaver. Massive stars, supernovae, and nucleosynthesis. In S. A. Bludman, R. Mochkovitch, and J. Zinn-Justin, editors, *Les Houches Session LIV: Supernovae*, pages 63–154, Amsterdam, Jan. 1994a. North-Holland.

S. E. Woosley and T. A. Weaver. Sub-Chandrasekhar mass models for Type Ia supernovae. *ApJ*, 423:371–379, Mar. 1994b.

S. E. Woosley and T. A. Weaver. The Evolution and Explosion of Massive Stars. II. Explosive Hydrodynamics and Nucleosynthesis. *ApJS*, 101:181–+, Nov. 1995.

S. E. Woosley, W. D. Arnett, and D. D. Clayton. The Explosive Burning of Oxygen and Silicon. *ApJS*, 26:231, Nov. 1973.

S. E. Woosley, R. E. Taam, and T. A. Weaver. Models for Type I supernova. I – Detonations in white dwarfs. *ApJ*, 301:601–623, Feb. 1986.

S. E. Woosley, A. R. Kerstein, V. Sankaran, A. J. Aspden, et al. Type Ia Supernovae: Calculations of Turbulent Flames Using the Linear Eddy Model. *ApJ*, 704:255–273, Oct. 2009.

S. E. Woosley, A. R. Kerstein, and A. J. Aspden. Flames in Type Ia Supernova: Deflagration-detonation Transition in the Oxygen-burning Flame. *ApJ*, 734:37–+, June 2011.

N. Wygoda, Y. Elbaz, and B. Katz. Type Ia supernovae have two physical width-luminosity relations and they favour sub-Chandrasekhar and direct collision models - I. Bolometric. *MNRAS*, 484(3):3941–3950, Apr. 2019.

Y. Xu, K. Takahashi, S. Goriely, M. Arnould, et al. NACRE II: an update of the NACRE compilation of charged-particle-induced thermonuclear reaction rates for nuclei with mass number A<16. *Nucl. Phys. A*, 918:61–169, Nov 2013.

S. Yoon, N. Langer, and S. Scheithauer. Effects of rotation on the helium burning shell source in accreting white dwarfs. *A&A*, 425:217–228, Oct. 2004.

L. R. Yungelson. Population synthesis for progenitors of type Ia supernovae. In E. M. Sion, S. Vennes, and H. L. Shipman, editors, *White dwarfs: cosmological and galactic probes*, volume 332 of *Astrophysics and Space Science Library*, pages 163–173, 2005.

Y. B. Zel'dovich. On the theory of the propagation of detonations on gaseous system. *Zh. Eksp. Teor. Fiz.*, 10:542–568, 1940. In Russian.

Appendices

A Nuclear reactions

Nuclear reactions are listed in Tables A.1 to A.3 for the different nuclear reaction networks included in the hydrodynamic simulations. Table A.2 only lists additional nuclear reactions which come into play when ^{14}N and ^{22}Ne are added to the network consisting of 33 isotopes. Weak reaction rates from Langanke and Martínez-Pinedo (2001) are not included. Multiple entries of the same reaction indicate that the reaction take place in different forms with varying rate parameters (see Rauscher and Thielemann 2000 for details).

Table A.1: List of nuclear reactions considered when using a 33 isotope nuclear reaction network.

n	$\longrightarrow$	p	^{13}N	$\longrightarrow$	p + ^{12}C
^{13}N	$\longrightarrow$	p + ^{12}C	^{16}O	$\longrightarrow$	^{4}He + ^{12}C
^{16}O	$\longrightarrow$	^{4}He + ^{12}C	^{16}O	$\longrightarrow$	^{4}He + ^{12}C
^{16}O	$\longrightarrow$	^{4}He + ^{12}C	^{20}Ne	$\longrightarrow$	^{4}He + ^{16}O
^{20}Ne	$\longrightarrow$	^{4}He + ^{16}O	^{20}Ne	$\longrightarrow$	^{4}He + ^{16}O
^{23}Na	$\longrightarrow$	n + ^{22}Na	^{24}Mg	$\longrightarrow$	p + ^{23}Na
^{24}Mg	$\longrightarrow$	p + ^{23}Na	^{24}Mg	$\longrightarrow$	p + ^{23}Na
^{24}Mg	$\longrightarrow$	^{4}He + ^{20}Ne	^{24}Mg	$\longrightarrow$	^{4}He + ^{20}Ne
^{24}Mg	$\longrightarrow$	^{4}He + ^{20}Ne	^{24}Mg	$\longrightarrow$	^{4}He + ^{20}Ne
^{25}Mg	$\longrightarrow$	n + ^{24}Mg	^{26}Mg	$\longrightarrow$	n + ^{25}Mg
^{27}Al	$\longrightarrow$	p + ^{26}Mg	^{27}Al	$\longrightarrow$	p + ^{26}Mg
^{27}Al	$\longrightarrow$	p + ^{26}Mg	^{27}Al	$\longrightarrow$	^{4}He + ^{23}Na
^{28}Si	$\longrightarrow$	p + ^{27}Al	^{28}Si	$\longrightarrow$	p + ^{27}Al
^{28}Si	$\longrightarrow$	p + ^{27}Al	^{28}Si	$\longrightarrow$	^{4}He + ^{24}Mg
^{28}Si	$\longrightarrow$	^{4}He + ^{24}Mg	^{29}Si	$\longrightarrow$	n + ^{28}Si
^{29}Si	$\longrightarrow$	^{4}He + ^{25}Mg	^{30}Si	$\longrightarrow$	n + ^{29}Si
^{30}Si	$\longrightarrow$	^{4}He + ^{26}Mg	^{30}Si	$\longrightarrow$	^{4}He + ^{26}Mg
^{31}P	$\longrightarrow$	p + ^{30}Si	^{31}P	$\longrightarrow$	p + ^{30}Si
^{31}P	$\longrightarrow$	p + ^{30}Si	^{31}P	$\longrightarrow$	^{4}He + ^{27}Al
^{32}S	$\longrightarrow$	p + ^{31}P	^{32}S	$\longrightarrow$	p + ^{31}P
^{32}S	$\longrightarrow$	p + ^{31}P	^{32}S	$\longrightarrow$	^{4}He + ^{28}Si
^{36}Ar	$\longrightarrow$	^{4}He + ^{32}S	^{40}Ca	$\longrightarrow$	^{4}He + ^{36}Ar
^{44}Ti	$\longrightarrow$	^{4}He + ^{40}Ca	^{45}Ti	$\longrightarrow$	n + ^{44}Ti
^{46}Ti	$\longrightarrow$	n + ^{45}Ti	^{47}V	$\longrightarrow$	p + ^{46}Ti
^{48}Cr	$\longrightarrow$	p + ^{47}V	^{48}Cr	$\longrightarrow$	p + ^{47}V
^{48}Cr	$\longrightarrow$	p + ^{47}V	^{48}Cr	$\longrightarrow$	p + ^{47}V
^{48}Cr	$\longrightarrow$	^{4}He + ^{44}Ti	^{49}Cr	$\longrightarrow$	n + ^{48}Cr
^{49}Cr	$\longrightarrow$	^{4}He + ^{45}Ti	^{50}Cr	$\longrightarrow$	n + ^{49}Cr
^{50}Cr	$\longrightarrow$	^{4}He + ^{46}Ti	^{51}Mn	$\longrightarrow$	p + ^{50}Cr
^{51}Mn	$\longrightarrow$	^{4}He + ^{47}V	^{52}Fe	$\longrightarrow$	p + ^{51}Mn
^{52}Fe	$\longrightarrow$	^{4}He + ^{48}Cr	^{53}Fe	$\longrightarrow$	n + ^{52}Fe
^{53}Fe	$\longrightarrow$	^{4}He + ^{49}Cr	^{54}Fe	$\longrightarrow$	n + ^{53}Fe
^{54}Fe	$\longrightarrow$	^{4}He + ^{50}Cr	^{55}Co	$\longrightarrow$	p + ^{54}Fe
^{55}Co	$\longrightarrow$	^{4}He + ^{51}Mn	^{56}Ni	$\longrightarrow$	p + ^{55}Co
^{56}Ni	$\longrightarrow$	^{4}He + ^{52}Fe	^{12}C	$\longrightarrow$	^{4}He + ^{4}He + ^{4}He
^{12}C	$\longrightarrow$	^{4}He + ^{4}He + ^{4}He	^{12}C	$\longrightarrow$	^{4}He + ^{4}He + ^{4}He
p + ^{12}C	$\longrightarrow$	^{13}N	p + ^{12}C	$\longrightarrow$	^{13}N

Table A.1 continued.

^{4}He + ^{12}C	$\longrightarrow$	^{16}O	^{4}He + ^{12}C	$\longrightarrow$	^{16}O
^{4}He + ^{12}C	$\longrightarrow$	^{16}O	^{4}He + ^{12}C	$\longrightarrow$	^{16}O
^{4}He + ^{16}O	$\longrightarrow$	^{20}Ne	^{4}He + ^{16}O	$\longrightarrow$	^{20}Ne
^{4}He + ^{16}O	$\longrightarrow$	^{20}Ne	^{4}He + ^{20}Ne	$\longrightarrow$	^{24}Mg
^{4}He + ^{20}Ne	$\longrightarrow$	^{24}Mg	^{4}He + ^{20}Ne	$\longrightarrow$	^{24}Mg
^{4}He + ^{20}Ne	$\longrightarrow$	^{24}Mg	n + ^{22}Na	$\longrightarrow$	^{23}Na
p + ^{23}Na	$\longrightarrow$	^{24}Mg	p + ^{23}Na	$\longrightarrow$	^{24}Mg
p + ^{23}Na	$\longrightarrow$	^{24}Mg	^{4}He + ^{23}Na	$\longrightarrow$	^{27}Al
n + ^{24}Mg	$\longrightarrow$	^{25}Mg	^{4}He + ^{24}Mg	$\longrightarrow$	^{28}Si
^{4}He + ^{24}Mg	$\longrightarrow$	^{28}Si	n + ^{25}Mg	$\longrightarrow$	^{26}Mg
^{4}He + ^{25}Mg	$\longrightarrow$	^{29}Si	p + ^{26}Mg	$\longrightarrow$	^{27}Al
p + ^{26}Mg	$\longrightarrow$	^{27}Al	p + ^{26}Mg	$\longrightarrow$	^{27}Al
^{4}He + ^{26}Mg	$\longrightarrow$	^{30}Si	^{4}He + ^{26}Mg	$\longrightarrow$	^{30}Si
p + ^{27}Al	$\longrightarrow$	^{28}Si	p + ^{27}Al	$\longrightarrow$	^{28}Si
p + ^{27}Al	$\longrightarrow$	^{28}Si	^{4}He + ^{27}Al	$\longrightarrow$	^{31}P
n + ^{28}Si	$\longrightarrow$	^{29}Si	^{4}He + ^{28}Si	$\longrightarrow$	^{32}S
n + ^{29}Si	$\longrightarrow$	^{30}Si	p + ^{30}Si	$\longrightarrow$	^{31}P
p + ^{30}Si	$\longrightarrow$	^{31}P	p + ^{30}Si	$\longrightarrow$	^{31}P
p + ^{31}P	$\longrightarrow$	^{32}S	p + ^{31}P	$\longrightarrow$	^{32}S
p + ^{31}P	$\longrightarrow$	^{32}S	^{4}He + ^{32}S	$\longrightarrow$	^{36}Ar
^{4}He + ^{36}Ar	$\longrightarrow$	^{40}Ca	^{4}He + ^{40}Ca	$\longrightarrow$	^{44}Ti
n + ^{44}Ti	$\longrightarrow$	^{45}Ti	^{4}He + ^{44}Ti	$\longrightarrow$	^{48}Cr
n + ^{45}Ti	$\longrightarrow$	^{46}Ti	^{4}He + ^{45}Ti	$\longrightarrow$	^{49}Cr
p + ^{46}Ti	$\longrightarrow$	^{47}V	^{4}He + ^{46}Ti	$\longrightarrow$	^{50}Cr
p + ^{47}V	$\longrightarrow$	^{48}Cr	p + ^{47}V	$\longrightarrow$	^{48}Cr
p + ^{47}V	$\longrightarrow$	^{48}Cr	p + ^{47}V	$\longrightarrow$	^{48}Cr
^{4}He + ^{47}V	$\longrightarrow$	^{51}Mn	n + ^{48}Cr	$\longrightarrow$	^{49}Cr
^{4}He + ^{48}Cr	$\longrightarrow$	^{52}Fe	n + ^{49}Cr	$\longrightarrow$	^{50}Cr
^{4}He + ^{49}Cr	$\longrightarrow$	^{53}Fe	p + ^{50}Cr	$\longrightarrow$	^{51}Mn
^{4}He + ^{50}Cr	$\longrightarrow$	^{54}Fe	p + ^{51}Mn	$\longrightarrow$	^{52}Fe
^{4}He + ^{51}Mn	$\longrightarrow$	^{55}Co	n + ^{52}Fe	$\longrightarrow$	^{53}Fe
^{4}He + ^{52}Fe	$\longrightarrow$	^{56}Ni	n + ^{53}Fe	$\longrightarrow$	^{54}Fe
p + ^{54}Fe	$\longrightarrow$	^{55}Co	p + ^{55}Co	$\longrightarrow$	^{56}Ni
^{12}C + ^{12}C	$\longrightarrow$	p + ^{23}Na	^{12}C + ^{12}C	$\longrightarrow$	^{4}He + ^{20}Ne
^{4}He + ^{13}N	$\longrightarrow$	p + ^{16}O	p + ^{16}O	$\longrightarrow$	^{4}He + ^{13}N
^{12}C + ^{16}O	$\longrightarrow$	p + ^{27}Al	^{12}C + ^{16}O	$\longrightarrow$	^{4}He + ^{24}Mg
^{16}O + ^{16}O	$\longrightarrow$	p + ^{31}P	^{16}O + ^{16}O	$\longrightarrow$	^{4}He + ^{28}Si
^{4}He + ^{20}Ne	$\longrightarrow$	p + ^{23}Na	^{4}He + ^{20}Ne	$\longrightarrow$	p + ^{23}Na
^{4}He + ^{20}Ne	$\longrightarrow$	p + ^{23}Na	^{4}He + ^{20}Ne	$\longrightarrow$	^{12}C + ^{12}C
^{12}C + ^{20}Ne	$\longrightarrow$	p + ^{31}P	^{12}C + ^{20}Ne	$\longrightarrow$	^{4}He + ^{28}Si
^{4}He + ^{22}Na	$\longrightarrow$	p + ^{25}Mg	p + ^{23}Na	$\longrightarrow$	^{4}He + ^{20}Ne
p + ^{23}Na	$\longrightarrow$	^{4}He + ^{20}Ne	p + ^{23}Na	$\longrightarrow$	^{4}He + ^{20}Ne
p + ^{23}Na	$\longrightarrow$	^{12}C + ^{12}C	^{4}He + ^{23}Na	$\longrightarrow$	p + ^{26}Mg

Table A.1 continued.

^{4}He + ^{24}Mg	$\longrightarrow$	p + ^{27}Al	^{4}He + ^{24}Mg	$\longrightarrow$	p + ^{27}Al
^{4}He + ^{24}Mg	$\longrightarrow$	p + ^{27}Al	^{4}He + ^{24}Mg	$\longrightarrow$	^{12}C + ^{16}O
p + ^{25}Mg	$\longrightarrow$	^{4}He + ^{22}Na	^{4}He + ^{25}Mg	$\longrightarrow$	n + ^{28}Si
^{4}He + ^{25}Mg	$\longrightarrow$	n + ^{28}Si	p + ^{26}Mg	$\longrightarrow$	^{4}He + ^{23}Na
^{4}He + ^{26}Mg	$\longrightarrow$	n + ^{29}Si	^{4}He + ^{26}Mg	$\longrightarrow$	n + ^{29}Si
p + ^{27}Al	$\longrightarrow$	^{4}He + ^{24}Mg	p + ^{27}Al	$\longrightarrow$	^{4}He + ^{24}Mg
p + ^{27}Al	$\longrightarrow$	^{4}He + ^{24}Mg	p + ^{27}Al	$\longrightarrow$	^{12}C + ^{16}O
^{4}He + ^{27}Al	$\longrightarrow$	p + ^{30}Si	n + ^{28}Si	$\longrightarrow$	^{4}He + ^{25}Mg
n + ^{28}Si	$\longrightarrow$	^{4}He + ^{25}Mg	^{4}He + ^{28}Si	$\longrightarrow$	p + ^{31}P
^{4}He + ^{28}Si	$\longrightarrow$	p + ^{31}P	^{4}He + ^{28}Si	$\longrightarrow$	p + ^{31}P
^{4}He + ^{28}Si	$\longrightarrow$	^{12}C + ^{20}Ne	^{4}He + ^{28}Si	$\longrightarrow$	^{16}O + ^{16}O
n + ^{29}Si	$\longrightarrow$	^{4}He + ^{26}Mg	n + ^{29}Si	$\longrightarrow$	^{4}He + ^{26}Mg
^{4}He + ^{29}Si	$\longrightarrow$	n + ^{32}S	p + ^{30}Si	$\longrightarrow$	^{4}He + ^{27}Al
p + ^{31}P	$\longrightarrow$	^{4}He + ^{28}Si	p + ^{31}P	$\longrightarrow$	^{4}He + ^{28}Si
p + ^{31}P	$\longrightarrow$	^{4}He + ^{28}Si	p + ^{31}P	$\longrightarrow$	^{12}C + ^{20}Ne
p + ^{31}P	$\longrightarrow$	^{16}O + ^{16}O	n + ^{32}S	$\longrightarrow$	^{4}He + ^{29}Si
^{4}He + ^{44}Ti	$\longrightarrow$	p + ^{47}V	^{4}He + ^{45}Ti	$\longrightarrow$	n + ^{48}Cr
^{4}He + ^{46}Ti	$\longrightarrow$	n + ^{49}Cr	p + ^{47}V	$\longrightarrow$	^{4}He + ^{44}Ti
^{4}He + ^{47}V	$\longrightarrow$	p + ^{50}Cr	n + ^{48}Cr	$\longrightarrow$	^{4}He + ^{45}Ti
^{4}He + ^{48}Cr	$\longrightarrow$	p + ^{51}Mn	n + ^{49}Cr	$\longrightarrow$	^{4}He + ^{46}Ti
^{4}He + ^{49}Cr	$\longrightarrow$	n + ^{52}Fe	p + ^{50}Cr	$\longrightarrow$	^{4}He + ^{47}V
^{4}He + ^{50}Cr	$\longrightarrow$	n + ^{53}Fe	p + ^{51}Mn	$\longrightarrow$	^{4}He + ^{48}Cr
^{4}He + ^{51}Mn	$\longrightarrow$	p + ^{54}Fe	n + ^{52}Fe	$\longrightarrow$	^{4}He + ^{49}Cr
^{4}He + ^{52}Fe	$\longrightarrow$	p + ^{55}Co	n + ^{53}Fe	$\longrightarrow$	^{4}He + ^{50}Cr
^{4}He + ^{53}Fe	$\longrightarrow$	n + ^{56}Ni	p + ^{54}Fe	$\longrightarrow$	^{4}He + ^{51}Mn
p + ^{55}Co	$\longrightarrow$	^{4}He + ^{52}Fe	n + ^{56}Ni	$\longrightarrow$	^{4}He + ^{53}Fe
^{4}He + ^{4}He + ^{4}He	$\longrightarrow$	^{12}C	^{4}He + ^{4}He + ^{4}He	$\longrightarrow$	^{12}C
^{4}He + ^{4}He + ^{4}He	$\longrightarrow$	^{12}C			

Table A.2: List of additional nuclear reactions when also including ^{14}N and ^{22}Ne.

^{22}Na	$\longrightarrow$	^{22}Ne	^{14}N	$\longrightarrow$	n + ^{13}N
^{14}N	$\longrightarrow$	n + ^{13}N	^{23}Na	$\longrightarrow$	p + ^{22}Ne
^{23}Na	$\longrightarrow$	p + ^{22}Ne	^{23}Na	$\longrightarrow$	p + ^{22}Ne
^{23}Na	$\longrightarrow$	p + ^{22}Ne	^{26}Mg	$\longrightarrow$	^{4}He + ^{22}Ne
^{26}Mg	$\longrightarrow$	^{4}He + ^{22}Ne	^{26}Mg	$\longrightarrow$	^{4}He + ^{22}Ne
^{26}Mg	$\longrightarrow$	^{4}He + ^{22}Ne	n + ^{13}N	$\longrightarrow$	^{14}N
n + ^{13}N	$\longrightarrow$	^{14}N	p + ^{22}Ne	$\longrightarrow$	^{23}Na
p + ^{22}Ne	$\longrightarrow$	^{23}Na	p + ^{22}Ne	$\longrightarrow$	^{23}Na
p + ^{22}Ne	$\longrightarrow$	^{23}Na	^{4}He + ^{22}Ne	$\longrightarrow$	^{26}Mg
^{4}He + ^{22}Ne	$\longrightarrow$	^{26}Mg	^{4}He + ^{22}Ne	$\longrightarrow$	^{26}Mg
^{4}He + ^{22}Ne	$\longrightarrow$	^{26}Mg	p + ^{22}Ne	$\longrightarrow$	n + ^{22}Na
^{4}He + ^{22}Ne	$\longrightarrow$	n + ^{25}Mg	^{4}He + ^{22}Ne	$\longrightarrow$	n + ^{25}Mg
^{4}He + ^{22}Ne	$\longrightarrow$	n + ^{25}Mg	n + ^{22}Na	$\longrightarrow$	p + ^{22}Ne
n + ^{25}Mg	$\longrightarrow$	^{4}He + ^{22}Ne	n + ^{25}Mg	$\longrightarrow$	^{4}He + ^{22}Ne
n + ^{25}Mg	$\longrightarrow$	^{4}He + ^{22}Ne			

Table A.3: List of nuclear reactions considered when using a 55 isotope nuclear reaction network.

n	$\longrightarrow$	p	^{13}N	$\longrightarrow$	^{13}C
^{15}O	$\longrightarrow$	^{15}N	^{22}Na	$\longrightarrow$	^{22}Ne
^{23}Mg	$\longrightarrow$	^{23}Na	^{25}Al	$\longrightarrow$	^{25}Mg
^{26}Al	$\longrightarrow$	^{26}Mg	^{26}Al	$\longrightarrow$	^{26}Mg
^{29}P	$\longrightarrow$	^{29}Si	^{30}P	$\longrightarrow$	^{30}Si
^{31}S	$\longrightarrow$	^{31}P	^{33}Cl	$\longrightarrow$	^{33}S
^{39}Ar	$\longrightarrow$	^{39}K	^{12}C	$\longrightarrow$	p + ^{11}B
^{12}C	$\longrightarrow$	p + ^{11}B	^{12}C	$\longrightarrow$	p + ^{11}B
^{13}C	$\longrightarrow$	n + ^{12}C	^{13}C	$\longrightarrow$	n + ^{12}C
^{13}N	$\longrightarrow$	p + ^{12}C	^{13}N	$\longrightarrow$	p + ^{12}C
^{14}N	$\longrightarrow$	n + ^{13}N	^{14}N	$\longrightarrow$	n + ^{13}N
^{14}N	$\longrightarrow$	p + ^{13}C	^{14}N	$\longrightarrow$	p + ^{13}C
^{14}N	$\longrightarrow$	p + ^{13}C	^{15}N	$\longrightarrow$	n + ^{14}N
^{15}O	$\longrightarrow$	p + ^{14}N	^{15}O	$\longrightarrow$	p + ^{14}N
^{15}O	$\longrightarrow$	p + ^{14}N	^{15}O	$\longrightarrow$	p + ^{14}N
^{16}O	$\longrightarrow$	n + ^{15}O	^{16}O	$\longrightarrow$	p + ^{15}N
^{16}O	$\longrightarrow$	p + ^{15}N	^{16}O	$\longrightarrow$	p + ^{15}N
^{16}O	$\longrightarrow$	^{4}He + ^{12}C	^{16}O	$\longrightarrow$	^{4}He + ^{12}C
^{16}O	$\longrightarrow$	^{4}He + ^{12}C	^{16}O	$\longrightarrow$	^{4}He + ^{12}C
^{17}O	$\longrightarrow$	n + ^{16}O	^{17}O	$\longrightarrow$	n + ^{16}O
^{18}F	$\longrightarrow$	p + ^{17}O	^{18}F	$\longrightarrow$	p + ^{17}O
^{18}F	$\longrightarrow$	p + ^{17}O	^{18}F	$\longrightarrow$	^{4}He + ^{14}N
^{18}F	$\longrightarrow$	^{4}He + ^{14}N	^{18}F	$\longrightarrow$	^{4}He + ^{14}N
^{19}Ne	$\longrightarrow$	p + ^{18}F	^{19}Ne	$\longrightarrow$	p + ^{18}F
^{19}Ne	$\longrightarrow$	p + ^{18}F	^{19}Ne	$\longrightarrow$	^{4}He + ^{15}O
^{19}Ne	$\longrightarrow$	^{4}He + ^{15}O	^{19}Ne	$\longrightarrow$	^{4}He + ^{15}O
^{20}Ne	$\longrightarrow$	n + ^{19}Ne	^{20}Ne	$\longrightarrow$	^{4}He + ^{16}O
^{20}Ne	$\longrightarrow$	^{4}He + ^{16}O	^{20}Ne	$\longrightarrow$	^{4}He + ^{16}O
^{21}Ne	$\longrightarrow$	n + ^{20}Ne	^{21}Ne	$\longrightarrow$	^{4}He + ^{17}O
^{21}Ne	$\longrightarrow$	^{4}He + ^{17}O	^{22}Ne	$\longrightarrow$	n + ^{21}Ne
^{22}Na	$\longrightarrow$	p + ^{21}Ne	^{22}Na	$\longrightarrow$	p + ^{21}Ne
^{22}Na	$\longrightarrow$	p + ^{21}Ne	^{22}Na	$\longrightarrow$	p + ^{21}Ne
^{22}Na	$\longrightarrow$	^{4}He + ^{18}F	^{23}Na	$\longrightarrow$	n + ^{22}Na
^{23}Na	$\longrightarrow$	p + ^{22}Ne	^{23}Na	$\longrightarrow$	p + ^{22}Ne
^{23}Na	$\longrightarrow$	p + ^{22}Ne	^{23}Na	$\longrightarrow$	p + ^{22}Ne
^{23}Mg	$\longrightarrow$	p + ^{22}Na	^{23}Mg	$\longrightarrow$	p + ^{22}Na
^{23}Mg	$\longrightarrow$	p + ^{22}Na	^{23}Mg	$\longrightarrow$	^{4}He + ^{19}Ne
^{24}Mg	$\longrightarrow$	n + ^{23}Mg	^{24}Mg	$\longrightarrow$	p + ^{23}Na
^{24}Mg	$\longrightarrow$	p + ^{23}Na	^{24}Mg	$\longrightarrow$	p + ^{23}Na
^{24}Mg	$\longrightarrow$	^{4}He + ^{20}Ne	^{24}Mg	$\longrightarrow$	^{4}He + ^{20}Ne
^{24}Mg	$\longrightarrow$	^{4}He + ^{20}Ne	^{24}Mg	$\longrightarrow$	^{4}He + ^{20}Ne
^{25}Mg	$\longrightarrow$	n + ^{24}Mg	^{25}Mg	$\longrightarrow$	^{4}He + ^{21}Ne
^{25}Mg	$\longrightarrow$	^{4}He + ^{21}Ne	^{26}Mg	$\longrightarrow$	n + ^{25}Mg
^{26}Mg	$\longrightarrow$	^{4}He + ^{22}Ne	^{26}Mg	$\longrightarrow$	^{4}He + ^{22}Ne
^{26}Mg	$\longrightarrow$	^{4}He + ^{22}Ne	^{26}Mg	$\longrightarrow$	^{4}He + ^{22}Ne
^{25}Al	$\longrightarrow$	p + ^{24}Mg	^{25}Al	$\longrightarrow$	p + ^{24}Mg
^{26}Al	$\longrightarrow$	n + ^{25}Al	^{26}Al	$\longrightarrow$	p + ^{25}Mg

Table A.3 continued.

^{26}Al	$\longrightarrow$	p + ^{25}Mg	^{26}Al	$\longrightarrow$	p + ^{25}Mg
^{26}Al	$\longrightarrow$	^{4}He + ^{22}Na	^{27}Al	$\longrightarrow$	n + ^{26}Al
^{27}Al	$\longrightarrow$	p + ^{26}Mg	^{27}Al	$\longrightarrow$	p + ^{26}Mg
^{27}Al	$\longrightarrow$	p + ^{26}Mg	^{27}Al	$\longrightarrow$	^{4}He + ^{23}Na
^{28}Si	$\longrightarrow$	p + ^{27}Al	^{28}Si	$\longrightarrow$	p + ^{27}Al
^{28}Si	$\longrightarrow$	p + ^{27}Al	^{28}Si	$\longrightarrow$	^{4}He + ^{24}Mg
^{28}Si	$\longrightarrow$	^{4}He + ^{24}Mg	^{29}Si	$\longrightarrow$	n + ^{28}Si
^{29}Si	$\longrightarrow$	^{4}He + ^{25}Mg	^{30}Si	$\longrightarrow$	n + ^{29}Si
^{30}Si	$\longrightarrow$	^{4}He + ^{26}Mg	^{30}Si	$\longrightarrow$	^{4}He + ^{26}Mg
^{29}P	$\longrightarrow$	p + ^{28}Si	^{29}P	$\longrightarrow$	p + ^{28}Si
^{29}P	$\longrightarrow$	^{4}He + ^{25}Al	^{30}P	$\longrightarrow$	n + ^{29}P
^{30}P	$\longrightarrow$	p + ^{29}Si	^{30}P	$\longrightarrow$	p + ^{29}Si
^{30}P	$\longrightarrow$	p + ^{29}Si	^{30}P	$\longrightarrow$	^{4}He + ^{26}Al
^{31}P	$\longrightarrow$	n + ^{30}P	^{31}P	$\longrightarrow$	p + ^{30}Si
^{31}P	$\longrightarrow$	p + ^{30}Si	^{31}P	$\longrightarrow$	p + ^{30}Si
^{31}P	$\longrightarrow$	^{4}He + ^{27}Al	^{31}S	$\longrightarrow$	p + ^{30}P
^{31}S	$\longrightarrow$	p + ^{30}P	^{32}S	$\longrightarrow$	n + ^{31}S
^{32}S	$\longrightarrow$	p + ^{31}P	^{32}S	$\longrightarrow$	p + ^{31}P
^{32}S	$\longrightarrow$	p + ^{31}P	^{32}S	$\longrightarrow$	^{4}He + ^{28}Si
^{33}S	$\longrightarrow$	n + ^{32}S	^{33}S	$\longrightarrow$	^{4}He + ^{29}Si
^{33}Cl	$\longrightarrow$	p + ^{32}S	^{33}Cl	$\longrightarrow$	p + ^{32}S
^{33}Cl	$\longrightarrow$	p + ^{32}S	^{33}Cl	$\longrightarrow$	^{4}He + ^{29}P
^{34}Cl	$\longrightarrow$	n + ^{33}Cl	^{34}Cl	$\longrightarrow$	p + ^{33}S
^{34}Cl	$\longrightarrow$	^{4}He + ^{30}P	^{35}Cl	$\longrightarrow$	n + ^{34}Cl
^{35}Cl	$\longrightarrow$	^{4}He + ^{31}P	^{36}Ar	$\longrightarrow$	p + ^{35}Cl
^{36}Ar	$\longrightarrow$	p + ^{35}Cl	^{36}Ar	$\longrightarrow$	p + ^{35}Cl
^{36}Ar	$\longrightarrow$	p + ^{35}Cl	^{36}Ar	$\longrightarrow$	^{4}He + ^{32}S
^{37}Ar	$\longrightarrow$	n + ^{36}Ar	^{37}Ar	$\longrightarrow$	^{4}He + ^{33}S
^{38}Ar	$\longrightarrow$	n + ^{37}Ar	^{39}Ar	$\longrightarrow$	n + ^{38}Ar
^{39}K	$\longrightarrow$	p + ^{38}Ar	^{39}K	$\longrightarrow$	^{4}He + ^{35}Cl
^{40}Ca	$\longrightarrow$	p + ^{39}K	^{40}Ca	$\longrightarrow$	^{4}He + ^{36}Ar
^{43}Sc	$\longrightarrow$	^{4}He + ^{39}K	^{44}Ti	$\longrightarrow$	p + ^{43}Sc
^{44}Ti	$\longrightarrow$	^{4}He + ^{40}Ca	^{47}V	$\longrightarrow$	^{4}He + ^{43}Sc
^{48}Cr	$\longrightarrow$	p + ^{47}V	^{48}Cr	$\longrightarrow$	p + ^{47}V
^{48}Cr	$\longrightarrow$	p + ^{47}V	^{48}Cr	$\longrightarrow$	p + ^{47}V
^{48}Cr	$\longrightarrow$	^{4}He + ^{44}Ti	^{51}Mn	$\longrightarrow$	^{4}He + ^{47}V
^{52}Fe	$\longrightarrow$	p + ^{51}Mn	^{52}Fe	$\longrightarrow$	^{4}He + ^{48}Cr
^{55}Co	$\longrightarrow$	^{4}He + ^{51}Mn	^{56}Ni	$\longrightarrow$	p + ^{55}Co
^{56}Ni	$\longrightarrow$	^{4}He + ^{52}Fe	^{59}Ni	$\longrightarrow$	n + ^{58}Ni
^{12}C	$\longrightarrow$	^{4}He + ^{4}He + ^{4}He	^{12}C	$\longrightarrow$	^{4}He + ^{4}He + ^{4}He
^{12}C	$\longrightarrow$	^{4}He + ^{4}He + ^{4}He	p + ^{11}B	$\longrightarrow$	^{12}C
p + ^{11}B	$\longrightarrow$	^{12}C	p + ^{11}B	$\longrightarrow$	^{12}C
n + ^{12}C	$\longrightarrow$	^{13}C	n + ^{12}C	$\longrightarrow$	^{13}C
p + ^{12}C	$\longrightarrow$	^{13}N	p + ^{12}C	$\longrightarrow$	^{13}N
^{4}He + ^{12}C	$\longrightarrow$	^{16}O	^{4}He + ^{12}C	$\longrightarrow$	^{16}O
^{4}He + ^{12}C	$\longrightarrow$	^{16}O	^{4}He + ^{12}C	$\longrightarrow$	^{16}O
p + ^{13}C	$\longrightarrow$	^{14}N	p + ^{13}C	$\longrightarrow$	^{14}N
p + ^{13}C	$\longrightarrow$	^{14}N	n + ^{13}N	$\longrightarrow$	^{14}N

Table A.3 continued.

n + ^{13}N	$\longrightarrow$	^{14}N	n + ^{14}N	$\longrightarrow$	^{15}N
p + ^{14}N	$\longrightarrow$	^{15}O	p + ^{14}N	$\longrightarrow$	^{15}O
p + ^{14}N	$\longrightarrow$	^{15}O	p + ^{14}N	$\longrightarrow$	^{15}O
^{4}He + ^{14}N	$\longrightarrow$	^{18}F	^{4}He + ^{14}N	$\longrightarrow$	^{18}F
^{4}He + ^{14}N	$\longrightarrow$	^{18}F	p + ^{15}N	$\longrightarrow$	^{16}O
p + ^{15}N	$\longrightarrow$	^{16}O	p + ^{15}N	$\longrightarrow$	^{16}O
n + ^{15}O	$\longrightarrow$	^{16}O	^{4}He + ^{15}O	$\longrightarrow$	^{19}Ne
^{4}He + ^{15}O	$\longrightarrow$	^{19}Ne	^{4}He + ^{15}O	$\longrightarrow$	^{19}Ne
n + ^{16}O	$\longrightarrow$	^{17}O	n + ^{16}O	$\longrightarrow$	^{17}O
^{4}He + ^{16}O	$\longrightarrow$	^{20}Ne	^{4}He + ^{16}O	$\longrightarrow$	^{20}Ne
^{4}He + ^{16}O	$\longrightarrow$	^{20}Ne	p + ^{17}O	$\longrightarrow$	^{18}F
p + ^{17}O	$\longrightarrow$	^{18}F	p + ^{17}O	$\longrightarrow$	^{18}F
^{4}He + ^{17}O	$\longrightarrow$	^{21}Ne	^{4}He + ^{17}O	$\longrightarrow$	^{21}Ne
p + ^{18}F	$\longrightarrow$	^{19}Ne	p + ^{18}F	$\longrightarrow$	^{19}Ne
p + ^{18}F	$\longrightarrow$	^{19}Ne	^{4}He + ^{18}F	$\longrightarrow$	^{22}Na
n + ^{19}Ne	$\longrightarrow$	^{20}Ne	^{4}He + ^{19}Ne	$\longrightarrow$	^{23}Mg
n + ^{20}Ne	$\longrightarrow$	^{21}Ne	^{4}He + ^{20}Ne	$\longrightarrow$	^{24}Mg
^{4}He + ^{20}Ne	$\longrightarrow$	^{24}Mg	^{4}He + ^{20}Ne	$\longrightarrow$	^{24}Mg
^{4}He + ^{20}Ne	$\longrightarrow$	^{24}Mg	n + ^{21}Ne	$\longrightarrow$	^{22}Ne
p + ^{21}Ne	$\longrightarrow$	^{22}Na	p + ^{21}Ne	$\longrightarrow$	^{22}Na
p + ^{21}Ne	$\longrightarrow$	^{22}Na	p + ^{21}Ne	$\longrightarrow$	^{22}Na
^{4}He + ^{21}Ne	$\longrightarrow$	^{25}Mg	^{4}He + ^{21}Ne	$\longrightarrow$	^{25}Mg
p + ^{22}Ne	$\longrightarrow$	^{23}Na	p + ^{22}Ne	$\longrightarrow$	^{23}Na
p + ^{22}Ne	$\longrightarrow$	^{23}Na	p + ^{22}Ne	$\longrightarrow$	^{23}Na
^{4}He + ^{22}Ne	$\longrightarrow$	^{26}Mg	^{4}He + ^{22}Ne	$\longrightarrow$	^{26}Mg
^{4}He + ^{22}Ne	$\longrightarrow$	^{26}Mg	^{4}He + ^{22}Ne	$\longrightarrow$	^{26}Mg
n + ^{22}Na	$\longrightarrow$	^{23}Na	p + ^{22}Na	$\longrightarrow$	^{23}Mg
p + ^{22}Na	$\longrightarrow$	^{23}Mg	p + ^{22}Na	$\longrightarrow$	^{23}Mg
^{4}He + ^{22}Na	$\longrightarrow$	^{26}Al	p + ^{23}Na	$\longrightarrow$	^{24}Mg
p + ^{23}Na	$\longrightarrow$	^{24}Mg	p + ^{23}Na	$\longrightarrow$	^{24}Mg
^{4}He + ^{23}Na	$\longrightarrow$	^{27}Al	n + ^{23}Mg	$\longrightarrow$	^{24}Mg
n + ^{24}Mg	$\longrightarrow$	^{25}Mg	p + ^{24}Mg	$\longrightarrow$	^{25}Al
p + ^{24}Mg	$\longrightarrow$	^{25}Al	^{4}He + ^{24}Mg	$\longrightarrow$	^{28}Si
^{4}He + ^{24}Mg	$\longrightarrow$	^{28}Si	n + ^{25}Mg	$\longrightarrow$	^{26}Mg
p + ^{25}Mg	$\longrightarrow$	^{26}Al	p + ^{25}Mg	$\longrightarrow$	^{26}Al
p + ^{25}Mg	$\longrightarrow$	^{26}Al	^{4}He + ^{25}Mg	$\longrightarrow$	^{29}Si
p + ^{26}Mg	$\longrightarrow$	^{27}Al	p + ^{26}Mg	$\longrightarrow$	^{27}Al
p + ^{26}Mg	$\longrightarrow$	^{27}Al	^{4}He + ^{26}Mg	$\longrightarrow$	^{30}Si
^{4}He + ^{26}Mg	$\longrightarrow$	^{30}Si	n + ^{25}Al	$\longrightarrow$	^{26}Al
^{4}He + ^{25}Al	$\longrightarrow$	^{29}P	n + ^{26}Al	$\longrightarrow$	^{27}Al
^{4}He + ^{26}Al	$\longrightarrow$	^{30}P	p + ^{27}Al	$\longrightarrow$	^{28}Si
p + ^{27}Al	$\longrightarrow$	^{28}Si	p + ^{27}Al	$\longrightarrow$	^{28}Si
^{4}He + ^{27}Al	$\longrightarrow$	^{31}P	n + ^{28}Si	$\longrightarrow$	^{29}Si
p + ^{28}Si	$\longrightarrow$	^{29}P	p + ^{28}Si	$\longrightarrow$	^{29}P
^{4}He + ^{28}Si	$\longrightarrow$	^{32}S	n + ^{29}Si	$\longrightarrow$	^{30}Si
p + ^{29}Si	$\longrightarrow$	^{30}P	p + ^{29}Si	$\longrightarrow$	^{30}P
p + ^{29}Si	$\longrightarrow$	^{30}P	^{4}He + ^{29}Si	$\longrightarrow$	^{33}S
p + ^{30}Si	$\longrightarrow$	^{31}P	p + ^{30}Si	$\longrightarrow$	^{31}P

Table A.3 continued.

p + ^{30}Si	$\longrightarrow$	^{31}P		n + ^{29}P	$\longrightarrow$	^{30}P	
^{4}He + ^{29}P	$\longrightarrow$	^{33}Cl		n + ^{30}P	$\longrightarrow$	^{31}P	
p + ^{30}P	$\longrightarrow$	^{31}S		p + ^{30}P	$\longrightarrow$	^{31}S	
^{4}He + ^{30}P	$\longrightarrow$	^{34}Cl		p + ^{31}P	$\longrightarrow$	^{32}S	
p + ^{31}P	$\longrightarrow$	^{32}S		p + ^{31}P	$\longrightarrow$	^{32}S	
^{4}He + ^{31}P	$\longrightarrow$	^{35}Cl		n + ^{31}S	$\longrightarrow$	^{32}S	
n + ^{32}S	$\longrightarrow$	^{33}S		p + ^{32}S	$\longrightarrow$	^{33}Cl	
p + ^{32}S	$\longrightarrow$	^{33}Cl		p + ^{32}S	$\longrightarrow$	^{33}Cl	
^{4}He + ^{32}S	$\longrightarrow$	^{36}Ar		p + ^{33}S	$\longrightarrow$	^{34}Cl	
^{4}He + ^{33}S	$\longrightarrow$	^{37}Ar		n + ^{33}Cl	$\longrightarrow$	^{34}Cl	
n + ^{34}Cl	$\longrightarrow$	^{35}Cl		p + ^{35}Cl	$\longrightarrow$	^{36}Ar	
p + ^{35}Cl	$\longrightarrow$	^{36}Ar		p + ^{35}Cl	$\longrightarrow$	^{36}Ar	
p + ^{35}Cl	$\longrightarrow$	^{36}Ar		^{4}He + ^{35}Cl	$\longrightarrow$	^{39}K	
n + ^{36}Ar	$\longrightarrow$	^{37}Ar		^{4}He + ^{36}Ar	$\longrightarrow$	^{40}Ca	
n + ^{37}Ar	$\longrightarrow$	^{38}Ar		n + ^{38}Ar	$\longrightarrow$	^{39}Ar	
p + ^{38}Ar	$\longrightarrow$	^{39}K		p + ^{39}K	$\longrightarrow$	^{40}Ca	
^{4}He + ^{39}K	$\longrightarrow$	^{43}Sc		^{4}He + ^{40}Ca	$\longrightarrow$	^{44}Ti	
p + ^{43}Sc	$\longrightarrow$	^{44}Ti		^{4}He + ^{43}Sc	$\longrightarrow$	^{47}V	
^{4}He + ^{44}Ti	$\longrightarrow$	^{48}Cr		p + ^{47}V	$\longrightarrow$	^{48}Cr	
p + ^{47}V	$\longrightarrow$	^{48}Cr		p + ^{47}V	$\longrightarrow$	^{48}Cr	
p + ^{47}V	$\longrightarrow$	^{48}Cr		^{4}He + ^{47}V	$\longrightarrow$	^{51}Mn	
^{4}He + ^{48}Cr	$\longrightarrow$	^{52}Fe		p + ^{51}Mn	$\longrightarrow$	^{52}Fe	
^{4}He + ^{51}Mn	$\longrightarrow$	^{55}Co		^{4}He + ^{52}Fe	$\longrightarrow$	^{56}Ni	
p + ^{55}Co	$\longrightarrow$	^{56}Ni		n + ^{58}Ni	$\longrightarrow$	^{59}Ni	
^{4}He + ^{11}B	$\longrightarrow$	n + ^{14}N		^{4}He + ^{11}B	$\longrightarrow$	n + ^{14}N	
^{4}He + ^{11}B	$\longrightarrow$	n + ^{14}N		^{4}He + ^{11}B	$\longrightarrow$	n + ^{14}N	
^{4}He + ^{12}C	$\longrightarrow$	n + ^{15}O		^{4}He + ^{12}C	$\longrightarrow$	p + ^{15}N	
^{4}He + ^{12}C	$\longrightarrow$	p + ^{15}N		^{4}He + ^{12}C	$\longrightarrow$	p + ^{15}N	
^{4}He + ^{12}C	$\longrightarrow$	p + ^{15}N		^{12}C + ^{12}C	$\longrightarrow$	n + ^{23}Mg	
^{12}C + ^{12}C	$\longrightarrow$	p + ^{23}Na		^{12}C + ^{12}C	$\longrightarrow$	^{4}He + ^{20}Ne	
p + ^{13}C	$\longrightarrow$	n + ^{13}N		^{4}He + ^{13}C	$\longrightarrow$	n + ^{16}O	
^{4}He + ^{13}C	$\longrightarrow$	n + ^{16}O		n + ^{13}N	$\longrightarrow$	p + ^{13}C	
^{4}He + ^{13}N	$\longrightarrow$	p + ^{16}O		n + ^{14}N	$\longrightarrow$	^{4}He + ^{11}B	
n + ^{14}N	$\longrightarrow$	^{4}He + ^{11}B		n + ^{14}N	$\longrightarrow$	^{4}He + ^{11}B	
n + ^{14}N	$\longrightarrow$	^{4}He + ^{11}B		^{4}He + ^{14}N	$\longrightarrow$	p + ^{17}O	
^{4}He + ^{14}N	$\longrightarrow$	p + ^{17}O		^{4}He + ^{14}N	$\longrightarrow$	p + ^{17}O	
^{4}He + ^{14}N	$\longrightarrow$	p + ^{17}O		p + ^{15}N	$\longrightarrow$	n + ^{15}O	
p + ^{15}N	$\longrightarrow$	^{4}He + ^{12}C		p + ^{15}N	$\longrightarrow$	^{4}He + ^{12}C	
p + ^{15}N	$\longrightarrow$	^{4}He + ^{12}C		p + ^{15}N	$\longrightarrow$	^{4}He + ^{12}C	
^{4}He + ^{15}N	$\longrightarrow$	n + ^{18}F		n + ^{15}O	$\longrightarrow$	p + ^{15}N	
n + ^{15}O	$\longrightarrow$	^{4}He + ^{12}C		^{4}He + ^{15}O	$\longrightarrow$	p + ^{18}F	
^{4}He + ^{15}O	$\longrightarrow$	p + ^{18}F		^{4}He + ^{15}O	$\longrightarrow$	p + ^{18}F	
n + ^{16}O	$\longrightarrow$	^{4}He + ^{13}C		n + ^{16}O	$\longrightarrow$	^{4}He + ^{13}C	
p + ^{16}O	$\longrightarrow$	^{4}He + ^{13}N		^{4}He + ^{16}O	$\longrightarrow$	n + ^{19}Ne	
^{12}C + ^{16}O	$\longrightarrow$	p + ^{27}Al		^{12}C + ^{16}O	$\longrightarrow$	^{4}He + ^{24}Mg	
^{16}O + ^{16}O	$\longrightarrow$	n + ^{31}S		^{16}O + ^{16}O	$\longrightarrow$	p + ^{31}P	
^{16}O + ^{16}O	$\longrightarrow$	^{4}He + ^{28}Si		p + ^{17}O	$\longrightarrow$	^{4}He + ^{14}N	
p + ^{17}O	$\longrightarrow$	^{4}He + ^{14}N		p + ^{17}O	$\longrightarrow$	^{4}He + ^{14}N	

Table A.3 continued.

p + ^{17}O	$\longrightarrow$	^{4}He + ^{14}N	^{4}He + ^{17}O	$\longrightarrow$	n + ^{20}Ne
^{4}He + ^{17}O	$\longrightarrow$	n + ^{20}Ne	^{4}He + ^{17}O	$\longrightarrow$	n + ^{20}Ne
n + ^{18}F	$\longrightarrow$	^{4}He + ^{15}N	p + ^{18}F	$\longrightarrow$	^{4}He + ^{15}O
p + ^{18}F	$\longrightarrow$	^{4}He + ^{15}O	p + ^{18}F	$\longrightarrow$	^{4}He + ^{15}O
^{4}He + ^{18}F	$\longrightarrow$	p + ^{21}Ne	n + ^{19}Ne	$\longrightarrow$	^{4}He + ^{16}O
^{4}He + ^{19}Ne	$\longrightarrow$	p + ^{22}Na	n + ^{20}Ne	$\longrightarrow$	^{4}He + ^{17}O
n + ^{20}Ne	$\longrightarrow$	^{4}He + ^{17}O	n + ^{20}Ne	$\longrightarrow$	^{4}He + ^{17}O
^{4}He + ^{20}Ne	$\longrightarrow$	n + ^{23}Mg	^{4}He + ^{20}Ne	$\longrightarrow$	p + ^{23}Na
^{4}He + ^{20}Ne	$\longrightarrow$	p + ^{23}Na	^{4}He + ^{20}Ne	$\longrightarrow$	p + ^{23}Na
^{4}He + ^{20}Ne	$\longrightarrow$	^{12}C + ^{12}C	^{12}C + ^{20}Ne	$\longrightarrow$	n + ^{31}S
^{12}C + ^{20}Ne	$\longrightarrow$	p + ^{31}P	^{12}C + ^{20}Ne	$\longrightarrow$	^{4}He + ^{28}Si
p + ^{21}Ne	$\longrightarrow$	^{4}He + ^{18}F	^{4}He + ^{21}Ne	$\longrightarrow$	n + ^{24}Mg
^{4}He + ^{21}Ne	$\longrightarrow$	n + ^{24}Mg	p + ^{22}Ne	$\longrightarrow$	n + ^{22}Na
^{4}He + ^{22}Ne	$\longrightarrow$	n + ^{25}Mg	^{4}He + ^{22}Ne	$\longrightarrow$	n + ^{25}Mg
^{4}He + ^{22}Ne	$\longrightarrow$	n + ^{25}Mg	n + ^{22}Na	$\longrightarrow$	p + ^{22}Ne
p + ^{22}Na	$\longrightarrow$	^{4}He + ^{19}Ne	^{4}He + ^{22}Na	$\longrightarrow$	n + ^{25}Al
^{4}He + ^{22}Na	$\longrightarrow$	p + ^{25}Mg	p + ^{23}Na	$\longrightarrow$	n + ^{23}Mg
p + ^{23}Na	$\longrightarrow$	^{4}He + ^{20}Ne	p + ^{23}Na	$\longrightarrow$	^{4}He + ^{20}Ne
p + ^{23}Na	$\longrightarrow$	^{4}He + ^{20}Ne	p + ^{23}Na	$\longrightarrow$	^{12}C + ^{12}C
^{4}He + ^{23}Na	$\longrightarrow$	n + ^{26}Al	^{4}He + ^{23}Na	$\longrightarrow$	n + ^{26}Al
^{4}He + ^{23}Na	$\longrightarrow$	n + ^{26}Al	^{4}He + ^{23}Na	$\longrightarrow$	p + ^{26}Mg
n + ^{23}Mg	$\longrightarrow$	p + ^{23}Na	n + ^{23}Mg	$\longrightarrow$	^{4}He + ^{20}Ne
n + ^{23}Mg	$\longrightarrow$	^{12}C + ^{12}C	^{4}He + ^{23}Mg	$\longrightarrow$	p + ^{26}Al
n + ^{24}Mg	$\longrightarrow$	^{4}He + ^{21}Ne	n + ^{24}Mg	$\longrightarrow$	^{4}He + ^{21}Ne
^{4}He + ^{24}Mg	$\longrightarrow$	p + ^{27}Al	^{4}He + ^{24}Mg	$\longrightarrow$	p + ^{27}Al
^{4}He + ^{24}Mg	$\longrightarrow$	p + ^{27}Al	^{4}He + ^{24}Mg	$\longrightarrow$	^{12}C + ^{16}O
n + ^{25}Mg	$\longrightarrow$	^{4}He + ^{22}Ne	n + ^{25}Mg	$\longrightarrow$	^{4}He + ^{22}Ne
n + ^{25}Mg	$\longrightarrow$	^{4}He + ^{22}Ne	p + ^{25}Mg	$\longrightarrow$	n + ^{25}Al
p + ^{25}Mg	$\longrightarrow$	^{4}He + ^{22}Na	^{4}He + ^{25}Mg	$\longrightarrow$	n + ^{28}Si
^{4}He + ^{25}Mg	$\longrightarrow$	n + ^{28}Si	p + ^{26}Mg	$\longrightarrow$	n + ^{26}Al
p + ^{26}Mg	$\longrightarrow$	n + ^{26}Al	p + ^{26}Mg	$\longrightarrow$	n + ^{26}Al
p + ^{26}Mg	$\longrightarrow$	^{4}He + ^{23}Na	^{4}He + ^{26}Mg	$\longrightarrow$	n + ^{29}Si
^{4}He + ^{26}Mg	$\longrightarrow$	n + ^{29}Si	n + ^{25}Al	$\longrightarrow$	p + ^{25}Mg
n + ^{25}Al	$\longrightarrow$	^{4}He + ^{22}Na	^{4}He + ^{25}Al	$\longrightarrow$	p + ^{28}Si
n + ^{26}Al	$\longrightarrow$	p + ^{26}Mg	n + ^{26}Al	$\longrightarrow$	p + ^{26}Mg
n + ^{26}Al	$\longrightarrow$	p + ^{26}Mg	n + ^{26}Al	$\longrightarrow$	^{4}He + ^{23}Na
n + ^{26}Al	$\longrightarrow$	^{4}He + ^{23}Na	n + ^{26}Al	$\longrightarrow$	^{4}He + ^{23}Na
p + ^{26}Al	$\longrightarrow$	^{4}He + ^{23}Mg	^{4}He + ^{26}Al	$\longrightarrow$	n + ^{29}P
^{4}He + ^{26}Al	$\longrightarrow$	p + ^{29}Si	p + ^{27}Al	$\longrightarrow$	^{4}He + ^{24}Mg
p + ^{27}Al	$\longrightarrow$	^{4}He + ^{24}Mg	p + ^{27}Al	$\longrightarrow$	^{4}He + ^{24}Mg
p + ^{27}Al	$\longrightarrow$	^{12}C + ^{16}O	^{4}He + ^{27}Al	$\longrightarrow$	n + ^{30}P
^{4}He + ^{27}Al	$\longrightarrow$	n + ^{30}P	^{4}He + ^{27}Al	$\longrightarrow$	p + ^{30}Si
n + ^{28}Si	$\longrightarrow$	^{4}He + ^{25}Mg	n + ^{28}Si	$\longrightarrow$	^{4}He + ^{25}Mg
p + ^{28}Si	$\longrightarrow$	^{4}He + ^{25}Al	^{4}He + ^{28}Si	$\longrightarrow$	n + ^{31}S
^{4}He + ^{28}Si	$\longrightarrow$	p + ^{31}P	^{4}He + ^{28}Si	$\longrightarrow$	p + ^{31}P
^{4}He + ^{28}Si	$\longrightarrow$	p + ^{31}P	^{4}He + ^{28}Si	$\longrightarrow$	^{12}C + ^{20}Ne
^{4}He + ^{28}Si	$\longrightarrow$	^{16}O + ^{16}O	n + ^{29}Si	$\longrightarrow$	^{4}He + ^{26}Mg
n + ^{29}Si	$\longrightarrow$	^{4}He + ^{26}Mg	p + ^{29}Si	$\longrightarrow$	n + ^{29}P

Table A.3 continued.

p + ^{29}Si	$\longrightarrow$	^{4}He + ^{26}Al		^{4}He + ^{29}Si	$\longrightarrow$	n + ^{32}S	
p + ^{30}Si	$\longrightarrow$	n + ^{30}P		p + ^{30}Si	$\longrightarrow$	^{4}He + ^{27}Al	
^{4}He + ^{30}Si	$\longrightarrow$	n + ^{33}S		n + ^{29}P	$\longrightarrow$	p + ^{29}Si	
n + ^{29}P	$\longrightarrow$	^{4}He + ^{26}Al		^{4}He + ^{29}P	$\longrightarrow$	p + ^{32}S	
n + ^{30}P	$\longrightarrow$	p + ^{30}Si		n + ^{30}P	$\longrightarrow$	^{4}He + ^{27}Al	
n + ^{30}P	$\longrightarrow$	^{4}He + ^{27}Al		^{4}He + ^{30}P	$\longrightarrow$	n + ^{33}Cl	
^{4}He + ^{30}P	$\longrightarrow$	p + ^{33}S		p + ^{31}P	$\longrightarrow$	n + ^{31}S	
p + ^{31}P	$\longrightarrow$	^{4}He + ^{28}Si		p + ^{31}P	$\longrightarrow$	^{4}He + ^{28}Si	
p + ^{31}P	$\longrightarrow$	^{4}He + ^{28}Si		p + ^{31}P	$\longrightarrow$	^{12}C + ^{20}Ne	
p + ^{31}P	$\longrightarrow$	^{16}O + ^{16}O		^{4}He + ^{31}P	$\longrightarrow$	n + ^{34}Cl	
n + ^{31}S	$\longrightarrow$	p + ^{31}P		n + ^{31}S	$\longrightarrow$	^{4}He + ^{28}Si	
n + ^{31}S	$\longrightarrow$	^{12}C + ^{20}Ne		n + ^{31}S	$\longrightarrow$	^{16}O + ^{16}O	
^{4}He + ^{31}S	$\longrightarrow$	p + ^{34}Cl		n + ^{32}S	$\longrightarrow$	^{4}He + ^{29}Si	
p + ^{32}S	$\longrightarrow$	^{4}He + ^{29}P		^{4}He + ^{32}S	$\longrightarrow$	p + ^{35}Cl	
^{4}He + ^{32}S	$\longrightarrow$	p + ^{35}Cl		^{4}He + ^{32}S	$\longrightarrow$	p + ^{35}Cl	
^{4}He + ^{32}S	$\longrightarrow$	p + ^{35}Cl		n + ^{33}S	$\longrightarrow$	^{4}He + ^{30}Si	
p + ^{33}S	$\longrightarrow$	n + ^{33}Cl		p + ^{33}S	$\longrightarrow$	^{4}He + ^{30}P	
^{4}He + ^{33}S	$\longrightarrow$	n + ^{36}Ar		n + ^{33}Cl	$\longrightarrow$	p + ^{33}S	
n + ^{33}Cl	$\longrightarrow$	^{4}He + ^{30}P		^{4}He + ^{33}Cl	$\longrightarrow$	p + ^{36}Ar	
n + ^{34}Cl	$\longrightarrow$	^{4}He + ^{31}P		p + ^{34}Cl	$\longrightarrow$	^{4}He + ^{31}S	
^{4}He + ^{34}Cl	$\longrightarrow$	p + ^{37}Ar		p + ^{35}Cl	$\longrightarrow$	^{4}He + ^{32}S	
p + ^{35}Cl	$\longrightarrow$	^{4}He + ^{32}S		p + ^{35}Cl	$\longrightarrow$	^{4}He + ^{32}S	
p + ^{35}Cl	$\longrightarrow$	^{4}He + ^{32}S		^{4}He + ^{35}Cl	$\longrightarrow$	p + ^{38}Ar	
n + ^{36}Ar	$\longrightarrow$	^{4}He + ^{33}S		p + ^{36}Ar	$\longrightarrow$	^{4}He + ^{33}Cl	
^{4}He + ^{36}Ar	$\longrightarrow$	p + ^{39}K		p + ^{37}Ar	$\longrightarrow$	^{4}He + ^{34}Cl	
^{4}He + ^{37}Ar	$\longrightarrow$	n + ^{40}Ca		p + ^{38}Ar	$\longrightarrow$	^{4}He + ^{35}Cl	
p + ^{39}Ar	$\longrightarrow$	n + ^{39}K		n + ^{39}K	$\longrightarrow$	p + ^{39}Ar	
p + ^{39}K	$\longrightarrow$	^{4}He + ^{36}Ar		n + ^{40}Ca	$\longrightarrow$	^{4}He + ^{37}Ar	
^{4}He + ^{40}Ca	$\longrightarrow$	p + ^{43}Sc		p + ^{43}Sc	$\longrightarrow$	^{4}He + ^{40}Ca	
^{4}He + ^{44}Ti	$\longrightarrow$	p + ^{47}V		p + ^{47}V	$\longrightarrow$	^{4}He + ^{44}Ti	
^{4}He + ^{48}Cr	$\longrightarrow$	p + ^{51}Mn		p + ^{51}Mn	$\longrightarrow$	^{4}He + ^{48}Cr	
^{4}He + ^{52}Fe	$\longrightarrow$	p + ^{55}Co		^{4}He + ^{56}Fe	$\longrightarrow$	n + ^{59}Ni	
p + ^{55}Co	$\longrightarrow$	^{4}He + ^{52}Fe		^{4}He + ^{55}Co	$\longrightarrow$	p + ^{58}Ni	
p + ^{58}Ni	$\longrightarrow$	^{4}He + ^{55}Co		n + ^{59}Ni	$\longrightarrow$	^{4}He + ^{56}Fe	
p + ^{11}B	$\longrightarrow$	^{4}He + ^{4}He + ^{4}He		p + ^{11}B	$\longrightarrow$	^{4}He + ^{4}He + ^{4}He	
^{4}He + ^{4}He + ^{4}He	$\longrightarrow$	^{12}C		^{4}He + ^{4}He + ^{4}He	$\longrightarrow$	^{12}C	
^{4}He + ^{4}He + ^{4}He	$\longrightarrow$	^{12}C					

B Abundances tables

B.1 Models at solar metallicity

The nucleosynthesis yields of the models presented in Chapter III are listed. As described in Section III.2.2, the abundances of stable and radioactive nuclei are split. The nucleosynthetic yields of stable isotopes are given at $t = 100\,\mathrm{s}$ after He detonation ignition in Tables B.1 to B.4. The abundances of radioactive nuclides with lifetime less than 2 Gyr are decayed to stability and included in those tables. Isotopes with longer lifetimes are listed with their abundances at $t = 100\,\mathrm{s}$. Tables B.5 to B.8 summaries the nucleosynthetic yields of selected radioactive nuclides at $t = 100\,\mathrm{s}$. For each model the abundances are split into those originating from the core and shell detonation. The tables are taken from Gronow et al. (2021a).

Table B.1: Asymptotic nucleosynthetic yields (in $M_\odot$) of Models M08_10_r, M08_05, and M08_03.

	M08_10_r		M08_05		M08_03	
	He det $[M_\odot]$	core det $[M_\odot]$	He det $[M_\odot]$	core det $[M_\odot]$	He det $[M_\odot]$	core det $[M_\odot]$
^{12}C	1.19e-04	1.05e-03	2.31e-03	7.46e-03	3.38e-03	1.25e-02
^{13}C	5.81e-11	1.12e-10	4.08e-10	1.22e-07	1.41e-09	3.50e-07
^{14}N	1.74e-05	1.73e-08	1.79e-05	7.46e-06	1.83e-05	1.02e-05
^{15}N	1.86e-08	6.51e-10	6.27e-08	1.48e-08	4.42e-07	2.06e-08
^{16}O	9.27e-03	8.08e-02	6.29e-03	1.16e-01	2.62e-03	1.45e-01
^{17}O	1.10e-08	5.33e-09	3.02e-08	1.84e-06	6.01e-08	3.68e-06
^{18}O	7.26e-08	2.52e-10	1.29e-07	3.27e-08	5.87e-07	4.98e-08
^{19}F	9.88e-09	1.58e-11	4.05e-08	6.43e-10	5.06e-07	2.45e-09
^{20}Ne	1.58e-04	2.86e-03	3.06e-03	5.23e-03	1.63e-03	6.24e-03
^{21}Ne	4.19e-08	1.40e-07	2.64e-07	2.73e-06	1.21e-06	3.13e-06
^{22}Ne	4.48e-07	3.45e-08	6.39e-07	7.21e-05	1.90e-06	2.67e-04
^{23}Na	1.56e-06	1.62e-05	1.63e-05	7.22e-05	1.04e-05	9.07e-05
^{24}Mg	3.16e-03	5.78e-03	4.21e-03	8.19e-03	2.09e-03	1.04e-02
^{25}Mg	2.69e-06	3.44e-05	2.39e-05	1.43e-04	4.02e-05	1.71e-04
^{26}Mg	2.60e-06	4.94e-05	3.72e-05	1.84e-04	3.55e-05	2.02e-04
^{27}Al	7.90e-05	3.25e-04	1.49e-04	4.83e-04	8.26e-05	6.10e-04
^{28}Si	1.28e-02	1.92e-01	9.25e-03	2.29e-01	4.21e-03	2.57e-01
^{29}Si	9.09e-05	6.14e-04	1.11e-04	9.26e-04	5.34e-05	1.13e-03
^{30}Si	1.07e-04	1.09e-03	1.07e-04	1.53e-03	6.99e-05	1.90e-03
^{31}P	7.68e-05	4.53e-04	8.82e-05	6.18e-04	6.60e-05	7.58e-04
^{32}S	5.51e-03	1.10e-01	4.69e-03	1.27e-01	2.40e-03	1.41e-01
^{33}S	7.60e-05	3.14e-04	5.34e-05	4.17e-04	1.37e-05	5.07e-04
^{34}S	1.31e-04	2.31e-03	2.57e-05	3.08e-03	1.14e-05	3.64e-03
^{36}S	4.17e-09	1.49e-07	1.23e-08	3.52e-07	2.18e-08	4.03e-07
^{35}Cl	3.31e-05	1.29e-04	4.85e-05	1.65e-04	4.91e-05	1.97e-04
^{37}Cl	7.87e-06	2.35e-05	1.01e-05	3.00e-05	8.90e-07	3.48e-05
^{36}Ar	1.81e-03	1.96e-02	2.11e-03	2.17e-02	1.11e-03	2.34e-02

Table B.1 continued.

	M08_10_r		M08_05		M08_03	
	He det $[M_\odot]$	core det $[M_\odot]$	He det $[M_\odot]$	core det $[M_\odot]$	He det $[M_\odot]$	core det $[M_\odot]$
^{38}Ar	4.12e-05	1.00e-03	1.49e-05	1.31e-03	2.62e-06	1.52e-03
^{40}Ar	6.85e-10	1.77e-08	9.59e-09	7.65e-08	2.04e-08	8.18e-08
^{39}K	9.17e-05	6.52e-05	1.37e-04	8.22e-05	1.04e-04	9.39e-05
^{41}K	3.57e-06	4.17e-06	9.55e-06	5.21e-06	5.35e-06	5.93e-06
^{40}Ca	6.23e-03	1.74e-02	8.00e-03	1.85e-02	3.10e-03	1.94e-02
^{42}Ca	7.70e-06	2.60e-05	6.18e-06	3.36e-05	7.83e-06	3.88e-05
^{43}Ca	2.99e-05	1.77e-07	2.00e-05	1.58e-07	1.93e-05	1.83e-07
^{44}Ca	1.79e-03	1.38e-05	2.68e-03	1.21e-05	2.16e-04	1.18e-05
^{46}Ca	2.18e-11	5.18e-09	3.62e-09	3.14e-08	7.55e-09	3.27e-08
^{48}Ca	6.30e-10	1.35e-10	9.97e-10	2.38e-09	1.84e-09	3.47e-09
^{45}Sc	4.24e-06	2.49e-07	5.86e-06	3.29e-07	1.15e-06	3.71e-07
^{46}Ti	7.74e-06	9.77e-06	3.51e-06	1.24e-05	1.14e-06	1.41e-05
^{47}Ti	7.00e-05	6.12e-07	8.07e-05	5.99e-07	7.22e-06	6.66e-07
^{48}Ti	3.82e-03	3.33e-04	2.59e-03	3.13e-04	7.37e-06	2.86e-04
^{49}Ti	3.55e-05	2.41e-05	2.49e-05	2.35e-05	2.72e-07	2.20e-05
^{50}Ti	1.02e-09	2.55e-08	8.32e-09	4.52e-08	1.89e-08	5.38e-08
^{50}V	6.01e-10	2.20e-08	1.34e-09	3.15e-08	1.23e-09	3.90e-08
^{51}V	2.96e-04	6.70e-05	1.19e-04	6.50e-05	2.64e-07	6.03e-05
^{50}Cr	3.80e-05	2.27e-04	9.65e-06	2.50e-04	1.49e-07	2.62e-04
^{52}Cr	7.48e-03	7.34e-03	8.05e-04	6.78e-03	1.14e-06	5.66e-03
^{53}Cr	1.13e-04	7.01e-04	2.29e-05	6.62e-04	1.03e-07	5.67e-04
^{54}Cr	5.56e-09	1.25e-07	4.06e-08	2.16e-07	8.08e-08	2.61e-07
^{55}Mn	9.42e-04	3.86e-03	3.17e-05	3.58e-03	5.87e-07	2.91e-03
^{54}Fe	7.33e-05	2.33e-02	1.08e-05	2.44e-02	1.27e-06	2.36e-02
^{56}Fe	1.49e-02	3.12e-01	8.14e-05	2.01e-01	2.21e-05	1.32e-01
^{57}Fe	1.34e-03	5.53e-03	1.24e-05	2.59e-03	3.50e-06	1.55e-03
^{58}Fe	1.55e-07	9.49e-07	2.75e-06	4.03e-06	4.14e-06	5.21e-06
^{59}Co	4.83e-05	1.33e-04	1.65e-05	1.90e-05	6.03e-06	1.06e-05
^{58}Ni	2.12e-04	7.84e-03	1.89e-05	3.25e-03	5.52e-06	2.03e-03
^{60}Ni	1.60e-03	1.98e-03	2.02e-05	2.17e-04	7.13e-06	1.22e-04
^{61}Ni	3.05e-04	8.07e-05	7.62e-06	1.43e-05	2.48e-06	1.23e-05
^{62}Ni	1.63e-04	6.73e-04	1.54e-05	1.07e-04	3.29e-06	8.82e-05
^{64}Ni	6.62e-08	2.67e-06	2.46e-07	3.72e-06	2.25e-07	4.57e-06
^{63}Cu	6.90e-06	4.82e-06	2.35e-06	7.33e-06	4.96e-07	8.82e-06
^{64}Zn	1.35e-04	9.67e-06	2.11e-06	6.50e-06	1.28e-07	8.02e-06
^{66}Zn	2.60e-05	3.18e-05	2.50e-06	2.92e-05	2.62e-07	3.58e-05
^{67}Zn	4.92e-06	5.55e-07	9.79e-07	6.99e-07	3.56e-08	8.23e-07
^{68}Zn	8.43e-06	2.24e-06	1.21e-06	2.99e-06	3.76e-08	3.70e-06
^{70}Zn	2.65e-10	2.31e-08	2.93e-09	3.09e-08	4.30e-09	3.64e-08
^{69}Ga	6.81e-07	9.18e-07	1.04e-07	1.17e-06	1.19e-08	1.40e-06
^{71}Ga	5.87e-08	2.01e-07	2.90e-08	2.30e-07	8.17e-09	2.70e-07

Table B.2: Asymptotic nucleosynthetic yields (in $M_\odot$) of Models M09_10_r, M09_05, and M09_03.

	M09_10_r		M09_05		M09_03	
	He det $[M_\odot]$	core det $[M_\odot]$	He det $[M_\odot]$	core det $[M_\odot]$	He det $[M_\odot]$	core det $[M_\odot]$
^{12}C	3.91e-05	1.32e-04	4.33e-04	2.63e-03	3.47e-03	4.88e-03
^{13}C	1.69e-09	7.02e-12	1.98e-11	5.27e-09	8.25e-10	1.01e-07
^{14}N	1.75e-05	2.17e-10	1.75e-05	6.02e-07	1.76e-05	3.94e-06
^{15}N	2.59e-08	3.01e-10	1.83e-08	2.41e-09	1.04e-07	7.66e-09
^{16}O	8.52e-03	5.50e-02	7.31e-03	7.78e-02	3.93e-03	9.22e-02
^{17}O	1.10e-08	3.79e-11	1.14e-08	1.22e-07	3.99e-08	1.08e-06
^{18}O	8.95e-08	2.01e-12	7.18e-08	3.73e-09	1.61e-07	1.62e-08
^{19}F	1.13e-08	9.74e-13	1.18e-08	1.04e-10	8.06e-08	4.31e-10
^{20}Ne	1.46e-05	6.24e-04	1.04e-03	3.56e-03	2.85e-03	3.32e-03
^{21}Ne	5.23e-08	2.05e-08	5.49e-08	5.77e-07	4.12e-07	1.68e-06
^{22}Ne	4.49e-07	5.40e-09	4.59e-07	2.69e-06	8.07e-07	5.20e-05
^{23}Na	3.33e-07	3.77e-06	5.48e-06	2.76e-05	1.89e-05	4.41e-05
^{24}Mg	2.48e-03	3.27e-03	3.25e-03	5.27e-03	3.17e-03	5.83e-03
^{25}Mg	1.03e-06	9.04e-06	6.67e-06	5.75e-05	3.34e-05	8.72e-05
^{26}Mg	9.01e-07	1.08e-05	1.02e-05	8.81e-05	4.53e-05	1.15e-04
^{27}Al	3.79e-05	1.74e-04	1.10e-04	2.96e-04	1.13e-04	3.27e-04
^{28}Si	1.26e-02	1.55e-01	9.97e-03	1.92e-01	5.77e-03	2.21e-01
^{29}Si	6.87e-05	3.38e-04	9.01e-05	6.20e-04	8.14e-05	6.75e-04
^{30}Si	9.22e-05	6.85e-04	9.71e-05	1.01e-03	8.29e-05	1.15e-03
^{31}P	4.48e-05	3.07e-04	8.41e-05	4.17e-04	7.09e-05	4.79e-04
^{32}S	4.28e-03	9.20e-02	4.42e-03	1.11e-01	2.76e-03	1.27e-01
^{33}S	4.56e-05	2.24e-04	6.80e-05	2.86e-04	2.31e-05	3.36e-04
^{34}S	2.21e-04	1.73e-03	5.56e-05	2.26e-03	1.22e-05	2.67e-03
^{36}S	3.74e-09	7.02e-08	3.36e-09	1.90e-07	1.90e-08	2.44e-07
^{35}Cl	1.95e-05	8.65e-05	3.92e-05	1.19e-04	4.14e-05	1.34e-04
^{37}Cl	3.64e-06	1.81e-05	9.30e-06	2.30e-05	3.03e-06	2.71e-05
^{36}Ar	1.24e-03	1.71e-02	1.53e-03	2.01e-02	1.13e-03	2.27e-02
^{38}Ar	5.95e-05	7.74e-04	2.38e-05	1.02e-03	4.08e-06	1.20e-03
^{40}Ar	2.76e-10	6.98e-09	1.32e-09	3.30e-08	1.65e-08	5.03e-08
^{39}K	4.38e-05	5.11e-05	9.64e-05	6.53e-05	8.09e-05	7.61e-05
^{41}K	1.40e-06	3.31e-06	6.57e-06	4.19e-06	1.04e-05	4.91e-06
^{40}Ca	4.72e-03	1.58e-02	5.10e-03	1.83e-02	3.98e-03	2.04e-02
^{42}Ca	4.08e-06	2.01e-05	8.51e-06	2.59e-05	5.50e-06	3.06e-05
^{43}Ca	1.34e-05	2.89e-07	2.43e-05	1.83e-07	1.07e-05	1.28e-07
^{44}Ca	8.85e-04	1.61e-05	2.03e-03	1.50e-05	7.20e-04	1.44e-05
^{46}Ca	1.51e-11	4.97e-10	3.57e-10	1.54e-08	6.10e-09	2.10e-08
^{48}Ca	6.28e-10	4.33e-12	6.53e-10	7.13e-10	1.29e-09	1.60e-09
^{45}Sc	1.12e-06	1.93e-07	4.53e-06	2.52e-07	5.19e-06	2.88e-07

Table B.2 continued.

	M09_10_r		M09_05		M09_03	
	He det $[M_\odot]$	core det $[M_\odot]$	He det $[M_\odot]$	core det $[M_\odot]$	He det $[M_\odot]$	core det $[M_\odot]$
^{46}Ti	3.61e-05	7.60e-06	4.43e-06	9.81e-06	2.79e-06	1.16e-05
^{47}Ti	5.43e-05	7.72e-07	5.93e-05	6.37e-07	4.40e-05	5.64e-07
^{48}Ti	1.92e-03	3.40e-04	4.60e-03	3.66e-04	1.06e-04	3.89e-04
^{49}Ti	2.40e-05	2.36e-05	4.71e-05	2.60e-05	3.83e-06	2.80e-05
^{50}Ti	9.27e-10	6.55e-09	1.91e-09	2.41e-08	1.62e-08	2.95e-08
^{50}V	3.10e-10	9.97e-09	1.00e-09	2.03e-08	1.57e-09	2.16e-08
^{51}V	2.57e-04	6.61e-05	3.91e-04	7.19e-05	5.09e-06	7.74e-05
^{50}Cr	2.08e-04	2.00e-04	2.15e-05	2.33e-04	1.51e-06	2.64e-04
^{52}Cr	3.99e-03	7.52e-03	5.15e-03	8.16e-03	4.41e-06	8.79e-03
^{53}Cr	7.08e-05	7.06e-04	1.54e-04	7.69e-04	5.07e-07	8.30e-04
^{54}Cr	4.30e-09	8.43e-08	1.04e-08	1.30e-07	8.43e-08	1.63e-07
^{55}Mn	3.75e-04	3.96e-03	4.12e-04	4.24e-03	7.16e-07	4.59e-03
^{54}Fe	5.02e-05	2.15e-02	9.12e-05	2.46e-02	1.01e-06	2.77e-02
^{56}Fe	2.61e-02	4.77e-01	2.01e-03	3.84e-01	1.60e-05	3.30e-01
^{57}Fe	2.47e-03	1.04e-02	1.44e-04	7.10e-03	3.93e-06	5.07e-03
^{58}Fe	7.34e-08	4.70e-07	5.12e-07	1.38e-06	5.13e-06	2.41e-06
^{59}Co	3.23e-04	3.68e-04	2.12e-05	1.92e-04	8.64e-06	7.76e-05
^{58}Ni	6.59e-04	1.55e-02	1.00e-04	1.04e-02	7.40e-06	7.00e-03
^{60}Ni	2.70e-03	5.73e-03	8.26e-05	2.89e-03	1.09e-05	9.51e-04
^{61}Ni	3.97e-04	2.30e-04	1.36e-05	1.15e-04	2.91e-06	3.91e-05
^{62}Ni	1.72e-04	1.92e-03	2.99e-05	9.71e-04	4.60e-06	3.35e-04
^{64}Ni	9.61e-09	9.45e-07	1.83e-07	2.35e-06	2.98e-07	2.44e-06
^{63}Cu	1.37e-05	2.65e-06	2.64e-06	5.16e-06	8.31e-07	5.02e-06
^{64}Zn	2.70e-04	1.93e-05	4.54e-06	1.08e-05	2.48e-07	5.92e-06
^{66}Zn	3.11e-05	4.90e-05	6.81e-06	3.23e-05	3.73e-07	2.41e-05
^{67}Zn	2.45e-06	1.98e-07	2.63e-06	4.89e-07	6.03e-08	4.72e-07
^{68}Zn	4.21e-06	1.41e-06	4.67e-06	1.64e-06	5.99e-08	2.01e-06
^{70}Zn	8.05e-11	7.42e-09	1.15e-09	2.07e-08	5.23e-09	2.04e-08
^{69}Ga	3.41e-07	6.68e-07	4.65e-07	6.68e-07	1.51e-08	8.02e-07
^{71}Ga	2.83e-08	1.10e-07	5.84e-08	1.41e-07	1.01e-08	1.57e-07

Table B.3: Asymptotic nucleosynthetic yields (in $M_\odot$) of Models M10_10, M010_05, and M10_03.

	M10_10		M10_05		M10_03	
	He det $[M_\odot]$	core det $[M_\odot]$	He det $[M_\odot]$	core det $[M_\odot]$	He det $[M_\odot]$	core det $[M_\odot]$
^{12}C	1.09e-05	1.65e-05	4.04e-05	4.36e-04	7.61e-04	1.23e-03
^{13}C	3.87e-09	4.13e-12	1.35e-10	1.86e-10	4.22e-11	1.95e-09
^{14}N	1.71e-05	2.86e-10	1.75e-05	3.63e-08	1.73e-05	1.78e-07
^{15}N	5.58e-10	9.98e-10	8.73e-09	3.86e-10	2.32e-08	8.45e-10
^{16}O	3.09e-03	2.73e-03	9.35e-03	6.08e-02	6.79e-03	4.88e-02
^{17}O	1.08e-08	1.24e-12	1.10e-08	8.33e-09	1.21e-08	3.84e-08
^{18}O	5.83e-08	5.00e-10	6.90e-08	2.98e-10	7.76e-08	1.10e-09
^{19}F	2.88e-09	1.49e-11	5.44e-09	8.21e-12	1.50e-08	3.69e-11
^{20}Ne	7.43e-06	1.46e-07	1.98e-05	1.50e-03	1.69e-03	1.78e-03
^{21}Ne	2.37e-08	8.14e-11	2.73e-08	6.52e-08	7.84e-08	2.26e-07
^{22}Ne	5.21e-07	6.42e-07	4.40e-07	2.37e-07	4.68e-07	9.12e-07
^{23}Na	1.45e-07	2.27e-09	4.94e-07	8.54e-06	8.07e-06	1.29e-05
^{24}Mg	2.51e-04	7.85e-05	2.94e-03	4.18e-03	3.49e-03	2.98e-03
^{25}Mg	1.09e-06	1.55e-08	1.24e-06	1.92e-05	9.85e-06	2.65e-05
^{26}Mg	1.02e-06	1.70e-08	1.05e-06	2.49e-05	1.65e-05	4.08e-05
^{27}Al	2.57e-06	1.90e-06	5.18e-05	2.38e-04	1.27e-04	1.59e-04
^{28}Si	3.70e-02	7.34e-02	1.31e-02	1.62e-01	8.87e-03	1.51e-01
^{29}Si	3.52e-05	1.25e-05	8.07e-05	4.31e-04	9.28e-05	3.57e-04
^{30}Si	5.51e-05	1.95e-05	1.01e-04	8.11e-04	9.96e-05	6.02e-04
^{31}P	2.39e-05	1.30e-05	5.59e-05	3.57e-04	8.50e-05	2.60e-04
^{32}S	1.59e-02	5.42e-02	4.89e-03	9.60e-02	3.68e-03	9.12e-02
^{33}S	1.62e-05	1.32e-05	6.05e-05	2.46e-04	5.70e-05	1.85e-04
^{34}S	1.51e-04	1.21e-04	1.69e-04	1.78e-03	2.91e-05	1.54e-03
^{36}S	6.62e-10	7.62e-10	4.44e-09	9.76e-08	3.89e-09	9.88e-08
^{35}Cl	8.81e-06	5.22e-06	1.67e-05	1.04e-04	3.07e-05	7.93e-05
^{37}Cl	1.62e-06	2.18e-06	5.46e-06	1.91e-05	7.76e-06	1.70e-05
^{36}Ar	2.78e-03	1.23e-02	1.38e-03	1.78e-02	1.21e-03	1.73e-02
^{38}Ar	4.38e-05	6.85e-05	4.62e-05	8.01e-04	1.34e-05	7.42e-04
^{40}Ar	1.31e-10	8.89e-11	3.50e-10	1.09e-08	2.05e-09	1.54e-08
^{39}K	1.14e-05	6.02e-06	4.63e-05	5.60e-05	4.93e-05	5.00e-05
^{41}K	3.87e-07	5.35e-07	2.08e-06	3.51e-06	6.35e-06	3.27e-06
^{40}Ca	3.42e-03	1.34e-02	4.26e-03	1.65e-02	3.26e-03	1.63e-02
^{42}Ca	1.03e-06	1.96e-06	5.25e-06	2.13e-05	3.38e-06	1.90e-05
^{43}Ca	4.60e-06	3.14e-07	1.36e-05	7.10e-07	5.50e-06	3.15e-07
^{44}Ca	2.72e-04	1.79e-05	7.87e-04	2.11e-05	1.09e-03	1.78e-05
^{46}Ca	1.28e-11	3.22e-13	1.48e-11	1.95e-09	8.30e-10	7.06e-09
^{48}Ca	5.96e-10	3.47e-12	6.17e-10	3.12e-11	6.77e-10	3.00e-10
^{45}Sc	3.09e-07	8.73e-08	2.47e-06	2.17e-07	3.31e-06	1.90e-07

Table B.3 continued.

	M10_10		M10_05		M10_03	
	He det $[M_\odot]$	core det $[M_\odot]$	He det $[M_\odot]$	core det $[M_\odot]$	He det $[M_\odot]$	core det $[M_\odot]$
^{46}Ti	8.00e-06	1.11e-06	5.39e-06	7.98e-06	2.43e-06	7.43e-06
^{47}Ti	1.68e-05	7.61e-07	3.20e-05	1.04e-06	4.01e-05	8.44e-07
^{48}Ti	5.55e-04	3.81e-04	2.08e-03	3.59e-04	1.67e-03	3.67e-04
^{49}Ti	9.97e-06	2.48e-05	2.33e-05	2.46e-05	1.31e-05	2.51e-05
^{50}Ti	9.14e-10	2.13e-08	8.92e-10	9.15e-09	3.12e-09	1.21e-08
^{50}V	2.24e-10	1.05e-10	3.60e-10	1.43e-08	1.19e-09	1.11e-08
^{51}V	8.14e-05	6.74e-05	1.51e-04	6.85e-05	6.42e-05	6.99e-05
^{50}Cr	9.37e-05	1.42e-04	2.34e-05	2.07e-04	4.66e-06	2.03e-04
^{52}Cr	1.98e-03	8.66e-03	4.10e-03	7.82e-03	6.56e-04	8.13e-03
^{53}Cr	6.03e-05	7.78e-04	6.72e-05	7.33e-04	1.36e-05	7.57e-04
^{54}Cr	1.08e-08	2.34e-07	3.89e-09	9.16e-08	1.65e-08	8.53e-08
^{55}Mn	2.69e-04	4.38e-03	4.85e-04	4.08e-03	1.74e-05	4.22e-03
^{54}Fe	1.09e-03	1.90e-02	4.20e-05	2.23e-02	5.54e-06	2.23e-02
^{56}Fe	3.93e-02	7.23e-01	8.25e-03	5.39e-01	6.99e-05	5.91e-01
^{57}Fe	1.48e-03	1.70e-02	5.94e-04	1.21e-02	5.82e-06	1.33e-02
^{58}Fe	2.52e-08	7.78e-07	7.79e-08	7.08e-07	1.03e-06	6.41e-07
^{59}Co	3.69e-04	6.89e-04	2.91e-05	4.78e-04	9.46e-06	5.08e-04
^{58}Ni	5.79e-04	2.55e-02	1.25e-04	1.83e-02	1.31e-05	2.05e-02
^{60}Ni	2.06e-03	1.03e-02	7.57e-04	8.20e-03	1.64e-05	8.01e-03
^{61}Ni	1.48e-04	4.03e-04	1.22e-04	3.19e-04	3.91e-06	3.19e-04
^{62}Ni	9.92e-05	3.42e-03	8.10e-05	2.51e-03	7.01e-06	2.70e-03
^{64}Ni	3.44e-09	2.18e-09	1.36e-08	1.54e-06	2.14e-07	1.21e-06
^{63}Cu	1.50e-05	1.66e-06	5.38e-06	4.24e-06	1.76e-06	3.59e-06
^{64}Zn	2.26e-04	2.97e-05	6.04e-05	2.69e-05	2.20e-06	2.39e-05
^{66}Zn	1.64e-05	6.08e-05	1.31e-05	6.29e-05	1.05e-06	5.68e-05
^{67}Zn	7.52e-07	4.15e-08	2.15e-06	3.30e-07	2.56e-07	2.79e-07
^{68}Zn	1.03e-06	2.97e-08	3.55e-06	1.56e-06	3.16e-07	8.09e-07
^{70}Zn	5.54e-11	5.12e-13	8.51e-11	1.21e-08	1.73e-09	1.02e-08
^{69}Ga	6.82e-08	5.57e-10	3.00e-07	8.07e-07	5.82e-08	3.33e-07
^{71}Ga	5.19e-09	2.61e-11	2.25e-08	1.49e-07	1.51e-08	6.96e-08

Table B.4: Asymptotic nucleosynthetic yields (in $M_\odot$) of Models M10_02 and M11_05.

	M10_02		M11_05	
	He det $[M_\odot]$	core det $[M_\odot]$	He det $[M_\odot]$	core det $[M_\odot]$
^{12}C	1.67e-03	1.95e-03	5.71e-06	2.48e-06
^{13}C	2.79e-10	2.74e-08	8.96e-10	9.04e-12
^{14}N	1.72e-05	1.00e-06	1.74e-05	9.72e-10
^{15}N	4.86e-08	2.25e-09	4.52e-09	3.70e-09
^{16}O	1.86e-03	5.70e-02	3.82e-03	7.53e-04
^{17}O	1.84e-08	2.49e-07	1.10e-08	8.18e-12
^{18}O	1.03e-07	4.29e-09	6.45e-08	2.14e-09
^{19}F	3.85e-08	1.24e-10	3.99e-09	1.17e-12
^{20}Ne	1.32e-03	1.90e-03	6.63e-06	4.34e-08
^{21}Ne	1.57e-07	5.59e-07	2.37e-08	2.17e-13
^{22}Ne	5.61e-07	1.15e-05	4.41e-07	1.77e-08
^{23}Na	8.80e-06	1.84e-05	1.50e-07	5.29e-09
^{24}Mg	1.52e-03	3.43e-03	3.28e-04	1.61e-05
^{25}Mg	1.44e-05	3.74e-05	5.91e-07	3.11e-09
^{26}Mg	2.01e-05	5.34e-05	6.69e-07	2.67e-09
^{27}Al	5.57e-05	1.85e-04	3.03e-06	3.58e-07
^{28}Si	2.93e-03	1.71e-01	5.58e-02	4.55e-02
^{29}Si	4.17e-05	4.08e-04	4.88e-05	3.78e-06
^{30}Si	4.34e-05	7.01e-04	6.69e-05	4.94e-06
^{31}P	3.77e-05	3.00e-04	3.80e-05	4.40e-06
^{32}S	1.60e-03	1.02e-01	2.44e-02	3.68e-02
^{33}S	1.32e-05	2.12e-04	2.74e-05	5.22e-06
^{34}S	9.85e-06	1.77e-03	1.89e-04	3.83e-05
^{36}S	7.65e-09	1.29e-07	7.76e-10	1.59e-10
^{35}Cl	2.57e-05	9.05e-05	1.07e-05	2.39e-06
^{37}Cl	2.04e-06	1.89e-05	3.73e-06	1.15e-06
^{36}Ar	7.88e-04	1.92e-02	4.31e-03	9.02e-03
^{38}Ar	2.49e-06	8.32e-04	8.33e-05	2.78e-05
^{40}Ar	6.89e-09	2.25e-08	1.78e-10	3.33e-11
^{39}K	5.79e-05	5.51e-05	1.75e-05	3.69e-06
^{41}K	4.73e-06	3.60e-06	1.13e-06	3.38e-07
^{40}Ca	2.38e-03	1.81e-02	5.72e-03	1.04e-02
^{42}Ca	2.45e-06	2.12e-05	2.52e-06	9.94e-07
^{43}Ca	5.21e-06	2.70e-07	2.51e-06	4.11e-07
^{44}Ca	5.69e-04	1.77e-05	1.59e-04	1.74e-05
^{46}Ca	2.85e-09	9.60e-09	1.33e-11	8.66e-14
^{48}Ca	9.16e-10	5.81e-10	6.11e-10	7.17e-15
^{45}Sc	2.59e-06	2.11e-07	5.62e-07	1.15e-07

Table B.4 continued.

	M10_02		M11_05	
	He det $[M_\odot]$	core det $[M_\odot]$	He det $[M_\odot]$	core det $[M_\odot]$
^{46}Ti	1.36e-06	8.21e-06	3.25e-06	6.85e-07
^{47}Ti	3.06e-05	7.75e-07	5.99e-06	9.53e-07
^{48}Ti	2.32e-04	3.94e-04	7.40e-04	3.24e-04
^{49}Ti	4.26e-06	2.72e-05	1.53e-05	2.03e-05
^{50}Ti	8.57e-09	1.52e-08	9.92e-10	1.31e-08
^{50}V	7.80e-10	1.30e-08	4.05e-10	3.22e-11
^{51}V	1.12e-05	7.54e-05	3.36e-05	5.54e-05
^{50}Cr	1.61e-06	2.25e-04	4.47e-05	1.00e-04
^{52}Cr	2.58e-05	8.82e-03	2.09e-03	7.31e-03
^{53}Cr	1.48e-06	8.21e-04	7.76e-05	6.48e-04
^{54}Cr	4.38e-08	9.85e-08	1.70e-08	1.45e-07
^{55}Mn	1.67e-06	4.57e-03	2.28e-04	3.68e-03
^{54}Fe	1.26e-06	2.48e-02	1.68e-03	1.46e-02
^{56}Fe	1.36e-05	5.41e-01	1.20e-02	8.26e-01
^{57}Fe	2.96e-06	1.13e-02	3.16e-04	2.10e-02
^{58}Fe	2.57e-06	9.30e-07	2.92e-08	4.87e-07
^{59}Co	5.40e-06	3.86e-04	4.13e-05	9.52e-04
^{58}Ni	5.76e-06	1.70e-02	2.06e-04	3.04e-02
^{60}Ni	5.65e-06	6.17e-03	2.67e-04	1.38e-02
^{61}Ni	1.76e-06	2.43e-04	2.04e-05	5.12e-04
^{62}Ni	2.87e-06	2.07e-03	2.41e-05	4.35e-03
^{64}Ni	1.50e-07	1.43e-06	3.53e-09	9.96e-10
^{63}Cu	5.14e-07	3.72e-06	8.06e-06	2.89e-06
^{64}Zn	2.05e-07	1.93e-05	3.20e-05	4.46e-05
^{66}Zn	2.46e-07	4.74e-05	3.19e-06	7.79e-05
^{67}Zn	5.97e-08	3.15e-07	3.04e-07	5.47e-08
^{68}Zn	5.84e-08	9.76e-07	3.43e-07	3.07e-08
^{70}Zn	2.75e-09	1.17e-08	5.80e-11	3.38e-16
^{69}Ga	9.76e-09	4.07e-07	2.51e-08	5.48e-11
^{71}Ga	5.62e-09	8.58e-08	3.59e-09	2.19e-12

Table B.5: Nucleosynthetic yields (in $M_\odot$) of select radioactive nuclides of Models M08_10_r, M08_05, and M08_03.

	M08_10_r		M08_05		M08_03	
	He det $[M_\odot]$	core det $[M_\odot]$	He det $[M_\odot]$	core det $[M_\odot]$	He det $[M_\odot]$	core det $[M_\odot]$
^{14}C	6.14e-12	4.85e-09	1.94e-08	4.11e-06	7.71e-08	5.50e-06
^{22}Na	1.33e-08	1.00e-08	8.39e-08	2.02e-08	9.95e-07	2.37e-08
^{26}Al	6.81e-07	5.68e-06	1.00e-05	9.38e-06	1.33e-05	1.16e-05
^{32}Si	2.45e-12	2.88e-10	3.20e-10	7.18e-09	2.33e-09	7.49e-09
^{32}P	2.07e-08	2.91e-07	1.54e-08	4.73e-07	1.09e-08	5.68e-07
^{33}P	1.65e-08	2.24e-07	6.81e-09	3.43e-07	6.61e-09	4.29e-07
^{35}S	1.14e-08	3.48e-07	1.43e-08	5.19e-07	8.69e-09	6.27e-07
^{36}Cl	7.68e-08	8.48e-07	2.88e-08	1.15e-06	6.12e-09	1.42e-06
^{37}Ar	7.80e-06	2.28e-05	1.01e-05	2.89e-05	8.25e-07	3.34e-05
^{39}Ar	5.98e-10	1.70e-08	1.17e-08	9.01e-08	2.74e-08	1.00e-07
^{40}K	4.83e-09	8.20e-08	7.00e-09	1.13e-07	4.16e-09	1.36e-07
^{41}Ca	3.57e-06	4.17e-06	9.55e-06	5.18e-06	5.34e-06	5.89e-06
^{44}Ti	1.79e-03	1.37e-05	2.68e-03	1.19e-05	2.16e-04	1.16e-05
^{48}V	1.21e-06	5.34e-08	1.21e-06	7.19e-08	1.10e-07	7.22e-08
^{49}V	3.98e-07	2.96e-07	3.74e-07	3.69e-07	3.40e-08	4.27e-07
^{48}Cr	3.82e-03	3.33e-04	2.59e-03	3.12e-04	7.23e-06	2.85e-04
^{49}Cr	3.51e-05	2.38e-05	2.45e-05	2.31e-05	2.33e-07	2.15e-05
^{51}Cr	2.61e-06	1.75e-06	1.35e-06	2.13e-06	1.04e-08	2.42e-06
^{51}Mn	2.94e-04	6.52e-05	1.18e-04	6.28e-05	2.37e-07	5.78e-05
^{52}Mn	9.81e-06	2.71e-06	2.06e-06	3.09e-06	9.67e-09	2.84e-06
^{53}Mn	5.69e-06	2.75e-05	1.43e-06	3.17e-05	3.39e-08	3.27e-05
^{54}Mn	2.66e-09	9.38e-08	9.85e-09	1.11e-07	6.18e-09	1.30e-07
^{52}Fe	7.47e-03	7.31e-03	8.02e-04	6.75e-03	8.84e-07	5.63e-03
^{53}Fe	1.07e-04	6.74e-04	2.14e-05	6.30e-04	3.33e-08	5.34e-04
^{55}Fe	1.35e-06	6.10e-05	4.44e-07	7.52e-05	9.53e-08	8.62e-05
^{59}Fe	4.29e-09	3.23e-07	9.78e-07	3.00e-06	2.50e-06	3.39e-06
^{60}Fe	1.28e-08	2.37e-06	1.90e-06	1.06e-05	3.93e-06	1.14e-05
^{55}Co	9.40e-04	3.80e-03	3.12e-05	3.50e-03	2.85e-07	2.82e-03
^{56}Co	3.59e-06	1.31e-05	5.30e-07	1.33e-05	3.05e-08	1.09e-05
^{57}Co	2.14e-06	8.08e-06	3.65e-06	9.72e-06	1.77e-06	1.09e-05
^{58}Co	5.92e-08	6.11e-08	4.99e-07	7.83e-08	1.72e-07	9.95e-08
^{60}Co	2.61e-08	1.36e-06	1.00e-06	2.68e-06	8.98e-07	3.28e-06
^{56}Ni	1.49e-02	3.12e-01	6.67e-05	2.01e-01	9.94e-07	1.32e-01
^{57}Ni	1.33e-03	5.52e-03	8.01e-06	2.58e-03	2.36e-07	1.54e-03
^{59}Ni	1.34e-05	1.83e-05	8.62e-06	4.60e-06	9.89e-07	3.71e-06
^{63}Ni	1.00e-08	1.22e-06	1.95e-07	2.48e-06	2.27e-07	2.75e-06
^{62}Zn	1.59e-04	6.25e-04	1.32e-05	3.83e-05	2.39e-06	1.73e-06
^{65}Zn	5.93e-07	7.73e-07	2.20e-07	9.29e-07	9.24e-09	1.17e-06
^{65}Ge	3.28e-06	2.53e-07	1.21e-07	1.22e-08	1.06e-08	9.76e-10

Table B.6: Nucleosynthetic yields (in $M_\odot$) of select radioactive nuclides of Models M09_10_r, M09_05, and M09_03.

	M09_10_r		M09_05		M09_03	
	He det $[M_\odot]$	core det $[M_\odot]$	He det $[M_\odot]$	core det $[M_\odot]$	He det $[M_\odot]$	core det $[M_\odot]$
^{14}C	1.09e-11	4.62e-13	5.06e-11	3.22e-07	3.63e-08	2.20e-06
^{22}Na	1.31e-08	4.67e-09	2.20e-08	1.35e-08	1.63e-07	1.29e-08
^{26}Al	1.18e-07	1.59e-06	3.04e-06	6.28e-06	1.37e-05	5.87e-06
^{32}Si	2.26e-12	1.08e-10	4.36e-12	1.68e-09	9.71e-10	4.75e-09
^{32}P	1.62e-08	1.71e-07	1.56e-08	2.95e-07	1.20e-08	3.42e-07
^{33}P	1.30e-08	1.39e-07	1.05e-08	2.02e-07	4.83e-09	2.46e-07
^{35}S	3.81e-09	1.67e-07	1.39e-08	3.33e-07	9.83e-09	3.64e-07
^{36}Cl	6.33e-08	5.35e-07	5.00e-08	7.53e-07	1.19e-08	8.56e-07
^{37}Ar	3.58e-06	1.76e-05	9.26e-06	2.24e-05	2.98e-06	2.62e-05
^{39}Ar	1.67e-10	6.89e-09	1.21e-09	3.23e-08	2.15e-08	5.73e-08
^{40}K	1.31e-09	4.36e-08	6.22e-09	7.47e-08	4.92e-09	8.02e-08
^{41}Ca	1.40e-06	3.31e-06	6.57e-06	4.18e-06	1.04e-05	4.89e-06
^{44}Ti	8.85e-04	1.60e-05	2.03e-03	1.48e-05	7.19e-04	1.43e-05
^{48}V	5.36e-07	4.44e-08	2.12e-06	5.58e-08	5.76e-07	6.57e-08
^{49}V	2.43e-07	2.24e-07	5.36e-07	2.83e-07	1.35e-07	3.25e-07
^{48}Cr	1.92e-03	3.39e-04	4.60e-03	3.66e-04	1.05e-04	3.89e-04
^{49}Cr	2.38e-05	2.34e-05	4.66e-05	2.57e-05	3.69e-06	2.76e-05
^{51}Cr	2.03e-06	1.39e-06	3.69e-06	1.75e-06	9.57e-08	2.04e-06
^{51}Mn	2.55e-04	6.47e-05	3.87e-04	7.01e-05	4.98e-06	7.53e-05
^{52}Mn	4.12e-06	2.56e-06	1.12e-05	2.96e-06	1.17e-07	3.50e-06
^{53}Mn	3.32e-06	2.45e-05	7.97e-06	2.90e-05	8.28e-08	3.42e-05
^{54}Mn	1.84e-09	6.70e-08	3.96e-09	8.50e-08	1.71e-08	9.77e-08
^{52}Fe	3.98e-03	7.50e-03	5.14e-03	8.13e-03	4.12e-06	8.76e-03
^{53}Fe	6.74e-05	6.81e-04	1.46e-04	7.40e-04	3.99e-07	7.96e-04
^{55}Fe	8.49e-07	4.69e-05	1.41e-06	6.13e-05	1.31e-07	7.20e-05
^{59}Fe	9.31e-10	1.83e-08	1.10e-07	9.79e-07	1.75e-06	1.74e-06
^{60}Fe	4.99e-10	2.90e-07	2.69e-07	5.75e-06	3.55e-06	6.96e-06
^{55}Co	3.74e-04	3.91e-03	4.11e-04	4.18e-03	4.33e-07	4.52e-03
^{56}Co	1.25e-06	1.41e-05	3.09e-06	1.47e-05	4.91e-08	1.56e-05
^{57}Co	1.10e-06	6.69e-06	1.96e-06	8.28e-06	2.39e-06	9.52e-06
^{58}Co	2.23e-08	4.02e-08	1.35e-07	5.35e-08	3.60e-07	5.90e-08
^{60}Co	1.34e-09	3.07e-07	2.60e-07	1.90e-06	2.21e-06	1.72e-06
^{56}Ni	2.61e-02	4.77e-01	1.99e-03	3.84e-01	1.01e-06	3.30e-01
^{57}Ni	2.47e-03	1.04e-02	1.42e-04	7.09e-03	3.20e-07	5.06e-03
^{59}Ni	6.92e-05	4.45e-05	9.19e-06	2.51e-05	2.31e-06	1.30e-05
^{63}Ni	5.86e-10	2.06e-07	8.28e-08	1.80e-06	2.48e-07	1.66e-06
^{62}Zn	1.68e-04	1.89e-03	2.69e-05	9.28e-04	3.39e-06	2.85e-04
^{65}Zn	3.13e-07	5.07e-07	4.31e-07	5.58e-07	3.13e-08	6.35e-07
^{65}Ge	4.25e-06	8.59e-07	4.18e-07	3.64e-07	9.86e-09	6.90e-08

Table B.7: Nucleosynthetic yields (in $M_\odot$) of select radioactive nuclides of Models M10_10, M10_05, and M10_03.

	M10_10		M10_05		M10_03	
	He det $[M_\odot]$	core det $[M_\odot]$	He det $[M_\odot]$	core det $[M_\odot]$	He det $[M_\odot]$	core det $[M_\odot]$
^{14}C	3.28e-13	1.15e-15	3.94e-12	1.78e-08	7.86e-10	9.35e-08
^{22}Na	8.03e-09	3.68e-09	5.29e-09	6.71e-09	3.05e-08	6.73e-09
^{26}Al	6.03e-07	1.27e-10	1.13e-07	3.35e-06	5.02e-06	3.18e-06
^{32}Si	5.03e-13	5.57e-13	2.80e-12	2.02e-10	1.10e-11	6.63e-10
^{32}P	4.21e-09	3.04e-09	2.08e-08	2.15e-07	1.44e-08	1.66e-07
^{33}P	1.75e-09	2.11e-09	1.68e-08	1.68e-07	8.37e-09	1.13e-07
^{35}S	8.87e-10	1.56e-09	5.33e-09	2.49e-07	1.44e-08	1.85e-07
^{36}Cl	8.43e-09	1.25e-08	7.85e-08	6.40e-07	3.97e-08	4.40e-07
^{37}Ar	1.61e-06	2.17e-06	5.39e-06	1.86e-05	7.72e-06	1.66e-05
^{39}Ar	4.68e-11	1.26e-10	2.32e-10	1.08e-08	1.90e-09	1.48e-08
^{40}K	3.45e-10	7.03e-10	1.90e-09	6.21e-08	6.33e-09	4.22e-08
^{41}Ca	3.86e-07	5.35e-07	2.08e-06	3.50e-06	6.35e-06	3.27e-06
^{44}Ti	2.72e-04	1.79e-05	7.87e-04	2.10e-05	1.09e-03	1.77e-05
^{48}V	1.65e-07	2.51e-08	5.88e-07	6.15e-08	5.47e-07	4.46e-08
^{49}V	5.74e-08	1.04e-07	2.21e-07	2.51e-07	1.64e-07	2.11e-07
^{48}Cr	5.54e-04	3.81e-04	2.08e-03	3.59e-04	1.66e-03	3.67e-04
^{49}Cr	9.91e-06	2.46e-05	2.31e-05	2.43e-05	1.29e-05	2.49e-05
^{51}Cr	4.42e-07	3.62e-07	1.13e-06	1.47e-06	5.51e-07	1.38e-06
^{51}Mn	8.10e-05	6.70e-05	1.50e-04	6.70e-05	6.36e-05	6.85e-05
^{52}Mn	1.25e-06	2.58e-06	4.71e-06	2.93e-06	9.90e-07	2.74e-06
^{53}Mn	2.21e-06	1.71e-05	2.86e-06	2.58e-05	6.41e-07	2.57e-05
^{54}Mn	8.54e-09	4.81e-09	1.61e-09	7.46e-08	5.06e-09	6.38e-08
^{52}Fe	1.98e-03	8.66e-03	4.10e-03	7.80e-03	6.55e-04	8.11e-03
^{53}Fe	5.80e-05	7.61e-04	6.44e-05	7.07e-04	1.30e-05	7.31e-04
^{55}Fe	3.06e-06	8.04e-06	7.56e-07	5.00e-05	2.12e-07	4.81e-05
^{59}Fe	3.98e-11	8.17e-11	4.98e-10	1.44e-07	2.63e-07	3.84e-07
^{60}Fe	1.98e-12	3.90e-11	7.63e-10	1.10e-06	6.27e-07	2.72e-06
^{55}Co	2.66e-04	4.38e-03	4.85e-04	4.03e-03	1.71e-05	4.17e-03
^{56}Co	8.57e-07	1.60e-05	1.59e-06	1.93e-05	1.85e-07	1.61e-05
^{57}Co	5.39e-07	1.92e-06	1.07e-06	7.34e-06	1.67e-06	7.10e-06
^{58}Co	3.97e-09	1.67e-09	2.48e-08	5.22e-08	2.34e-07	3.46e-08
^{60}Co	2.75e-11	8.99e-11	1.82e-09	7.75e-07	5.09e-07	9.98e-07
^{56}Ni	3.93e-02	7.23e-01	8.23e-03	5.38e-01	5.97e-05	5.91e-01
^{57}Ni	1.48e-03	1.70e-02	5.93e-04	1.21e-02	3.77e-06	1.33e-02
^{59}Ni	4.28e-05	8.10e-05	6.80e-06	5.79e-05	6.23e-06	6.11e-05
^{63}Ni	1.70e-11	1.76e-10	9.19e-10	5.27e-07	1.29e-07	9.05e-07
^{62}Zn	9.89e-05	3.42e-03	7.65e-05	2.47e-03	4.42e-06	2.68e-03
^{65}Zn	2.97e-08	1.25e-08	1.81e-07	7.04e-07	3.26e-07	3.02e-07
^{65}Ge	3.24e-06	1.47e-06	1.72e-06	1.33e-06	3.98e-08	1.16e-06

Table B.8: Nucleosynthetic yields (in $M_\odot$) of select radioactive nuclides of Models M10_02 and M11_05.

	M10_02		M11_05	
	He det $[M_\odot]$	core det $[M_\odot]$	He det $[M_\odot]$	core det $[M_\odot]$
^{14}C	9.14e-09	5.64e-07	2.64e-12	3.26e-16
^{22}Na	8.07e-08	7.15e-09	6.13e-09	1.58e-08
^{26}Al	6.95e-06	3.35e-06	2.23e-07	1.21e-10
^{32}Si	2.77e-10	1.70e-09	6.21e-13	9.58e-14
^{32}P	5.46e-09	1.99e-07	5.58e-09	6.89e-10
^{33}P	1.87e-09	1.38e-07	2.11e-09	4.20e-10
^{35}S	4.19e-09	2.24e-07	1.13e-09	3.73e-10
^{36}Cl	6.06e-09	5.18e-07	1.30e-08	3.45e-09
^{37}Ar	2.01e-06	1.85e-05	3.71e-06	1.14e-06
^{39}Ar	8.16e-09	2.39e-08	7.60e-11	4.00e-11
^{40}K	2.67e-09	5.00e-08	7.49e-10	2.79e-10
^{41}Ca	4.72e-06	3.59e-06	1.13e-06	3.38e-07
^{44}Ti	5.69e-04	1.76e-05	1.59e-04	1.74e-05
^{48}V	3.38e-07	5.02e-08	1.28e-07	1.85e-08
^{49}V	8.35e-08	2.37e-07	7.80e-08	7.53e-08
^{48}Cr	2.32e-04	3.94e-04	7.39e-04	3.24e-04
^{49}Cr	4.17e-06	2.69e-05	1.52e-05	2.03e-05
^{51}Cr	1.25e-07	1.52e-06	3.60e-07	2.39e-07
^{51}Mn	1.11e-05	7.39e-05	3.32e-05	5.52e-05
^{52}Mn	1.88e-07	3.02e-06	1.01e-06	1.96e-06
^{53}Mn	1.10e-07	2.80e-05	3.29e-06	1.26e-05
^{54}Mn	8.39e-09	7.02e-08	1.46e-08	2.26e-09
^{52}Fe	2.54e-05	8.80e-03	2.08e-03	7.30e-03
^{53}Fe	1.35e-06	7.93e-04	7.43e-05	6.35e-04
^{55}Fe	9.19e-08	5.27e-05	6.88e-06	4.48e-06
^{59}Fe	8.76e-07	6.07e-07	1.82e-10	5.21e-11
^{60}Fe	1.79e-06	3.30e-06	2.32e-11	2.51e-11
^{55}Co	1.47e-06	4.52e-03	2.21e-04	3.68e-03
^{56}Co	6.43e-08	1.67e-05	9.84e-07	1.46e-05
^{57}Co	1.75e-06	7.51e-06	8.71e-07	1.62e-06
^{58}Co	1.86e-07	3.86e-08	5.75e-09	7.42e-10
^{60}Co	1.04e-06	1.03e-06	7.02e-11	5.83e-11
^{56}Ni	1.87e-06	5.41e-01	1.20e-02	8.26e-01
^{57}Ni	4.81e-07	1.13e-02	3.15e-04	2.10e-02
^{59}Ni	1.54e-06	4.68e-05	3.58e-06	1.04e-04
^{63}Ni	1.26e-07	9.72e-07	3.80e-11	1.09e-10
^{62}Zn	2.25e-06	2.04e-03	2.39e-05	4.35e-03
^{65}Zn	1.86e-08	3.69e-07	6.13e-09	1.43e-08
^{65}Ge	9.83e-09	8.86e-07	8.24e-07	2.03e-06

B.2 Models at 0.01 $Z_\odot$, 0.1 $Z_\odot$, and 3 $Z_\odot$ metallicity

The nucleosynthesis yields of the models included in the parameter study involving different metallicities (Chapter IV) are given in Tables B.9 to B.30 in the same way as described in Appendix B.1 (from Gronow et al. 2021b). The abundances of stable nuclides (including radioactive isotopes with lifetimes longer than 2 Gyr) are found in Tables B.9 to B.19. Tables B.20 to B.30 list the nucleosynthetic yields of some radioactive isotopes at $t = 100$ s after He detonation ignition.

Table B.9: Asymptotic nucleosynthetic yields (in $M_\odot$) of Model M08_03 with 0.01, 0.1, and 3 $Z_\odot$.

	M08_03_001		M08_03_01		M08_03_3	
	He det $[M_\odot]$	core det $[M_\odot]$	He det $[M_\odot]$	core det $[M_\odot]$	He det $[M_\odot]$	core det $[M_\odot]$
^{12}C	3.43e-03	1.26e-02	3.43e-03	1.26e-02	3.33e-03	1.21e-02
^{13}C	1.81e-09	2.42e-07	1.80e-09	2.32e-07	1.19e-09	9.05e-07
^{14}N	6.43e-07	9.97e-06	1.73e-06	9.67e-06	3.67e-05	1.29e-05
^{15}N	2.33e-07	2.11e-08	2.47e-07	2.06e-08	6.49e-07	2.62e-08
^{16}O	2.51e-03	1.44e-01	2.52e-03	1.44e-01	2.83e-03	1.46e-01
^{17}O	5.55e-08	3.48e-06	5.73e-08	3.40e-06	9.40e-08	4.32e-06
^{18}O	2.69e-07	4.71e-08	2.93e-07	4.54e-08	1.04e-06	6.96e-08
^{19}F	2.68e-07	6.87e-10	2.83e-07	7.22e-10	7.35e-07	4.97e-09
^{20}Ne	1.58e-03	6.42e-03	1.58e-03	6.42e-03	1.70e-03	5.70e-03
^{21}Ne	8.07e-07	2.38e-06	8.34e-07	2.29e-06	1.67e-06	7.77e-06
^{22}Ne	9.42e-07	1.47e-04	1.00e-06	1.43e-04	2.60e-06	8.18e-04
^{23}Na	1.03e-05	7.12e-05	1.03e-05	7.01e-05	1.06e-05	1.73e-04
^{24}Mg	2.04e-03	1.26e-02	2.04e-03	1.30e-02	2.16e-03	5.77e-03
^{25}Mg	3.46e-05	1.07e-04	3.49e-05	1.05e-04	4.90e-05	3.82e-04
^{26}Mg	3.56e-05	1.34e-04	3.56e-05	1.31e-04	3.71e-05	5.19e-04
^{27}Al	8.23e-05	5.28e-04	8.22e-05	5.31e-04	8.48e-05	6.76e-04
^{28}Si	4.15e-03	2.57e-01	4.16e-03	2.57e-01	4.38e-03	2.54e-01
^{29}Si	5.74e-05	7.62e-04	5.71e-05	7.54e-04	5.47e-05	2.56e-03
^{30}Si	7.15e-05	1.06e-03	7.14e-05	1.05e-03	7.29e-05	5.61e-03
^{31}P	6.62e-05	5.29e-04	6.62e-05	5.22e-04	6.89e-05	1.46e-03
^{32}S	2.34e-03	1.45e-01	2.35e-03	1.45e-01	2.59e-03	1.23e-01
^{33}S	1.33e-05	4.07e-04	1.33e-05	4.01e-04	1.58e-05	7.46e-04
^{34}S	1.14e-05	2.10e-03	1.14e-05	2.05e-03	1.32e-05	9.81e-03
^{36}S	6.46e-10	6.35e-08	3.18e-09	6.99e-08	3.24e-08	6.19e-06
^{35}Cl	4.61e-05	1.31e-04	4.63e-05	1.28e-04	5.50e-05	3.45e-04
^{37}Cl	6.60e-07	2.79e-05	6.76e-07	2.73e-05	1.22e-06	5.40e-05
^{36}Ar	1.06e-03	2.53e-02	1.07e-03	2.52e-02	1.23e-03	1.81e-02
^{38}Ar	2.00e-06	8.73e-04	2.05e-06	8.44e-04	3.66e-06	3.96e-03
^{40}Ar	4.72e-10	6.21e-09	4.13e-09	1.03e-08	3.25e-08	5.95e-07
^{39}K	9.16e-05	6.68e-05	9.23e-05	6.53e-05	1.20e-04	1.48e-04
^{41}K	5.60e-06	4.64e-06	5.56e-06	4.54e-06	4.82e-06	8.14e-06
^{40}Ca	3.13e-03	2.15e-02	3.13e-03	2.15e-02	3.03e-03	1.46e-02
^{42}Ca	6.36e-06	2.25e-05	6.42e-06	2.16e-05	8.27e-06	9.31e-05

Table B.9 continued.

	M08_03_001		M08_03_01		M08_03_3	
	He det $[M_\odot]$	core det $[M_\odot]$	He det $[M_\odot]$	core det $[M_\odot]$	He det $[M_\odot]$	core det $[M_\odot]$
^{43}Ca	1.78e-05	7.20e-08	1.79e-05	7.15e-08	2.00e-05	5.33e-07
^{44}Ca	2.26e-04	1.30e-05	2.25e-04	1.30e-05	1.91e-04	1.01e-05
^{46}Ca	1.56e-10	2.64e-10	1.50e-09	2.35e-09	1.23e-08	2.82e-07
^{48}Ca	2.86e-11	3.09e-11	2.73e-10	3.00e-10	5.21e-09	2.60e-08
^{45}Sc	1.13e-06	2.23e-07	1.13e-06	2.23e-07	9.56e-07	7.69e-07
^{46}Ti	9.30e-07	8.28e-06	9.34e-07	7.99e-06	1.07e-06	3.04e-05
^{47}Ti	7.18e-06	3.23e-07	7.14e-06	3.17e-07	5.88e-06	1.80e-06
^{48}Ti	8.33e-06	3.21e-04	8.23e-06	3.22e-04	6.14e-06	2.17e-04
^{49}Ti	2.86e-07	1.87e-05	2.83e-07	1.86e-05	2.20e-07	2.56e-05
^{50}Ti	1.25e-10	7.16e-10	1.28e-09	4.64e-09	4.33e-08	7.48e-07
^{50}V	1.28e-10	4.15e-09	1.77e-10	5.15e-09	3.84e-09	1.98e-07
^{51}V	2.57e-07	4.51e-05	2.56e-07	4.46e-05	2.47e-07	9.21e-05
^{50}Cr	1.30e-07	1.39e-04	1.30e-07	1.37e-04	1.29e-07	6.93e-04
^{52}Cr	8.65e-07	6.20e-03	8.78e-07	6.21e-03	1.35e-06	4.87e-03
^{53}Cr	2.90e-08	4.66e-04	3.19e-08	4.62e-04	1.55e-07	8.24e-04
^{54}Cr	2.74e-10	2.17e-08	2.82e-09	3.62e-08	1.19e-07	1.42e-06
^{55}Mn	1.09e-07	2.19e-03	1.28e-07	2.17e-03	8.88e-07	4.61e-03
^{54}Fe	2.20e-08	1.34e-02	7.53e-08	1.31e-02	1.87e-06	5.41e-02
^{56}Fe	8.98e-07	1.40e-01	1.75e-06	1.40e-01	3.40e-05	1.17e-01
^{57}Fe	9.69e-08	1.22e-03	2.00e-07	1.22e-03	6.39e-06	2.21e-03
^{58}Fe	8.95e-09	3.13e-08	9.77e-08	2.65e-07	7.06e-06	9.47e-06
^{59}Co	3.05e-08	1.21e-06	2.12e-07	1.57e-06	8.03e-06	2.77e-05
^{58}Ni	4.26e-08	1.15e-03	1.89e-07	1.13e-03	9.23e-06	4.60e-03
^{60}Ni	1.17e-07	8.42e-06	5.49e-07	1.37e-05	6.29e-06	2.15e-04
^{61}Ni	3.38e-08	2.36e-07	2.13e-07	7.28e-07	2.13e-06	2.60e-05
^{62}Ni	4.93e-08	1.36e-06	3.73e-07	4.28e-06	2.71e-06	1.43e-04
^{64}Ni	1.13e-09	1.29e-08	1.16e-08	1.25e-07	2.08e-07	1.17e-05
^{63}Cu	7.17e-09	4.58e-08	4.31e-08	4.49e-07	5.17e-07	1.06e-05
^{64}Zn	1.08e-08	9.90e-08	2.24e-08	7.80e-07	1.27e-07	2.13e-06
^{66}Zn	4.87e-09	2.01e-07	3.44e-08	1.78e-06	1.91e-07	1.94e-05
^{67}Zn	8.20e-10	2.89e-09	6.37e-09	2.79e-08	2.46e-08	1.70e-06
^{68}Zn	7.00e-10	1.00e-08	5.59e-09	9.69e-08	3.67e-08	3.47e-06
^{70}Zn	6.84e-12	9.76e-11	7.75e-11	9.44e-10	7.45e-09	7.57e-08
^{69}Ga	7.03e-11	5.99e-09	6.65e-10	5.83e-08	1.43e-08	5.47e-07
^{71}Ga	3.99e-11	7.92e-10	4.02e-10	7.54e-09	9.63e-09	2.25e-07

Table B.10: Asymptotic nucleosynthetic yields (in $M_\odot$) of Model M08_05 with 0.01, 0.1, and 3 $Z_\odot$.

	M08_05_001		M08_05_01		M08_05_3	
	He det $[M_\odot]$	core det $[M_\odot]$	He det $[M_\odot]$	core det $[M_\odot]$	He det $[M_\odot]$	core det $[M_\odot]$
^{12}C	2.34e-03	7.55e-03	2.33e-03	7.55e-03	2.27e-03	7.25e-03
^{13}C	5.16e-10	7.76e-08	5.15e-10	7.40e-08	3.61e-10	4.36e-07
^{14}N	3.44e-07	6.82e-06	1.42e-06	6.57e-06	3.62e-05	1.08e-05
^{15}N	3.46e-08	1.49e-08	3.62e-08	1.45e-08	9.03e-08	1.95e-08
^{16}O	6.07e-03	1.16e-01	6.10e-03	1.16e-01	6.61e-03	1.18e-01
^{17}O	2.19e-08	1.67e-06	2.35e-08	1.62e-06	6.59e-08	2.37e-06
^{18}O	3.67e-08	2.99e-08	4.63e-08	2.88e-08	3.53e-07	4.39e-08
^{19}F	2.08e-08	4.93e-10	2.19e-08	4.75e-10	5.84e-08	1.52e-09
^{20}Ne	3.05e-03	5.39e-03	3.05e-03	5.39e-03	3.07e-03	4.75e-03
^{21}Ne	2.30e-07	2.02e-06	2.32e-07	1.93e-06	3.14e-07	7.43e-06
^{22}Ne	1.66e-07	3.39e-05	1.89e-07	3.26e-05	8.76e-07	3.07e-04
^{23}Na	1.65e-05	5.54e-05	1.65e-05	5.44e-05	1.63e-05	1.49e-04
^{24}Mg	4.17e-03	1.00e-02	4.18e-03	1.03e-02	4.27e-03	4.54e-03
^{25}Mg	2.25e-05	8.73e-05	2.25e-05	8.56e-05	2.67e-05	3.33e-04
^{26}Mg	3.82e-05	1.21e-04	3.81e-05	1.18e-04	3.76e-05	4.75e-04
^{27}Al	1.47e-04	4.19e-04	1.47e-04	4.21e-04	1.51e-04	5.37e-04
^{28}Si	9.24e-03	2.28e-01	9.24e-03	2.28e-01	9.41e-03	2.26e-01
^{29}Si	1.15e-04	6.29e-04	1.14e-04	6.23e-04	1.13e-04	2.07e-03
^{30}Si	1.05e-04	8.54e-04	1.05e-04	8.45e-04	1.10e-04	4.51e-03
^{31}P	8.62e-05	4.32e-04	8.63e-05	4.26e-04	9.14e-05	1.19e-03
^{32}S	4.69e-03	1.31e-01	4.69e-03	1.31e-01	4.81e-03	1.11e-01
^{33}S	5.55e-05	3.34e-04	5.53e-05	3.30e-04	5.46e-05	6.19e-04
^{34}S	2.75e-05	1.78e-03	2.73e-05	1.73e-03	2.76e-05	8.29e-03
^{36}S	1.98e-09	5.30e-08	3.22e-09	5.93e-08	1.93e-08	5.06e-06
^{35}Cl	4.36e-05	1.11e-04	4.38e-05	1.08e-04	5.49e-05	2.89e-04
^{37}Cl	1.03e-05	2.40e-05	1.03e-05	2.35e-05	1.04e-05	4.66e-05
^{36}Ar	2.09e-03	2.34e-02	2.10e-03	2.34e-02	2.16e-03	1.69e-02
^{38}Ar	1.29e-05	7.54e-04	1.30e-05	7.30e-04	1.71e-05	3.43e-03
^{40}Ar	5.12e-10	5.24e-09	2.08e-09	9.26e-09	1.60e-08	5.27e-07
^{39}K	1.07e-04	5.86e-05	1.09e-04	5.73e-05	1.66e-04	1.30e-04
^{41}K	9.15e-06	4.08e-06	9.15e-06	3.99e-06	1.06e-05	7.17e-06
^{40}Ca	7.85e-03	2.04e-02	7.86e-03	2.04e-02	8.47e-03	1.41e-02
^{42}Ca	4.36e-06	1.95e-05	4.44e-06	1.87e-05	8.01e-06	8.10e-05
^{43}Ca	1.93e-05	6.43e-08	1.93e-05	6.41e-08	2.31e-05	4.50e-07
^{44}Ca	2.57e-03	1.33e-05	2.58e-03	1.33e-05	2.87e-03	1.02e-05
^{46}Ca	6.73e-11	2.55e-10	6.49e-10	2.29e-09	6.20e-09	2.48e-07
^{48}Ca	1.40e-11	1.95e-11	1.35e-10	1.85e-10	2.87e-09	2.16e-08
^{45}Sc	4.73e-06	2.01e-07	4.78e-06	2.00e-07	7.28e-06	6.66e-07

Table B.10 continued.

	M08_05_001		M08_05_01		M08_05_3	
	He det $[M_\odot]$	core det $[M_\odot]$	He det $[M_\odot]$	core det $[M_\odot]$	He det $[M_\odot]$	core det $[M_\odot]$
^{46}Ti	2.65e-06	7.26e-06	2.69e-06	7.01e-06	4.32e-06	2.68e-05
^{47}Ti	6.88e-05	3.01e-07	6.94e-05	2.96e-07	9.45e-05	1.56e-06
^{48}Ti	2.67e-03	3.48e-04	2.66e-03	3.49e-04	2.43e-03	2.40e-04
^{49}Ti	2.03e-05	1.98e-05	2.05e-05	1.97e-05	2.83e-05	2.79e-05
^{50}Ti	5.56e-11	6.15e-10	5.66e-10	2.79e-09	2.04e-08	5.87e-07
^{50}V	4.16e-11	3.44e-09	1.77e-10	4.28e-09	3.41e-09	1.55e-07
^{51}V	1.12e-04	4.83e-05	1.12e-04	4.78e-05	1.17e-04	9.96e-05
^{50}Cr	7.60e-06	1.33e-04	7.69e-06	1.31e-04	1.12e-05	6.63e-04
^{52}Cr	8.92e-04	7.37e-03	8.84e-04	7.39e-03	6.40e-04	5.77e-03
^{53}Cr	2.00e-05	5.39e-04	2.01e-05	5.35e-04	2.20e-05	9.48e-04
^{54}Cr	2.18e-10	1.96e-08	1.52e-09	2.51e-08	6.56e-08	1.19e-06
^{55}Mn	3.04e-05	2.65e-03	3.04e-05	2.63e-03	2.76e-05	5.77e-03
^{54}Fe	8.74e-06	1.37e-02	8.81e-06	1.35e-02	1.07e-05	5.72e-02
^{56}Fe	7.54e-05	2.10e-01	7.51e-05	2.10e-01	7.40e-05	1.79e-01
^{57}Fe	6.53e-06	2.04e-03	6.71e-06	2.02e-03	1.57e-05	3.73e-03
^{58}Fe	6.06e-09	2.48e-08	6.49e-08	1.95e-07	5.09e-06	7.55e-06
^{59}Co	8.19e-07	9.85e-06	1.33e-06	1.01e-05	2.39e-05	3.28e-05
^{58}Ni	2.64e-06	1.81e-03	3.03e-06	1.78e-03	3.25e-05	7.82e-03
^{60}Ni	1.39e-06	1.49e-04	2.41e-06	1.54e-04	2.17e-05	2.39e-04
^{61}Ni	5.72e-07	4.44e-06	9.83e-07	4.84e-06	8.73e-06	2.41e-05
^{62}Ni	6.61e-07	2.57e-05	1.58e-06	2.77e-05	1.57e-05	1.67e-04
^{64}Ni	1.44e-09	1.09e-08	1.43e-08	1.06e-07	2.57e-07	9.25e-06
^{63}Cu	5.06e-08	4.72e-08	2.14e-07	3.82e-07	2.53e-06	8.72e-06
^{64}Zn	1.31e-07	3.96e-07	2.48e-07	9.31e-07	2.35e-06	1.80e-06
^{66}Zn	8.59e-08	4.94e-07	2.42e-07	1.76e-06	1.97e-06	1.63e-05
^{67}Zn	2.72e-08	2.72e-09	8.30e-08	2.46e-08	7.25e-07	1.37e-06
^{68}Zn	3.58e-08	8.24e-09	1.20e-07	7.91e-08	6.68e-07	2.77e-06
^{70}Zn	7.38e-12	8.42e-11	7.73e-11	8.14e-10	5.30e-09	6.08e-08
^{69}Ga	2.87e-09	5.06e-09	1.05e-08	4.93e-08	6.18e-08	4.48e-07
^{71}Ga	5.64e-10	6.97e-10	2.62e-09	6.65e-09	2.24e-08	1.82e-07

Table B.11: Asymptotic nucleosynthetic yields (in $M_\odot$) of Model M08_10_r with 0.01, 0.1, and 3 $Z_\odot$.

	M08_10_r_001		M08_10_r_01		M08_10_r_3	
	He det $[M_\odot]$	core det $[M_\odot]$	He det $[M_\odot]$	core det $[M_\odot]$	He det $[M_\odot]$	core det $[M_\odot]$
^{12}C	1.18e-04	1.07e-03	1.17e-04	1.07e-03	1.17e-04	1.04e-03
^{13}C	7.87e-11	6.23e-11	7.69e-11	5.96e-11	4.72e-11	7.91e-10
^{14}N	1.62e-07	1.02e-08	1.22e-06	8.98e-09	3.53e-05	1.02e-07
^{15}N	1.00e-08	1.14e-09	1.05e-08	1.36e-09	2.70e-08	4.79e-10
^{16}O	9.09e-03	8.03e-02	9.10e-03	8.02e-02	9.60e-03	8.17e-02
^{17}O	1.86e-10	2.94e-09	1.58e-09	2.79e-09	4.65e-08	2.67e-08
^{18}O	8.37e-09	1.50e-10	1.62e-08	1.44e-10	2.67e-07	1.02e-09
^{19}F	4.11e-09	1.21e-11	4.42e-09	1.20e-11	1.41e-08	7.68e-11
^{20}Ne	1.56e-04	2.93e-03	1.55e-04	2.93e-03	1.60e-04	2.67e-03
^{21}Ne	1.51e-08	7.23e-08	1.65e-08	6.98e-08	6.13e-08	6.82e-07
^{22}Ne	1.21e-08	2.04e-08	3.11e-08	1.97e-08	6.44e-07	6.34e-07
^{23}Na	1.45e-06	1.36e-05	1.45e-06	1.36e-05	1.62e-06	2.86e-05
^{24}Mg	3.05e-03	7.07e-03	3.09e-03	7.26e-03	3.20e-03	3.22e-03
^{25}Mg	2.23e-06	1.99e-05	2.29e-06	1.94e-05	3.38e-06	9.07e-05
^{26}Mg	2.20e-06	3.30e-05	2.22e-06	3.22e-05	3.31e-06	1.41e-04
^{27}Al	7.63e-05	2.83e-04	7.71e-05	2.84e-04	7.98e-05	3.55e-04
^{28}Si	1.28e-02	1.91e-01	1.28e-02	1.91e-01	1.30e-02	1.90e-01
^{29}Si	8.93e-05	4.17e-04	8.96e-05	4.13e-04	9.29e-05	1.42e-03
^{30}Si	1.02e-04	6.09e-04	1.03e-04	6.02e-04	1.10e-04	3.28e-03
^{31}P	7.62e-05	3.17e-04	7.61e-05	3.13e-04	7.81e-05	8.81e-04
^{32}S	5.58e-03	1.13e-01	5.56e-03	1.13e-01	5.59e-03	9.62e-02
^{33}S	7.76e-05	2.51e-04	7.71e-05	2.48e-04	7.67e-05	4.72e-04
^{34}S	1.31e-04	1.33e-03	1.31e-04	1.30e-03	1.35e-04	6.24e-03
^{36}S	3.73e-09	3.36e-08	3.78e-09	3.25e-08	5.07e-09	3.29e-06
^{35}Cl	3.14e-05	8.59e-05	3.13e-05	8.35e-05	3.61e-05	2.29e-04
^{37}Cl	7.89e-06	1.88e-05	7.84e-06	1.84e-05	8.15e-06	3.65e-05
^{36}Ar	1.82e-03	2.10e-02	1.82e-03	2.10e-02	1.84e-03	1.55e-02
^{38}Ar	3.92e-05	5.76e-04	3.90e-05	5.57e-04	4.52e-05	2.64e-03
^{40}Ar	5.79e-10	3.76e-09	5.79e-10	3.78e-09	9.88e-10	2.07e-07
^{39}K	7.96e-05	4.67e-05	8.02e-05	4.56e-05	1.04e-04	1.04e-04
^{41}K	3.21e-06	3.27e-06	3.21e-06	3.21e-06	4.16e-06	5.72e-06
^{40}Ca	6.22e-03	1.91e-02	6.22e-03	1.91e-02	6.34e-03	1.36e-02
^{42}Ca	6.48e-06	1.50e-05	6.52e-06	1.44e-05	9.41e-06	6.28e-05
^{43}Ca	2.98e-05	1.39e-07	2.98e-05	1.38e-07	3.01e-05	3.13e-07
^{44}Ca	1.78e-03	1.52e-05	1.78e-03	1.52e-05	1.83e-03	1.10e-05
^{46}Ca	1.08e-12	5.56e-11	3.99e-12	3.29e-10	5.82e-11	9.89e-08
^{48}Ca	6.43e-12	1.58e-12	6.44e-11	1.12e-11	1.94e-09	4.61e-09
^{45}Sc	3.73e-06	1.73e-07	3.75e-06	1.70e-07	4.99e-06	4.48e-07

Table B.11 continued.

	M08_10_r_001		M08_10_r_01		M08_10_r_3	
	He det $[M_\odot]$	core det $[M_\odot]$	He det $[M_\odot]$	core det $[M_\odot]$	He det $[M_\odot]$	core det $[M_\odot]$
^{46}Ti	7.92e-06	5.71e-06	7.88e-06	5.51e-06	7.62e-06	2.14e-05
^{47}Ti	6.90e-05	4.01e-07	6.90e-05	3.95e-07	7.23e-05	1.28e-06
^{48}Ti	3.78e-03	3.68e-04	3.79e-03	3.69e-04	3.92e-03	2.58e-04
^{49}Ti	3.06e-05	2.01e-05	3.09e-05	2.00e-05	4.20e-05	2.92e-05
^{50}Ti	2.10e-11	8.20e-09	1.03e-10	1.51e-07	2.48e-09	4.25e-07
^{50}V	2.60e-10	2.91e-09	2.80e-10	3.23e-09	1.26e-09	1.14e-07
^{51}V	2.92e-04	4.96e-05	2.92e-04	4.91e-05	3.11e-04	1.03e-04
^{50}Cr	4.27e-05	1.21e-04	4.23e-05	1.19e-04	3.49e-05	6.06e-04
^{52}Cr	7.36e-03	7.93e-03	7.37e-03	7.94e-03	7.90e-03	6.23e-03
^{53}Cr	9.66e-05	5.68e-04	9.77e-05	5.65e-04	1.36e-04	9.99e-04
^{54}Cr	3.27e-10	3.32e-08	6.48e-10	1.94e-07	9.85e-09	8.86e-07
^{55}Mn	9.20e-04	2.83e-03	9.22e-04	2.81e-03	9.72e-04	6.29e-03
^{54}Fe	6.25e-05	1.30e-02	6.32e-05	1.28e-02	8.74e-05	5.57e-02
^{56}Fe	1.49e-02	3.24e-01	1.49e-02	3.24e-01	1.49e-02	2.79e-01
^{57}Fe	1.29e-03	4.50e-03	1.29e-03	4.47e-03	1.31e-03	7.84e-03
^{58}Fe	1.03e-09	1.76e-08	8.95e-09	1.18e-07	2.79e-07	2.70e-06
^{59}Co	4.16e-05	1.00e-04	4.18e-05	9.93e-05	5.33e-05	1.80e-04
^{58}Ni	1.74e-04	4.15e-03	1.76e-04	4.07e-03	2.47e-04	2.04e-02
^{60}Ni	1.59e-03	2.17e-03	1.59e-03	2.18e-03	1.57e-03	1.35e-03
^{61}Ni	2.97e-04	6.96e-05	2.97e-04	6.96e-05	2.86e-04	8.84e-05
^{62}Ni	1.24e-04	3.90e-04	1.26e-04	3.86e-04	1.80e-04	1.20e-03
^{64}Ni	3.95e-10	7.29e-09	3.78e-09	7.00e-08	8.19e-08	6.80e-06
^{63}Cu	5.67e-06	1.74e-07	5.72e-06	3.85e-07	6.82e-06	6.42e-06
^{64}Zn	1.43e-04	6.61e-06	1.42e-04	7.06e-06	1.13e-04	3.78e-06
^{66}Zn	1.56e-05	7.05e-06	1.61e-05	7.90e-06	2.39e-05	2.68e-05
^{67}Zn	1.34e-06	5.95e-09	1.50e-06	2.27e-08	4.03e-06	1.06e-06
^{68}Zn	8.78e-07	7.59e-09	1.37e-06	6.14e-08	4.36e-06	2.11e-06
^{70}Zn	1.60e-12	5.33e-11	1.55e-11	5.05e-10	3.57e-10	4.68e-08
^{69}Ga	5.31e-08	4.05e-09	1.03e-07	3.96e-08	3.10e-07	3.37e-07
^{71}Ga	3.32e-09	6.53e-10	8.27e-09	6.24e-09	2.68e-08	1.45e-07

Table B.12: Asymptotic nucleosynthetic yields (in $M_\odot$) of Model M09_03 with 0.01, 0.1, and 3 $Z_\odot$.

	M09_03_001		M09_03_01		M09_03_3	
	He det $[M_\odot]$	core det $[M_\odot]$	He det $[M_\odot]$	core det $[M_\odot]$	He det $[M_\odot]$	core det $[M_\odot]$
^{12}C	3.52e-03	4.94e-03	3.51e-03	4.94e-03	3.42e-03	4.74e-03
^{13}C	1.07e-09	6.50e-08	1.07e-09	6.18e-08	7.16e-10	3.37e-07
^{14}N	3.59e-07	3.81e-06	1.42e-06	3.67e-06	3.57e-05	5.32e-06
^{15}N	5.76e-08	8.09e-09	6.03e-08	7.90e-09	1.50e-07	1.03e-08
^{16}O	3.78e-03	9.17e-02	3.79e-03	9.15e-02	4.17e-03	9.31e-02
^{17}O	3.34e-08	1.01e-06	3.49e-08	9.85e-07	7.45e-08	1.30e-06
^{18}O	5.35e-08	1.55e-08	6.39e-08	1.49e-08	3.99e-07	2.23e-08
^{19}F	4.24e-08	3.01e-10	4.46e-08	2.90e-10	1.17e-07	1.05e-09
^{20}Ne	2.81e-03	3.43e-03	2.81e-03	3.43e-03	2.91e-03	3.02e-03
^{21}Ne	3.60e-07	1.25e-06	3.64e-07	1.19e-06	4.97e-07	4.64e-06
^{22}Ne	3.02e-07	2.56e-05	3.28e-07	2.47e-05	1.09e-06	2.05e-04
^{23}Na	1.92e-05	3.40e-05	1.92e-05	3.34e-05	1.90e-05	9.11e-05
^{24}Mg	3.12e-03	7.17e-03	3.12e-03	7.37e-03	3.23e-03	3.19e-03
^{25}Mg	3.09e-05	5.32e-05	3.10e-05	5.22e-05	3.80e-05	2.06e-04
^{26}Mg	4.71e-05	7.52e-05	4.70e-05	7.34e-05	4.58e-05	3.05e-04
^{27}Al	1.14e-04	2.84e-04	1.14e-04	2.85e-04	1.15e-04	3.62e-04
^{28}Si	5.76e-03	2.20e-01	5.77e-03	2.20e-01	5.88e-03	2.19e-01
^{29}Si	8.69e-05	4.69e-04	8.65e-05	4.65e-04	8.20e-05	1.47e-03
^{30}Si	8.52e-05	6.45e-04	8.51e-05	6.38e-04	8.51e-05	3.41e-03
^{31}P	7.16e-05	3.37e-04	7.16e-05	3.32e-04	7.29e-05	9.23e-04
^{32}S	2.74e-03	1.31e-01	2.74e-03	1.31e-01	2.88e-03	1.11e-01
^{33}S	2.41e-05	2.67e-04	2.40e-05	2.64e-04	2.39e-05	5.13e-04
^{34}S	1.29e-05	1.54e-03	1.29e-05	1.50e-03	1.36e-05	7.20e-03
^{36}S	1.15e-09	3.94e-08	3.30e-09	4.32e-08	2.87e-08	3.40e-06
^{35}Cl	3.86e-05	9.08e-05	3.88e-05	8.84e-05	4.64e-05	2.36e-04
^{37}Cl	3.00e-06	2.14e-05	3.00e-06	2.10e-05	3.15e-06	4.22e-05
^{36}Ar	1.10e-03	2.44e-02	1.11e-03	2.44e-02	1.21e-03	1.80e-02
^{38}Ar	3.39e-06	6.85e-04	3.43e-06	6.64e-04	5.14e-06	3.17e-03
^{40}Ar	4.34e-10	3.89e-09	3.34e-09	6.44e-09	2.66e-08	3.48e-07
^{39}K	6.89e-05	5.42e-05	6.96e-05	5.30e-05	9.54e-05	1.22e-04
^{41}K	1.04e-05	3.82e-06	1.03e-05	3.75e-06	1.10e-05	6.80e-06
^{40}Ca	3.95e-03	2.23e-02	3.95e-03	2.23e-02	4.07e-03	1.59e-02
^{42}Ca	3.92e-06	1.75e-05	4.00e-06	1.68e-05	7.15e-06	7.50e-05
^{43}Ca	8.68e-06	6.57e-08	8.78e-06	6.51e-08	1.39e-05	3.38e-07
^{44}Ca	7.50e-04	1.58e-05	7.47e-04	1.58e-05	6.50e-04	1.19e-05
^{46}Ca	1.20e-10	1.74e-10	1.15e-09	1.54e-09	1.01e-08	1.64e-07
^{48}Ca	2.09e-11	1.32e-11	1.99e-10	1.25e-10	3.60e-09	1.48e-08
^{45}Sc	4.60e-06	1.92e-07	4.63e-06	1.91e-07	5.30e-06	5.30e-07

Table B.12 continued.

	M09_03_001		M09_03_01		M09_03_3	
	He det $[M_\odot]$	core det $[M_\odot]$	He det $[M_\odot]$	core det $[M_\odot]$	He det $[M_\odot]$	core det $[M_\odot]$
^{46}Ti	2.23e-06	6.73e-06	2.25e-06	6.51e-06	3.17e-06	2.53e-05
^{47}Ti	4.07e-05	3.13e-07	4.07e-05	3.08e-07	4.13e-05	1.38e-06
^{48}Ti	1.26e-04	4.29e-04	1.24e-04	4.30e-04	7.52e-05	3.02e-04
^{49}Ti	3.70e-06	2.34e-05	3.69e-06	2.32e-05	3.17e-06	3.39e-05
^{50}Ti	1.07e-10	7.98e-10	1.09e-09	1.98e-09	3.77e-08	3.97e-07
^{50}V	3.04e-10	2.57e-09	3.74e-10	3.13e-09	4.33e-09	1.08e-07
^{51}V	5.48e-06	5.72e-05	5.42e-06	5.67e-05	3.74e-06	1.19e-04
^{50}Cr	1.37e-06	1.41e-04	1.37e-06	1.38e-04	1.34e-06	7.01e-04
^{52}Cr	5.26e-06	9.50e-03	5.17e-06	9.51e-03	3.14e-06	7.45e-03
^{53}Cr	4.67e-07	6.72e-04	4.65e-07	6.67e-04	4.37e-07	1.18e-03
^{54}Cr	3.18e-10	2.14e-08	2.99e-09	2.24e-08	1.25e-07	1.01e-06
^{55}Mn	2.61e-07	3.37e-03	2.76e-07	3.34e-03	9.72e-07	7.50e-03
^{54}Fe	1.53e-07	1.55e-02	1.88e-07	1.52e-02	1.45e-06	6.63e-02
^{56}Fe	8.12e-07	3.43e-01	1.38e-06	3.43e-01	2.62e-05	2.95e-01
^{57}Fe	1.09e-07	4.05e-03	2.14e-07	4.02e-03	7.64e-06	7.28e-03
^{58}Fe	1.13e-08	2.32e-08	1.23e-07	1.19e-07	8.69e-06	4.88e-06
^{59}Co	4.38e-08	5.84e-05	3.01e-07	5.81e-05	1.19e-05	9.69e-05
^{58}Ni	4.99e-08	3.78e-03	2.37e-07	3.71e-03	1.28e-05	1.77e-02
^{60}Ni	1.35e-07	1.04e-03	7.78e-07	1.05e-03	9.88e-06	5.98e-04
^{61}Ni	3.92e-08	3.14e-05	2.69e-07	3.16e-05	2.54e-06	4.02e-05
^{62}Ni	5.63e-08	1.84e-04	4.65e-07	1.83e-04	3.87e-06	4.98e-04
^{64}Ni	1.54e-09	7.28e-09	1.57e-08	7.06e-08	2.79e-07	6.07e-06
^{63}Cu	8.89e-09	8.71e-08	7.59e-08	3.12e-07	8.26e-07	5.90e-06
^{64}Zn	1.85e-08	2.15e-06	4.00e-08	2.54e-06	2.35e-07	1.79e-06
^{66}Zn	6.70e-09	2.45e-06	4.80e-08	3.34e-06	2.77e-07	1.49e-05
^{67}Zn	1.15e-09	2.93e-09	9.15e-09	1.83e-08	4.25e-08	8.87e-07
^{68}Zn	1.10e-09	5.97e-09	8.89e-09	5.40e-08	5.31e-08	1.88e-06
^{70}Zn	8.56e-12	5.68e-11	9.59e-11	5.51e-10	9.23e-09	3.93e-08
^{69}Ga	1.03e-10	3.47e-09	9.17e-10	3.39e-08	1.85e-08	3.09e-07
^{71}Ga	6.12e-11	4.95e-10	6.04e-10	4.74e-09	1.09e-08	1.23e-07

Table B.13: Asymptotic nucleosynthetic yields (in $M_\odot$) of Model M09_05 with 0.01, 0.1, and 3 $Z_\odot$.

	M09_05_001		M09_05_01		M09_05_3	
	He det $[M_\odot]$	core det $[M_\odot]$	He det $[M_\odot]$	core det $[M_\odot]$	He det $[M_\odot]$	core det $[M_\odot]$
^{12}C	4.37e-04	2.67e-03	4.36e-04	2.66e-03	4.29e-04	2.58e-03
^{13}C	2.49e-11	3.02e-09	2.40e-11	2.83e-09	1.87e-11	3.17e-08
^{14}N	1.66e-07	4.48e-07	1.23e-06	4.26e-07	3.54e-05	1.70e-06
^{15}N	1.00e-08	2.92e-09	1.06e-08	2.93e-09	2.67e-08	4.12e-09
^{16}O	7.12e-03	7.73e-02	7.14e-03	7.71e-02	7.61e-03	7.86e-02
^{17}O	6.28e-10	9.49e-08	2.03e-09	9.06e-08	4.70e-08	2.48e-07
^{18}O	7.88e-09	2.76e-09	1.57e-08	2.65e-09	2.67e-07	9.41e-09
^{19}F	5.20e-09	7.40e-11	5.58e-09	7.09e-11	1.71e-08	3.94e-10
^{20}Ne	1.05e-03	3.65e-03	1.04e-03	3.65e-03	1.03e-03	3.26e-03
^{21}Ne	2.89e-08	3.53e-07	3.03e-08	3.33e-07	7.42e-08	2.49e-06
^{22}Ne	1.88e-08	9.32e-07	3.82e-08	8.74e-07	6.58e-07	2.48e-05
^{23}Na	5.44e-06	2.20e-05	5.41e-06	2.17e-05	5.55e-06	5.77e-05
^{24}Mg	3.19e-03	6.48e-03	3.20e-03	6.66e-03	3.28e-03	2.89e-03
^{25}Mg	6.19e-06	3.29e-05	6.24e-06	3.21e-05	7.53e-06	1.58e-04
^{26}Mg	1.00e-05	5.66e-05	1.00e-05	5.51e-05	1.10e-05	2.68e-04
^{27}Al	1.08e-04	2.58e-04	1.08e-04	2.59e-04	1.12e-04	3.32e-04
^{28}Si	9.96e-03	1.91e-01	9.97e-03	1.91e-01	1.01e-02	1.90e-01
^{29}Si	9.01e-05	4.23e-04	9.00e-05	4.19e-04	9.22e-05	1.38e-03
^{30}Si	9.47e-05	5.68e-04	9.49e-05	5.62e-04	1.00e-04	2.96e-03
^{31}P	8.31e-05	2.93e-04	8.31e-05	2.89e-04	8.59e-05	8.01e-04
^{32}S	4.46e-03	1.14e-01	4.46e-03	1.14e-01	4.49e-03	9.72e-02
^{33}S	6.94e-05	2.28e-04	6.92e-05	2.24e-04	6.91e-05	4.37e-04
^{34}S	5.41e-05	1.30e-03	5.41e-05	1.27e-03	5.88e-05	6.11e-03
^{36}S	2.52e-09	3.43e-08	2.55e-09	3.49e-08	4.77e-09	3.12e-06
^{35}Cl	3.74e-05	8.04e-05	3.74e-05	7.83e-05	4.21e-05	2.09e-04
^{37}Cl	9.44e-06	1.82e-05	9.41e-06	1.78e-05	9.55e-06	3.61e-05
^{36}Ar	1.53e-03	2.15e-02	1.53e-03	2.15e-02	1.56e-03	1.60e-02
^{38}Ar	2.13e-05	5.80e-04	2.14e-05	5.62e-04	2.67e-05	2.69e-03
^{40}Ar	6.19e-10	3.38e-09	7.13e-10	4.48e-09	2.21e-09	2.99e-07
^{39}K	8.48e-05	4.65e-05	8.54e-05	4.55e-05	1.07e-04	1.05e-04
^{41}K	6.35e-06	3.26e-06	6.35e-06	3.20e-06	7.10e-06	5.83e-06
^{40}Ca	5.08e-03	1.99e-02	5.08e-03	1.99e-02	5.22e-03	1.44e-02
^{42}Ca	7.13e-06	1.48e-05	7.19e-06	1.42e-05	1.01e-05	6.38e-05
^{43}Ca	2.44e-05	1.50e-07	2.43e-05	1.49e-07	2.49e-05	3.22e-07
^{44}Ca	1.99e-03	1.65e-05	2.00e-03	1.66e-05	2.13e-03	1.18e-05
^{46}Ca	6.66e-12	1.08e-10	5.97e-11	9.20e-10	6.68e-10	1.58e-07
^{48}Ca	6.87e-12	4.52e-12	6.85e-11	4.15e-11	2.00e-09	1.20e-08
^{45}Sc	4.00e-06	1.68e-07	4.02e-06	1.67e-07	5.34e-06	4.76e-07

Table B.13 continued.

	M09_05_001		M09_05_01		M09_05_3	
	He det $[M_\odot]$	core det $[M_\odot]$	He det $[M_\odot]$	core det $[M_\odot]$	He det $[M_\odot]$	core det $[M_\odot]$
^{46}Ti	3.56e-06	5.70e-06	3.60e-06	5.51e-06	5.23e-06	2.16e-05
^{47}Ti	5.47e-05	4.25e-07	5.50e-05	4.21e-07	6.80e-05	1.30e-06
^{48}Ti	4.48e-03	4.03e-04	4.49e-03	4.04e-04	4.97e-03	2.86e-04
^{49}Ti	4.11e-05	2.16e-05	4.14e-05	2.15e-05	5.48e-05	3.19e-05
^{50}Ti	1.92e-11	3.30e-10	1.53e-10	1.32e-09	4.80e-09	3.44e-07
^{50}V	1.25e-10	2.16e-09	2.15e-10	2.76e-09	2.43e-09	9.38e-08
^{51}V	3.73e-04	5.30e-05	3.74e-04	5.25e-05	4.23e-04	1.11e-04
^{50}Cr	1.83e-05	1.25e-04	1.85e-05	1.22e-04	2.49e-05	6.20e-04
^{52}Cr	5.09e-03	8.80e-03	5.10e-03	8.81e-03	5.27e-03	6.91e-03
^{53}Cr	1.36e-04	6.21e-04	1.37e-04	6.17e-04	1.72e-04	1.09e-03
^{54}Cr	2.85e-10	1.61e-08	7.55e-10	1.86e-08	1.84e-08	8.47e-07
^{55}Mn	4.12e-04	3.10e-03	4.12e-04	3.07e-03	3.95e-04	6.94e-03
^{54}Fe	8.26e-05	1.38e-02	8.31e-05	1.35e-02	9.72e-05	5.93e-02
^{56}Fe	2.13e-03	3.98e-01	2.12e-03	3.98e-01	1.72e-03	3.45e-01
^{57}Fe	1.38e-04	5.79e-03	1.38e-04	5.76e-03	1.31e-04	1.01e-02
^{58}Fe	1.67e-09	1.16e-08	1.52e-08	7.01e-08	1.05e-06	3.01e-06
^{59}Co	1.22e-05	1.45e-04	1.25e-05	1.44e-04	2.37e-05	2.55e-04
^{58}Ni	7.34e-05	5.47e-03	7.42e-05	5.36e-03	1.12e-04	2.72e-02
^{60}Ni	7.56e-05	3.21e-03	7.56e-05	3.22e-03	6.70e-05	1.89e-03
^{61}Ni	1.00e-05	1.01e-04	1.01e-05	1.01e-04	1.27e-05	1.19e-04
^{62}Ni	1.30e-05	5.82e-04	1.37e-05	5.75e-04	3.05e-05	1.70e-03
^{64}Ni	1.17e-09	7.32e-09	1.12e-08	7.10e-08	2.05e-07	5.24e-06
^{63}Cu	5.36e-07	2.40e-07	6.37e-07	4.51e-07	3.07e-06	6.80e-06
^{64}Zn	1.48e-06	9.50e-06	1.66e-06	9.89e-06	4.52e-06	4.26e-06
^{66}Zn	9.24e-07	1.04e-05	1.21e-06	1.10e-05	6.33e-06	3.04e-05
^{67}Zn	2.57e-07	7.43e-09	3.69e-07	2.34e-08	2.21e-06	8.20e-07
^{68}Zn	3.75e-07	6.68e-09	6.45e-07	4.70e-08	2.59e-06	1.54e-06
^{70}Zn	6.03e-12	6.02e-11	5.60e-11	5.82e-10	1.73e-09	3.47e-08
^{69}Ga	3.35e-08	2.96e-09	6.63e-08	2.90e-08	2.23e-07	2.67e-07
^{71}Ga	2.83e-09	4.88e-10	7.19e-09	4.69e-09	3.17e-08	1.02e-07

Table B.14: Asymptotic nucleosynthetic yields (in $M_\odot$) of Model M09_10_r with 0.01, 0.1, and 3 $Z_\odot$.

	M09_10_r_001		M09_10_r_01		M09_10_r_3	
	He det $[M_\odot]$	core det $[M_\odot]$	He det $[M_\odot]$	core det $[M_\odot]$	He det $[M_\odot]$	core det $[M_\odot]$
^{12}C	3.82e-05	1.36e-04	3.82e-05	1.35e-04	3.80e-05	1.32e-04
^{13}C	1.89e-09	5.87e-12	1.88e-09	5.74e-12	1.55e-09	2.21e-11
^{14}N	2.49e-07	1.93e-10	1.31e-06	1.93e-10	3.55e-05	4.65e-10
^{15}N	1.39e-08	3.94e-10	1.47e-08	4.25e-10	3.74e-08	2.34e-10
^{16}O	8.36e-03	5.46e-02	8.37e-03	5.45e-02	8.82e-03	5.55e-02
^{17}O	2.08e-10	2.45e-11	1.61e-09	2.37e-11	4.67e-08	1.29e-10
^{18}O	1.69e-08	1.80e-12	2.53e-08	1.31e-12	2.93e-07	4.78e-12
^{19}F	4.86e-09	5.08e-13	5.22e-09	4.89e-13	1.62e-08	3.78e-12
^{20}Ne	8.63e-06	6.41e-04	8.84e-06	6.38e-04	1.82e-05	5.90e-04
^{21}Ne	1.95e-08	1.31e-08	2.13e-08	1.27e-08	7.74e-08	7.73e-08
^{22}Ne	1.11e-08	6.66e-09	3.03e-08	6.32e-09	6.47e-07	8.89e-09
^{23}Na	1.93e-07	3.57e-06	1.98e-07	3.39e-06	3.95e-07	6.21e-06
^{24}Mg	2.37e-03	4.04e-03	2.40e-03	4.16e-03	2.51e-03	1.80e-03
^{25}Mg	5.95e-07	5.91e-06	6.37e-07	5.81e-06	1.72e-06	2.01e-05
^{26}Mg	4.63e-07	7.57e-06	5.03e-07	7.32e-06	1.60e-06	2.48e-05
^{27}Al	3.59e-05	1.52e-04	3.65e-05	1.53e-04	3.82e-05	1.86e-04
^{28}Si	1.26e-02	1.54e-01	1.26e-02	1.55e-01	1.28e-02	1.54e-01
^{29}Si	6.67e-05	2.44e-04	6.71e-05	2.42e-04	7.00e-05	7.32e-04
^{30}Si	8.74e-05	3.80e-04	8.87e-05	3.76e-04	9.40e-05	2.09e-03
^{31}P	4.43e-05	2.17e-04	4.44e-05	2.14e-04	4.56e-05	5.96e-04
^{32}S	4.37e-03	9.47e-02	4.35e-03	9.46e-02	4.31e-03	8.07e-02
^{33}S	4.66e-05	1.78e-04	4.63e-05	1.76e-04	4.58e-05	3.44e-04
^{34}S	2.28e-04	9.94e-04	2.26e-04	9.70e-04	2.21e-04	4.67e-03
^{36}S	3.24e-09	2.00e-08	3.32e-09	1.97e-08	4.56e-09	1.42e-06
^{35}Cl	1.90e-05	5.96e-05	1.90e-05	5.79e-05	2.06e-05	1.54e-04
^{37}Cl	3.61e-06	1.44e-05	3.58e-06	1.41e-05	3.77e-06	2.80e-05
^{36}Ar	1.24e-03	1.83e-02	1.24e-03	1.82e-02	1.25e-03	1.37e-02
^{38}Ar	6.03e-05	4.42e-04	5.98e-05	4.28e-04	6.11e-05	2.04e-03
^{40}Ar	1.73e-10	2.39e-09	1.79e-10	2.38e-09	5.15e-10	7.22e-08
^{39}K	3.80e-05	3.69e-05	3.82e-05	3.60e-05	4.97e-05	8.22e-05
^{41}K	1.14e-06	2.59e-06	1.15e-06	2.54e-06	1.74e-06	4.58e-06
^{40}Ca	4.70e-03	1.72e-02	4.70e-03	1.72e-02	4.81e-03	1.26e-02
^{42}Ca	3.54e-06	1.16e-05	3.54e-06	1.11e-05	4.91e-06	4.90e-05
^{43}Ca	1.36e-05	3.10e-07	1.36e-05	3.10e-07	1.34e-05	2.68e-07
^{44}Ca	8.70e-04	1.81e-05	8.71e-04	1.81e-05	9.07e-04	1.18e-05
^{46}Ca	6.34e-13	4.57e-11	2.14e-12	1.43e-10	4.49e-11	1.99e-08
^{48}Ca	6.43e-12	4.24e-12	6.43e-11	6.42e-12	1.94e-09	4.36e-08
^{45}Sc	8.47e-07	1.44e-07	8.58e-07	1.41e-07	1.53e-06	3.01e-07

Table B.14 continued.

	M09_10_r_001		M09_10_r_01		M09_10_r_3	
	He det $[M_\odot]$	core det $[M_\odot]$	He det $[M_\odot]$	core det $[M_\odot]$	He det $[M_\odot]$	core det $[M_\odot]$
^{46}Ti	4.17e-05	4.43e-06	4.13e-05	4.28e-06	3.06e-05	1.69e-05
^{47}Ti	5.70e-05	6.54e-07	5.68e-05	6.48e-07	5.25e-05	1.09e-06
^{48}Ti	1.88e-03	3.74e-04	1.88e-03	3.74e-04	1.99e-03	2.63e-04
^{49}Ti	2.04e-05	1.96e-05	2.07e-05	1.95e-05	2.80e-05	2.91e-05
^{50}Ti	2.12e-11	4.05e-10	8.87e-11	1.64e-09	2.25e-09	1.10e-06
^{50}V	2.00e-10	1.88e-09	1.99e-10	1.94e-09	5.53e-10	6.62e-08
^{51}V	2.67e-04	4.88e-05	2.66e-04	4.83e-05	2.50e-04	1.02e-04
^{50}Cr	2.26e-04	1.07e-04	2.25e-04	1.05e-04	1.86e-04	5.33e-04
^{52}Cr	3.98e-03	8.10e-03	3.98e-03	8.12e-03	4.08e-03	6.35e-03
^{53}Cr	6.05e-05	5.69e-04	6.11e-05	5.66e-04	8.41e-05	9.98e-04
^{54}Cr	2.57e-10	1.63e-08	4.38e-10	2.02e-08	7.17e-09	1.03e-06
^{55}Mn	3.68e-04	2.89e-03	3.69e-04	2.86e-03	3.83e-04	6.49e-03
^{54}Fe	4.00e-05	1.20e-02	4.05e-05	1.18e-02	6.01e-05	5.23e-02
^{56}Fe	2.60e-02	4.93e-01	2.60e-02	4.93e-01	2.65e-02	4.29e-01
^{57}Fe	2.40e-03	8.62e-03	2.40e-03	8.57e-03	2.42e-03	1.45e-02
^{58}Fe	4.63e-10	1.17e-08	3.79e-09	4.41e-08	1.12e-07	1.66e-06
^{59}Co	3.57e-04	2.81e-04	3.56e-04	2.79e-04	3.01e-04	4.97e-04
^{58}Ni	6.69e-04	8.16e-03	6.68e-04	7.99e-03	6.42e-04	4.14e-02
^{60}Ni	2.70e-03	6.39e-03	2.70e-03	6.41e-03	2.68e-03	3.82e-03
^{61}Ni	3.93e-04	2.11e-04	3.92e-04	2.10e-04	3.75e-04	2.39e-04
^{62}Ni	1.65e-04	1.19e-03	1.65e-04	1.18e-03	1.68e-04	3.50e-03
^{64}Ni	5.11e-11	2.43e-09	5.06e-10	2.14e-08	1.29e-08	3.72e-06
^{63}Cu	1.36e-05	4.85e-07	1.36e-05	5.66e-07	1.35e-05	4.08e-06
^{64}Zn	2.59e-04	2.11e-05	2.59e-04	2.15e-05	2.71e-04	8.70e-06
^{66}Zn	2.44e-05	2.32e-05	2.46e-05	2.35e-05	3.08e-05	5.69e-05
^{67}Zn	9.43e-07	1.43e-08	1.00e-06	1.91e-08	2.02e-06	5.60e-07
^{68}Zn	5.22e-07	8.47e-09	7.67e-07	3.93e-08	2.09e-06	1.53e-06
^{70}Zn	4.77e-13	1.48e-11	4.59e-12	1.35e-10	1.11e-10	2.51e-08
^{69}Ga	3.26e-08	2.50e-09	5.93e-08	2.43e-08	1.37e-07	2.72e-07
^{71}Ga	2.18e-09	2.99e-10	4.92e-09	2.84e-09	9.66e-09	1.11e-07

Table B.15: Asymptotic nucleosynthetic yields (in $M_\odot$) of Model M10_02 with 0.01, 0.1, and 3 $Z_\odot$.

	M10_02_001		M10_02_01		M10_02_3	
	He det $[M_\odot]$	core det $[M_\odot]$	He det $[M_\odot]$	core det $[M_\odot]$	He det $[M_\odot]$	core det $[M_\odot]$
^{12}C	1.69e-03	1.97e-03	1.69e-03	1.97e-03	1.65e-03	1.90e-03
^{13}C	3.51e-10	1.77e-08	3.50e-10	1.67e-08	2.44e-10	9.78e-08
^{14}N	2.02e-07	9.45e-07	1.25e-06	9.07e-07	3.50e-05	1.55e-06
^{15}N	2.72e-08	2.50e-09	2.85e-08	2.46e-09	6.99e-08	3.17e-09
^{16}O	1.77e-03	5.67e-02	1.78e-03	5.66e-02	2.02e-03	5.76e-02
^{17}O	8.79e-09	2.32e-07	1.02e-08	2.26e-07	5.32e-08	3.20e-07
^{18}O	2.43e-08	3.93e-09	3.29e-08	3.77e-09	3.11e-07	6.90e-09
^{19}F	1.96e-08	8.79e-11	2.07e-08	8.47e-11	5.59e-08	3.43e-10
^{20}Ne	1.30e-03	1.96e-03	1.30e-03	1.96e-03	1.35e-03	1.75e-03
^{21}Ne	1.16e-07	3.91e-07	1.19e-07	3.73e-07	2.00e-07	1.84e-06
^{22}Ne	9.70e-08	5.45e-06	1.19e-07	5.24e-06	7.90e-07	5.14e-05
^{23}Na	8.84e-06	1.44e-05	8.83e-06	1.42e-05	8.92e-06	3.84e-05
^{24}Mg	1.50e-03	4.27e-03	1.50e-03	4.38e-03	1.56e-03	1.86e-03
^{25}Mg	1.32e-05	2.23e-05	1.32e-05	2.18e-05	1.68e-05	9.46e-05
^{26}Mg	2.03e-05	3.49e-05	2.03e-05	3.40e-05	2.11e-05	1.51e-04
^{27}Al	5.56e-05	1.62e-04	5.56e-05	1.63e-04	5.68e-05	2.03e-04
^{28}Si	2.92e-03	1.70e-01	2.92e-03	1.70e-01	3.00e-03	1.70e-01
^{29}Si	4.44e-05	2.86e-04	4.42e-05	2.83e-04	4.23e-05	8.85e-04
^{30}Si	4.46e-05	3.99e-04	4.46e-05	3.94e-04	4.46e-05	2.05e-03
^{31}P	3.79e-05	2.12e-04	3.79e-05	2.09e-04	3.89e-05	5.81e-04
^{32}S	1.58e-03	1.05e-01	1.58e-03	1.05e-01	1.67e-03	8.95e-02
^{33}S	1.37e-05	1.67e-04	1.36e-05	1.65e-04	1.38e-05	3.35e-04
^{34}S	1.14e-05	1.02e-03	1.13e-05	9.91e-04	1.05e-05	4.80e-03
^{36}S	6.19e-10	2.33e-08	1.46e-09	2.41e-08	1.22e-08	1.98e-06
^{35}Cl	2.35e-05	6.10e-05	2.36e-05	5.95e-05	2.92e-05	1.62e-04
^{37}Cl	1.96e-06	1.47e-05	1.96e-06	1.44e-05	2.22e-06	3.03e-05
^{36}Ar	7.64e-04	2.06e-02	7.66e-04	2.06e-02	8.49e-04	1.55e-02
^{38}Ar	2.12e-06	4.68e-04	2.14e-06	4.54e-04	3.20e-06	2.23e-03
^{40}Ar	1.89e-10	2.40e-09	1.38e-09	3.27e-09	1.15e-08	1.79e-07
^{39}K	4.79e-05	3.91e-05	4.85e-05	3.83e-05	7.02e-05	9.01e-05
^{41}K	4.61e-06	2.77e-06	4.61e-06	2.72e-06	5.18e-06	5.09e-06
^{40}Ca	2.32e-03	1.96e-02	2.33e-03	1.97e-02	2.52e-03	1.44e-02
^{42}Ca	1.74e-06	1.19e-05	1.78e-06	1.14e-05	3.18e-06	5.33e-05
^{43}Ca	4.35e-06	2.86e-07	4.39e-06	2.86e-07	6.67e-06	2.78e-07
^{44}Ca	5.72e-04	1.99e-05	5.72e-04	1.99e-05	5.54e-04	1.31e-05
^{46}Ca	5.62e-11	7.27e-11	5.40e-10	6.29e-10	4.78e-09	9.12e-08
^{48}Ca	1.25e-11	4.35e-12	1.21e-10	4.08e-11	2.68e-09	7.35e-09
^{45}Sc	2.18e-06	1.50e-07	2.20e-06	1.49e-07	2.95e-06	3.62e-07

Table B.15 continued.

	M10_02_001		M10_02_01		M10_02_3	
	He det $[M_\odot]$	core det $[M_\odot]$	He det $[M_\odot]$	core det $[M_\odot]$	He det $[M_\odot]$	core det $[M_\odot]$
^{46}Ti	1.08e-06	4.71e-06	1.09e-06	4.56e-06	1.58e-06	1.85e-05
^{47}Ti	2.73e-05	6.31e-07	2.75e-05	6.28e-07	3.15e-05	1.18e-06
^{48}Ti	2.53e-04	4.32e-04	2.51e-04	4.33e-04	1.95e-04	3.06e-04
^{49}Ti	3.65e-06	2.25e-05	3.67e-06	2.24e-05	4.30e-06	3.35e-05
^{50}Ti	5.78e-11	2.10e-10	5.92e-10	8.31e-10	1.99e-08	2.21e-07
^{50}V	8.61e-11	1.41e-09	1.26e-10	1.80e-09	2.34e-09	6.25e-08
^{51}V	1.10e-05	5.55e-05	1.10e-05	5.50e-05	9.88e-06	1.16e-04
^{50}Cr	1.36e-06	1.20e-04	1.37e-06	1.18e-04	1.64e-06	6.02e-04
^{52}Cr	2.92e-05	9.50e-03	2.89e-05	9.51e-03	1.98e-05	7.44e-03
^{53}Cr	1.29e-06	6.62e-04	1.29e-06	6.57e-04	1.35e-06	1.16e-03
^{54}Cr	1.73e-10	1.38e-08	1.59e-09	1.55e-08	6.43e-08	7.00e-07
^{55}Mn	1.28e-06	3.34e-03	1.29e-06	3.30e-03	1.62e-06	7.51e-03
^{54}Fe	5.00e-07	1.38e-02	5.30e-07	1.35e-02	1.55e-06	6.04e-02
^{56}Fe	1.87e-06	5.59e-01	2.33e-06	5.59e-01	2.03e-05	4.87e-01
^{57}Fe	3.03e-07	9.28e-03	3.85e-07	9.23e-03	5.05e-06	1.59e-02
^{58}Fe	5.78e-09	8.59e-09	6.29e-08	4.47e-08	4.29e-06	2.23e-06
^{59}Co	7.96e-08	2.94e-04	2.56e-07	2.91e-04	7.37e-06	5.20e-04
^{58}Ni	9.22e-08	8.91e-03	2.53e-07	8.73e-03	9.67e-06	4.55e-02
^{60}Ni	1.35e-07	6.90e-03	4.66e-07	6.92e-03	5.31e-06	4.05e-03
^{61}Ni	5.07e-08	2.20e-04	1.76e-07	2.19e-04	1.65e-06	2.49e-04
^{62}Ni	5.97e-08	1.27e-03	2.99e-07	1.26e-03	2.41e-06	3.73e-03
^{64}Ni	7.97e-10	4.46e-09	8.13e-09	4.33e-08	1.40e-07	3.16e-06
^{63}Cu	8.85e-09	5.00e-07	4.80e-08	6.27e-07	4.93e-07	5.56e-06
^{64}Zn	1.29e-08	2.24e-05	2.74e-08	2.28e-05	1.78e-07	8.56e-06
^{66}Zn	6.43e-09	2.46e-05	3.23e-08	2.48e-05	1.63e-07	5.70e-05
^{67}Zn	1.59e-09	1.47e-08	8.25e-09	2.44e-08	3.43e-08	5.27e-07
^{68}Zn	1.62e-09	7.74e-09	9.24e-09	3.17e-08	3.89e-08	9.38e-07
^{70}Zn	4.88e-12	3.38e-11	5.42e-11	3.26e-10	4.69e-09	2.05e-08
^{69}Ga	1.26e-10	1.82e-09	8.43e-10	1.78e-08	1.03e-08	1.60e-07
^{71}Ga	4.64e-11	3.03e-10	3.95e-10	2.90e-09	6.05e-09	6.13e-08

Table B.16: Asymptotic nucleosynthetic yields (in $M_\odot$) of Model M10_03 with 0.01, 0.1, and 3 $Z_\odot$.

	M10_03_001		M10_03_01		M10_03_3	
	He det $[M_\odot]$	core det $[M_\odot]$	He det $[M_\odot]$	core det $[M_\odot]$	He det $[M_\odot]$	core det $[M_\odot]$
^{12}C	7.71e-04	1.24e-03	7.68e-04	1.24e-03	7.55e-04	1.20e-03
^{13}C	4.95e-11	1.12e-09	4.92e-11	1.04e-09	3.96e-11	1.19e-08
^{14}N	1.71e-07	1.37e-07	1.22e-06	1.29e-07	3.51e-05	5.12e-07
^{15}N	1.27e-08	1.12e-09	1.33e-08	1.12e-09	3.35e-08	1.27e-09
^{16}O	6.60e-03	4.85e-02	6.62e-03	4.84e-02	7.09e-03	4.93e-02
^{17}O	1.55e-09	3.01e-08	2.94e-09	2.87e-08	4.73e-08	8.03e-08
^{18}O	1.11e-08	8.35e-10	1.91e-08	7.95e-10	2.74e-07	2.83e-09
^{19}F	6.87e-09	2.58e-11	7.33e-09	2.47e-11	2.16e-08	1.52e-10
^{20}Ne	1.70e-03	1.83e-03	1.69e-03	1.83e-03	1.68e-03	1.64e-03
^{21}Ne	4.93e-08	1.34e-07	5.10e-08	1.27e-07	1.02e-07	1.03e-06
^{22}Ne	2.89e-08	3.28e-07	4.84e-08	3.08e-07	6.70e-07	8.38e-06
^{23}Na	8.08e-06	1.04e-05	8.05e-06	1.03e-05	8.14e-06	2.59e-05
^{24}Mg	3.44e-03	3.71e-03	3.45e-03	3.80e-03	3.51e-03	1.61e-03
^{25}Mg	9.30e-06	1.52e-05	9.34e-06	1.48e-05	1.09e-05	7.31e-05
^{26}Mg	1.65e-05	2.64e-05	1.64e-05	2.57e-05	1.73e-05	1.25e-04
^{27}Al	1.25e-04	1.40e-04	1.25e-04	1.40e-04	1.29e-04	1.76e-04
^{28}Si	8.88e-03	1.51e-01	8.88e-03	1.51e-01	8.96e-03	1.50e-01
^{29}Si	9.37e-05	2.48e-04	9.36e-05	2.46e-04	9.48e-05	7.82e-04
^{30}Si	9.79e-05	3.42e-04	9.80e-05	3.38e-04	1.02e-04	1.76e-03
^{31}P	8.39e-05	1.83e-04	8.39e-05	1.81e-04	8.71e-05	5.04e-04
^{32}S	3.70e-03	9.38e-02	3.70e-03	9.38e-02	3.74e-03	7.98e-02
^{33}S	5.85e-05	1.45e-04	5.83e-05	1.43e-04	5.79e-05	2.93e-04
^{34}S	2.87e-05	8.86e-04	2.87e-05	8.66e-04	3.07e-05	4.20e-03
^{36}S	2.22e-09	1.92e-08	2.39e-09	1.91e-08	6.01e-09	1.65e-06
^{35}Cl	2.93e-05	5.36e-05	2.94e-05	5.23e-05	3.32e-05	1.42e-04
^{37}Cl	7.94e-06	1.32e-05	7.92e-06	1.29e-05	7.96e-06	2.70e-05
^{36}Ar	1.20e-03	1.84e-02	1.20e-03	1.84e-02	1.25e-03	1.39e-02
^{38}Ar	1.20e-05	4.18e-04	1.20e-05	4.06e-04	1.49e-05	1.99e-03
^{40}Ar	5.42e-10	1.97e-09	7.76e-10	2.38e-09	3.60e-09	1.47e-07
^{39}K	4.00e-05	3.56e-05	4.04e-05	3.49e-05	5.93e-05	8.11e-05
^{41}K	6.33e-06	2.52e-06	6.32e-06	2.48e-06	6.70e-06	4.60e-06
^{40}Ca	3.19e-03	1.77e-02	3.20e-03	1.77e-02	3.46e-03	1.30e-02
^{42}Ca	2.59e-06	1.07e-05	2.63e-06	1.03e-05	4.11e-06	4.77e-05
^{43}Ca	5.19e-06	3.56e-07	5.20e-06	3.57e-07	6.40e-06	2.65e-07
^{44}Ca	1.05e-03	2.01e-05	1.05e-03	2.02e-05	1.17e-03	1.27e-05
^{46}Ca	1.51e-11	4.74e-11	1.43e-10	3.95e-10	1.49e-09	7.98e-08
^{48}Ca	7.45e-12	1.82e-12	7.39e-11	1.66e-11	2.06e-09	5.89e-09
^{45}Sc	2.97e-06	1.37e-07	2.98e-06	1.36e-07	3.77e-06	3.22e-07

Table B.16 continued.

	M10_03_001		M10_03_01		M10_03_3	
	He det $[M_\odot]$	core det $[M_\odot]$	He det $[M_\odot]$	core det $[M_\odot]$	He det $[M_\odot]$	core det $[M_\odot]$
^{46}Ti	1.94e-06	4.27e-06	1.96e-06	4.14e-06	2.76e-06	1.67e-05
^{47}Ti	3.38e-05	7.36e-07	3.41e-05	7.33e-07	4.74e-05	1.12e-06
^{48}Ti	1.71e-03	4.03e-04	1.71e-03	4.04e-04	1.55e-03	2.86e-04
^{49}Ti	1.14e-05	2.07e-05	1.14e-05	2.06e-05	1.39e-05	3.12e-05
^{50}Ti	2.46e-11	1.73e-10	2.31e-10	6.26e-10	7.80e-09	1.83e-07
^{50}V	7.62e-11	1.19e-09	1.93e-10	1.52e-09	2.91e-09	5.25e-08
^{51}V	6.08e-05	5.14e-05	6.09e-05	5.09e-05	6.20e-05	1.08e-04
^{50}Cr	3.87e-06	1.08e-04	3.90e-06	1.06e-04	5.06e-06	5.40e-04
^{52}Cr	7.32e-04	8.74e-03	7.25e-04	8.76e-03	5.14e-04	6.87e-03
^{53}Cr	1.27e-05	6.09e-04	1.27e-05	6.05e-04	1.22e-05	1.07e-03
^{54}Cr	1.23e-10	1.27e-08	7.42e-10	1.42e-08	2.83e-08	6.21e-07
^{55}Mn	1.74e-05	3.07e-03	1.73e-05	3.04e-03	1.44e-05	6.94e-03
^{54}Fe	4.67e-06	1.24e-02	4.69e-06	1.22e-02	5.33e-06	5.44e-02
^{56}Fe	6.96e-05	6.10e-01	6.90e-05	6.11e-01	5.93e-05	5.33e-01
^{57}Fe	3.40e-06	1.11e-02	3.45e-06	1.10e-02	7.22e-06	1.87e-02
^{58}Fe	2.26e-09	7.07e-09	2.40e-08	3.25e-08	2.06e-06	1.59e-06
^{59}Co	3.87e-07	3.88e-04	6.65e-07	3.85e-04	1.39e-05	6.88e-04
^{58}Ni	2.33e-06	1.08e-02	2.56e-06	1.06e-02	2.22e-05	5.49e-02
^{60}Ni	8.46e-07	8.97e-03	1.67e-06	9.00e-03	1.82e-05	5.24e-03
^{61}Ni	2.10e-07	2.91e-04	4.06e-07	2.90e-04	4.42e-06	3.25e-04
^{62}Ni	2.62e-07	1.69e-03	7.12e-07	1.67e-03	6.75e-06	4.85e-03
^{64}Ni	1.36e-09	3.80e-09	1.34e-08	3.69e-08	2.30e-07	2.61e-06
^{63}Cu	3.34e-08	6.63e-07	1.57e-07	7.67e-07	1.76e-06	5.94e-06
^{64}Zn	8.45e-08	2.91e-05	2.39e-07	2.95e-05	2.16e-06	1.06e-05
^{66}Zn	3.27e-08	3.25e-05	1.12e-07	3.25e-05	8.35e-07	6.99e-05
^{67}Zn	8.82e-09	1.92e-08	2.68e-08	2.73e-08	1.76e-07	4.57e-07
^{68}Zn	1.18e-08	9.11e-09	4.01e-08	2.89e-08	1.78e-07	7.86e-07
^{70}Zn	6.94e-12	3.01e-11	6.98e-11	2.91e-10	2.80e-09	1.69e-08
^{69}Ga	1.17e-09	1.49e-09	5.73e-09	1.45e-08	4.70e-08	1.35e-07
^{71}Ga	2.42e-10	2.50e-10	1.33e-09	2.40e-09	1.42e-08	4.95e-08

Table B.17: Asymptotic nucleosynthetic yields (in $M_\odot$) of Model M10_05 with 0.01, 0.1, and 3 $Z_\odot$.

	M10_05_001		M10_05_01		M10_05_3	
	He det $[M_\odot]$	core det $[M_\odot]$	He det $[M_\odot]$	core det $[M_\odot]$	He det $[M_\odot]$	core det $[M_\odot]$
^{12}C	3.96e-05	4.45e-04	3.95e-05	4.43e-04	3.97e-05	4.30e-04
^{13}C	1.91e-10	1.25e-10	1.88e-10	1.20e-10	9.33e-11	7.98e-10
^{14}N	1.49e-07	2.49e-08	1.21e-06	2.40e-08	3.55e-05	7.19e-08
^{15}N	4.65e-09	5.90e-10	4.93e-09	1.08e-09	1.25e-08	7.36e-10
^{16}O	9.17e-03	6.04e-02	9.18e-03	6.03e-02	9.67e-03	6.15e-02
^{17}O	1.81e-10	6.15e-09	1.58e-09	5.94e-09	4.67e-08	1.72e-08
^{18}O	6.40e-09	1.93e-10	1.42e-08	1.83e-10	2.63e-07	5.29e-10
^{19}F	1.60e-09	5.51e-12	1.80e-09	5.44e-12	7.77e-09	2.81e-11
^{20}Ne	1.42e-05	1.54e-03	1.44e-05	1.53e-03	2.26e-05	1.41e-03
^{21}Ne	7.07e-09	3.61e-08	8.12e-09	3.58e-08	3.97e-08	2.66e-07
^{22}Ne	6.14e-09	1.18e-07	2.51e-08	1.15e-07	6.34e-07	9.70e-07
^{23}Na	3.58e-07	7.28e-06	3.62e-07	7.30e-06	5.55e-07	1.41e-05
^{24}Mg	2.82e-03	5.14e-03	2.86e-03	5.27e-03	2.98e-03	2.31e-03
^{25}Mg	8.31e-07	1.15e-05	8.73e-07	1.13e-05	1.87e-06	4.73e-05
^{26}Mg	6.27e-07	1.71e-05	6.66e-07	1.67e-05	1.73e-06	6.51e-05
^{27}Al	4.93e-05	2.08e-04	5.01e-05	2.09e-04	5.23e-05	2.56e-04
^{28}Si	1.31e-02	1.61e-01	1.31e-02	1.62e-01	1.32e-02	1.60e-01
^{29}Si	7.85e-05	2.98e-04	7.90e-05	2.95e-04	8.22e-05	9.91e-04
^{30}Si	9.60e-05	4.52e-04	9.74e-05	4.47e-04	1.04e-04	2.43e-03
^{31}P	5.55e-05	2.50e-04	5.55e-05	2.47e-04	5.67e-05	6.91e-04
^{32}S	4.98e-03	9.88e-02	4.95e-03	9.87e-02	4.94e-03	8.43e-02
^{33}S	6.19e-05	1.96e-04	6.14e-05	1.93e-04	6.09e-05	3.73e-04
^{34}S	1.71e-04	1.02e-03	1.70e-04	9.94e-04	1.73e-04	4.85e-03
^{36}S	3.94e-09	2.43e-08	4.02e-09	2.35e-08	5.29e-09	2.18e-06
^{35}Cl	1.58e-05	7.05e-05	1.57e-05	6.86e-05	1.82e-05	1.86e-04
^{37}Cl	5.46e-06	1.52e-05	5.41e-06	1.49e-05	5.67e-06	2.98e-05
^{36}Ar	1.39e-03	1.90e-02	1.38e-03	1.90e-02	1.40e-03	1.43e-02
^{38}Ar	4.51e-05	4.56e-04	4.47e-05	4.43e-04	4.97e-05	2.12e-03
^{40}Ar	2.52e-10	3.04e-09	2.56e-10	2.97e-09	5.93e-10	1.26e-07
^{39}K	4.03e-05	4.09e-05	4.06e-05	4.00e-05	5.21e-05	8.75e-05
^{41}K	1.84e-06	2.74e-06	1.84e-06	2.69e-06	2.43e-06	4.82e-06
^{40}Ca	4.26e-03	1.79e-02	4.26e-03	1.79e-02	4.31e-03	1.31e-02
^{42}Ca	4.59e-06	1.24e-05	4.58e-06	1.20e-05	6.16e-06	5.11e-05
^{43}Ca	1.38e-05	7.77e-07	1.38e-05	7.77e-07	1.35e-05	4.92e-07
^{44}Ca	7.79e-04	2.42e-05	7.80e-04	2.43e-05	8.10e-04	1.41e-05
^{46}Ca	7.74e-13	2.41e-11	2.15e-12	1.09e-10	4.35e-11	4.89e-08
^{48}Ca	6.33e-12	1.31e-12	6.33e-11	4.67e-12	1.90e-09	1.74e-09
^{45}Sc	2.19e-06	1.56e-07	2.19e-06	1.53e-07	2.87e-06	3.59e-07

Table B.17 continued.

	M10_05_001		M10_05_01		M10_05_3	
	He det $[M_\odot]$	core det $[M_\odot]$	He det $[M_\odot]$	core det $[M_\odot]$	He det $[M_\odot]$	core det $[M_\odot]$
^{46}Ti	5.21e-06	4.64e-06	5.20e-06	4.49e-06	5.46e-06	1.76e-05
^{47}Ti	3.15e-05	9.28e-07	3.15e-05	9.23e-07	3.33e-05	1.29e-06
^{48}Ti	2.06e-03	3.95e-04	2.06e-03	3.96e-04	2.15e-03	2.77e-04
^{49}Ti	2.05e-05	2.03e-05	2.07e-05	2.02e-05	2.64e-05	3.03e-05
^{50}Ti	2.22e-11	2.29e-10	8.62e-11	6.06e-10	2.17e-09	2.66e-07
^{50}V	2.45e-10	2.02e-09	2.41e-10	2.22e-09	6.34e-10	8.63e-08
^{51}V	1.48e-04	5.05e-05	1.48e-04	5.00e-05	1.59e-04	1.06e-04
^{50}Cr	2.56e-05	1.11e-04	2.54e-05	1.08e-04	2.13e-05	5.51e-04
^{52}Cr	4.02e-03	8.43e-03	4.03e-03	8.44e-03	4.37e-03	6.61e-03
^{53}Cr	5.77e-05	5.91e-04	5.83e-05	5.87e-04	7.91e-05	1.04e-03
^{54}Cr	2.97e-10	1.39e-08	4.68e-10	1.69e-08	6.75e-09	7.03e-07
^{55}Mn	4.78e-04	2.98e-03	4.79e-04	2.95e-03	4.94e-04	6.71e-03
^{54}Fe	3.50e-05	1.24e-02	3.54e-05	1.22e-02	4.98e-05	5.43e-02
^{56}Fe	8.32e-03	5.56e-01	8.31e-03	5.57e-01	8.10e-03	4.85e-01
^{57}Fe	5.75e-04	1.01e-02	5.76e-04	1.00e-02	5.73e-04	1.69e-02
^{58}Fe	3.88e-10	7.81e-09	3.23e-09	3.34e-08	1.31e-07	2.03e-06
^{59}Co	2.75e-05	3.67e-04	2.75e-05	3.63e-04	3.03e-05	6.40e-04
^{58}Ni	1.02e-04	9.59e-03	1.03e-04	9.40e-03	1.44e-04	4.89e-02
^{60}Ni	7.48e-04	9.15e-03	7.48e-04	9.17e-03	7.29e-04	5.44e-03
^{61}Ni	1.20e-04	2.92e-04	1.20e-04	2.92e-04	1.12e-04	3.28e-04
^{62}Ni	5.98e-05	1.57e-03	6.07e-05	1.55e-03	8.78e-05	4.54e-03
^{64}Ni	7.39e-11	3.84e-09	7.39e-10	3.63e-08	1.77e-08	4.93e-06
^{63}Cu	5.17e-06	8.00e-07	5.17e-06	9.36e-07	4.87e-06	6.29e-06
^{64}Zn	6.41e-05	3.05e-05	6.37e-05	3.11e-05	4.88e-05	1.19e-05
^{66}Zn	7.08e-06	3.22e-05	7.35e-06	3.25e-05	1.21e-05	7.46e-05
^{67}Zn	5.48e-07	2.13e-08	6.18e-07	2.98e-08	1.73e-06	8.28e-07
^{68}Zn	3.67e-07	1.05e-08	5.71e-07	4.54e-08	1.86e-06	1.66e-06
^{70}Zn	4.68e-13	2.51e-11	4.60e-12	2.29e-10	1.18e-10	3.56e-08
^{69}Ga	2.39e-08	3.16e-09	4.57e-08	3.08e-08	1.43e-07	3.10e-07
^{71}Ga	1.47e-09	4.21e-10	3.43e-09	4.00e-09	9.10e-09	1.37e-07

Table B.18: Asymptotic nucleosynthetic yields (in $M_\odot$) of Model M10_10 with 0.01, 0.1, and 3 $Z_\odot$.

	M10_10_001		M10_10_01		M10_10_3	
	He det $[M_\odot]$	core det $[M_\odot]$	He det $[M_\odot]$	core det $[M_\odot]$	He det $[M_\odot]$	core det $[M_\odot]$
^{12}C	7.39e-06	2.46e-06	7.25e-06	2.47e-06	7.52e-06	1.12e-06
^{13}C	4.23e-09	2.49e-12	4.21e-09	2.57e-12	3.65e-09	1.12e-12
^{14}N	1.25e-07	3.04e-12	1.16e-06	3.13e-12	3.46e-05	1.88e-11
^{15}N	3.15e-10	2.12e-12	3.27e-10	2.13e-12	8.11e-10	4.36e-11
^{16}O	3.02e-03	2.70e-03	3.02e-03	2.70e-03	3.24e-03	2.75e-03
^{17}O	1.98e-10	4.28e-16	1.57e-09	4.26e-16	4.56e-08	6.50e-16
^{18}O	1.61e-09	1.60e-17	8.88e-09	1.59e-17	2.43e-07	1.62e-11
^{19}F	2.39e-10	1.53e-19	3.53e-10	1.54e-19	4.14e-09	9.82e-15
^{20}Ne	1.74e-06	1.05e-07	1.98e-06	1.03e-07	9.96e-06	1.16e-07
^{21}Ne	1.17e-08	5.33e-13	1.23e-08	5.27e-13	2.91e-08	9.70e-13
^{22}Ne	1.53e-08	5.44e-13	3.33e-08	5.57e-13	6.18e-07	1.84e-10
^{23}Na	1.61e-09	1.12e-10	7.83e-09	1.10e-10	2.09e-07	3.51e-10
^{24}Mg	2.27e-04	1.02e-04	2.32e-04	1.06e-04	2.53e-04	4.12e-05
^{25}Mg	7.32e-07	1.50e-08	7.62e-07	1.57e-08	1.68e-06	1.00e-08
^{26}Mg	8.44e-07	1.08e-08	8.66e-07	1.12e-08	1.59e-06	2.23e-08
^{27}Al	2.11e-06	1.68e-06	2.16e-06	1.73e-06	2.67e-06	1.94e-06
^{28}Si	3.68e-02	7.28e-02	3.68e-02	7.28e-02	3.75e-02	7.29e-02
^{29}Si	3.33e-05	1.07e-05	3.36e-05	1.08e-05	3.61e-05	2.40e-05
^{30}Si	5.15e-05	1.10e-05	5.22e-05	1.10e-05	5.60e-05	6.55e-05
^{31}P	2.31e-05	9.49e-06	2.31e-05	9.43e-06	2.45e-05	3.10e-05
^{32}S	1.59e-02	5.55e-02	1.59e-02	5.56e-02	1.61e-02	4.85e-02
^{33}S	1.58e-05	1.02e-05	1.58e-05	1.00e-05	1.67e-05	2.77e-05
^{34}S	1.50e-04	6.91e-05	1.50e-04	6.76e-05	1.51e-04	3.53e-04
^{36}S	3.34e-10	3.68e-10	4.01e-10	3.63e-10	1.35e-09	4.22e-09
^{35}Cl	8.94e-06	3.81e-06	8.89e-06	3.74e-06	8.95e-06	1.19e-05
^{37}Cl	1.63e-06	1.67e-06	1.62e-06	1.64e-06	1.68e-06	4.14e-06
^{36}Ar	2.79e-03	1.28e-02	2.79e-03	1.28e-02	2.82e-03	1.05e-02
^{38}Ar	4.40e-05	3.90e-05	4.37e-05	3.77e-05	4.51e-05	1.96e-04
^{40}Ar	3.76e-11	5.19e-11	4.70e-11	5.00e-11	3.35e-10	2.82e-10
^{39}K	9.96e-06	4.57e-06	1.00e-05	4.49e-06	1.29e-05	1.17e-05
^{41}K	3.19e-07	4.10e-07	3.21e-07	4.03e-07	4.79e-07	8.57e-07
^{40}Ca	3.43e-03	1.42e-02	3.43e-03	1.42e-02	3.48e-03	1.14e-02
^{42}Ca	8.96e-07	1.15e-06	8.95e-07	1.11e-06	1.26e-06	4.89e-06
^{43}Ca	4.65e-06	4.09e-07	4.62e-06	4.11e-07	4.55e-06	1.09e-07
^{44}Ca	2.68e-04	2.04e-05	2.68e-04	2.04e-05	2.78e-04	1.25e-05
^{46}Ca	1.38e-13	3.20e-14	1.57e-12	2.73e-14	3.94e-11	5.58e-12
^{48}Ca	6.10e-12	3.16e-15	6.11e-11	3.86e-19	1.83e-09	9.46e-15
^{45}Sc	2.59e-07	5.86e-08	2.60e-07	5.80e-08	4.16e-07	1.06e-07

Table B.18 continued.

	M10_10_001		M10_10_01		M10_10_3	
	He det $[M_\odot]$	core det $[M_\odot]$	He det $[M_\odot]$	core det $[M_\odot]$	He det $[M_\odot]$	core det $[M_\odot]$
^{46}Ti	9.78e-06	5.98e-07	9.66e-06	5.80e-07	6.51e-06	3.16e-06
^{47}Ti	1.72e-05	7.81e-07	1.71e-05	7.80e-07	1.66e-05	5.36e-07
^{48}Ti	5.30e-04	4.14e-04	5.32e-04	4.14e-04	5.97e-04	3.00e-04
^{49}Ti	9.15e-06	2.01e-05	9.20e-06	1.99e-05	1.12e-05	3.18e-05
^{50}Ti	1.23e-11	2.15e-10	1.10e-10	8.78e-11	2.11e-09	1.79e-08
^{50}V	3.23e-11	3.83e-11	3.89e-11	4.36e-11	3.28e-10	8.07e-10
^{51}V	8.52e-05	4.91e-05	8.50e-05	4.86e-05	7.96e-05	1.05e-04
^{50}Cr	1.03e-04	7.59e-05	1.03e-04	7.44e-05	8.37e-05	3.89e-04
^{52}Cr	1.97e-03	9.27e-03	1.97e-03	9.28e-03	2.06e-03	7.22e-03
^{53}Cr	5.50e-05	6.23e-04	5.53e-05	6.19e-04	6.65e-05	1.07e-03
^{54}Cr	1.74e-09	1.14e-08	1.95e-09	1.72e-09	1.44e-08	2.51e-07
^{55}Mn	2.52e-04	3.16e-03	2.53e-04	3.13e-03	2.78e-04	7.24e-03
^{54}Fe	9.41e-04	1.05e-02	9.48e-04	1.03e-02	1.17e-03	4.89e-02
^{56}Fe	3.95e-02	7.45e-01	3.95e-02	7.45e-01	3.90e-02	6.52e-01
^{57}Fe	1.37e-03	1.41e-02	1.37e-03	1.40e-02	1.50e-03	2.49e-02
^{58}Fe	4.72e-10	1.44e-07	1.60e-09	7.18e-10	3.52e-08	6.49e-07
^{59}Co	4.51e-04	5.19e-04	4.47e-04	5.14e-04	3.19e-04	1.18e-03
^{58}Ni	5.86e-04	1.39e-02	5.86e-04	1.36e-02	5.58e-04	6.84e-02
^{60}Ni	2.07e-03	1.16e-02	2.07e-03	1.16e-02	2.02e-03	6.70e-03
^{61}Ni	1.41e-04	3.81e-04	1.41e-04	3.80e-04	1.44e-04	4.02e-04
^{62}Ni	9.91e-05	2.25e-03	9.90e-05	2.22e-03	9.61e-05	6.05e-03
^{64}Ni	1.65e-11	2.03e-07	1.65e-10	1.07e-11	4.92e-09	8.11e-09
^{63}Cu	1.39e-05	8.70e-07	1.39e-05	8.56e-07	1.60e-05	3.90e-06
^{64}Zn	2.16e-04	3.69e-05	2.16e-04	3.72e-05	2.26e-04	1.27e-05
^{66}Zn	1.44e-05	4.25e-05	1.45e-05	4.20e-05	1.63e-05	7.98e-05
^{67}Zn	3.23e-07	2.45e-08	3.40e-07	2.37e-08	5.96e-07	7.59e-08
^{68}Zn	1.38e-07	1.02e-08	2.05e-07	9.21e-09	4.85e-07	8.51e-08
^{70}Zn	2.69e-13	4.07e-11	2.68e-12	9.93e-16	7.94e-11	2.10e-12
^{69}Ga	6.90e-09	3.71e-12	1.34e-08	2.28e-11	2.27e-08	2.98e-10
^{71}Ga	3.88e-10	1.60e-12	9.89e-10	7.60e-13	1.84e-09	3.99e-11

Table B.19: Asymptotic nucleosynthetic yields (in $M_\odot$) of Model M11_05 with 0.01, 0.1, and 3 $Z_\odot$.

	M11_05_001		M11_05_01		M11_05_3	
	He det $[M_\odot]$	core det $[M_\odot]$	He det $[M_\odot]$	core det $[M_\odot]$	He det $[M_\odot]$	core det $[M_\odot]$
^{12}C	5.24e-06	3.11e-06	5.27e-06	3.12e-06	5.65e-06	1.23e-06
^{13}C	1.01e-09	3.17e-12	1.00e-09	3.27e-12	8.18e-10	1.04e-12
^{14}N	1.38e-07	7.05e-13	1.20e-06	7.21e-13	3.54e-05	4.99e-11
^{15}N	2.43e-09	1.14e-12	2.56e-09	1.15e-12	6.49e-09	1.37e-10
^{16}O	3.74e-03	7.48e-04	3.74e-03	7.47e-04	4.02e-03	7.62e-04
^{17}O	1.96e-10	1.02e-16	1.60e-09	1.02e-16	4.67e-08	5.95e-16
^{18}O	4.18e-09	3.96e-18	1.18e-08	3.96e-18	2.56e-07	6.23e-11
^{19}F	8.08e-10	9.86e-20	9.57e-10	9.97e-20	5.73e-09	3.40e-14
^{20}Ne	7.67e-07	4.48e-08	1.02e-06	4.43e-08	9.37e-06	3.90e-08
^{21}Ne	7.03e-09	1.52e-13	7.80e-09	1.51e-13	3.29e-08	2.64e-13
^{22}Ne	1.11e-08	1.74e-13	2.98e-08	1.77e-13	6.33e-07	6.86e-10
^{23}Na	2.98e-09	3.96e-11	9.36e-09	3.91e-11	2.15e-07	3.04e-10
^{24}Mg	2.98e-04	2.07e-05	3.03e-04	2.15e-05	3.40e-04	9.17e-06
^{25}Mg	2.44e-07	2.90e-09	2.72e-07	3.04e-09	1.19e-06	1.83e-09
^{26}Mg	3.30e-07	1.89e-09	3.59e-07	1.97e-09	1.31e-06	3.77e-09
^{27}Al	2.51e-06	3.15e-07	2.57e-06	3.23e-07	3.20e-06	3.61e-07
^{28}Si	5.55e-02	4.54e-02	5.55e-02	4.54e-02	5.62e-02	4.43e-02
^{29}Si	4.59e-05	3.15e-06	4.62e-05	3.18e-06	5.07e-05	7.57e-06
^{30}Si	6.09e-05	2.80e-06	6.15e-05	2.88e-06	6.96e-05	1.62e-05
^{31}P	3.60e-05	3.34e-06	3.62e-05	3.33e-06	3.94e-05	1.03e-05
^{32}S	2.45e-02	3.76e-02	2.45e-02	3.76e-02	2.45e-02	3.35e-02
^{33}S	2.65e-05	3.98e-06	2.65e-05	3.94e-06	2.85e-05	1.06e-05
^{34}S	1.80e-04	2.18e-05	1.80e-04	2.15e-05	1.96e-04	1.15e-04
^{36}S	4.31e-10	8.10e-11	4.67e-10	8.51e-11	1.50e-09	7.47e-10
^{35}Cl	1.00e-05	1.85e-06	1.00e-05	1.83e-06	1.15e-05	4.61e-06
^{37}Cl	3.57e-06	8.73e-07	3.57e-06	8.62e-07	3.95e-06	1.94e-06
^{36}Ar	4.34e-03	9.35e-03	4.34e-03	9.36e-03	4.35e-03	7.97e-03
^{38}Ar	7.81e-05	1.57e-05	7.81e-05	1.52e-05	8.93e-05	7.88e-05
^{40}Ar	7.68e-11	1.97e-11	8.59e-11	1.92e-11	3.92e-10	9.32e-11
^{39}K	1.51e-05	2.95e-06	1.52e-05	2.92e-06	1.98e-05	5.22e-06
^{41}K	9.97e-07	2.58e-07	1.00e-06	2.55e-07	1.30e-06	4.85e-07
^{40}Ca	5.72e-03	1.09e-02	5.72e-03	1.09e-02	5.85e-03	9.10e-03
^{42}Ca	2.19e-06	6.32e-07	2.20e-06	6.16e-07	2.93e-06	2.14e-06
^{43}Ca	2.60e-06	5.40e-07	2.59e-06	5.43e-07	2.42e-06	1.29e-07
^{44}Ca	1.53e-04	2.05e-05	1.53e-04	2.05e-05	1.74e-04	1.15e-05
^{46}Ca	1.45e-13	2.14e-15	1.40e-12	6.86e-15	4.08e-11	4.18e-13
^{48}Ca	6.27e-12	3.32e-21	6.27e-11	1.37e-19	1.88e-09	7.17e-15
^{45}Sc	4.64e-07	4.56e-08	4.68e-07	4.52e-08	7.37e-07	8.50e-08

Table B.19 continued.

	M11_05_001		M11_05_01		M11_05_3	
	He det $[M_\odot]$	core det $[M_\odot]$	He det $[M_\odot]$	core det $[M_\odot]$	He det $[M_\odot]$	core det $[M_\odot]$
^{46}Ti	2.95e-06	3.22e-07	2.96e-06	3.14e-07	3.55e-06	1.59e-06
^{47}Ti	5.71e-06	9.79e-07	5.72e-06	9.79e-07	6.56e-06	5.31e-07
^{48}Ti	7.17e-04	3.52e-04	7.19e-04	3.53e-04	8.03e-04	2.57e-04
^{49}Ti	1.39e-05	1.63e-05	1.40e-05	1.62e-05	1.67e-05	2.68e-05
^{50}Ti	1.32e-11	1.44e-12	7.86e-11	2.04e-11	2.30e-09	1.32e-08
^{50}V	5.28e-11	1.14e-11	6.52e-11	1.50e-11	6.19e-10	2.61e-10
^{51}V	3.15e-05	4.01e-05	3.16e-05	3.97e-05	3.63e-05	8.80e-05
^{50}Cr	4.09e-05	5.39e-05	4.10e-05	5.29e-05	4.57e-05	2.66e-04
^{52}Cr	2.04e-03	7.80e-03	2.05e-03	7.81e-03	2.24e-03	6.11e-03
^{53}Cr	7.19e-05	5.16e-04	7.21e-05	5.13e-04	8.16e-05	8.97e-04
^{54}Cr	4.45e-09	7.59e-10	4.77e-09	1.14e-09	2.32e-08	1.71e-07
^{55}Mn	2.14e-04	2.63e-03	2.15e-04	2.61e-03	2.32e-04	6.14e-03
^{54}Fe	1.48e-03	7.96e-03	1.49e-03	7.82e-03	1.77e-03	3.78e-02
^{56}Fe	1.24e-02	8.47e-01	1.24e-02	8.48e-01	1.14e-02	7.46e-01
^{57}Fe	3.04e-04	1.77e-02	3.04e-04	1.76e-02	3.00e-04	3.35e-02
^{58}Fe	1.15e-09	2.69e-10	2.46e-09	4.32e-10	3.98e-08	4.95e-07
^{59}Co	5.17e-05	7.12e-04	5.10e-05	7.06e-04	3.47e-05	2.05e-03
^{58}Ni	1.91e-04	1.83e-02	1.91e-04	1.79e-02	2.11e-04	8.08e-02
^{60}Ni	2.72e-04	1.54e-02	2.71e-04	1.54e-02	2.42e-04	8.87e-03
^{61}Ni	2.01e-05	5.15e-04	2.00e-05	5.14e-04	1.78e-05	5.10e-04
^{62}Ni	2.09e-05	3.08e-03	2.10e-05	3.04e-03	2.27e-05	7.57e-03
^{64}Ni	1.73e-11	1.23e-13	1.72e-10	1.22e-12	5.06e-09	1.28e-09
^{63}Cu	7.84e-06	1.22e-06	7.82e-06	1.20e-06	7.33e-06	5.23e-06
^{64}Zn	3.52e-05	4.88e-05	3.49e-05	4.92e-05	2.72e-05	1.69e-05
^{66}Zn	2.86e-06	5.82e-05	2.86e-06	5.75e-05	2.69e-06	1.01e-04
^{67}Zn	1.76e-07	3.39e-08	1.80e-07	3.34e-08	1.95e-07	9.78e-08
^{68}Zn	8.39e-08	1.34e-08	1.09e-07	1.31e-08	1.30e-07	1.00e-07
^{70}Zn	2.98e-13	4.12e-19	2.94e-12	4.02e-18	8.27e-11	1.07e-15
^{69}Ga	3.50e-09	5.02e-13	6.67e-09	3.00e-12	7.07e-09	2.14e-11
^{71}Ga	2.93e-10	3.84e-14	7.98e-10	1.26e-13	1.31e-09	1.23e-12

Table B.20: Nucleosynthetic yields (in $M_\odot$) of select radioactive nuclides of Model M08_03 with 0.01, 0.1, and 3 $Z_\odot$.

	M08_03_001		M08_03_01		M08_03_3	
	He det $[M_\odot]$	core det $[M_\odot]$	He det $[M_\odot]$	core det $[M_\odot]$	He det $[M_\odot]$	core det $[M_\odot]$
^{14}C	7.29e-08	4.85e-06	7.43e-08	4.62e-06	9.15e-08	8.76e-06
^{22}Na	5.45e-07	2.50e-08	5.75e-07	2.50e-08	1.44e-06	1.74e-08
^{26}Al	1.13e-05	1.37e-05	1.14e-05	1.37e-05	1.53e-05	5.47e-06
^{32}Si	8.10e-10	7.80e-10	1.39e-09	1.05e-09	2.34e-09	8.25e-08
^{32}P	7.78e-09	2.23e-07	8.35e-09	2.19e-07	1.27e-08	3.92e-06
^{33}P	1.94e-09	1.65e-07	2.43e-09	1.64e-07	1.25e-08	2.53e-06
^{35}S	1.95e-09	1.61e-07	2.68e-09	1.55e-07	1.51e-08	5.73e-06
^{36}Cl	4.68e-09	6.97e-07	4.80e-09	6.76e-07	8.63e-09	5.33e-06
^{37}Ar	6.59e-07	2.73e-05	6.69e-07	2.68e-05	1.07e-06	4.70e-05
^{39}Ar	3.73e-10	6.49e-09	3.50e-09	1.27e-08	6.29e-08	5.16e-07
^{40}K	4.30e-10	4.27e-08	8.18e-10	4.18e-08	9.09e-09	4.46e-07
^{41}Ca	5.60e-06	4.63e-06	5.56e-06	4.54e-06	4.80e-06	7.89e-06
^{44}Ti	2.26e-04	1.29e-05	2.25e-04	1.29e-05	1.91e-04	8.87e-06
^{48}V	1.00e-07	5.76e-08	1.00e-07	5.72e-08	8.65e-08	1.10e-07
^{49}V	2.03e-08	2.07e-07	2.09e-08	2.10e-07	4.18e-08	1.04e-06
^{48}Cr	8.23e-06	3.21e-04	8.13e-06	3.21e-04	5.97e-06	2.14e-04
^{49}Cr	2.66e-07	1.85e-05	2.62e-07	1.84e-05	1.59e-07	2.42e-05
^{51}Cr	5.82e-09	1.03e-06	6.12e-09	1.02e-06	1.33e-08	1.51e-05
^{51}Mn	2.51e-07	4.40e-05	2.49e-07	4.36e-05	2.07e-07	7.59e-05
^{52}Mn	7.45e-09	2.69e-06	7.56e-09	2.68e-06	1.02e-08	3.93e-06
^{53}Mn	2.85e-09	1.86e-05	4.03e-09	1.84e-05	5.36e-08	1.70e-04
^{54}Mn	2.56e-11	2.10e-08	2.24e-10	2.35e-08	9.49e-09	9.59e-07
^{52}Fe	8.56e-07	6.19e-03	8.59e-07	6.20e-03	9.58e-07	4.49e-03
^{53}Fe	2.61e-08	4.47e-04	2.65e-08	4.44e-04	4.07e-08	6.53e-04
^{55}Fe	6.43e-10	3.00e-05	4.00e-09	2.94e-05	1.73e-07	5.90e-04
^{59}Fe	7.18e-09	1.68e-08	7.71e-08	1.70e-07	3.24e-06	4.15e-06
^{60}Fe	2.88e-08	4.48e-08	2.86e-07	4.40e-07	2.96e-06	2.83e-05
^{55}Co	1.08e-07	2.16e-03	1.14e-07	2.14e-03	4.29e-07	4.02e-03
^{56}Co	6.58e-10	7.18e-06	1.76e-09	7.11e-06	4.64e-08	2.11e-05
^{57}Co	6.74e-09	3.83e-06	6.70e-08	3.77e-06	2.96e-06	6.27e-05
^{58}Co	4.52e-10	7.29e-09	4.72e-09	1.25e-08	3.25e-07	2.42e-07
^{60}Co	7.49e-09	1.64e-08	7.39e-08	1.64e-07	6.22e-07	3.34e-06
^{56}Ni	8.04e-07	1.40e-01	8.11e-07	1.40e-01	1.18e-06	1.14e-01
^{57}Ni	8.62e-08	1.22e-03	9.15e-08	1.21e-03	3.13e-07	2.14e-03
^{59}Ni	5.68e-09	9.79e-07	3.92e-08	1.05e-06	1.28e-06	1.30e-05
^{63}Ni	1.02e-09	1.04e-08	1.03e-08	1.00e-07	2.66e-07	4.72e-06
^{62}Zn	3.26e-08	1.03e-06	2.23e-07	1.02e-06	1.94e-06	3.43e-06
^{65}Zn	1.02e-10	9.59e-09	8.96e-10	9.77e-08	7.30e-09	2.67e-07
^{65}Ge	4.73e-10	8.68e-10	2.25e-09	8.64e-10	8.75e-09	1.03e-09

Table B.21: Nucleosynthetic yields (in $M_\odot$) of select radioactive nuclides of Model M08_05 with 0.01, 0.1, and 3 $Z_\odot$.

	M08_05_001		M08_05_01		M08_05_3	
	He det $[M_\odot]$	core det $[M_\odot]$	He det $[M_\odot]$	core det $[M_\odot]$	He det $[M_\odot]$	core det $[M_\odot]$
^{14}C	2.09e-08	3.37e-06	2.12e-08	3.19e-06	2.26e-08	7.51e-06
^{22}Na	5.09e-08	2.15e-08	5.29e-08	2.15e-08	1.16e-07	1.47e-08
^{26}Al	9.81e-06	1.12e-05	9.79e-06	1.12e-05	1.03e-05	4.40e-06
^{32}Si	9.42e-11	8.05e-10	1.77e-10	1.02e-09	3.25e-10	8.08e-08
^{32}P	1.44e-08	1.87e-07	1.47e-08	1.83e-07	1.65e-08	3.20e-06
^{33}P	5.99e-09	1.32e-07	6.08e-09	1.31e-07	8.27e-09	2.04e-06
^{35}S	1.14e-08	1.35e-07	1.17e-08	1.29e-07	1.82e-08	4.64e-06
^{36}Cl	2.73e-08	5.66e-07	2.74e-08	5.49e-07	3.23e-08	4.26e-06
^{37}Ar	1.03e-05	2.35e-05	1.03e-05	2.30e-05	1.03e-05	4.10e-05
^{39}Ar	4.60e-10	5.56e-09	1.77e-09	1.11e-08	2.67e-08	4.59e-07
^{40}K	2.94e-09	3.57e-08	3.31e-09	3.51e-08	1.38e-08	3.58e-07
^{41}Ca	9.15e-06	4.07e-06	9.15e-06	3.99e-06	1.06e-05	6.95e-06
^{44}Ti	2.57e-03	1.33e-05	2.58e-03	1.33e-05	2.87e-03	9.29e-06
^{48}V	9.56e-07	5.98e-08	9.69e-07	5.94e-08	1.45e-06	1.04e-07
^{49}V	2.54e-07	1.86e-07	2.61e-07	1.88e-07	5.02e-07	8.95e-07
^{48}Cr	2.67e-03	3.48e-04	2.66e-03	3.49e-04	2.43e-03	2.38e-04
^{49}Cr	2.01e-05	1.96e-05	2.02e-05	1.95e-05	2.78e-05	2.67e-05
^{51}Cr	1.17e-06	9.24e-07	1.18e-06	9.05e-07	1.45e-06	1.33e-05
^{51}Mn	1.11e-04	4.74e-05	1.11e-04	4.69e-05	1.15e-04	8.55e-05
^{52}Mn	1.78e-06	2.95e-06	1.78e-06	2.95e-06	2.13e-06	4.12e-06
^{53}Mn	1.12e-06	1.86e-05	1.13e-06	1.84e-05	1.54e-06	1.54e-04
^{54}Mn	1.15e-10	1.90e-08	4.65e-10	2.06e-08	1.67e-08	8.36e-07
^{52}Fe	8.90e-04	7.36e-03	8.82e-04	7.38e-03	6.37e-04	5.44e-03
^{53}Fe	1.89e-05	5.20e-04	1.89e-05	5.17e-04	2.04e-05	7.94e-04
^{55}Fe	1.47e-07	2.64e-05	1.58e-07	2.58e-05	6.40e-07	5.17e-04
^{59}Fe	2.59e-09	1.46e-08	2.76e-08	1.49e-07	1.47e-06	3.79e-06
^{60}Fe	1.16e-08	4.22e-08	1.16e-07	4.15e-07	1.69e-06	2.51e-05
^{55}Co	3.03e-05	2.63e-03	3.02e-05	2.60e-03	2.68e-05	5.25e-03
^{56}Co	2.83e-07	9.27e-06	2.92e-07	9.19e-06	6.31e-07	2.57e-05
^{57}Co	7.32e-08	3.48e-06	1.72e-07	3.42e-06	7.17e-06	5.64e-05
^{58}Co	1.12e-09	6.48e-09	1.18e-08	1.03e-08	9.80e-07	2.09e-07
^{60}Co	6.32e-09	1.37e-08	6.23e-08	1.37e-07	9.31e-07	2.68e-06
^{56}Ni	7.50e-05	2.10e-01	7.42e-05	2.10e-01	4.98e-05	1.77e-01
^{57}Ni	6.45e-06	2.03e-03	6.51e-06	2.02e-03	6.95e-06	3.68e-03
^{59}Ni	2.28e-07	2.10e-06	4.91e-07	2.14e-06	1.24e-05	1.32e-05
^{63}Ni	1.47e-09	9.60e-09	1.42e-08	9.27e-08	2.06e-07	4.08e-06
^{62}Zn	6.36e-07	2.54e-05	1.36e-06	2.51e-05	1.34e-05	5.56e-05
^{65}Zn	2.49e-09	7.76e-09	1.69e-08	7.82e-08	2.15e-07	2.15e-07
^{65}Ge	8.95e-09	1.15e-08	1.74e-08	1.15e-08	9.34e-08	1.05e-08

Table B.22: Nucleosynthetic yields (in $M_\odot$) of select radioactive nuclides of Model M08_10_r with 0.01, 0.1, and 3 $Z_\odot$.

	M08_10_r_001		M08_10_r_01		M08_10_r_3	
	He det $[M_\odot]$	core det $[M_\odot]$	He det $[M_\odot]$	core det $[M_\odot]$	He det $[M_\odot]$	core det $[M_\odot]$
^{14}C	2.53e-12	2.17e-09	2.81e-12	1.29e-09	1.15e-11	5.76e-08
^{22}Na	8.66e-09	1.03e-08	8.97e-09	1.04e-08	1.79e-08	7.49e-09
^{26}Al	6.65e-07	6.65e-06	6.63e-07	6.67e-06	7.06e-07	2.76e-06
^{32}Si	2.18e-12	8.20e-10	2.24e-12	4.33e-11	2.54e-12	1.41e-08
^{32}P	2.00e-08	1.19e-07	2.01e-08	1.16e-07	2.14e-08	2.09e-06
^{33}P	1.59e-08	9.33e-08	1.60e-08	9.05e-08	1.70e-08	1.36e-06
^{35}S	1.17e-08	9.64e-08	1.16e-08	9.04e-08	1.18e-08	3.50e-06
^{36}Cl	7.72e-08	4.18e-07	7.66e-08	4.05e-07	7.95e-08	3.24e-06
^{37}Ar	7.83e-06	1.84e-05	7.79e-06	1.81e-05	8.08e-06	3.28e-05
^{39}Ar	6.02e-10	4.02e-09	5.91e-10	3.96e-09	6.93e-10	1.51e-07
^{40}K	4.76e-09	2.83e-08	4.66e-09	2.71e-08	5.58e-09	2.71e-07
^{41}Ca	3.21e-06	3.27e-06	3.21e-06	3.21e-06	4.16e-06	5.64e-06
^{44}Ti	1.78e-03	1.52e-05	1.78e-03	1.52e-05	1.83e-03	1.04e-05
^{48}V	1.01e-06	4.33e-08	1.02e-06	4.29e-08	1.53e-06	8.12e-08
^{49}V	3.26e-07	1.59e-07	3.29e-07	1.59e-07	5.10e-07	7.22e-07
^{48}Cr	3.78e-03	3.68e-04	3.79e-03	3.69e-04	3.92e-03	2.57e-04
^{49}Cr	3.03e-05	2.00e-05	3.06e-05	1.99e-05	4.15e-05	2.83e-05
^{51}Cr	2.49e-06	7.82e-07	2.50e-06	7.66e-07	2.88e-06	1.11e-05
^{51}Mn	2.89e-04	4.88e-05	2.90e-04	4.83e-05	3.09e-04	9.16e-05
^{52}Mn	8.90e-06	2.55e-06	8.96e-06	2.55e-06	1.13e-05	3.71e-06
^{53}Mn	4.78e-06	1.67e-05	4.84e-06	1.65e-05	6.96e-06	1.30e-04
^{54}Mn	3.05e-10	2.43e-08	4.66e-10	2.29e-08	5.57e-09	6.93e-07
^{52}Fe	7.35e-03	7.92e-03	7.36e-03	7.93e-03	7.88e-03	5.96e-03
^{53}Fe	9.18e-05	5.52e-04	9.29e-05	5.48e-04	1.29e-04	8.69e-04
^{55}Fe	9.68e-07	2.18e-05	9.85e-07	2.15e-05	1.73e-06	4.28e-04
^{59}Fe	2.84e-11	1.49e-09	2.75e-10	1.53e-08	6.90e-09	3.33e-07
^{60}Fe	8.26e-11	7.26e-09	8.13e-10	6.97e-08	1.27e-08	9.60e-06
^{55}Co	9.19e-04	2.81e-03	9.21e-04	2.79e-03	9.70e-04	5.87e-03
^{56}Co	3.02e-06	8.91e-06	3.05e-06	8.82e-06	4.15e-06	2.65e-05
^{57}Co	1.07e-06	3.01e-06	1.11e-06	3.02e-06	2.81e-06	4.73e-05
^{58}Co	3.90e-10	5.81e-09	2.39e-09	8.90e-09	1.07e-07	1.71e-07
^{60}Co	1.59e-10	5.96e-09	1.55e-09	5.88e-08	2.97e-08	1.84e-06
^{56}Ni	1.49e-02	3.24e-01	1.49e-02	3.24e-01	1.49e-02	2.78e-01
^{57}Ni	1.29e-03	4.50e-03	1.29e-03	4.47e-03	1.31e-03	7.79e-03
^{59}Ni	9.42e-06	1.28e-05	9.54e-06	1.28e-05	1.61e-05	3.07e-05
^{63}Ni	7.89e-11	3.81e-09	7.46e-10	3.63e-08	1.10e-08	2.66e-06
^{62}Zn	1.24e-04	3.90e-04	1.26e-04	3.84e-04	1.75e-04	1.12e-03
^{65}Zn	2.13e-07	8.52e-09	2.32e-07	6.73e-08	6.21e-07	1.77e-07
^{65}Ge	2.95e-06	2.37e-07	2.95e-06	2.36e-07	2.93e-06	2.15e-07

Table B.23: Nucleosynthetic yields (in $M_\odot$) of select radioactive nuclides of Model M09_03 with 0.01, 0.1, and 3 $Z_\odot$.

	M09_03_001		M09_03_01		M09_03_3	
	He det $[M_\odot]$	core det $[M_\odot]$	He det $[M_\odot]$	core det $[M_\odot]$	He det $[M_\odot]$	core det $[M_\odot]$
^{14}C	3.68e-08	1.93e-06	3.73e-08	1.83e-06	4.31e-08	3.71e-06
^{22}Na	9.34e-08	1.38e-08	9.78e-08	1.38e-08	2.32e-07	9.36e-09
^{26}Al	1.33e-05	7.04e-06	1.33e-05	7.09e-06	1.45e-05	2.74e-06
^{32}Si	3.09e-10	5.35e-10	5.69e-10	6.89e-10	9.61e-10	5.47e-08
^{32}P	1.00e-08	1.39e-07	1.05e-08	1.36e-07	1.32e-08	2.22e-06
^{33}P	2.57e-09	9.66e-08	2.82e-09	9.56e-08	7.86e-09	1.43e-06
^{35}S	5.02e-09	9.84e-08	5.57e-09	9.44e-08	1.51e-08	3.14e-06
^{36}Cl	1.06e-08	4.32e-07	1.07e-08	4.19e-07	1.48e-08	3.04e-06
^{37}Ar	3.00e-06	2.10e-05	2.99e-06	2.06e-05	3.04e-06	3.82e-05
^{39}Ar	3.54e-10	4.23e-09	2.82e-09	7.54e-09	4.90e-08	2.97e-07
^{40}K	8.71e-10	2.69e-08	1.26e-09	2.63e-08	1.11e-08	2.47e-07
^{41}Ca	1.04e-05	3.82e-06	1.03e-05	3.74e-06	1.10e-05	6.65e-06
^{44}Ti	7.50e-04	1.57e-05	7.47e-04	1.58e-05	6.50e-04	1.12e-05
^{48}V	4.44e-07	5.42e-08	4.50e-07	5.37e-08	6.06e-07	9.88e-08
^{49}V	8.92e-08	1.80e-07	9.15e-08	1.80e-07	1.64e-07	7.95e-07
^{48}Cr	1.25e-04	4.29e-04	1.23e-04	4.30e-04	7.45e-05	3.00e-04
^{49}Cr	3.61e-06	2.32e-05	3.60e-06	2.30e-05	3.00e-06	3.29e-05
^{51}Cr	7.69e-08	8.98e-07	7.77e-08	8.81e-07	9.33e-08	1.27e-05
^{51}Mn	5.40e-06	5.63e-05	5.34e-06	5.58e-05	3.62e-06	1.06e-04
^{52}Mn	1.00e-07	3.34e-06	1.01e-07	3.34e-06	9.94e-08	4.58e-06
^{53}Mn	3.67e-08	2.09e-05	3.81e-08	2.07e-05	1.13e-07	1.53e-04
^{54}Mn	9.17e-11	1.84e-08	6.34e-10	1.94e-08	2.56e-08	7.84e-07
^{52}Fe	5.16e-06	9.49e-03	5.06e-06	9.50e-03	2.75e-06	7.13e-03
^{53}Fe	4.30e-07	6.51e-04	4.26e-07	6.47e-04	2.81e-07	1.03e-03
^{55}Fe	3.58e-09	2.55e-05	7.93e-09	2.49e-05	2.34e-07	4.94e-04
^{59}Fe	4.71e-09	8.35e-09	5.04e-08	8.51e-08	2.48e-06	2.26e-06
^{60}Fe	2.46e-08	2.75e-08	2.44e-07	2.71e-07	2.84e-06	1.66e-05
^{55}Co	2.57e-07	3.34e-03	2.60e-07	3.31e-03	5.27e-07	7.01e-03
^{56}Co	4.61e-09	1.08e-05	6.05e-09	1.07e-05	7.43e-08	3.14e-05
^{57}Co	8.22e-09	3.50e-06	7.74e-08	3.43e-06	4.55e-06	5.49e-05
^{58}Co	7.42e-10	6.24e-09	8.00e-09	8.64e-09	7.18e-07	1.94e-07
^{60}Co	1.77e-08	8.85e-09	1.75e-07	8.88e-08	1.61e-06	1.72e-06
^{56}Ni	7.45e-07	3.43e-01	7.54e-07	3.43e-01	1.26e-06	2.94e-01
^{57}Ni	9.79e-08	4.04e-03	1.06e-07	4.02e-03	4.22e-07	7.22e-03
^{59}Ni	1.12e-08	8.88e-06	8.45e-08	8.85e-06	3.02e-06	2.32e-05
^{63}Ni	1.40e-09	6.59e-09	1.38e-08	6.37e-08	2.81e-07	2.61e-06
^{62}Zn	3.80e-08	1.84e-04	2.97e-07	1.81e-04	2.81e-06	4.16e-04
^{65}Zn	2.98e-10	6.09e-09	2.76e-09	5.40e-08	2.43e-08	1.55e-07
^{65}Ge	4.03e-10	6.83e-08	1.90e-09	6.82e-08	8.78e-09	4.42e-08

Table B.24: Nucleosynthetic yields (in $M_\odot$) of select radioactive nuclides of Model M09_05 with 0.01, 0.1, and 3 $Z_\odot$.

	M09_05_001		M09_05_01		M09_05_3	
	He det $[M_\odot]$	core det $[M_\odot]$	He det $[M_\odot]$	core det $[M_\odot]$	He det $[M_\odot]$	core det $[M_\odot]$
^{14}C	6.91e-11	2.08e-07	6.95e-11	1.95e-07	5.21e-11	1.18e-06
^{22}Na	1.49e-08	1.41e-08	1.54e-08	1.41e-08	2.93e-08	1.00e-08
^{26}Al	3.04e-06	7.54e-06	3.03e-06	7.58e-06	3.06e-06	2.94e-06
^{32}Si	4.31e-12	2.23e-10	4.13e-12	2.40e-10	4.67e-12	3.72e-08
^{32}P	1.54e-08	1.19e-07	1.54e-08	1.16e-07	1.63e-08	2.06e-06
^{33}P	1.04e-08	8.24e-08	1.04e-08	8.06e-08	1.10e-08	1.22e-06
^{35}S	1.40e-08	9.21e-08	1.39e-08	8.71e-08	1.48e-08	2.98e-06
^{36}Cl	5.00e-08	3.72e-07	4.98e-08	3.61e-07	5.24e-08	2.70e-06
^{37}Ar	9.40e-06	1.79e-05	9.38e-06	1.75e-05	9.50e-06	3.27e-05
^{39}Ar	6.51e-10	3.68e-09	7.05e-10	4.77e-09	2.14e-09	2.27e-07
^{40}K	5.22e-09	2.44e-08	5.25e-09	2.39e-08	8.56e-09	2.28e-07
^{41}Ca	6.35e-06	3.26e-06	6.35e-06	3.20e-06	7.10e-06	5.71e-06
^{44}Ti	1.99e-03	1.65e-05	2.00e-03	1.65e-05	2.13e-03	1.12e-05
^{48}V	1.83e-06	4.56e-08	1.85e-06	4.53e-08	2.54e-06	8.44e-08
^{49}V	4.35e-07	1.54e-07	4.41e-07	1.54e-07	6.76e-07	6.86e-07
^{48}Cr	4.47e-03	4.03e-04	4.49e-03	4.04e-04	4.97e-03	2.84e-04
^{49}Cr	4.06e-05	2.14e-05	4.10e-05	2.13e-05	5.42e-05	3.10e-05
^{51}Cr	3.41e-06	7.68e-07	3.43e-06	7.54e-07	4.14e-06	1.08e-05
^{51}Mn	3.69e-04	5.23e-05	3.71e-04	5.18e-05	4.19e-04	9.97e-05
^{52}Mn	1.03e-05	2.80e-06	1.04e-05	2.80e-06	1.23e-05	3.96e-06
^{53}Mn	6.93e-06	1.76e-05	6.99e-06	1.75e-05	9.00e-06	1.31e-04
^{54}Mn	2.57e-10	1.58e-08	4.91e-10	1.68e-08	8.01e-09	6.71e-07
^{52}Fe	5.08e-03	8.79e-03	5.09e-03	8.80e-03	5.25e-03	6.65e-03
^{53}Fe	1.29e-04	6.03e-04	1.30e-04	5.99e-04	1.63e-04	9.62e-04
^{55}Fe	1.09e-06	2.17e-05	1.11e-06	2.12e-05	1.63e-06	4.21e-04
^{59}Fe	2.81e-10	4.66e-09	2.98e-09	4.79e-08	1.83e-07	1.16e-06
^{60}Fe	1.59e-09	2.06e-08	1.58e-08	2.01e-07	2.61e-07	1.57e-05
^{55}Co	4.11e-04	3.08e-03	4.11e-04	3.05e-03	3.94e-04	6.52e-03
^{56}Co	2.72e-06	1.03e-05	2.74e-06	1.02e-05	3.18e-06	2.94e-05
^{57}Co	6.54e-07	3.11e-06	6.95e-07	3.05e-06	2.95e-06	4.75e-05
^{58}Co	5.51e-10	5.41e-09	4.09e-09	7.77e-09	2.80e-07	1.66e-07
^{60}Co	1.50e-09	9.69e-09	1.43e-08	9.68e-08	2.83e-07	1.81e-06
^{56}Ni	2.13e-03	3.98e-01	2.12e-03	3.98e-01	1.70e-03	3.43e-01
^{57}Ni	1.37e-04	5.79e-03	1.37e-04	5.76e-03	1.27e-04	1.00e-02
^{59}Ni	2.90e-06	1.82e-05	3.09e-06	1.80e-05	1.17e-05	3.98e-05
^{63}Ni	6.78e-10	6.72e-09	6.50e-09	6.48e-08	8.20e-08	2.91e-06
^{62}Zn	1.29e-05	5.82e-04	1.35e-05	5.73e-04	2.72e-05	1.63e-03
^{65}Zn	1.15e-08	7.67e-09	3.72e-08	5.04e-08	4.48e-07	1.33e-07
^{65}Ge	1.14e-07	3.45e-07	1.27e-07	3.44e-07	4.07e-07	2.90e-07

Table B.25: Nucleosynthetic yields (in $M_\odot$) of select radioactive nuclides of Model M09_10_r with 0.01, 0.1, and 3 $Z_\odot$.

	M09_10_r_001		M09_10_r_01		M09_10_r_3	
	He det $[M_\odot]$	core det $[M_\odot]$	He det $[M_\odot]$	core det $[M_\odot]$	He det $[M_\odot]$	core det $[M_\odot]$
^{14}C	3.84e-12	2.80e-13	4.47e-12	1.73e-13	2.36e-11	3.61e-11
^{22}Na	7.85e-09	5.73e-09	8.22e-09	5.68e-09	1.83e-08	6.08e-09
^{26}Al	9.78e-08	1.84e-06	9.91e-08	1.84e-06	1.43e-07	7.96e-07
^{32}Si	1.93e-12	4.35e-10	2.03e-12	7.81e-11	2.34e-12	3.41e-09
^{32}P	1.52e-08	7.62e-08	1.55e-08	7.39e-08	1.65e-08	1.07e-06
^{33}P	1.22e-08	6.01e-08	1.25e-08	5.81e-08	1.32e-08	8.09e-07
^{35}S	3.80e-09	5.22e-08	3.78e-09	4.92e-08	3.93e-09	1.55e-06
^{36}Cl	6.30e-08	2.80e-07	6.30e-08	2.71e-07	6.46e-08	1.91e-06
^{37}Ar	3.56e-06	1.41e-05	3.53e-06	1.39e-05	3.70e-06	2.59e-05
^{39}Ar	1.60e-10	2.51e-09	1.57e-10	2.40e-09	2.07e-10	4.74e-08
^{40}K	1.23e-09	1.80e-08	1.20e-09	1.70e-08	1.52e-09	1.45e-07
^{41}Ca	1.14e-06	2.59e-06	1.15e-06	2.54e-06	1.74e-06	4.55e-06
^{44}Ti	8.70e-04	1.81e-05	8.71e-04	1.81e-05	9.07e-04	1.15e-05
^{48}V	4.23e-07	3.68e-08	4.30e-07	3.63e-08	7.18e-07	6.74e-08
^{49}V	1.98e-07	1.37e-07	2.00e-07	1.35e-07	3.03e-07	5.57e-07
^{48}Cr	1.88e-03	3.73e-04	1.88e-03	3.74e-04	1.99e-03	2.62e-04
^{49}Cr	2.02e-05	1.95e-05	2.05e-05	1.93e-05	2.77e-05	2.84e-05
^{51}Cr	2.06e-06	6.40e-07	2.05e-06	6.28e-07	2.05e-06	8.69e-06
^{51}Mn	2.65e-04	4.81e-05	2.64e-04	4.77e-05	2.48e-04	9.26e-05
^{52}Mn	3.70e-06	2.42e-06	3.73e-06	2.42e-06	4.78e-06	3.45e-06
^{53}Mn	2.77e-06	1.54e-05	2.81e-06	1.52e-05	3.99e-06	1.06e-04
^{54}Mn	2.38e-10	1.56e-08	3.08e-10	1.72e-08	3.64e-09	5.43e-07
^{52}Fe	3.98e-03	8.09e-03	3.98e-03	8.11e-03	4.08e-03	6.14e-03
^{53}Fe	5.77e-05	5.54e-04	5.83e-05	5.50e-04	8.01e-05	8.92e-04
^{55}Fe	3.69e-07	1.69e-05	3.88e-07	1.66e-05	1.24e-06	3.32e-04
^{59}Fe	2.72e-11	1.07e-10	2.05e-10	1.07e-09	8.18e-10	2.42e-08
^{60}Fe	1.38e-11	1.92e-09	9.32e-11	1.18e-08	4.44e-10	1.89e-06
^{55}Co	3.68e-04	2.87e-03	3.69e-04	2.84e-03	3.82e-04	6.16e-03
^{56}Co	1.01e-06	1.00e-05	1.02e-06	9.96e-06	1.47e-06	2.78e-05
^{57}Co	5.21e-07	2.67e-06	5.43e-07	2.62e-06	1.39e-06	3.86e-05
^{58}Co	1.53e-10	4.51e-09	1.02e-09	6.04e-09	3.38e-08	1.36e-07
^{60}Co	1.28e-11	1.21e-09	1.05e-10	1.17e-08	1.56e-09	5.26e-07
^{56}Ni	2.60e-02	4.93e-01	2.60e-02	4.93e-01	2.65e-02	4.28e-01
^{57}Ni	2.40e-03	8.62e-03	2.40e-03	8.57e-03	2.42e-03	1.45e-02
^{59}Ni	7.59e-05	3.31e-05	7.56e-05	3.29e-05	6.49e-05	6.60e-05
^{63}Ni	5.55e-12	5.83e-10	4.89e-11	5.31e-09	6.79e-10	6.46e-07
^{62}Zn	1.65e-04	1.19e-03	1.65e-04	1.17e-03	1.63e-04	3.45e-03
^{65}Zn	2.41e-07	1.03e-08	2.43e-07	4.42e-08	3.06e-07	1.62e-07
^{65}Ge	4.13e-06	8.10e-07	4.13e-06	8.08e-07	3.88e-06	7.19e-07

Table B.26: Nucleosynthetic yields (in $M_\odot$) of select radioactive nuclides of Model M10_02 with 0.01, 0.1, and 3 $Z_\odot$.

	M10_02_001		M10_02_01		M10_02_3	
	He det $[M_\odot]$	core det $[M_\odot]$	He det $[M_\odot]$	core det $[M_\odot]$	He det $[M_\odot]$	core det $[M_\odot]$
^{14}C	9.13e-09	4.82e-07	9.25e-09	4.55e-07	1.07e-08	1.09e-06
^{22}Na	4.63e-08	7.63e-09	4.85e-08	7.62e-09	1.15e-07	5.23e-09
^{26}Al	6.68e-06	4.05e-06	6.69e-06	4.08e-06	7.41e-06	1.57e-06
^{32}Si	9.92e-11	2.11e-10	1.67e-10	2.53e-10	2.82e-10	2.52e-08
^{32}P	4.98e-09	8.29e-08	5.13e-09	8.09e-08	5.94e-09	1.31e-06
^{33}P	1.26e-09	5.62e-08	1.33e-09	5.51e-08	2.79e-09	8.13e-07
^{35}S	2.55e-09	6.27e-08	2.74e-09	5.95e-08	6.27e-09	1.94e-06
^{36}Cl	5.32e-09	2.60e-07	5.39e-09	2.52e-07	7.63e-09	1.82e-06
^{37}Ar	1.96e-06	1.45e-05	1.96e-06	1.42e-05	2.17e-06	2.80e-05
^{39}Ar	1.42e-10	2.70e-09	1.08e-09	3.69e-09	1.89e-08	1.44e-07
^{40}K	4.62e-10	1.74e-08	6.79e-10	1.69e-08	6.00e-09	1.51e-07
^{41}Ca	4.61e-06	2.77e-06	4.61e-06	2.71e-06	5.17e-06	5.02e-06
^{44}Ti	5.72e-04	1.99e-05	5.72e-04	1.99e-05	5.54e-04	1.27e-05
^{48}V	2.60e-07	4.18e-08	2.64e-07	4.15e-08	3.83e-07	7.60e-08
^{49}V	5.38e-08	1.38e-07	5.52e-08	1.38e-07	1.08e-07	5.80e-07
^{48}Cr	2.53e-04	4.32e-04	2.51e-04	4.33e-04	1.95e-04	3.05e-04
^{49}Cr	3.59e-06	2.24e-05	3.61e-06	2.22e-05	4.19e-06	3.28e-05
^{51}Cr	1.01e-07	6.76e-07	1.02e-07	6.65e-07	1.30e-07	9.60e-06
^{51}Mn	1.09e-05	5.49e-05	1.09e-05	5.43e-05	9.73e-06	1.06e-04
^{52}Mn	1.46e-07	2.87e-06	1.47e-07	2.87e-06	1.91e-07	4.00e-06
^{53}Mn	6.49e-08	1.76e-05	6.64e-08	1.74e-05	1.29e-07	1.20e-04
^{54}Mn	5.15e-11	1.37e-08	3.21e-10	1.44e-08	1.25e-08	5.87e-07
^{52}Fe	2.91e-05	9.49e-03	2.87e-05	9.51e-03	1.93e-05	7.21e-03
^{53}Fe	1.22e-06	6.44e-04	1.22e-06	6.40e-04	1.19e-06	1.04e-03
^{55}Fe	1.08e-08	1.86e-05	1.37e-08	1.82e-05	1.51e-07	3.72e-04
^{59}Fe	2.37e-09	2.82e-09	2.54e-08	2.89e-08	1.23e-06	8.06e-07
^{60}Fe	1.27e-08	1.21e-08	1.26e-07	1.19e-07	1.41e-06	9.11e-06
^{55}Co	1.27e-06	3.32e-03	1.27e-06	3.29e-03	1.32e-06	7.14e-03
^{56}Co	1.81e-08	1.21e-05	1.97e-08	1.20e-05	8.33e-08	3.24e-05
^{57}Co	1.04e-08	2.94e-06	6.76e-08	2.90e-06	3.05e-06	4.34e-05
^{58}Co	4.09e-10	4.69e-09	4.36e-09	6.07e-09	3.61e-07	1.45e-07
^{60}Co	8.52e-09	5.15e-09	8.40e-08	5.15e-08	7.48e-07	1.09e-06
^{56}Ni	1.80e-06	5.59e-01	1.80e-06	5.59e-01	1.79e-06	4.86e-01
^{57}Ni	2.90e-07	9.28e-03	2.97e-07	9.23e-03	4.86e-07	1.58e-02
^{59}Ni	1.85e-08	3.47e-05	6.98e-08	3.44e-05	2.07e-06	6.96e-05
^{63}Ni	7.22e-10	3.78e-09	7.13e-09	3.65e-08	1.41e-07	1.52e-06
^{62}Zn	5.05e-08	1.27e-03	2.17e-07	1.26e-03	1.84e-06	3.69e-03
^{65}Zn	1.82e-10	9.79e-09	1.43e-09	3.76e-08	1.42e-08	9.24e-08
^{65}Ge	8.47e-10	8.36e-07	2.07e-09	8.34e-07	6.04e-09	7.22e-07

Table B.27: Nucleosynthetic yields (in $M_\odot$) of select radioactive nuclides of Model M10_03 with 0.01, 0.1, and 3 $Z_\odot$.

	M10_03_001		M10_03_01		M10_03_3	
	He det $[M_\odot]$	core det $[M_\odot]$	He det $[M_\odot]$	core det $[M_\odot]$	He det $[M_\odot]$	core det $[M_\odot]$
^{14}C	8.73e-10	6.33e-08	8.84e-10	5.84e-08	8.62e-10	3.51e-07
^{22}Na	1.96e-08	7.01e-09	2.04e-08	6.99e-09	4.12e-08	4.96e-09
^{26}Al	5.01e-06	3.83e-06	5.00e-06	3.85e-06	5.07e-06	1.49e-06
^{32}Si	7.27e-12	9.32e-11	8.88e-12	9.69e-11	1.12e-11	1.72e-08
^{32}P	1.43e-08	6.92e-08	1.43e-08	6.73e-08	1.50e-08	1.13e-06
^{33}P	8.37e-09	4.71e-08	8.35e-09	4.59e-08	8.74e-09	6.75e-07
^{35}S	1.41e-08	5.25e-08	1.41e-08	4.95e-08	1.57e-08	1.62e-06
^{36}Cl	3.95e-08	2.21e-07	3.94e-08	2.14e-07	4.22e-08	1.54e-06
^{37}Ar	7.91e-06	1.30e-05	7.89e-06	1.28e-05	7.92e-06	2.50e-05
^{39}Ar	5.67e-10	2.20e-09	7.15e-10	2.55e-09	3.91e-09	1.10e-07
^{40}K	4.48e-09	1.46e-08	4.61e-09	1.42e-08	1.00e-08	1.27e-07
^{41}Ca	6.33e-06	2.52e-06	6.32e-06	2.48e-06	6.70e-06	4.54e-06
^{44}Ti	1.05e-03	2.01e-05	1.05e-03	2.02e-05	1.17e-03	1.24e-05
^{48}V	4.48e-07	3.68e-08	4.52e-07	3.66e-08	6.26e-07	6.81e-08
^{49}V	1.12e-07	1.24e-07	1.16e-07	1.24e-07	2.21e-07	5.16e-07
^{48}Cr	1.71e-03	4.03e-04	1.71e-03	4.03e-04	1.55e-03	2.85e-04
^{49}Cr	1.13e-05	2.06e-05	1.13e-05	2.05e-05	1.36e-05	3.06e-05
^{51}Cr	4.72e-07	6.15e-07	4.75e-07	6.07e-07	5.91e-07	8.57e-06
^{51}Mn	6.03e-05	5.08e-05	6.04e-05	5.03e-05	6.14e-05	9.90e-05
^{52}Mn	9.08e-07	2.59e-06	9.08e-07	2.59e-06	9.37e-07	3.64e-06
^{53}Mn	5.24e-07	1.60e-05	5.27e-07	1.59e-05	6.62e-07	1.08e-04
^{54}Mn	8.14e-11	1.25e-08	3.24e-10	1.33e-08	9.76e-09	5.31e-07
^{52}Fe	7.31e-04	8.74e-03	7.24e-04	8.75e-03	5.12e-04	6.66e-03
^{53}Fe	1.22e-05	5.93e-04	1.22e-05	5.89e-04	1.16e-05	9.63e-04
^{55}Fe	5.64e-08	1.70e-05	6.23e-08	1.68e-05	3.26e-07	3.31e-04
^{59}Fe	6.53e-10	1.77e-09	6.99e-09	1.82e-08	4.26e-07	4.55e-07
^{60}Fe	3.80e-09	9.38e-09	3.79e-08	9.12e-08	5.80e-07	7.94e-06
^{55}Co	1.74e-05	3.06e-03	1.73e-05	3.02e-03	1.40e-05	6.61e-03
^{56}Co	1.14e-07	1.19e-05	1.16e-07	1.18e-05	1.97e-07	3.06e-05
^{57}Co	2.59e-08	2.85e-06	6.87e-08	2.82e-06	3.40e-06	3.94e-05
^{58}Co	5.28e-10	4.33e-09	5.48e-09	5.66e-09	4.94e-07	1.31e-07
^{60}Co	2.93e-09	5.03e-09	2.90e-08	5.02e-08	5.19e-07	9.67e-07
^{56}Ni	6.95e-05	6.10e-01	6.85e-05	6.11e-01	4.25e-05	5.32e-01
^{57}Ni	3.37e-06	1.11e-02	3.37e-06	1.10e-02	3.09e-06	1.86e-02
^{59}Ni	9.35e-08	4.59e-05	2.81e-07	4.55e-05	9.02e-06	8.90e-05
^{63}Ni	1.08e-09	3.39e-09	1.04e-08	3.26e-08	1.26e-07	1.45e-06
^{62}Zn	2.42e-07	1.69e-03	5.20e-07	1.67e-03	4.01e-06	4.81e-03
^{65}Zn	2.87e-09	1.15e-08	2.59e-08	3.40e-08	3.17e-07	7.87e-08
^{65}Ge	4.42e-09	1.10e-06	7.68e-09	1.10e-06	2.61e-08	9.23e-07

Table B.28: Nucleosynthetic yields (in $M_\odot$) of select radioactive nuclides of Model M10_05 with 0.01, 0.1, and 3 $Z_\odot$.

	M10_05_001		M10_05_01		M10_05_3	
	He det $[M_\odot]$	core det $[M_\odot]$	He det $[M_\odot]$	core det $[M_\odot]$	He det $[M_\odot]$	core det $[M_\odot]$
^{14}C	1.41e-12	1.03e-08	1.64e-12	9.76e-09	8.35e-12	4.47e-08
^{22}Na	3.59e-09	7.16e-09	3.71e-09	8.19e-09	7.09e-09	6.42e-09
^{26}Al	1.11e-07	3.88e-06	1.11e-07	3.89e-06	1.24e-07	1.64e-06
^{32}Si	2.44e-12	8.01e-10	2.54e-12	8.60e-11	2.90e-12	6.30e-09
^{32}P	1.97e-08	9.13e-08	2.00e-08	8.83e-08	2.12e-08	1.50e-06
^{33}P	1.59e-08	7.06e-08	1.61e-08	6.81e-08	1.71e-08	1.02e-06
^{35}S	5.37e-09	7.25e-08	5.33e-09	6.83e-08	5.50e-09	2.46e-06
^{36}Cl	7.84e-08	3.19e-07	7.82e-08	3.09e-07	8.05e-08	2.47e-06
^{37}Ar	5.40e-06	1.49e-05	5.35e-06	1.46e-05	5.59e-06	2.71e-05
^{39}Ar	2.36e-10	3.24e-09	2.30e-10	3.12e-09	2.63e-10	8.73e-08
^{40}K	1.86e-09	2.33e-08	1.82e-09	2.21e-08	2.17e-09	2.12e-07
^{41}Ca	1.84e-06	2.74e-06	1.84e-06	2.69e-06	2.42e-06	4.77e-06
^{44}Ti	7.79e-04	2.42e-05	7.80e-04	2.43e-05	8.10e-04	1.37e-05
^{48}V	4.79e-07	5.44e-08	4.86e-07	5.40e-08	7.56e-07	8.20e-08
^{49}V	1.85e-07	1.43e-07	1.87e-07	1.43e-07	2.72e-07	6.16e-07
^{48}Cr	2.06e-03	3.95e-04	2.06e-03	3.96e-04	2.15e-03	2.75e-04
^{49}Cr	2.03e-05	2.02e-05	2.05e-05	2.01e-05	2.61e-05	2.96e-05
^{51}Cr	1.07e-06	6.55e-07	1.07e-06	6.49e-07	1.27e-06	9.06e-06
^{51}Mn	1.47e-04	4.98e-05	1.47e-04	4.93e-05	1.58e-04	9.63e-05
^{52}Mn	4.23e-06	2.81e-06	4.27e-06	2.80e-06	5.45e-06	3.80e-06
^{53}Mn	2.40e-06	1.60e-05	2.43e-06	1.59e-05	3.42e-06	1.11e-04
^{54}Mn	2.78e-10	1.38e-08	3.49e-10	1.58e-08	3.43e-09	5.76e-07
^{52}Fe	4.02e-03	8.42e-03	4.03e-03	8.43e-03	4.36e-03	6.39e-03
^{53}Fe	5.53e-05	5.75e-04	5.59e-05	5.71e-04	7.56e-05	9.27e-04
^{55}Fe	4.09e-07	1.77e-05	4.22e-07	1.74e-05	1.08e-06	3.47e-04
^{59}Fe	9.45e-12	6.17e-10	7.11e-11	6.38e-09	6.18e-10	1.31e-07
^{60}Fe	7.26e-12	3.88e-09	6.09e-11	3.51e-08	7.48e-10	4.85e-06
^{55}Co	4.77e-04	2.96e-03	4.78e-04	2.93e-03	4.93e-04	6.37e-03
^{56}Co	1.33e-06	1.51e-05	1.34e-06	1.50e-05	1.84e-06	3.30e-05
^{57}Co	4.61e-07	2.97e-06	4.83e-07	2.92e-06	1.43e-06	4.05e-05
^{58}Co	1.54e-10	4.61e-09	1.00e-09	7.07e-09	4.24e-08	1.46e-07
^{60}Co	1.07e-11	3.41e-09	1.00e-10	3.36e-08	2.27e-09	1.05e-06
^{56}Ni	8.32e-03	5.56e-01	8.31e-03	5.57e-01	8.07e-03	4.84e-01
^{57}Ni	5.75e-04	1.01e-02	5.75e-04	1.00e-02	5.71e-04	1.69e-02
^{59}Ni	5.36e-06	4.35e-05	5.39e-06	4.31e-05	7.93e-06	8.35e-05
^{63}Ni	6.77e-12	1.58e-09	6.42e-11	1.51e-08	1.06e-09	1.34e-06
^{62}Zn	5.98e-05	1.57e-03	6.04e-05	1.55e-03	8.24e-05	4.48e-03
^{65}Zn	6.44e-08	1.57e-08	6.96e-08	6.41e-08	1.93e-07	1.95e-07
^{65}Ge	1.52e-06	1.26e-06	1.52e-06	1.25e-06	1.51e-06	1.10e-06

Table B.29: Nucleosynthetic yields (in $M_\odot$) of select radioactive nuclides of Model M10_10 with 0.01, 0.1, and 3 $Z_\odot$.

	M10_10_001		M10_10_01		M10_10_3	
	He det $[M_\odot]$	core det $[M_\odot]$	He det $[M_\odot]$	core det $[M_\odot]$	He det $[M_\odot]$	core det $[M_\odot]$
^{14}C	3.58e-14	7.47e-16	7.04e-14	7.84e-16	1.08e-12	2.09e-15
^{22}Na	1.25e-08	3.21e-13	1.22e-08	3.20e-13	6.93e-09	1.65e-10
^{26}Al	8.09e-07	1.46e-10	7.98e-07	1.50e-10	5.20e-07	5.55e-11
^{32}Si	4.10e-13	2.13e-13	5.85e-13	2.19e-13	5.18e-13	6.99e-12
^{32}P	3.87e-09	1.77e-09	3.93e-09	1.78e-09	4.29e-09	1.01e-08
^{33}P	1.58e-09	1.12e-09	1.63e-09	1.12e-09	1.78e-09	9.16e-09
^{35}S	8.28e-10	8.03e-10	8.54e-10	7.88e-10	9.10e-10	5.69e-09
^{36}Cl	8.25e-09	7.97e-09	8.24e-09	7.82e-09	8.67e-09	3.00e-08
^{37}Ar	1.63e-06	1.66e-06	1.62e-06	1.63e-06	1.65e-06	4.09e-06
^{39}Ar	4.45e-11	6.70e-11	4.50e-11	6.45e-11	5.23e-11	4.16e-10
^{40}K	3.04e-10	4.33e-10	3.00e-10	4.18e-10	3.91e-10	1.70e-09
^{41}Ca	3.19e-07	4.10e-07	3.21e-07	4.03e-07	4.78e-07	8.56e-07
^{44}Ti	2.68e-04	2.04e-05	2.68e-04	2.04e-05	2.78e-04	1.25e-05
^{48}V	1.28e-07	2.54e-08	1.28e-07	2.54e-08	2.28e-07	2.60e-08
^{49}V	4.58e-08	8.20e-08	4.62e-08	8.14e-08	7.37e-08	1.66e-07
^{48}Cr	5.30e-04	4.14e-04	5.32e-04	4.14e-04	5.96e-04	3.00e-04
^{49}Cr	9.11e-06	2.00e-05	9.16e-06	1.99e-05	1.11e-05	3.16e-05
^{51}Cr	3.81e-07	2.28e-07	3.79e-07	2.23e-07	4.86e-07	2.04e-06
^{51}Mn	8.48e-05	4.88e-05	8.46e-05	4.83e-05	7.91e-05	1.02e-04
^{52}Mn	1.10e-06	2.52e-06	1.11e-06	2.52e-06	1.47e-06	3.11e-06
^{53}Mn	1.66e-06	1.32e-05	1.67e-06	1.31e-05	2.55e-06	3.98e-05
^{54}Mn	1.71e-09	1.37e-09	1.76e-09	1.50e-09	1.12e-08	6.67e-08
^{52}Fe	1.96e-03	9.26e-03	1.97e-03	9.28e-03	2.05e-03	7.19e-03
^{53}Fe	5.34e-05	6.10e-04	5.36e-05	6.06e-04	6.39e-05	1.03e-03
^{55}Fe	1.77e-06	3.22e-06	1.80e-06	3.00e-06	3.65e-06	8.56e-05
^{59}Fe	7.84e-13	3.86e-10	5.87e-12	8.77e-16	4.55e-11	6.54e-11
^{60}Fe	1.60e-13	1.57e-09	9.65e-13	2.09e-17	1.60e-12	3.40e-11
^{55}Co	2.50e-04	3.16e-03	2.51e-04	3.13e-03	2.74e-04	7.15e-03
^{56}Co	7.09e-07	1.24e-05	7.17e-07	1.23e-05	9.47e-07	3.08e-05
^{57}Co	3.22e-07	1.17e-06	3.30e-07	1.12e-06	6.31e-07	1.19e-05
^{58}Co	3.28e-10	4.92e-10	4.63e-10	4.41e-10	5.09e-09	1.61e-08
^{60}Co	2.96e-13	6.85e-11	2.26e-12	4.86e-14	3.61e-11	7.93e-11
^{56}Ni	3.95e-02	7.45e-01	3.95e-02	7.45e-01	3.89e-02	6.52e-01
^{57}Ni	1.37e-03	1.41e-02	1.37e-03	1.40e-02	1.50e-03	2.49e-02
^{59}Ni	5.24e-05	6.09e-05	5.19e-05	6.04e-05	3.69e-05	1.41e-04
^{63}Ni	1.41e-13	2.85e-09	1.19e-12	4.59e-13	2.23e-11	1.61e-10
^{62}Zn	9.91e-05	2.25e-03	9.89e-05	2.21e-03	9.57e-05	6.05e-03
^{65}Zn	2.51e-08	1.19e-08	2.52e-08	1.19e-08	2.77e-08	1.01e-08
^{65}Ge	3.17e-06	1.42e-06	3.16e-06	1.42e-06	2.97e-06	1.13e-06

Table B.30: Nucleosynthetic yields (in $M_\odot$) of select radioactive nuclides of Model M11_05 with 0.01, 0.1, and 3 $Z_\odot$.

	M11_05_001		M11_05_01		M11_05_3	
	He det $[M_\odot]$	core det $[M_\odot]$	He det $[M_\odot]$	core det $[M_\odot]$	He det $[M_\odot]$	core det $[M_\odot]$
^{14}C	1.02e-12	1.39e-16	1.15e-12	1.46e-16	5.25e-12	4.72e-16
^{22}Na	7.64e-09	1.36e-13	7.56e-09	1.35e-13	6.16e-09	6.06e-10
^{26}Al	2.78e-07	3.39e-11	2.75e-07	3.48e-11	2.00e-07	1.71e-11
^{32}Si	5.17e-13	3.42e-14	5.32e-13	6.53e-14	6.65e-13	9.46e-13
^{32}P	5.12e-09	4.12e-10	5.18e-09	4.19e-10	5.77e-09	2.17e-09
^{33}P	1.91e-09	2.25e-10	1.94e-09	2.35e-10	2.18e-09	1.75e-09
^{35}S	1.04e-09	1.92e-10	1.05e-09	1.93e-10	1.18e-09	1.37e-09
^{36}Cl	1.24e-08	2.21e-09	1.24e-08	2.17e-09	1.36e-08	8.57e-09
^{37}Ar	3.56e-06	8.71e-07	3.56e-06	8.60e-07	3.93e-06	1.93e-06
^{39}Ar	6.85e-11	2.07e-11	6.88e-11	2.01e-11	8.86e-11	1.39e-10
^{40}K	6.61e-10	1.70e-10	6.62e-10	1.65e-10	8.37e-10	6.83e-10
^{41}Ca	9.97e-07	2.58e-07	1.00e-06	2.55e-07	1.30e-06	4.85e-07
^{44}Ti	1.53e-04	2.05e-05	1.53e-04	2.05e-05	1.74e-04	1.15e-05
^{48}V	9.25e-08	1.90e-08	9.44e-08	1.90e-08	1.85e-07	1.77e-08
^{49}V	6.15e-08	5.94e-08	6.21e-08	5.90e-08	9.53e-08	1.12e-07
^{48}Cr	7.16e-04	3.52e-04	7.19e-04	3.53e-04	8.03e-04	2.57e-04
^{49}Cr	1.38e-05	1.62e-05	1.39e-05	1.61e-05	1.66e-05	2.67e-05
^{51}Cr	2.25e-07	1.57e-07	2.29e-07	1.56e-07	4.43e-07	8.98e-07
^{51}Mn	3.12e-05	4.00e-05	3.14e-05	3.96e-05	3.59e-05	8.71e-05
^{52}Mn	8.78e-07	1.91e-06	8.86e-07	1.91e-06	1.17e-06	2.26e-06
^{53}Mn	2.42e-06	9.85e-06	2.44e-06	9.79e-06	3.72e-06	2.33e-05
^{54}Mn	4.42e-09	7.53e-10	4.64e-09	1.09e-09	1.98e-08	2.86e-08
^{52}Fe	2.04e-03	7.79e-03	2.04e-03	7.80e-03	2.23e-03	6.09e-03
^{53}Fe	6.94e-05	5.06e-04	6.97e-05	5.03e-04	7.79e-05	8.74e-04
^{55}Fe	4.55e-06	1.85e-06	4.60e-06	1.89e-06	7.97e-06	3.42e-05
^{59}Fe	5.94e-12	1.69e-17	4.37e-11	1.60e-16	1.46e-10	5.21e-11
^{60}Fe	2.83e-12	9.92e-20	1.68e-11	3.32e-18	1.14e-11	2.51e-11
^{55}Co	2.10e-04	2.63e-03	2.10e-04	2.61e-03	2.24e-04	6.11e-03
^{56}Co	8.28e-07	1.23e-05	8.35e-07	1.23e-05	1.04e-06	2.63e-05
^{57}Co	5.44e-07	1.13e-06	5.51e-07	1.15e-06	1.01e-06	5.85e-06
^{58}Co	9.70e-10	2.38e-10	1.16e-09	3.29e-10	7.19e-09	6.47e-09
^{60}Co	2.78e-12	4.02e-15	1.80e-11	1.46e-14	7.02e-11	5.90e-11
^{56}Ni	1.24e-02	8.47e-01	1.23e-02	8.48e-01	1.14e-02	7.46e-01
^{57}Ni	3.03e-04	1.77e-02	3.03e-04	1.76e-02	2.99e-04	3.35e-02
^{59}Ni	4.36e-06	7.82e-05	4.30e-06	7.76e-05	3.04e-06	2.24e-04
^{63}Ni	6.87e-13	8.60e-15	5.30e-12	8.55e-14	4.06e-11	1.12e-10
^{62}Zn	2.09e-05	3.08e-03	2.10e-05	3.04e-03	2.24e-05	7.57e-03
^{65}Zn	2.04e-09	1.43e-08	2.15e-09	1.43e-08	5.73e-09	1.12e-08
^{65}Ge	8.14e-07	2.04e-06	8.07e-07	2.04e-06	6.46e-07	1.53e-06

Acknowledgements

This work could not have been carried out without the support of other people. First and foremost, I thank Fritz Röpke for his supervision of the project. It would not have been realized without his initiation. His help and advice was always appreciated. Further, I am grateful for the support Sabine Reffert and Stefan Jordan gave me while overseeing the progress of my thesis.

My thanks go to Volker Springel who provided me with the access to the Arepo code which allowed me to carry out the simulations in the way presented here. In connection to this, many thanks go to Rüdiger Pakmor who was always available for discussions and to answer questions. The close collaboration with Christine E. Collins and Stuart S. Sim in Belfast has always been very positive and fruitful. Thank you for the nice working environment and the many SN meetings we had throughout the years.

Moreover, the work has always been great with the people of the PSO group, thanks to Flo, Leo, Theo, Christian and many others. The time spent at HITS, Philosophenweg or Marstall has been wonderful. I especially want to thank those who proof-read my thesis.

I am further grateful to HITS and the Klaus Tschira Foundation for providing me with the needed computational resources and wonderful workspace. Many friendships were formed during my time at the institute.

Last but not least, I thank my family and friends, Simone, Salvador, Daniel, Tobias, and Anton, for being there when I needed to talk.